THE ROLE OF INTERACTING STELLAR WINDS FEEDING SAGITTARIUS A*

Diego Nicolás Calderón Espinoza

PONTIFICIA
UNIVERSIDAD
CATÓLICA
DE CHILE

FACULTAD DE FÍSICA
INSTITUTO DE ASTROFÍSICA

THE ROLE OF INTERACTING STELLAR WINDS FEEDING SAGITTARIUS A*

BY

DIEGO NICOLÁS CALDERÓN ESPINOZA

Thesis submitted to the Faculty of Physics at
Pontificia Universidad Católica de Chile in partial fulfillment
of the requirements for the degree of Doctor in Astrophysics

Thesis Adviser
Dr. JORGE CUADRA
Thesis Co-adviser
Dr. MARC SCHARTMANN

Santiago de Chile, October 2019

PONTIFICIA
UNIVERSIDAD
CATÓLICA
DE CHILE

FACULTAD DE FÍSICA

INSTITUTO DE ASTROFÍSICA

THE ROLE OF INTERACTING STELLAR WINDS FEEDING SAGITTARIUS A*

BY

DIEGO NICOLÁS CALDERÓN ESPINOZA

Members of the Committee

Dr. Jorge Cuadra	(Pontificia Universidad Católica de Chile)
Dr. Marc Schartmann	(Ludwig Maximilian University of Munich)
Dr. Joaquín Prieto	(Universidad de Chile)
Dr. Nelson Padilla	(Pontificia Universidad Católica de Chile)
Dr. Patricia Tissera	(Universidad Andrés Bello)

Santiago de Chile, October 2019

“There is no such thing as truth in this world.

That is our reality.

Anyone can become a god or a devil.

All it takes is for someone claim it for it to be true."

Eren Kruger

To Ignacio.

Published Research

Although some of them are not an integral part of the work presented in this thesis, I have published some articles in peer-reviewed scientific journals as well as conference proceedings during my time working as a Ph.D. student. Those articles are listed here in reverse chronological order.

1. **Stellar winds pump the heart of the Milky Way**
   Calderón, D., Cuadra, J., Schartmann, M., Burkert, A., Russell, C. M. P. , 2019
   Submitted to Astrophysical Journal Letters
   e-print arXiv:1910.06976

2. **3D simulations of clump formation in stellar wind collisions**
   Calderón, D., Cuadra, J., Schartmann, M., Burkert, A., Prieto, J., Russell, C. M. P., 2019
   Submitted to Monthly Notices of the Royal Astronomical Society
   e-print arXiv:1906.04181

3. **The Galactic Centre source G2 was unlikely born in any of the known massive binaries**
   Calderón, D., Cuadra, J., Schartmann, M., Burkert, A., Plewa, P., Eisenhauer, F., Habibi, M., 2018
   Monthly Notices of the Royal Astronomical Society, 478, 3494

4. **A massive binary system can feed Sgr A***
   Calderón, D., Cuadra, J., 2017
   Published in "XV Latin American Regional IAU Meeting"
   Revista Mexicana de Astronomía y Astrofísica, 49, 101

5. **Clump formation through colliding stellar winds in the Galactic Centre**

   Calderón, D., Cuadra, J., Ballone, A., Schartmann, M., Burkert, A., Prieto, J., Gillessen, S., 2017

   Published in "The Multi-Messenger Astrophysics of the Galactic Centre" Proceedings of the International Astronomical Union, IAU Symposium, 322, 204

6. **Searching for molecular outflows in hyperluminous infrared galaxies**

   Calderón, D., Bauer, F. E., Veilleux, S., Graciá-Carpio, J., Sturm, E., Lira, P., Schulze, S., Kim, S., 2016

   Published in Monthly Notices of the Royal Astronomical Society, 460, 3052

7. **Clump formation through colliding stellar winds in the Galactic Centre**

   Calderón, D., Ballone, A., Cuadra, J., Schartmann, M., Burkert, A., Gillessen, S., 2016

   Published in Monthly Notices of the Royal Astronomical Society, 455, 4388

8. **Formation of the infalling Galactic Centre cloud G2 by collision of stellar winds**

   Calderón, D., Ballone, A., Cuadra, J., Schartmann, M., Burkert, A., Gillessen, S., 2015

   Published in "Wolf-Rayet Stars", Proceedings of an International Workshop held in Potsdam, 356

ACKNOWLEDGEMENTS

It is has been a long way reaching this stage, but I must say that I am very happy with how things turned out to be. This thesis is the result of years of dedication in which, I was not alone at all. All of you (even yourself, the reader) have supported me during both the developing of this work and this stage of my life.

First of all, none of this would have been possible without the guidance and support of my adviser, Prof. Jorge Cuadra. Thanks to his academic, and also human, advice I was able to complete this work, and becoming a much more mature researcher. I am strongly convinced that I have been extremely lucky for having such a committed tutor who has trusted in my skills (even at times when I did not), and has bet through encouragement and funding to participate in internships, conferences, summer schools, as well as by sharing his ideas, which are the motivation for the largest fraction of this work. Secondly, I am deeply grateful to Dr. Marc Schartmann for advising me during each of my many visits to Garching, without having to do so. His support, ideas, and critical thought on this work definitively helped to improve it significantly as well as made my visits to Garching much more pleasurable (of course, together with Birgit and Anna). At the same level of importance, I thank Prof. Andreas Burkert for having allowed and supported my visits to Garching, and for pushing me to do a better job and think critically sometimes even beyond my capabilities. Thirdly, I would like to say thanks to Dr. Joaquín Prieto and Dr. Christopher M. P. Russell, whom with I have collaborated, and gave me crucial guidelines for improving my work, especially on the numerical aspects at the early and late stages of my PhD studies, respectively. Furthermore, I thank to many researchers with whom I have had constructive discussions, which helped to improve this work. Among them, in no particular order are Prof. Franz E. Bauer, Dr. Alessandro Ballone, Dr. Stefan Gillessen, Dr. Frank Eisenhauer, Dr. Maryam Habibi, Dr. Philipp Plewa, and Dr. Almudena Prieto.

Of course, I would like to extend my gratitude my fellow graduate students (some of them already graduated) for bringing encouraging words, enjoying coffee, sweets, and memes together during our (many) work breaks: Dr. Felipe G. Goicovic, Johanna Coronado, Dr. Gergely Hajdu, Rodrigo Carvajal, Dr. Camila Navarrete, Francisco Aros, Dr. Sebastian Stammler, Katerine Joachimi, Enrique Paillas, Lorena Guitérrez, Camila Órdenes, Carolina Andonie, Camilo Fontecilla, Matías Gárate, Jonathan Quirola, and Tianwen Cao. Also, to the members of the PLAGA group at PUC, PGN at MPE, and CAST at LMU. In the same context, special thanks to the administrative staff at Instituto de Astrofísica at PUC for making the work environment much more friendly: Mauricio Barz, Carmen Gloria Cordovez, Mariela Villanueva, Giselle Ulloa, Cynthia Castillo, María José Sepúlveda, and Juan Véliz. Furthermore, to my fellows at the MPE, Dr. Matías Blaña, Manuel Behrendt, Carolina Agurto, Martha Lippich, Martina Karl, and Jiamin Hou.

To my friends at Santiago and Garching, for their support as well as making my life happier, Claudia Sepúlveda, Alonso Fabres, Cynthia Vega, Eric Abello, Carol Rojas, and Romina Henríquez; Manca Novinec, Sašo Drenik, their daughters Mina and Leni, Andrés Cathey, Paula Espinosa, Mauricio Cuevas, Farah Atour, Alejandro Berendsen, and Loretto Paredes.

To the entire Espinoza family from Los Ángeles, Chile, for believing in me and supporting my career as well as my life since I was born. Special thanks to my grandparents Alicia Caballero and Elsa Aguilera, as well as Nolberto Espinoza†, each one uncles, aunts, and cousins, especially to Daniela (and Nicolás) and Javier (and María Ignacia) during the last and most difficult period of my studies. To the young toddlers and babies who bring happiness and joy into my world every time we meet: Antonio, Domingo, and Simón. To my dear Carolina, for the things we shared through these years, especially during our time living abroad. But the most important words of gratitude go to my family nucleus: my parents Lorena and Luis, and Mireya for taking care of me despite having left home in Los Ángeles about 10 years ago. Finally, to our brotherhood that keeps me living as a happy human being, my most sincere gratitude to my brother, Ignacio.

Additionally, I would like to say thanks to every taxpayer from Chile and Germany, since

their contribution has indirectly funded my entire scientific career until the present. I have been funded through the program CONICYT-PCHA/Doctorado Nacional (2015-21151574). I acknowledge the kind hospitality of the Max Planck Institute for Extraterrestrial Physics during my many visits throughout my PhD studies. Also, to the funding from the Max Planck Society through a “Partner Group" grant (PI: Jorge Cuadra), and the support from CONICYT project Basal AFB-170002.

AGRADECIMIENTOS

Ha sido un largo camino llegar hasta esta etapa y poder terminarla. Debo admitir que, a pesar de todo, estoy muy satisfecho con como resultaron las cosas. Esta tesis es el resultado de años de dedicación durante los cuales nunca estuve solo. Todos Ustedes (incluso tú, el lector) me han apoyado a lo largo de este trabajo y también en esta importante fase de mi vida.

Primero que todo, nada de esto hubiera sido posible sin el apoyo y la tutela de mi Profesor guía, Jorge Cuadra. Gracias no sólo a sus consejos académicos, sino también humanos fui capaz de desarrollar este trabajo y, al mismo tiempo, convertirme en un investigador mucho más experimentado. Estoy seguro que he sido inmensamente afortunado por haber tenido un profesor guía tan comprometido, que confió en mis habilidades (incluso cuando yo no lo hacía), y quiso apostar en mí incentivando mi participación en pasantías, conferencias, escuelas de verano, además de compartir sus ideas que motivaron una gran parte de este trabajo. En segundo lugar, estoy muy agradecido con el Dr. Marc Schartmann actuar como mi co-tutor durante cada una de mis visitas a Garching sin tener la obligación de hacerlo. Su apoyo, ideas y pensamiento crítico contribuyeron a mejorar significativamente la calidad y rigurosidad de este trabajo, además de haber hecho mucho más agradables mis visitas a Garching (por supuesto, junto a su familia: Birgit y Anna). En esta misma línea, le agradezco al Profesor Andreas Burkert por haber permitido y apoyado mis visitas a Garching, además de presionarme a hacer un mejor trabajo y pensar críticamente, algunas veces incluso más allá de mis capacidades. En tercer lugar, me gustaría darle las gracias a los investigadores Dr. Joaquín Prieto y Dr. Christopher M. P. Russell, con quienes he trabajado y me han guiado en ciertos aspectos de mi trabajo, especialmente, en la parte numérica durante las etapas iniciales y finales de mis estudios doctorales, respectivamente. También quisiera agradecerle a varios científicos con los que tuve discusiones constructivas que ayudaron a mejorar este

trabajo. Dentro de ellos, en ningún orden particular: Profesor Franz E. Bauer, Dr. Alessandro Ballone, Dr. Stefan Gillessen, Dr. Frank Eisenhauer, Dra. Maryam Habibi, Dr. Philipp Plewa y Dra. Almudena Prieto.

Por supuesto, me gustaría extender mis palabras de gratitud a mis compañeros de postgrado (algunos de ellos ya graduados) por sus palabras de apoyo y del disfrutar café, dulces y memes juntos durante nuestros (muchos) descansos: Dr. Felipe G. Goicovic, Johanna Coronado, Dr. Gergely Hajdu, Rodrigo Carvajal, Dra. Camila Navarrete, Francisco Aros, Dr. Sebastian Stammler, Katerine Joachimi, Enrique Paillas, Lorena Gutiérrez, Camila Órdenes, Carolina Andonie, Camilo Fontecilla, Matías Gárate, Jonathan Quirola y Tianwen Cao. También a los miembros del grupo PLAGA en la PUC, PGN en el MPE y CAST en la LMU. En este mismo contexto, muchas gracias a los trabajadores administrativos del Instituto de Astrofísica por hacer mucho más grato el ambiente laboral: Mauricio Barz, Carmen Gloria Cordovez, Mariela Villanueva, Giselle Ulloa, Cynthia Castillo, María José Sepúlveda y Juan Véliz. Además, a mis compañeros del MPE, Dr. Matías Blaña, Manuel Behrendt, Carolina Agurto, Martha Lippich, Martina Karl y Jiamin Hou.

A mis amigos que viven en Santiago o Garching, por su apoyo y por hacer mi vida mucho más feliz durante este período: Claudia Sepúlveda, Alonso Fabres, Cynthia Vega, Eric Abello, Carol Rojas y Romina Henríquez; Manca Novinec, Sašo Drenik, sus hijas Mina y Leni, Andrés Cathey, Paula Espinosa, Mauricio Cuevas, Farah Atour, Alejandro Berendsen y Loretto Paredes.

A toda mi familia Espinoza de Los Ángeles en Chile, por creer en mí y apoyarme a lo largo de toda mi carrera y durante toda mi vida desde que nací. Agradecimientos especiales a mis abuelos Alicia Caballero, Elsa Aguilera y Nolberto Espinoza†, a cada uno de mis tíos, tías y primos, especialmente les agradezco a Daniela (y Nicolás) y Javier (y María Ignacia) por su apoyo durante la última y más difícil etapa de este proceso. A los pequeños infantes y bebés que traen alegría y gozo a mi mundo cada vez que los veo: Antonio, Domingo y Simón. A mi querida Carolina, por las cosas que compartimos a través de estos años, especialmente por nuestra vida juntos en el extranjero. Pero mis más sinceras palabras de gratitud van para mi

núcleo familiar: mis padres Lorena y Luis, y Mireya por cuidarme hasta el día de hoy, a pesar de haber dejado mi hogar en Los Ángeles hace ya más de 10 años. Finalmente, a nuestra hermandad que me mantiene vivo como un hombre feliz, mis más sinceros agradecimientos a mi querido hermano, Ignacio.

Adicionalmente, me gustaría darle las gracias a todos los contribuyentes de Chile y Alemania, dado que indirectamente son ellos quienes han financiado toda mi carrera científica hasta el día de hoy. Mis estudios doctorales han sido financiados a través del programa CONICYT-PCHA/Doctorado Nacional (2015-21151574). Agradezco enormemente la hospitalidad del Instituto Max Planck de Física Extraterrestre durante mis múltiples visitas. También, le agradezco a la Sociedad Max Planck que financió parte de este trabajo a través de un programa "'Partner Group" (IP: Jorge Cuadra) y el apoyo de CONICYT mediante el projecto Basal AFB-170002.

CONTENTS

LIST OF TABLES

LIST OF FIGURES

ABSTRACT

The central parsec of the Milky Way is among the most enigmatic regions in the entire Galaxy. The existence of the central super-massive black hole, Sgr A*, and its proximity allow us to use it as a laboratory for understanding the astrophysics of galactic nuclei, in general. Although it is well known that this is a very hostile environment due to the presence of tens of Wolf-Rayet (WR) stars with strong outflows, the recent detection of cold gas ($\sim 10^4$ K) has challenged our understanding of the gas dynamics and thermodynamics of the region. The so-called G2 source, the dusty sources in the IRS 13E cluster, as well as the disc-like structure in the immediate vicinity of Sgr A* are examples of such cold material.

In this thesis, we present a detailed study of the formation of cold gas as a potential result of the collision of the many stellar winds, which are constantly taking place. The main aims of this study are: *i*) testing the hypothesis of G2 being a gaseous clump formed in a massive binary system, *ii*) constraining the initial properties and final fate of clumps formed in unstable wind interactions, *iii*) establishing whether it is possible or not for the system of WR stars orbiting Sgr A* to reach and remain in a steady state between the supplying and inflowing/outflowing material.

We find that the properties and dynamics of the clumps produced in the known massive binaries are not consistent with G2's, ruling out this hypothesis. Additionally, we perform adaptive-mesh refinement hydrodynamical simulations of idealised stellar wind collisions in order to characterise the clump formation process. The results show that clumps formed through thin-shell instabilities are not massive enough to impact significantly the state of the material enclosed within the inner parsec. Finally, the simulation of the complete system of WR stars orbiting Sgr A* shows that the natural outcome of its long-term evolution is the accumulation of material at its centre. Thus, we speculate that the WR stars and their outflows could explain all the phenomenology related to the activity of Sgr A* inferred from observations without the need of invoking external agents.

Keywords: Galaxy: center — hydrodynamics — stars: winds, outflows — accretion.

RESUMEN

El pársec central de la Vía Láctea es una de las regiones más enigmáticas de la Galaxia. La existencia del agujero negro súper-masivo central, Sgr A*, y su cercanía lo hacen un laboratorio ideal para estudiar la astrofísica de núcleos galácticos, en general. A pesar de conocer bien la hostilidad del entorno debido a la presencia de decenas de estrellas Wolf-Rayet (WR) con poderosas eyecciones de material, la detección de gas frío ($\sim 10^4$ K) ha desafiado nuestro entendimiento de la dinámica del gas y termodinámica de la región. El objeto conocido como G2, las fuentes polvorientas en IRS 13E y la estructura en forma de disco en la vecindad de Sgr A* son algunos ejemplos de dicho material frío.

En esta tesis, se presenta un estudio de la formación de gas frío como posible resultado de la colisión de los muchos vientos estelares que se encuentran interactuando constantemente. Los objetivos de este trabajo son: *i*) estudiar la hipótesis en la cual G2 es una nube gaseosa formada en un sistema binario de estrellas masivas, *ii*) constreñir las propiedades iniciales y destino final de los grumos formados en colisiones inestables de vientos estelares, y *iii*) estudiar la posibilidad de que el sistema de estrellas WR que orbitan a Sgr A* alcance un estado estacionario entre el material suministrado y el de entrada/salida de la región.

Los resultados muestran que las propiedades y la dinámica de los grumos creados en binarias masivas no son consistentes con las de G2, por tanto, la hipótesis es rechazada. Además, se desarrollan simulaciones hidrodinámicas idealizadas de colisiones inestables de vientos estelares para caracterizar el proceso de formación de grumos. Los hallazgos establecen que los grumos creados mediante inestabilidades de placa delgada no son lo suficientemente masivos para afectar el estado del gas en el pársec central. Finalmente, la simulación del sistema de estrellas WR orbitando a Sgr A* muestra que el resultado natural de la evolución del sistema en escalas largas de tiempo es la acumulación de material en su centro. Se especula que estas estrellas y sus vientos podrían explicar toda la fenomenología relacionada con la actividad de Sgr A* que se infiere de las observaciones, sin la necesidad de la acción de agentes externos.

Palabras Clave: La Galaxia: el centro – hidrodinámica – estrellas: vientos, salidas – acreción

1

Introduction

The Galactic Centre is by far the closest galactic nucleus we have access to. Despite the high extinction in the optical (about ~30 magnitudes), it is possible to observe it either at longer wavelengths (e.g. sub-mm, infrared) or at higher energies such as X- and γ-rays. The fact that the region harbors gas in many phases, an extremely dense star cluster, as well as a super-massive black hole (SMBH) makes it one of the most intriguing environments of our Galaxy. Before describing some of the puzzles of the region and the main goals of this work, we give a brief summary of the physical properties of the Galactic Centre in Section 1.1. This content is mostly based on the reviews by Genzel, Eisenhauer, and Gillessen (2010), and Mapelli and Gualandris (2016). Then, we give a description of the numerical hydrodynamics tools used in this work in Section 1.2. Basically, we introduce the foundations of grid-based numerical hydrodynamics following the review by Teyssier (2015). Finally, in Section 1.3 we present the motivation and main goals of this work.

1.1 The Galactic Centre

The centre of the Milky Way contains neutral, ionised, and extremely hot gas, as well as a very dense, luminous star cluster. Additionally, it hosts the closest SMBH seen from Earth, Sagittarius A* (hereafter Sgr A*)[1], at a distance of only ~8.3 kpc (~24000 light-years; Gillessen et al., 2017). In this section, we introduce the main components present in its vicinity. Firstly, we review the properties and structure of the gas in different phases from parsec to milliparsec scales in Section 1.1.1. Then, we give a description of the current

[1] Pronounced as “Sagittarius A-Star".

knowledge of the nuclear star cluster, focusing on the young, massive stars that inhabit the central parsec in Section 1.1.2. In Section 1.1.3, we summarise the evidence supporting the hypothesis of Sgr A* being a SMBH, and its properties. Finally, in Section 1.1.4 we describe the physics of the enigmatic G2 object, discussing observations and hypotheses of its nature.

1.1.1 The gaseous component

In general, the interstellar medium in the central region of the Galaxy can be described as an ionised gas cavity at scales of ~1–1.5 pc from Sgr A*. This cavity is surrounded by streamers of dense molecular gas and warm dust that corresponds to the so-called circum-nuclear disc (CND) that extends between ~1.5–4 pc (e.g. Jackson et al., 1993; Christopher et al., 2005). Beyond this radius the environment is populated by several massive molecular clouds (Mezger, Duschl, and Zylka, 1996). The top panels of Figure 1.1, especially the top right panel, show the location and shape of these structures.

The ionised gas corresponds to the structures known as Sgr A East and Sgr A West, both observable in radio wavelengths (Novak et al., 2000; Zhao et al., 2009). The former is conceived as a supernova remnant due to its elliptical shell shape and non-thermal emission (Yusef-Zadeh and Morris, 1987; Novak et al., 2000). It is a relatively large scale structure of about 10 pc along its major axis, and whose centre is ~2.5 pc to the East from Sgr A*. The latter is known as the *minispiral* due to its geometry of three streamers that are apparently falling towards the centre (see top panels of Figure 1.1; Roberts and Goss, 1993; Paumard, Maillard, and Morris, 2004; Zhao et al., 2009; Zhao et al., 2010). These arms reach further inside up to a few arcseconds from Sgr A*[2]. The strong ultraviolet (UV) radiation field of the young, massive stars located closer in is thought to keep this material ionised (Martins et al., 2007). Radio and infrared (IR) recombination line observations suggest that the temperature of the gas in the minispiral is in the range ~10^3–10^4 K (e.g. Maloney, Hollenbach, and Townes, 1992; Roberts and Goss, 1993). Based on these observations, the total mass of

[2]A single arcsecond at the distance of the Galactic Centre (~8.3 kpc) corresponds to ~0.04 pc.

ionised gas is calculated to be ~25 $M_\odot$. On top of this, there is a neutral gas component of ~300 $M_\odot$ (Jackson et al., 1993), and few ~$M_\odot$ of warm dust (Davidson et al., 1992). The observed “opened cavity" (see top panels of Figure 1.1) is likely to be the result of the stellar winds of the young, massive stars pushing some of this material outwards (see bottom panels of Figure 1.1; Genzel, Hollenbach, and Townes, 1994). Given the properties of the minispiral, the mass inflow rate into the central arcseconds is estimated to be ~10^{-3} $M_\odot yr^{-1}$ (Genzel, Hollenbach, and Townes, 1994).

The CND is the reservoir of dense warm molecular, and atomic gas within ~5 pc. It is observed as rotating disc or a couple of filaments that reach a radius of ~1.5pc, i.e. the maximum extension of the minispiral (see top panels of Figure 1.1). The CND contains clumps of material that if virialised and stable would have masses of ~10^4 $M_\odot$. Although uncertain, the total mass in this structure is estimated to be between ~10^5–10^6 $M_\odot$ (Christopher et al., 2005; Montero-Castaño, Herrnstein, and Ho, 2009). Based on this calculation and the noncircular motions of the CND, the mass inflow rate at this scale is inferred to be about ~10^{-2} $M_\odot$ yr^{-1}.

The central parsec also shows diffuse, hard X-ray line and continuum emission of a plasma at very high temperatures (~10^7–10^8 K), which is observed in the energy range 1–10 keV (see Goldwurm, 2011, for a review). The diffuse emission is consistent with a thermal emission from a ~1 keV plasma whose mean density is ~10 cm^{-3} (Baganoff et al., 2003). Additionally, it is possible to detect a compact source associated to Sgr A*, as well as other compact stellar objects in the region (Baganoff et al., 2003; Xu et al., 2006). A remarkable feature in the region is observed at the location of the IRS 13E cluster (see lower panels of Figure 1.1). At larger scales (~10–30 pc), it is possible to detect the 6.4 keV Kα emission line from neutral Fe together with hard X-ray continuum at the location of some molecular clouds. These signatures have been interpreted as reflection or fluorescence of cold gas, which was illuminated by a time variable source likely Sgr A* (see Figure 1.2; Muno et al., 2007). In Section 1.1.3.2 we come back to discuss this topic further.

Finally, the innermost parsec hosts enigmatic, dusty sources composed mainly of cold gas (~10^4 K). Among these are the bright knots observed in the IRS 13E cluster (see Sec-

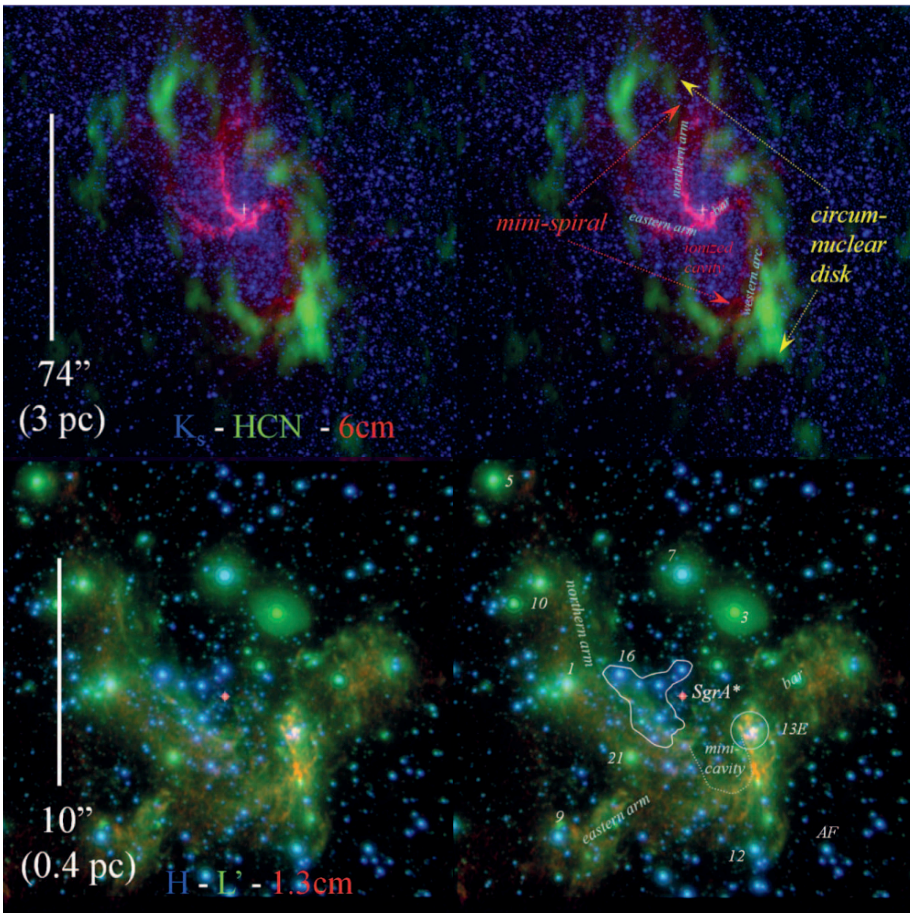

Figure 1.1: Multiwavelength overview of the central few parsecs of the Milky Way. Top and bottom panels are large (~3 pc) and small (~0.4 pc) scale multicolour images of the Galactic Centre, respectively. The top left panel shows Very Large Array (VLA) radio 6 cm emission in pink, Owens Valley Radio Observatory (OVRO) HCN 1-0 emission in green, and a K-band (2.2 μm) image in blue. The top right panel is identical to top left panel but highlighting some structures, such as the circumnuclear disc and the minispiral. The bottom left panel shows a composite near-IR adaptive optics image, where blue, green, and red represent the observation in the H band (1.6 μm), L’ band (3.8 μm), and VLA 1.3 cm continuum, respectively. The bottom right panel is identical to bottom left panel but indicating the names and IDs of relevant structures in the region. The location of the radio source Sgr A* is shown with a cross at the centre of each image. The Figure is an adaptation of Figure 1 of Genzel, Eisenhauer, and Gillessen (2010), and is a compilation of many observations (Genzel, Eisenhauer, and Gillessen, 2010, and references therein).

tion 1.1.2.5). Furthermore, the so-called G2-like objects correspond to these kind of sources (see Section 1.1.4). Although small ($\lesssim$ 200 au), their potential infalling onto the central SMBH makes them very intriguing sources (see Section 1.1.3.2). However, what is the physics behind them and how they can be formed in such a hot, hostile environment are unknowns without explanation until the present day.

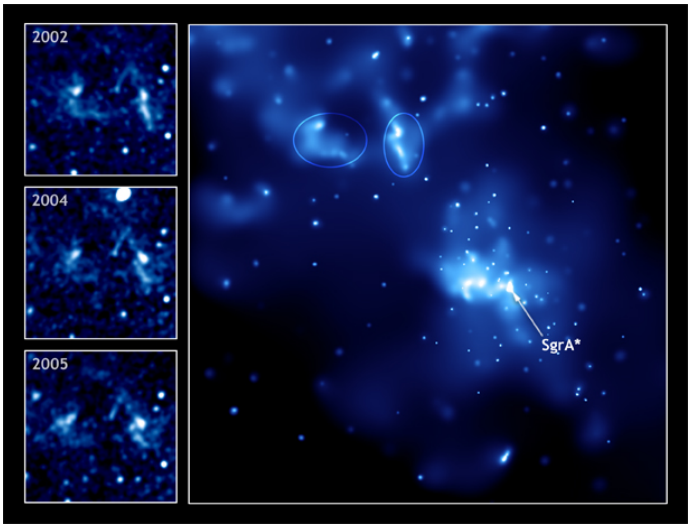

Figure 1.2: CHANDRA view of the of the centre of the Galaxy. The right panel corresponds to 12.5 arcmin across, while the smaller panels on the left side are close up images of 5 arcmin across. Image credits to NASA/CXC/Caltech/Muno et al. (2007).

1.1.2 The stellar component

1.1.2.1 The nuclear star cluster

The stars that inhabit the Galactic Centre (the central few parsecs) are known as the nuclear star cluster (NSC) of the Galaxy. In the Milky Way, the NSC is the only cluster of its kind where single stars can be resolved, and their proper motion detection is possible due to its proximity. This fact makes it a unique laboratory to study the spectral and dynamical properties of its stellar populations. Chatzopoulos et al. (2015) estimated that the mass of the

nuclear star cluster enclosed within ~100 arcsec (4 pc) is about ~9.3×10^6 $M_\odot$, which makes it even larger than the SMBH's.

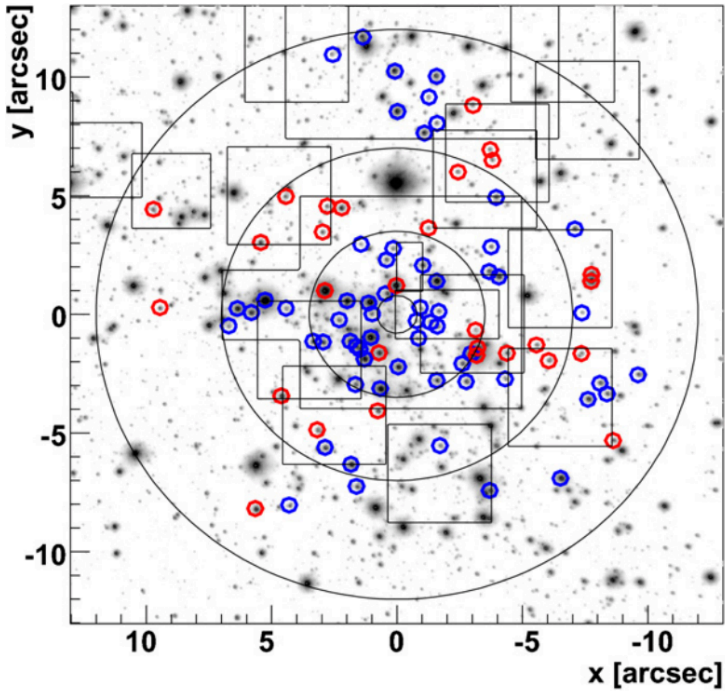

Figure 1.3: Sky-projected distribution of 90 WR/O stars in the central 0.5 pc of our Galaxy. Blue circles highlight 61 stars that have clockwise orbits, while the red circles show 29 stars with counterclockwise orbits. The concentric black circles indicate projected distances of 0.8, 3.5, 7, and 12 arcsec from Sgr A*. The black squares show the fields observed at high resolution with SINFONI spectroscopy. Figure taken from Bartko et al. (2009).

The NSC is one of the richest environments in terms of young (~6 Myr), massive ($\gtrsim$ 10 $M_\odot$) stars in the whole Galaxy. Thanks to the deep spectroscopic studies, it has been possible to identify about ~180 stars of this kind present in the region (see Figure 1.3). This considers luminous blue supergiants and Wolf-Rayet (WR) stars, as well as dwarf and giant main-sequence O- and B-type stars (Paumard et al., 2006; Martins et al., 2007; Bartko et al., 2009; Bartko et al., 2010; Habibi et al., 2017). However, they still correspond to a very small fraction of the total number of stars in the cluster. About 96% of the observed stars within

the central parsec are relatively old (>1 Gyr), late-type giants stars, while others are on the horizontal branch, or in the red clump. They have low to intermediate masses (0.5–4 $M_{\odot}$). Finally, there some stars in the asymptotic giant branch, and massive red supergiants (Blum et al., 2003).

The fact that the Galactic Centre hosts a large number of young, massive stars has been a puzzle for a long time, as it is hard to conceive star formation taking place in such a hostile environment. This is one of the reasons why the NSC has been monitored for decades, which has allowed to determine the stellar properties of its population with high accuracy. The radial velocities, proper motions, and spectral types of the stars have been constrained precisely thanks to the current era observational facilities, such as the near-IR camera NACO and the integral field spectrograph SINFONI at the Very Large Telescopes (VLTs), as well as the near-IR camera NIRC2 and the OH-Suppressing Infrared Imaging Spectrograph (OSIRIS) at the Keck telescopes.

1.1.2.2 The disc of young stars

Through the analysis of the angular momentum direction of the orbits of the young (or early-type) stars it was found that some of them are located on a disc, which is known as the *clockwise disc* due to its sky-projected motion (Levin and Beloborodov, 2003; Paumard et al., 2006; Bartko et al., 2009; Do et al., 2013; Yelda et al., 2014). The fraction of the early-type stars located on the disc is in the range ~20-50% (Do et al., 2013; Yelda et al., 2014). Additionally, there were claims of the existence of another but less defined stellar disc, although rotating counterclockwise instead (Bartko et al., 2009; Lu et al., 2009).

The most recent observations have confirmed the existence of the clockwise disc (see Figure 1.4), but indicated that it is smaller than originally thought, having a radius of only ~0.13 pc (Yelda et al., 2014). Furthermore, they found no statistically significant evidence for the existence of the counterclockwise disc. The same study showed that the orbital eccentricity distribution shows a peak around 0.2–0.4. Regarding the age of the young,

massive ($\gtrsim$10 $M_\odot$) stars, Paumard et al. (2006) estimated it to be 6 ± 2 Myr. However, the most recent analysis concluded is about 2.5–6 Myr (Lu et al., 2013).

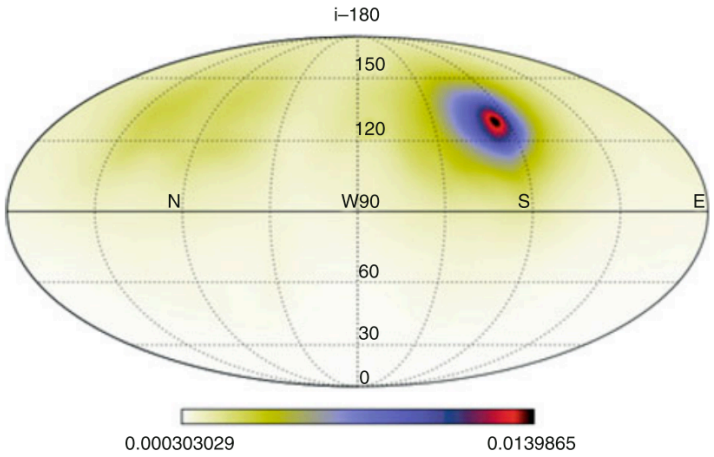

Figure 1.4: Density of the angular momentum orientation of the stars located at 0.8–3.2 arcsec (~0.032–0.128 pc) from Sgr A*. The horizontal lines represent orbital inclination i, and are spaced in 30°; while the longitudinal lines stand for the longitude of the ascending node Ω, and are separated by 45° (E being Ω = 0). Notice the highest density that represents the clockwise disc is located at Ω = 96° and i = 130°. Although not shown here, this features fades at larger distances from the SMBH. Figure taken from Yelda et al. (2014).

Out of these ~180 stars, 30 have been spectroscopically identified as WR. This type of stars experience strong mass outflows being launched at supersonic speeds. Martins et al. (2007) modelled the atmospheres of this sample in order to reproduce their H- and K-band SINFONI spectra, and determine the properties of their stellar winds. They could derive precisely the mass-loss rates and terminal wind velocities of 18 out of the 30 WR stars. Based on spectral similarities, Cuadra, Nayakshin, and Martins (2008) assigned approximate values for such properties to the 12 stars left (see Table 4.1 in Appendix 4.A). Thus, it was possible to characterise the motion, as well as the wind properties of the entire sample of mass-losing stars in the region. This result is crucial for understanding the formation of cold gas (~10^4 K) in the central parsec, which might be formed as a result of the collisions of these stellar winds

that are constantly taking place in the region (see Section 1.3).

1.1.2.3 Massive binaries

Currently, there are three confirmed massive binary systems in the Galactic Centre. IRS 16SW is a system of two equally massive stars with 50 $M_\odot$ each, and a period of 19.5 days (Martins et al., 2006). This binary was identified due to its large photometric and spectroscopic variability as it is an eclipsing binary. Additionally, it is observed to be part of the clockwise disc. More recently, Pfuhl et al. (2014) identified two more massive binaries: IRS 16NE and E60. The former corresponds to a system with an orbital period of 224 days, and enough mass for being a dynamically hard binary. Thus, it is expected to survive dynamical evaporation, even in such a dense cluster like the NSC. The latter was found to be another eclipsing binary located at a distance of ~5 arcsec from Sgr A*. Its period is ~2.3 days, and the stellar masses are 20 and 10 $M_\odot$. None of these binaries is observed to lie on the clockwise disc.

Besides those three systems, there are other four binary candidates in the region. IRS 7E2 and IRS 29N show certain variability, although it seems to be intrinsic rather than due to the presence of a companion star. Furthermore, no periodicity has been detected yet, therefore, more data is needed either to confirm or rule out their binarity. The other couple of candidates are located significantly further from Sgr A* ($\gtrsim$ 30 arcsec). This is why they have not been included in the latest surveys, so they remain as potential but unconfirmed binaries (Pfuhl et al., 2014). However, they are viable targets for future spectroscopic follow-ups.

Among the most interesting aspects of the presence of massive binaries within the inner parsec, it is their potential role as sources of cold gas in form of clumps (see Section 1.1.4; Calderón et al., 2016). As we discussed in Section 1.1.1, the presence of cold gas in the region is still a puzzle to solve, and the hypothesis of massive binaries being the sources of such material is one of the ideas that we develop in this work.

1.1.2.4 The S-stars

The stars orbiting Sgr A* within the innermost arcsecond ($\lesssim$ 0.04 pc) belong to the so-called S-star cluster (e.g. Schödel et al., 2003; Gillessen et al., 2009a). These stars correspond to B-type stars with ages around 6–400 Myr (Eisenhauer et al., 2005). Since they have been monitored from 1992 until the present day, and their orbital periods are relatively short, it has been possible to constrain their orbits with high precision. Furthermore, it has been observed that these orbits are isotropically distributed consistent with a thermal distribution (Schödel et al., 2003; Gillessen et al., 2009a; Gillessen et al., 2017).

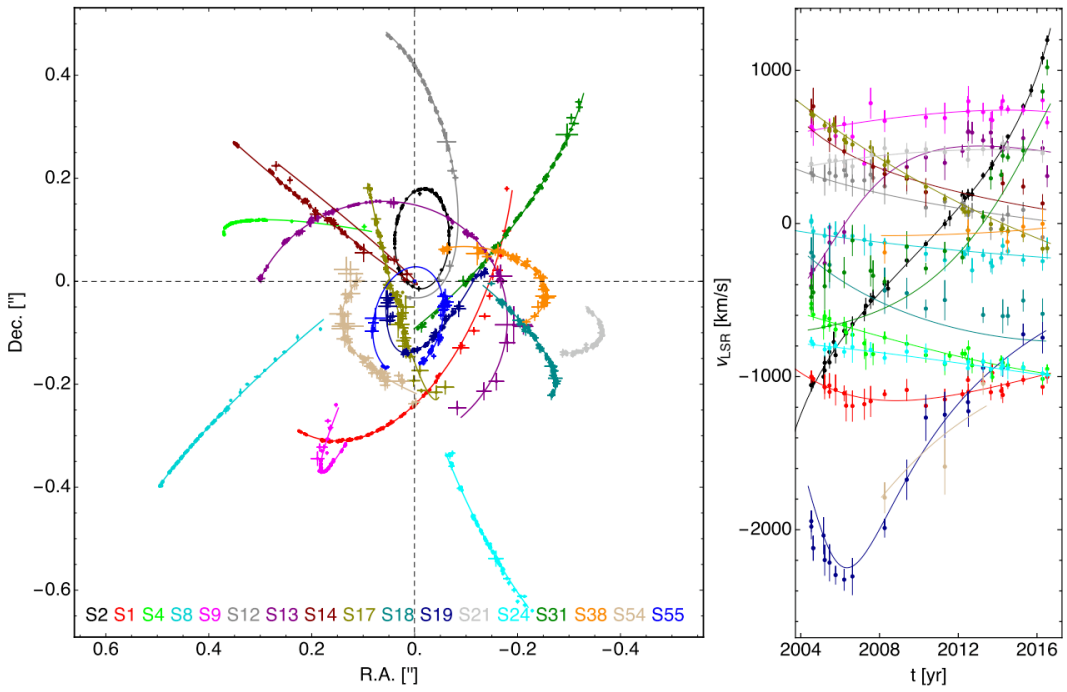

Figure 1.5: Proper motions and line-of-sight velocities of the S-stars. The left panel shows astrometric data (dots) of 17 stars together with the best fit to each of their orbits (solid lines). Each colour represents a single S-star. Sgr A* is considered to be at the origin of the reference frame. The right panel contains line-of-sight velocity as a function of time. The colour coding is the same as in the other panel. The velocities of each star (dots) are shown along with the best fit to the orbits as well (solid lines). This Figure was taken from Gillessen et al. (2017).

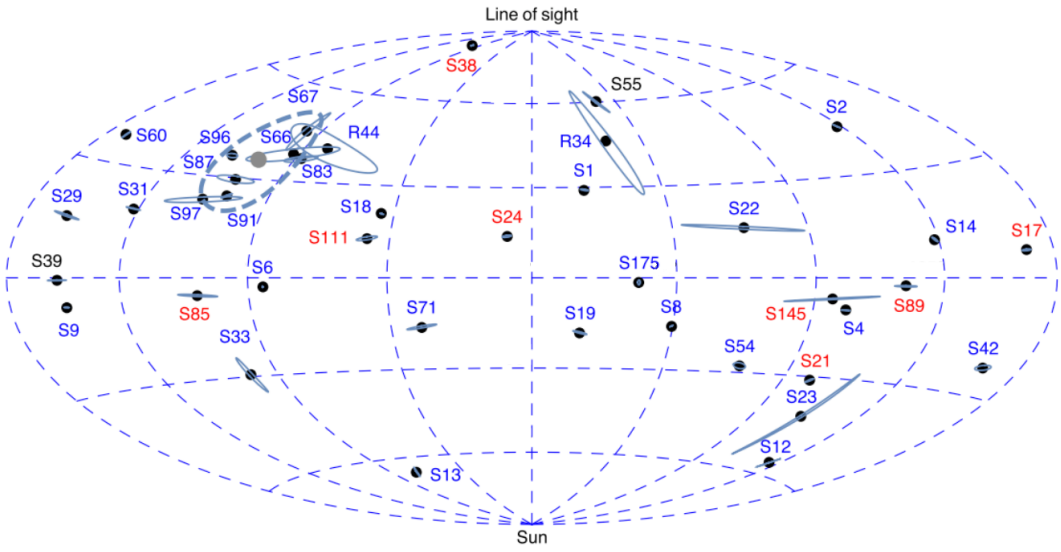

Figure 1.6: The vertical dimension indicates the inclination i of the orbital plane while the horizontal dimension the longitud of the ascendent node Ω. Thus, a star in a face-on, clockwise orbit relative to the line-of-sight would be located at the top of the Figure, while a star in an edge-on orbit would be at the equator. Each dot represents a single star whose orbit has been derived with their associated error measurements (grey ellipses). The larger grey dot represents the orientation of the clockwise disc at $\Omega = 104°$ and $i = 126°$ (Bartko et al., 2009; Yelda et al., 2014). Without considering the stars located on the disc, the stars are oriented randomly. This Figure was taken from Gillessen et al. (2017).

Very recently, Habibi et al. (2017) combined and analysed 12 years of high-resolution spectroscopic data of eight of them. Based on this, they concluded that the stars have high surface gravity with relatively high effective temperatures ($\sim 2 \times 10^4$ K), masses in the range 8–14 $M_\odot$, and ages of less than 15 Myr. The most recent observations of their orbits were reported by Gillessen et al. (2017) setting tighter constraints on their motions. Figure 1.5 shows more than a decade of astrometry and velocity measurements of 17 S-stars. The left panel shows the sky-projected location through the years (dots) along with the best orbital fit for each star (lines). Notice that there is only one star whose orbit has been monitored completely. This corresponds to S2 (or S0-2), which has been crucial for cementing Sgr A* as

a SMBH (see Section 1.1.3.1). The right panel shows the line-of-sight velocity measurements as a function of time, also with fits to their orbits. The same authors confirmed that the angular momentum direction of the stars is randomly distributed (see Figure 1.6). However, they noticed that some orbits are aligned with the clockwise disc instead.

1.1.2.5 The IRS 13E cluster

IRS 13E is an intriguing overdensity of sources located at ~5 arcsec from Sgr A*. It corresponds to an association of three blue supergiant stars: two WR (E2 and E4) and an O/B supergiant (E1) stars, inside a region of ~0.3 arcsec of radius (see Figure 1.7). The region displays X-ray emission as well as some prominent local radio enhancements. Additionally, there are many other sources nearby detected in the H,K, and L' bands. Maillard et al. (2004) proposed that the system could be a self-gravitating star cluster with an embedded intermediate mass black hole (IMBH). By then, the argument was solely based on the fact that the source concentration was above the expected statistical fluctuations. Through the analysis of proper motions and line-of-sight velocities, it was possible to set constraints on the required mass for keeping the system bounded (Maillard et al., 2004; Paumard et al., 2006). However, many of the observed sources in the region did not show clear signs of being actual stars. Fritz et al. (2010) observed that some of them are peaks of hot dust and ionised gas but did not find evidence of stellar objects in them. Without compact objects within the knots (especially in E3, see Figure 1.7), it is not possible to relay on their motion to compute the enclosed mass as it is not justified using them as test particles. Furthermore, it is possible to explain the X-ray emission through the interaction of the WR stellar winds or with the gaseous medium (Coker and Pittard, 2000; Coker, Pittard, and Kastner, 2002; Baganoff et al., 2003) without the need of an IMBH. In a recent study, Tsuboi et al. (2017) presented new H30α recombination line together with radio continuum observations. Based on the detection of a large velocity gradient in a small region, specifically in E3 (see Figure 1.7), they claimed the potential existence of a gaseous disc around a compact massive object of about ~10^4 $M_\odot$, i.e. an IMBH.

Thus, the IRS 13E cluster remains as an interesting environment for hosting an IMBH but not entirely convincing yet.

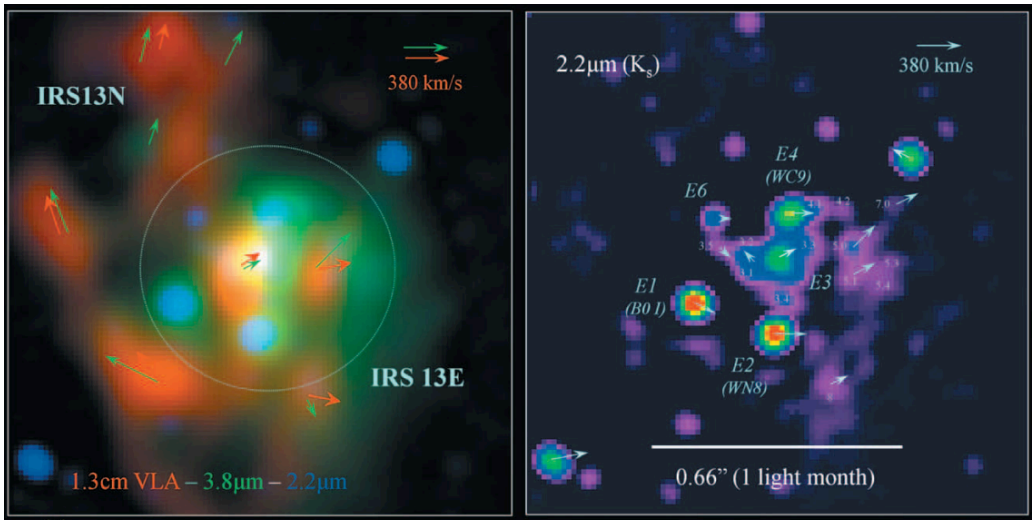

Figure 1.7: The compact stellar group IRS 13E. The left panel shows a multicolour image where K_s is blue, L' is green, and VLA 1.3 cm continuum emission is red. The arrows represent the proper motion of the sources. The right panel is a NACO adaptive optics image in the K_s band. The sources with labels E1, E2, and E4 are identified as blue supergiants. This Figure is an adaptation from Genzel, Eisenhauer, and Gillessen (2010), and originally taken from Fritz et al. (2010).

1.1.3 The central super-massive black hole: Sgr A*

1.1.3.1 Sgr A* as a SMBH

During the present year it was observed, for the first time, the shadow cast due the presence of a SMBH in the centre of the galaxy M87 (Event Horizon Telescope Collaboration et al., 2019). However, before this discovery, Sgr A* was without any doubt the strongest proof of the existence of SMBH in galactic nuclei. The progression to arrive to this conclusion involved the research of many groups through decades.

The first piece of evidence came from the detection of a very compact radio source within the central parsec of the Milky Way (Balick and Brown, 1974), which was identified as Sgr A*. A couple of years later, it was possible to calculate the enclosed mass in the innermost parsec of the Galaxy through the measurements of radial velocities of the ionised gas in the minispiral (Lacy et al., 1980). Figure 1.8 shows a VLA continuum radio map of the minispiral together with the [Ne II] emission lines indicating the derived velocities.

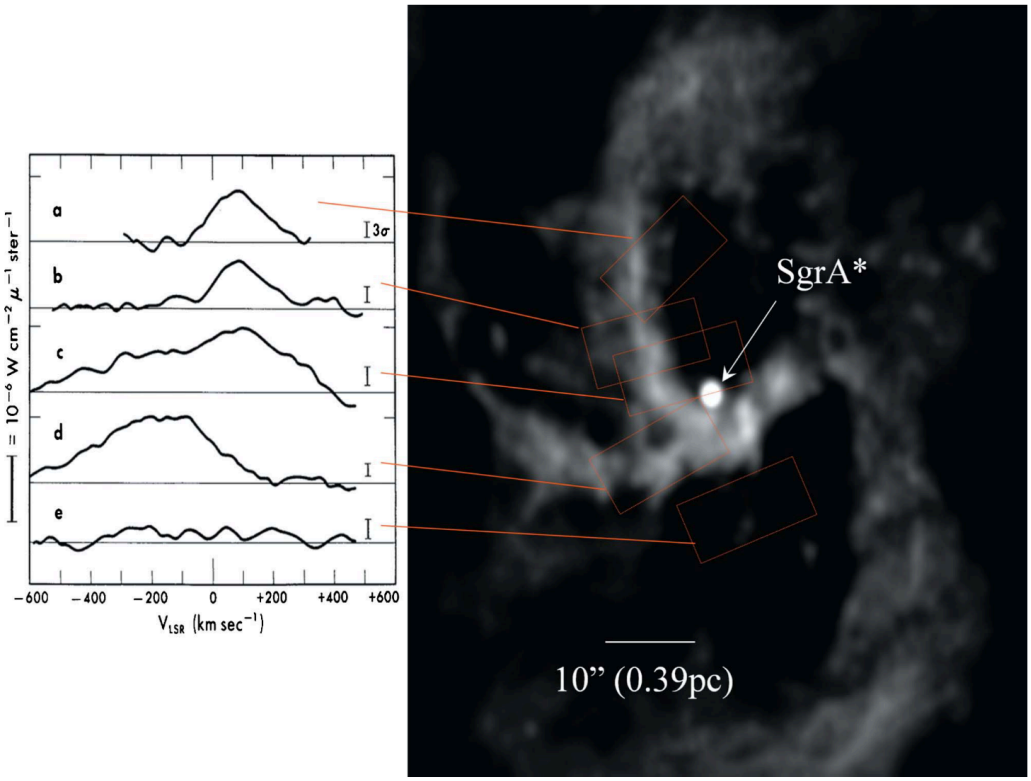

Figure 1.8: The right panel shows a VLA continuum map observed at 3.6 cm of the central parsec (Roberts and Goss, 1993), while the left panel contains the [Ne II] line profiles at 12 μm from Wollman et al. (1977). The emission captures the ionised gas filaments, which are part of the minispiral orbiting Sgr A*. This Figure was taken from Genzel, Eisenhauer, and Gillessen (2010).

Nevertheless, this evidence was not convincing at the time, because the gas dynamics might be influenced by other forces besides gravity, such as pressure gradients and magnetic fields. Furthermore, there was no detection of a luminous IR or X-ray counterpart at the location of Sgr A*. More solid evidence came years later, once it was possible to estimate the radial velocity of the unresolved stellar population through near-IR observations (McGinn et al., 1989; Sellgren et al., 1990; Haller et al., 1996). This showed that the mass enclosed within a projected radius of 0.1 pc was about $\sim 3 \times 10^6$ $M_\odot$, which implied a minimum density of $\sim 3 \times 10^9$ $M_\odot$ pc^{-3}. However, this estimation could not rule out the presence of a very compact cluster of stellar remnants (Maoz, 1998), for favouring the SMBH hypothesis. It was only until it was possible to obtain the first proper motions of single stars through diffraction limited observations in the near-IR that the constraints became tighter (Eckart and Genzel, 1997; Genzel et al., 1997; Ghez et al., 1998).

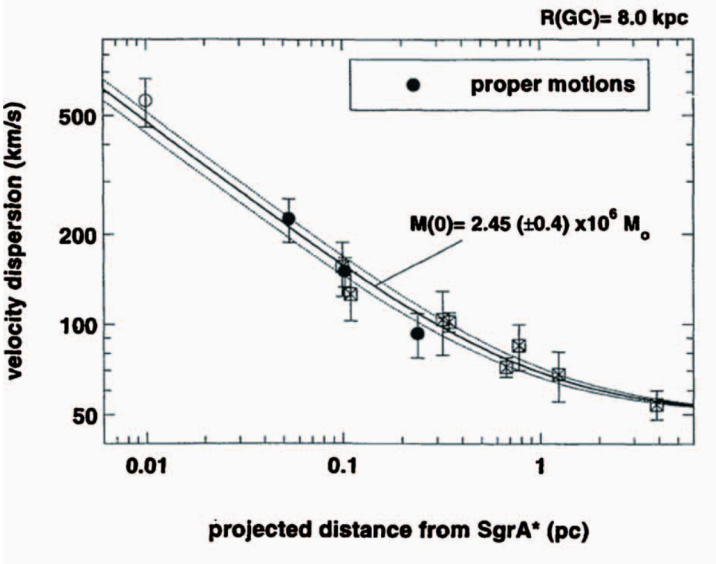

Figure 1.9: Stellar velocity dispersion as a function of projected separation from Sgr A* (Eckart and Genzel, 1997; Genzel et al., 1997). Circles represent data obtained from proper motions while crossed squares from line-of-sight velocities. The best model (solid line) fits a point mass and is shown with 1σ uncertainties. Figure taken from Genzel, Eisenhauer, and Gillessen (2010).

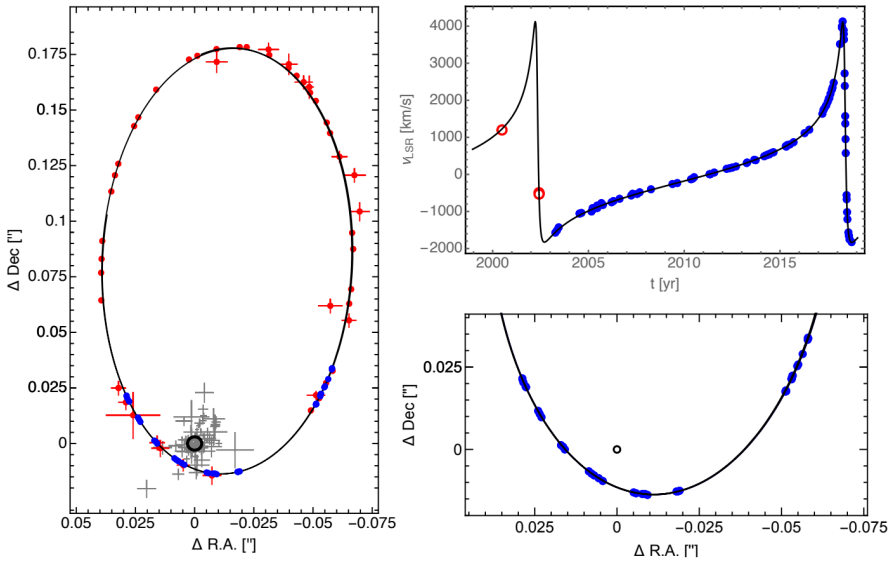

Figure 1.10: S2 astrometric and velocity data. The left panel shows the sky-projected orbit. The red and blue dots, represent the data obtained with the adaptive-optics and interferometric techniques, respectively. The best fit of a Keplerian orbit is shown as a black solid line through all the panels. The black circle represents the position of Sgr A*, while the grey crosses show the location of its detected flares (see Section 1.1.3.2). The right top panel shows the line-of-sight velocity of S2 as a function of time. The blue dots are data obtained with the VLT (e.g. Gillessen et al., 2009a; Gillessen et al., 2009b; Gillessen et al., 2017), while the red circles are observations with the Keck telescopes (Ghez et al., 2008). The right bottom panel is a zoom into the pericentre of the orbit of S2. These data correspond to interferometric GRAVITY measurements, and are shown with errors bars but they are smaller than the dots. Figure taken from Gravity Collaboration et al. (2019).

This suggested that the enclosed mass at ~0.01 pc was $\sim 2.6 \times 10^6$ $M_\odot$, which increased the density to a minimum of $\sim 10^{12}$ $M_\odot$ pc^{-3}. Figure 1.9 illustrates these results as it shows the combination of the proper motions and radial velocity measurements as a function of projected radius from Sgr A*. Based on these data, Genzel et al. (1997) ruled out the hypothesis of the star cluster made out compact remnants. Thus, the SMBH hypothesis became the preferred explanation for such mass concentration. The next leap took place when Schödel

et al. (2002) managed to trace two-thirds of the orbit of one of the brightest and closest stars to Sgr A*, S2. Thanks to its orbital period of only about ~16 yrs, it was possible to set stronger constraints on the mass and size of the enclosed mass. The orbit of S2 was consistent with a point mass of $\sim 4 \times 10^6$ $M_\odot$ inside a radius of 6×10^{-4} pc. The monitoring of this orbit has continued until the present, so the precision of the measurements has improved significantly (e.g. Ghez et al., 2008; Gillessen et al., 2009a; Gillessen et al., 2009b). Very recently thanks to the development of the near-IR interferometer GRAVITY, it was even possible to detect the gravitational redshift of S2 during its pericentre passage (see Figure 1.10; Gravity Collaboration et al., 2018; Gravity Collaboration et al., 2019).

1.1.3.2 The activity of Sgr A*

Since its discovery it has been observed that Sgr A* might not be bright enough to be conceived as a SMBH. In general, its luminosity is about $\sim 10^{36}$ erg s^{-1} ($\sim 10^3$ $L_\odot$), and it is mostly emitted at sub-mm wavelengths with a peak of $\sim 5 \times 10^{35}$ erg s^{-1} (see Figure 1.11; Serabyn et al., 1997). However, there is also a variable component, especially in the IR and X-ray, which corresponds to the so-called *flares*. Typically, their periodicity is about a few times per day, lasting for about 100 minutes. During the flares the luminosity released is about $\sim 10^{36}$ erg s^{-1}, on top of the steady state emission. The radiation emitted by Sgr A* is well described as synchrotron radiation from a thermal distribution of relativistic electrons, although the radiation mechanism of the flares is not completely understood yet. Figure 1.11 shows the spectral energy distribution in quiescent (or steady) state, highlighting the radiation mechanism of each part of the spectrum according to the model of Yuan, Quataert, and Narayan (2003).

If we compare Sgr A* with a quasar, which accretes and radiates at a significant fraction of the Eddington limit[3], the central engine of the Galaxy is surprisingly underluminous. Specifically, its luminosity is about eight orders of magnitude smaller with respect to its Ed-

[3]The Eddington limit is defined as the luminosity of an object, like a star, necessary for balancing the radiation force and its self-gravity, which act outwards and inwards, respectively.

dington limit, which is about $\sim 1.5 \times 10^{11}$ $L_{\odot}$, and at least four orders of magnitudes smaller from the luminosity calculated from the accretion rate at the Bondi radius.

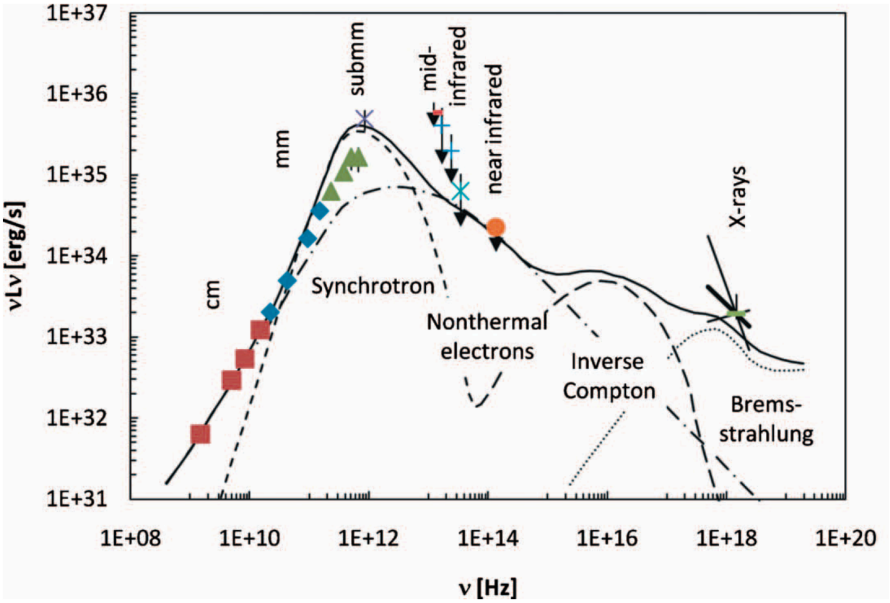

Figure 1.11: Spectral energy distribution of Sgr A* in quiescent state. The data points are shown with markers and arrows, while the models of the emission mechanism are shown with lines. The solid black line corresponds to the sum of each of the components of the model by Yuan, Quataert, and Narayan (2003). This Figure is a compilation of data and models made by Genzel, Eisenhauer, and Gillessen (2010).

Currently, it is thought that the luminosity of Sgr A* is dominated by the accretion of material coming from the stellar winds blown mainly by the WR stars within the innermost parsec, which in total supply $\sim 10^{-3}$ $M_{\odot}$ yr^{-1} (Martins et al., 2007). Based on this fact, the gas dynamics in the region have been modelled since the early 1990s, and such models have improved significantly until the present. Melia (1992) started with a hydrodynamical model of a bow shock of gas from the IRS 16 complex. Coker and Melia (1997) managed to include randomly distributed point sources of material. The next step was taken by Quataert (2004) who developed a spherically symmetric hydrodynamic model. However, with the advent of

more sophisticated numerical tools, and the knowledge of the properties of the orbits and stellar winds, Cuadra, Nayakshin, and Martins (2008) conducted 3D numerical simulations of the hydrodynamics of the region. They found that the accretion rate at the Bondi radius was dominated by a few slow stellar winds ($\lesssim$ 750 km s^{-1}) that orbit closer to Sgr A*, and is of the order of $\sim 10^{-6}$ M$_\odot$ yr^{-1}. This model showed reasonable agreement with the estimation derived from the X-ray observations at the Bondi radius (Baganoff et al., 2003). Through the comparison with these observations of the shocked stellar winds (Baganoff et al., 2003; Xu et al., 2006), it was possible to explain such emission as thermal bremsstrahlung (Quataert, 2002). In a recent study, Russell, Wang, and Cuadra (2017) synthesised mock X-ray observations and spectra of the region taking into account the different abundances in the stellar winds finding good agreement with the data, which supported the fact that the region is indeed filled by the winds, and that the wind properties are accurately determined. More recently, Ressler, Quataert, and Stone (2018) developed the first Eulerian hydrodynamics modelling (see Section 1.2) of the mass-losing stars orbiting around Sgr A*. They focused on increasing the resolution close to Sgr A*, so that it was possible to follow the gas dynamics deeper in the potential well. Using these results, they extrapolated the mass inflow rate to the event horizon scales finding agreement with the observational constraints.

At scales of $\sim 3\times10^{-5}$–3×10^{-4} pc from Sgr A*[4], the mass accretion rate has been constrained through the detection of linear polarisation in the radio emission (Aitken et al., 2000; Macquart et al., 2006; Marrone et al., 2006). These observations set the accretion rate to be $<10^{-6}$ M$_\odot$ yr^{-1}, because a larger value should be able to depolarise the emission due to Faraday rotation gradients (Agol, 2000; Quataert and Gruzinov, 2000). At even smaller scales, the sub-mm observations of Faraday rotation constrain the mass accretion rate to be between $10^{-9} - 10^{-7}$ M$_\odot$ yr^{-1} depending on the assumptions related to the electron distribution and magnetic fields (Marrone et al., 2006; Marrone et al., 2007). Table 1.1 is a summary of the mass inflow rate at different scales in the Galactic Centre, starting at the minispiral up to the

[4]Sgr A* Schwarzschild radius is about $R_{\rm Sch} \approx 4 \times 10^{-7}$ pc.

inner accretion zone. Overall, the material being effectively accreted is observed to be $\sim 10^{-6}$ of the total supplied at parsec scales.

Table 1.1: Mass inflow rate as a function of distance from Sgr A*.

Region	Radius pc	Mass inflow rate $M_\odot$ yr^{-1}
Minispiral and stellar cluster	< 1.7	$10^{-4} - 10^{-3}$
Stellar winds at Bondi radius	0.05	$\sim 10^{-6}$
Outer accretion zone	$\sim 3\times10^{-5} - 3\times10^{-4}$	$< 10^{-6}$
Inner accretion zone	$< \sim 3\times10^{-5}$	$10^{-9} - 10^{-7}$

Notes. Adapted from Genzel, Eisenhauer, and Gillessen (2010).

However, the activity of Sgr A* might not have been always like this. The detection of the 6.4 keV Fe Kα fluorescent line emitted from many molecular clouds in the Galactic Centre could suggest that the SMBH might have been more active in the past (Sunyaev, Markevitch, and Pavlinsky, 1993; Ponti et al., 2010). The observations of such clouds are simply not consistent with the current X-ray sources nearby. Instead, it is plausible that a transient single point source could have been the responsible of such light echoes (see Figure 1.2). Thus, if we consider that the clouds are reflecting the X-ray emission of Sgr A* in the past, this would implied that the SMBH was significantly more active several hundreds of years ago, and/or even some decades ago (Muno et al., 2007). This timescale is set by the distance between the molecular clouds and Sgr A*, as well as considering the fact that the light speed is finite. The reason behind a more active past is not known yet, although some posibilites include the tidal disruption of a scattered star or the accretion of a gas cloud that might have fallen onto the black hole (Koyama et al., 1996; Yu et al., 2011; Morris, Meyer, and Ghez, 2012).

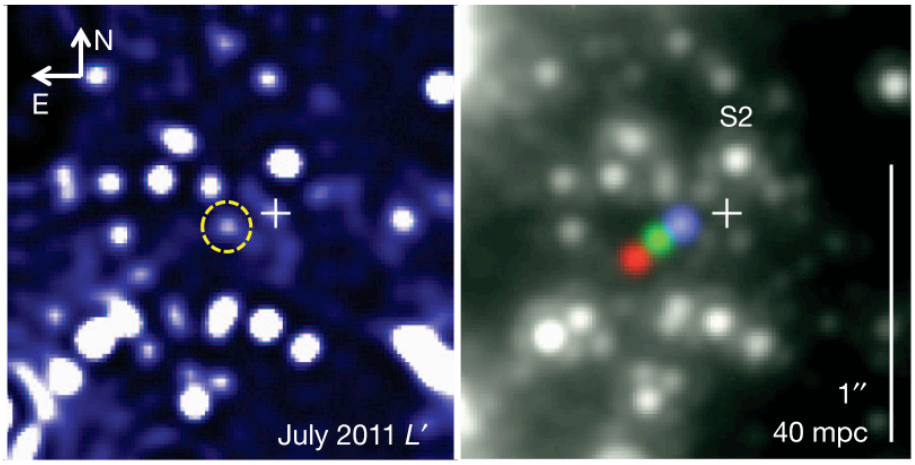

Figure 1.12: NACO VLT images in the L' band of the discovery of G2. The left panel shows the G2 cloud detected in the L' band, and it is highlighted with a dashed yellow circle. The white cross represents the location of Sgr A*. The right panel shows the proper motion of G2 derived from the L' band observations. The red, green, and blue show the position of G2 in 2004.5, 2008.3, and 2011.3, respectively. The velocity derived from the proper motion is ~1700 km s^{-1} in 2011. The background image corresponds to a K_s band image in which G2 is not detected. Figures taken from Gillessen et al. (2012).

1.1.4 The G2 object

In 2012, Gillessen et al. (2012) discovered a faint dusty object on its way towards Sgr A* on a very eccentric orbit ($e \approx 0.98$), which implied a very close pericentre of about ~200 au. The object was observed as an unresolved source in the L' band at 3.8 μm with magnitude ~14 (see left panel of Figure 1.12), marginally resolved through the Br-γ hydrogen recombination line with a luminosity of $\sim 10^{30}$ erg s^{-1}, also detected in Pa-α at 1.875 μm, and He I at 2.058 μm (e.g. Gillessen et al., 2012; Phifer et al., 2013; Witzel et al., 2014; Pfuhl et al., 2015). These observations suggest that the object is made out mostly of ionised gas at recombination temperature $\sim 10^4$ K together with cool dust at ~560 K (Gillessen et al., 2012; Gillessen et al., 2013a; Gillessen et al., 2013b; Eckart et al., 2013). If the object is solely composed of gas and dust, its mass is estimated to be ~3 $M_\oplus$ (Gillessen et al., 2012). At the time of the

discovery, nobody knew how the object was going to evolve, especially during its pericentre passage. Despite its small mass, G2 pericentre passage could potentially have an impact on the accretion of Sgr A*. However, as its nature was (and still is) unknown it was difficult to make predictions about the close encounter.

The constant monitoring of the region allowed tracing back the object motion up to the year 2003. Since then, its evolution has been tracked by many research groups until the present (e.g. Witzel et al., 2014; Valencia-S. et al., 2015; Gillessen et al., 2019). It was observed that most of the source passed pericentre in 2014. Although there were predictions of Sgr A* becoming more active, and therefore brighter either in the near-IR or X-ray, during G2 pericentre passage there has not been any observed enhancement yet (Haggard et al., 2014). Additionally, during this period it was observed that the dust emission remained as a point source (Witzel et al., 2014; Plewa et al., 2017). However, the gaseous component was stretched during its closest encounter to Sgr A*. Figure 1.13 shows the evolution of the source in position-velocity diagrams through the years 2003–2016 (Plewa et al., 2017). These measurements are based on the Br-γ and He I line emission, and show the evolution of the source along its orbit and line-of-sight velocity. This analysis clearly shows how the object started being relatively round, and then becoming elongated due to the tidal forces of Sgr A* between ~2012–2015, to finally recover its original shape more or less. The data observed up to then was consistent with a purely Keplerian motion (but see below). The best orbital fit shows that the plane of its orbit is approximately aligned with respect the clockwise disc of the young stars. Even the rotation direction of G2 is also clockwise when seen on the sky. This might be a hint related to its origins. However, its extremely high eccentricity is a very enigmatic property as the average eccentricity of the clockwise disc is only about ~ 0.3.

Pfuhl et al. (2015) showed that, apparently, there are more objects like G2. The so-called G1 object was detected on almost the same orbit as G2's but ~13 yr ahead. It was also detected in the L' band and in the Br-γ emission line. Its pericentre passage should have taken place between 2001–2002. In Figure 1.13, it is possible to spot it clearly in the panel of 2006 on the blueshifted side (lower panels). Additionally, Witzel et al. (2017) observed that

the source also became extended close to pericentre, and then got smaller overtime, although they found that its orbit differs significantly from G2's.

Currently, there are many hypotheses trying to explain the nature of G2, some of them assume it is a purely gaseous object, while others consider that there is a hidden stellar object within the gas. In the former scenario, G2 would be a relatively cold ($\sim 10^4$ K) gas clump confined by the hot ($\sim 10^7$ K), diffuse surrounding medium. However, the medium cannot cool down efficiently due to its long cooling timescale compared to its dynamical timescale (Cuadra et al., 2005; Burkert et al., 2012), therefore it is not straightforward creating such cold material from it. A plausible explanation is that the cloud is the result of the stellar winds blown by the WR stars present in the region (Gillessen et al., 2012; Burkert et al., 2012). In this scenario, the shocked gas is heated up and compressed enough to radiate its energy efficiently, for then condensing as a cold clump. Thus, either a single dense wind or the collision of two might be able to create G2. Calderón et al. (2016) conducted a study based on the properties of the mass-losing stars in the region with the aim of establishing whether it is possible or not forming a clump as massive as G2 through the collision of stellar winds. This study showed that, in theory, it is possible to produce such massive clouds under certain conditions. The winds involved need to be dense ($\sim 10^{-5}$ $M_\odot$ yr^{-1}) and slow ($\lesssim 750$ km s^{-1}) but, more importantly, the stars blowing them should be relatively close to each other (< 2000 au), so that the compressed material at the collision can be dense enough to radiate its energy. Based on the orbital properties of the mass-losing stars, Calderón et al. (2016) concluded that the scenario can take place but it is unlikely to occur. Nevertheless, it was pointed out that colliding wind binaries are promising sources of clumps in the region, especially IRS 16SW, and deserve further study.

Another explanation could be the development of a cooling instability in the accretion flow toward Sgr A*, which could explain its high orbital eccentricity (Gillessen et al., 2013a). Finally, the partial tidal disruption of a giant star could have produced a stream of material from which clumps could be condensed and fall onto Sgr A* with certain periodicity being G1 and G2 a couple of them (Guillochon et al., 2014). The detection of material following G2,

the so-called G2-tail, might support the idea of these objects being bright knots of a larger streamer of material infalling onto Sgr A* (Pfuhl et al., 2015). Interestingly, these authors extrapolated the location of this material back in time in the position-velocity diagrams finding roughly agreement with both the position and velocity of the massive binary IRS 16SW.

On the other side, the other set of hypotheses state that there is a stellar object within the observed gas and dust envelope. In this context, the object might have been formed in the clockwise disc, and then scattered onto such an eccentric orbit. Some of these hypotheses are that G2 is a planetary nebula (Gillessen et al., 2012), a proto-planetary disc around a low-mass star (Murray-Clay and Loeb, 2012), a gas disc around an old star with a low mass disrupted by stellar mass black hole (Miralda-Escudé, 2012), the wind of a T-Tauri star (Scoville and Burkert, 2013; Ballone et al., 2013), the result of a binary star merger event (Prodan, Antonini, and Perets, 2015), and a planetary embryo (Mapelli and Ripamonti, 2015).

Ballone et al. (2016) showed through hydrodynamics simulations that an outflow of a T-Tauri-like star can reproduce accurately the location of G2 and its tail in the observed position-velocity diagrams. Ballone et al. (2018) extended these numerical models concluding that if in the next years ~5–10 yr there is a decoupling between G2's core and its tail, this could be its true nature.

In summary, G2 remains as one of the many puzzles that the Galactic Centre holds. However, with the constant monitoring of the region we should be able to set more constraints on its post-pericentre evolution. The latest observations showed that the gaseous component of G2 is deviating from its purely Keplerian motion likely due the effect of a drag force acting on it (Gillessen et al., 2019). Only the continuous monitoring of the source will give us enough information for finally understand its true nature, and detect its potential impact on Sgr A*.

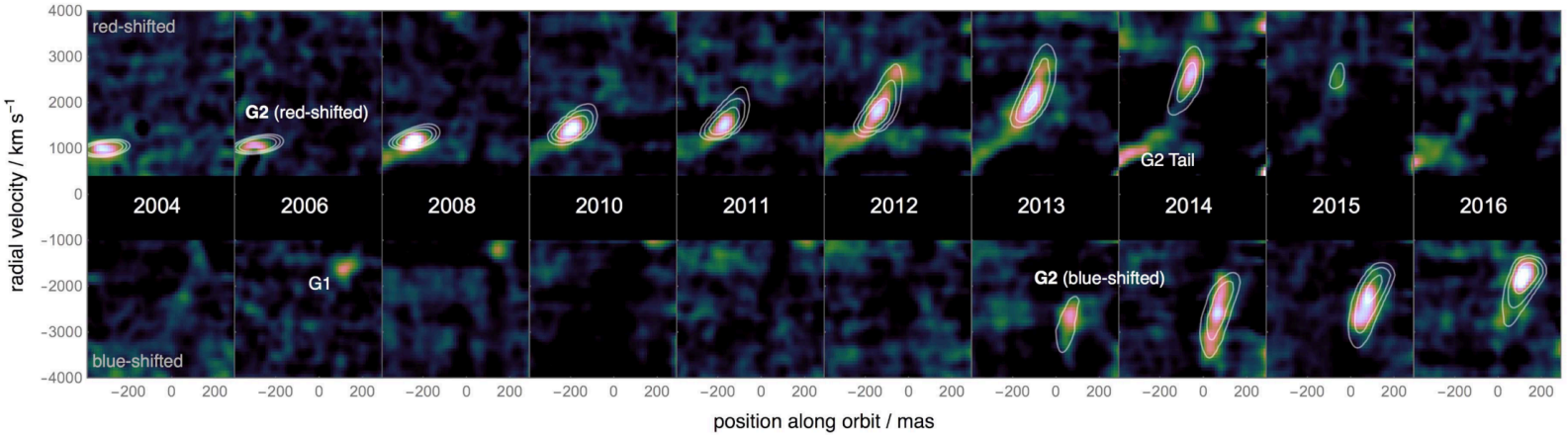

Figure 1.13: Position-velocity diagrams of the evolution computed from the Br-γ and He I line emission of G2. It contains observations from 2004 until 2016 (from left to right). The upper and lower panels show the redshifted and blueshifted components of the line-of-sight velocity. The region around zero velocity is not shown due to the effects of the background emission. The white contours represent the test-particle model that best fits the data. Notice that starting on 2013 it is possible to detect part of the object on the blueshifted side, and by 2016 the complete source on this side. This Figure was taken from Plewa et al. (2017).

1.2 Numerical hydrodynamics

Over the course of this work we make use of numerical tools, specifically of the adaptive-mesh refinement (AMR) hydrodynamics code RAMSES (Teyssier, 2002), in particular in Chapters 3 and 4. This is why in this section we briefly summarise the foundations of the Euler equations of hydrodynamics, and present the numerical method that we use in this work.

The content of this section is based on the review by Teyssier (2015). Firstly, we describe and derive the equations that govern the fluid dynamics in the Lagrangian form in Section 1.2.1. From this set of equations, we proceed to derive the hydrodynamics equations in their Eulerian form, and present their solution using the Godunov method in Section 1.2.2. Finally, we present a brief explanation of the AMR technique in Section 1.2.3.

1.2.1 The Euler equations

Let us consider an infinitesimally small fluid element as it moves in space, and evolves in time. We start considering that the volume of this element is V, and its mass is m. Thus, its density is given by $\rho = m/V$, which is the property that will evolve as the fluid element deforms. Based on the Newton laws of dynamics the motion of the fluid element can be estimated making use of the Lagrangian time derivative:

$$\rho \frac{D\mathbf{u}}{Dt} = -\nabla P, \tag{1.1}$$

where $\mathbf{u}$ and P correspond to the fluid velocity vector and its pressure, respectively.

The next equation is derived from the first principle of thermodynamics, which describes the evolution of the fluid internal energy due to work exertion. Here we consider an adiabatic process, therefore, there is no heat exchange ($Q = 0$). Then,

$$m \frac{D\epsilon}{Dt} = -P \frac{DV}{Dt}, \tag{1.2}$$

where ϵ represents the specific internal energy, i.e. internal energy per unit mass. Now, we

shall impose that the mass of the fluid should be conserved through

$$\frac{Dm}{Dt} = 0, \tag{1.3}$$

and by making use of the velocity divergence as a measure of the rate of change of the fluid volume, i.e.

$$\frac{1}{V}\frac{DV}{Dt} = \nabla \cdot \mathbf{u}, \tag{1.4}$$

we arrive to the set of equations that describe the evolution of the fluid element in the Lagrangian form:

$$\frac{1}{\rho}\frac{D\rho}{Dt} = -\nabla \cdot \mathbf{u}, \tag{1.5}$$

$$\rho\frac{D\mathbf{u}}{Dt} = -\nabla P, \tag{1.6}$$

$$\rho\frac{D\epsilon}{Dt} = -P\nabla \cdot \mathbf{u}. \tag{1.7}$$

However, it is still necessary to specify an equation of state for being able to solve the set of equations, i.e. a relation between the thermal pressure as a function of density and internal energy $P = P(\rho, \epsilon)$. Finally, establishing the initial conditions of the system it is possible to solve this set of differential equations through numerical analysis.

The Lagrangian approach of the Euler equations, in principle, is very simple and can be used to develop numerical Lagrangian codes. Nevertheless, an important issue of the Lagrangian (nonconservative) formalism of the Euler equation is that it is valid only in smooth regions of the fluid. Thus, it is not valid in discontinuities, such as shocks, and contact discontinuities, which are common phenomena in gas dynamics. In this context, it is appropriate to consider the Euler equations in their conservative, and Eulerian form as well.

1.2.2 The Eulerian approach

Let us consider the set of equations governing the hydrodynamics in the Lagrangian form that we have just presented (Equations 1.5, 1.6, and 1.7), and apply the Reynolds' transport theorem. This theorem relates the Lagrangian time derivative of any intensive quantity (e.g. mass, linear momentum, total energy) with the generation and flux of its corresponding extensive property (e.g. mass, linear momentum and energy densities). Thus, it establishes an equivalence between the Lagrangian time derivative and the Eulerian space and time derivatives as follows:

$$\frac{D(\cdot)}{Dt} = \frac{\partial(\cdot)}{\partial t} + \mathbf{u} \cdot \nabla(\cdot). \tag{1.8}$$

Through this exercise, it is possible to obtain the set of Euler equations in their Eulerian form:

$$\frac{\partial \rho}{\partial t} + \nabla \cdot (\rho \mathbf{u}) = 0, \tag{1.9}$$

$$\frac{\partial}{\partial t}(\rho \mathbf{u}) + \nabla \cdot (\rho \mathbf{u} \otimes \mathbf{u} + P\mathbb{I}) = \mathbf{0}, \tag{1.10}$$

$$\frac{\partial E}{\partial t} + \nabla \cdot [\mathbf{u}(E + P)] = 0, \tag{1.11}$$

where E is the fluid total energy per unit volume as is given by

$$E = \rho\epsilon + \frac{1}{2}\rho \mathbf{u} \cdot \mathbf{u}. \tag{1.12}$$

The most important feature of the Euler equations in this form, it is their conservative nature. Thus, if we discretise an arbitrary volume into fixed volume elements, the time evolution of the conserved quantities, which are mass, linear momentum, and total energy, are going to be calculated as the sum of the net fluxes through the computational cell faces. Thanks to this, now it is possible for the flow variables to be discontinuous. The only requirement is that the flux functions, i.e. the quantities to which the divergence is applied to, must be continuous through the cells faces.

Another property of these equations is that it is possible to linearise them making use of the primitive variables $(\rho, \mathbf{u}, P)$. If we assume the fluid to be an ideal gas, we have that its equation of state is given by $P = (\gamma - 1)\rho\epsilon$, where γ corresponds to the adiabatic index of the fluid. Combining it with the set of equations we can modify them to arrive to their quasi-linear form:

$$\frac{\partial \rho}{\partial t} + \mathbf{u} \cdot \nabla \rho + \rho \nabla \cdot \mathbf{u} = 0, \tag{1.13}$$

$$\frac{\partial \mathbf{u}}{\partial t} + \mathbf{u} \cdot \nabla \mathbf{u} + \frac{1}{\rho} \nabla P = \mathbf{0}, \tag{1.14}$$

$$\frac{\partial P}{\partial t} + \mathbf{u} \cdot \nabla P + \gamma P \nabla \cdot \mathbf{u} = 0. \tag{1.15}$$

Unfortunately, these equations are not valid at discontinuities. However, they are extremely useful to obtain a linearised version of the Euler equations for deriving the dispersion relation of sounds waves:

$$c_s^2 = \frac{\gamma P}{\rho}, \tag{1.16}$$

where c_s corresponds to the sound speed of the fluid.

As we have a system of conservation laws with propagating waves, we can make use of the most popular numerical technique to solve the system of partial differential equations, which is the Godunov method (Godunov, 1959). It makes use of cell-averaged generalised conservative variables $\mathbf{U}(\mathbf{x}, t)$, which in our case correspond to mass, linear momentum, and total energy, each per unit volume, i.e. $(\rho, \rho\mathbf{u}, E)$. Then, the cell-averaged value of the generalised variable is

$$\mathbf{U}_i^n = \frac{1}{V_i} \int_{V_i} \mathbf{U}(\mathbf{x}, t) dV, \tag{1.17}$$

where i and n are indexes related to the cell ordering and the discrete time coordinates, respectively. Bearing in mind the divergence theorem, we can compute the exact integral

form of the set of equations through the general equation of the conservation laws:

$$\frac{\mathbf{U}_i^{n+1} - \mathbf{U}_i^n}{\Delta t} + \frac{1}{V_i} \int_{S_i} \bar{\mathbf{F}} \cdot \mathbf{n} dS = 0, \tag{1.18}$$

where $\bar{\mathbf{F}}$ is the time-averaged flux function given by

$$\bar{\mathbf{F}} = \frac{1}{\Delta t} \int_n^{n+1} \mathbf{F}(\mathbf{x}, t) dt. \tag{1.19}$$

In principle, this method can be used to develop numerical tools of any order of accuracy and any mesh geometry. However, here we restrict the description only to the Cartesian mesh geometry.

The generic Godunov method of first order assumes that the numerical solution is piecewise constant within each cell, i.e. the cell average corresponds to the solution in the entire cell (Godunov, 1959). Nevertheless, the accuracy of the method can be improved using higher-order methods. The first one developed is the so-called *Monotonic Upwind Scheme for Conservation Laws* (MUSCL) scheme (van Leer, 1976; van Leer, 1979). This corresponds to a second-order scheme, which is based on a linear interpolation between cell interfaces. Then, within each cell the solution would not be constant anymore but piecewise linear.

In general, the most difficult part of the method is related to estimate numerically the time-averaged flux functions. In the case of the first-order method, the solution is constant, therefore we can recognise the Riemann problem at each interface between cells. Fortunately, the solution of the Riemann problem is self-similar for the variable x/t, which allows a trivial estimation of the flux functions. Then, the time-averaged solution is identical to the initial value at $x/t = 0$. This makes the problem significantly simpler, and the general flux function results to be:

$$\mathbf{F} = \mathbf{F}(\mathbf{U}_L, \mathbf{U}_R), \tag{1.20}$$

which corresponds to the solution of the Riemann problem for the input left and right of the piecewise constant states at $x/t = 0$. In general, the exact solution of the Riemann

problem is not often used as it can be computationally expensive. Fortunately, there are many approximate so-called Riemann solvers, which are more efficient, and can be accurate enough. As an example here we describe briefly one of them: the Lax-Friedrich flux function (LeVeque, 1992),

$$\mathbf{F}(\mathbf{U}_L, \mathbf{U}_R) = \frac{\mathbf{F}_L + \mathbf{F}_R}{2} - \frac{S_{\max}}{2}(\mathbf{U}_L - \mathbf{U}_R), \tag{1.21}$$

where $S_{\max}$ contains information of the maximum wave speed in the two cells involved in each step. Notice that first term on the right-hand side is just the average of the flux on each side, while the second helps to stabilise the numerical solution. This term is given by

$$S_{\max} = \max\left\{|\mathbf{u}\cdot\mathbf{n}|_L + c_{s,L}, |\mathbf{u}\cdot\mathbf{n}|_R + c_{s,R}\right\}. \tag{1.22}$$

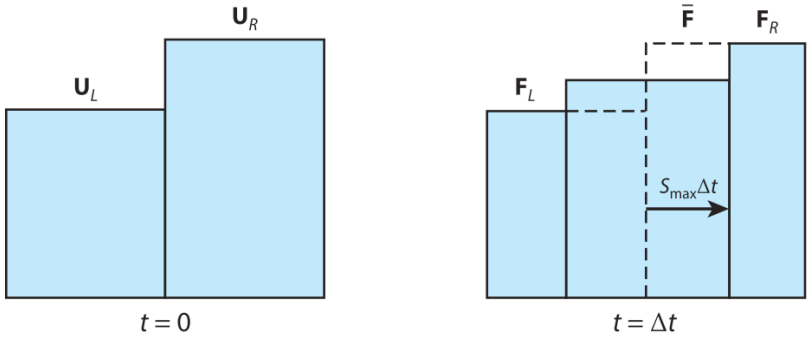

Figure 1.14: Schematic representation of the 1D Riemann problem to illustrate the computation of the flux function at the cell interfaces using the Godunov method. The Figure was taken from Teyssier (2015).

Figure 1.14 shows a schematic representation of the one-dimensional Riemann problem. On the left side, it shows the initial state of the system at $t = 0$, where each side has a different hydrodynamic state $\mathbf{U}_L$ and $\mathbf{U}_R$. On the right side, now the flux functions are presented

schematically, where at the interface the flux now has a value between $\mathbf{F}_L$ and $\mathbf{F}_R$. Also, the factor $S_{\max}\Delta t$ illustrates how far such flux can travel in a given timestep Δt.

Unfortunately, this method is particularly diffusive and, therefore, presents difficulties for modelling shocks properly. However, there are other Riemann solvers, which can overcome this kind of issues. For instance, the Harten-Lax-von Leer (HLL) Riemann approximation is of second-order in space and time, and makes use of the integral form of the conservation equations, taking into account the largest and smallest velocities at each interface. The disadvantage of those methods is that they can produce large spurious oscillations in the fluid solution due to the linear extrapolations of the cell states to their interfaces can create new extrema. In order to enforce the stability of each scheme and the solutions to be smooth it is necessary to introduce slope limiters (e.g. van Leer, 1977; Roe, 1986). Finally, to make sure the solution converges when solving the advection of the flow it is necessary to impose the Courant-Friedrichs-Lewy (CFL) condition (Courant, Friedrichs, and Lewy, 1967). This requires that the timestep has to be limited by the sound speed, the fluid speed, and the cell size. In the simplest 1D case the Courant number C should be smaller than unity in the following expression

$$C = \frac{(|\mathbf{u}| + c_s\Delta t)}{\Delta x} < 1 \Rightarrow \Delta t < \frac{\Delta x}{|\mathbf{u}| + c_s}. \tag{1.23}$$

This ensures that the fluid at a given cell (wave solutions) will not move further than to the next cell per timestep, otherwise the solution would be extremely unstable. In the finite volume approach, i.e. grid-based codes, the Courant number C is typically set to 0.8. However, depending on the problem it can be smaller.

1.2.3 The adaptive-mesh refinement technique

The concept behind the AMR technique is to increase the resolution (having a finer grid) in certain regions of the domain according to a user defined criterion (or criteria). This technique was introduced by Berger and Oliger (1984) and Berger and Colella (1989), and

used in astrophysics for the first time by Klein, McKee, and Colella (1994). In general, there are two main requirements that the AMR algorithms must satisfy. Firstly, they need to be able to deal with much more complex mesh geometry. For instance, they must keep their conservative nature when cells of different sizes (unrefined and refined) have to interact exchanging fluxes. Secondly, the user must be very careful with the choice of the refinement strategy as the AMR is supposed to improve the quality of the solution, and not to make it worse. This can be ensured through the selection of physically motivated refinement criteria, which give an estimate of the truncation errors. For instance,

$$\text{if } \Delta x \left| \frac{\partial^2 U}{\partial x^2} \right| > C_1 \left| \frac{\partial U}{\partial x} \right|, \text{ then refine,} \tag{1.24}$$

where C_1 is an input parameter that must be chosen by the user according to the desired accuracy and available resources. When considering more physical processes in the hydrodynamics code such as radiative cooling and/or gravity, the criteria might be different in the case that those processes could be limited by the resolution. For example, being able to resolve the Jeans length or making sure that each cell contains a minimum amount of mass where gravity is crucial.

1.3 This thesis

In Section 1.1, we have described the sources and structure located inside the central parsec, including some of the questions that the Galactic Centre holds. We have discussed how the hot plasma can be observed in the X-ray, and that its radiation is well-understood, and even has been modelled successfully in agreement with observations (Russell, Wang, and Cuadra, 2017). In contrast, the existence of cold gas in the region is a problem, due to our limited knowledge of its origins and properties. While there are observations of dust and gas within the inner parsec, it is not known how such material can be formed. The presence of a diffuse, extremely hot plasma under the influence of the strong gravitational field of Sgr A* makes it a vert hostile environment for forming and hosting such cold components. The fact that the cold phase material is observed in enigmatic regions like the cluster IRS 13E, and through the G2-like objects at very small distances from Sgr A*, suggests that there is a significant amount of these sources, and that some of them can (approximately) free-fall onto the central SMBH.

The hydrodynamical models of the system of the WR stars orbiting Sgr A* have shown that cold dense clumps can form as a result of stellar wind collisions when either the winds are slow (e.g. 33E) and/or the stars are at a small distance from each other (e.g. E2 and E4, see Figure 1.15; Cuadra, Nayakshin, and Martins, 2008). This formation theory could be a potential explanation for the presence of the cold material in the region. Furthermore, these models showed that the mass inflow rate can indeed be affected by such clumps, if they reach the innermost region, causing variability on timescales of hundreds of years. However, there were concerns about whether such clumps were physical or a result of the limitations of the numerical techniques employed. Cuadra, Nayakshin, and Martins (2008) made use of the classic Smoothed Particle Hydrodynamics (SPH) technique, which is a Lagrangian approach for modelling fluid dynamics. As we discussed in Section 1.2.1, the Lagrangian formalism can describe well smooth regions of the fluid, but it is not accurate modelling contact discontinuities or shocks. The WR stellar winds are highly supersonic, thus it is

possible that these models cannot simulate properly the interaction of stellar winds in this context.

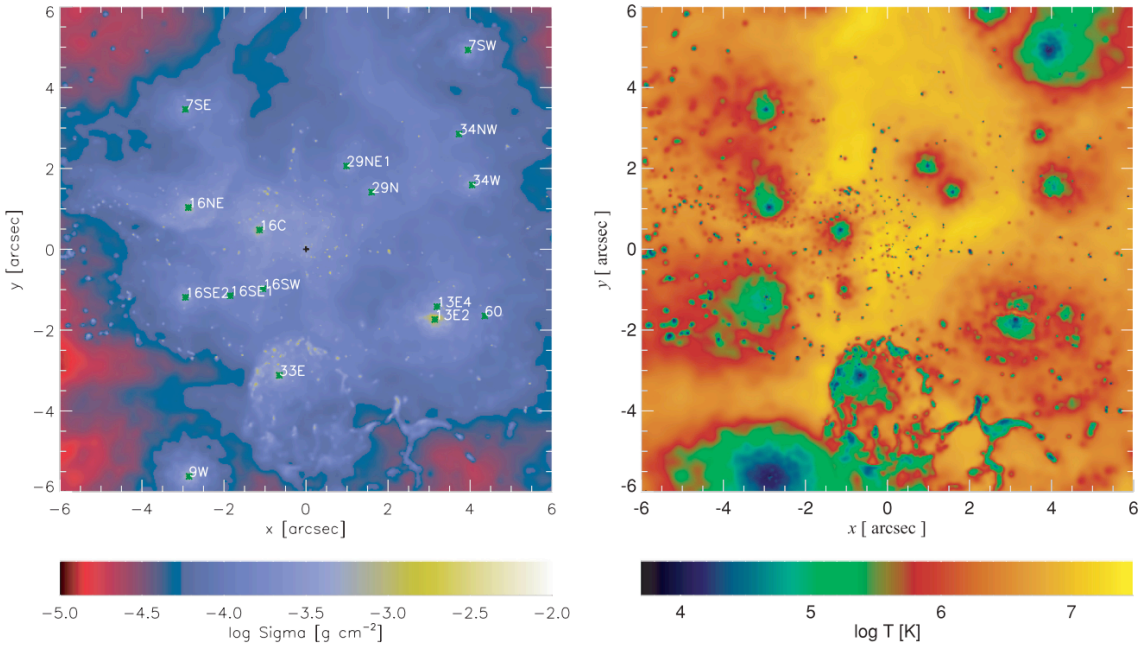

Figure 1.15: Gas morphology at the present time of the system of WR stars orbiting Sgr A* from Cuadra, Nayakshin, and Martins (2008). The left panel shows the column density of gas in the inner six arcseconds from Sgr A* including labels for identifying the WR stars. The right panel contains the averaged temperature of the same region. Notice that there are many small dense cold clumps in the region, especially around the slow-wind-emitting star 33E. Furthermore, there are clumps in the IRS 13E group generated from the slow wind from E2.

Calderón et al. (2016) performed an analytical study in order to estimate whether we should expect clump formation as a result of the stellar wind collisions or not, given the known properties of the WR stars in the Galactic Centre. It was concluded that, in general, we should not; unless stars experience very close encounters (< 2000 au). This result pointed out that massive binaries might be constant clump sources, especially close binaries. In a recent study, Ressler, Quataert, and Stone (2018) simulated again the system of mass-losing stars in the Galactic Centre. However, this time the simulation was carried out making use of a

state-of-the-art hydrodynamics grid-based code that follows the Eulerian formalism. Thanks to the more appropriate treatment of discontinuities, shocks indeed were modelled more accurately compared to the earlier SPH models. Thus, this model did not show formation of cold gas from wind collision as predicted by Calderón et al. (2016). Nevertheless, they did not consider neither WR binaries in the region nor improved significantly the resolution at the wind interactions. Instead, they opted for using the static-mesh refinement (SMC) technique in order to increase the resolution locally around Sgr A*, as their goal was to follow the gas into smaller scales, closer to the SMBH.

So far, there have not been studies focusing on studying the interactions of stellar winds making sure of capturing the process in detail for quantifying the cold gas formation, either in general or in the specific case of the Galactic Centre.

In this context, the aim of this study is to describe in detail the interaction of stellar winds both in ideal isolated environments, as well as in the Galactic Centre region. Each specific problem was handled with either analytical and/or numerical tools. As we discussed in Section 1.2, the numerical tool of choice is the grid-based code RAMSES (Teyssier, 2002) that uses the AMR technique for resolving properly the interaction of the stellar winds without increasing significantly the computational cost of the simulations. The main unknowns we would like to answer are the following:

1. Could the source G2 be conceived as a cold clump formed in a stellar wind collision, likely in any of the known massive binaries?

2. In general, what are the properties of clumps formed in stellar wind collisions? What is the maximum mass they can have?

3. Can clumps be formed, at all, in the Galactic Centre environment? If so, is it possible for them to fall onto Sgr A*?

In order to answer these research questions, we have developed three projects, each one addressing one of the questions above,

1. Studying the hypothesis of G2 being formed in a massive binary system.
2. A parameter study of stellar wind collisions making use of 3D numerical hydrodynamical simulations in an ideal setup.
3. Testing if the gas blown by WR stars orbiting around Sgr A* can reach a stationary state through numerical modelling.

Every study led to a single scientific article: Calderón et al. (2018), Calderón et al. (2019a), Calderón et al. (2019b). These studies are presented as Chapters 2, 3, and 4 of this thesis, respectively. Finally, in Chapter 5, we summarise the main results of this thesis, while also present guidelines for future follow-up projects for improving and extending this work.

References

Agol, Eric (2000). "Sagittarius A* Polarization: No Advection-dominated Accretion Flow, Low Accretion Rate, and Nonthermal Synchrotron Emission". In: ApJ 538.2, pp. L121–L124. DOI: 10.1086/312818. arXiv: astro-ph/0005051 [astro-ph].

Aitken, D. K. et al. (2000). "Detection of Polarized Millimeter and Submillimeter Emission from Sagittarius A*". In: ApJ 534.2, pp. L173–L176. DOI: 10.1086/312685.

Baganoff, F. K. et al. (2003). "Chandra X-Ray Spectroscopic Imaging of Sagittarius A* and the Central Parsec of the Galaxy". In: ApJ 591.2, pp. 891–915. DOI: 10.1086/375145. arXiv: astro-ph/0102151 [astro-ph].

Balick, B. and R. L. Brown (1974). "Intense sub-arcsecond structure in the galactic centre." In: *H II Regions and the Galactic Centre*, pp. 261–265.

Ballone, A. et al. (2013). "Hydrodynamical Simulations of a Compact Source Scenario for the Galactic Center Cloud G2". In: ApJ 776.1, 13, p. 13. DOI: 10.1088/0004-637X/776/1/13. arXiv: 1305.7238 [astro-ph.GA].

Ballone, A. et al. (2016). "The G2+G2t Complex as a Fast and Massive Outflow?" In: ApJ 819.2, L28, p. L28. DOI: 10.3847/2041-8205/819/2/L28. arXiv: 1602.07305 [astro-ph.GA].

Ballone, A. et al. (2018). "3D AMR hydrosimulations of a compact-source scenario for the Galactic Centre cloud G2". In: MNRAS 479.4, pp. 5288–5302. DOI: 10.1093/mnras/sty1408. arXiv: 1706.08547 [astro-ph.GA].

Bartko, H. et al. (2009). "Evidence for Warped Disks of Young Stars in the Galactic Center". In: ApJ 697.2, pp. 1741–1763. DOI: 10.1088/0004-637X/697/2/1741. arXiv: 0811.3903 [astro-ph].

Bartko, H. et al. (2010). "An Extremely Top-Heavy Initial Mass Function in the Galactic Center Stellar Disks". In: ApJ 708.1, pp. 834–840. DOI: 10.1088/0004-637X/708/1/834. arXiv: 0908.2177 [astro-ph.GA].

Berger, Marsha and Joseph Oliger (1984). "Adaptive mesh refinement for hyperbolic partial differential equations". English (US). In: *Journal of Computational Physics* 53.3, pp. 484–512. ISSN: 0021-9991. DOI: 10.1016/0021-9991(84)90073-1.

Berger, M.J. and P. Colella (1989). "Local adaptive mesh refinement for shock hydrodynamics". In: *Journal of Computational Physics* 82.1, pp. 64 –84. ISSN: 0021-9991. DOI: https://doi.org/10.1016/0021-9991(89)90035-1. URL: http://www.sciencedirect.com/science/article/pii/0021999189900351.

Blum, R. D. et al. (2003). "Really Cool Stars and the Star Formation History at the Galactic Center". In: ApJ 597.1, pp. 323–346. DOI: 10.1086/378380. arXiv: astro-ph/0307291 [astro-ph].

Burkert, A. et al. (2012). "Physics of the Galactic Center Cloud G2, on Its Way toward the Supermassive Black Hole". In: ApJ 750.1, 58, p. 58. DOI: 10.1088/0004-637X/750/1/58. arXiv: 1201.1414 [astro-ph.GA].

Calderón, D. et al. (2016). "Clump formation through colliding stellar winds in the Galactic Centre". In: MNRAS 455.4, pp. 4388–4398. DOI: 10.1093/mnras/stv2644. arXiv: 1507.07012 [astro-ph.GA].

Calderón, D. et al. (2018). "The Galactic Centre source G2 was unlikely born in any of the known massive binaries". In: MNRAS 478.3, pp. 3494–3505. DOI: 10.1093/mnras/sty1330. arXiv: 1805.05341 [astro-ph.GA].

Calderón, Diego et al. (2019a). "3D simulations of clump formation in stellar wind collisions". In: *arXiv e-prints*, arXiv:1906.04181, arXiv:1906.04181. arXiv: 1906.04181 [astro-ph.GA].

Calderón, Diego et al. (2019b). "Stellar winds pump the heart of the Milky Way". In: *arXiv e-prints*, arXiv:1910.06976, arXiv:1910.06976. arXiv: 1910.06976 [astro-ph.GA].

Chatzopoulos, S. et al. (2015). "The old nuclear star cluster in the Milky Way: dynamics, mass, statistical parallax, and black hole mass". In: MNRAS 447.1, pp. 948–968. DOI: 10.1093/mnras/stu2452. arXiv: 1403.5266 [astro-ph.GA].

Christopher, M. H. et al. (2005). "HCN and HCO^+ Observations of the Galactic Circumnuclear Disk". In: ApJ 622.1, pp. 346–365. DOI: 10.1086/427911. arXiv: astro-ph/0502532 [astro-ph].

Coker, R. F. and J. M. Pittard (2000). "An X-ray binary model for the Galactic Center source IRS 13E". In: A&A 361, pp. L13–L16. arXiv: astro-ph/0008091 [astro-ph].

Coker, R. F., J. M. Pittard, and J. H. Kastner (2002). "The Galactic Centre source IRS 13E: A post-LBV Wolf-Rayet colliding wind binary?" In: A&A 383, pp. 568–573. DOI: 10.1051/0004-6361:20011745. arXiv: astro-ph/0112029 [astro-ph].

Coker, Robert F. and Fulvio Melia (1997). "Hydrodynamical Accretion onto Sagittarius A* from Distributed Point Sources". In: ApJ 488.2, pp. L149–L152. DOI: 10.1086/310925. arXiv: astro-ph/9708089 [astro-ph].

Courant, R., K. Friedrichs, and H. Lewy (1967). "On the Partial Difference Equations of Mathematical Physics". In: *IBM Journal of Research and Development* 11, pp. 215–234. DOI: 10.1147/rd.112.0215.

Cuadra, Jorge, Sergei Nayakshin, and Fabrice Martins (2008). "Variable accretion and emission from the stellar winds in the Galactic Centre". In: MNRAS 383.2, pp. 458–466. DOI: 10.1111/j.1365-2966.2007.12573.x. arXiv: 0705.0769 [astro-ph].

Cuadra, Jorge et al. (2005). "Accretion of cool stellar winds on to Sgr A*: another puzzle of the Galactic Centre?" In: MNRAS 360.1, pp. L55–L59. DOI: 10.1111/j.1745-3933.2005.00045.x. arXiv: astro-ph/0502044 [astro-ph].

Davidson, J. A. et al. (Mar. 1992). "The luminosity of the Galactic center". In: ApJ 387, pp. 189–211. DOI: 10.1086/171071.

Do, T. et al. (2013). "Stellar Populations in the Central 0.5 pc of the Galaxy. I. A New Method for Constructing Luminosity Functions and Surface-density Profiles". In: ApJ 764.2, 154, p. 154. DOI: 10.1088/0004-637X/764/2/154. arXiv: 1301.0539 [astro-ph.SR].

Eckart, A. and R. Genzel (1997). "Stellar proper motions in the central 0.1 PC of the Galaxy". In: MNRAS 284.3, pp. 576–598. DOI: 10.1093/mnras/284.3.576.

Eckart, A. et al. (2013). "Near-infrared proper motions and spectroscopy of infrared excess sources at the Galactic center". In: A&A 551, A18, A18. DOI: 10.1051/0004-6361/201219994. arXiv: 1208.1907 [astro-ph.IM].

Eisenhauer, F. et al. (2005). "SINFONI in the Galactic Center: Young Stars and Infrared Flares in the Central Light-Month". In: ApJ 628.1, pp. 246–259. DOI: 10.1086/430667. arXiv: astro-ph/0502129 [astro-ph].

Event Horizon Telescope Collaboration et al. (2019). "First M87 Event Horizon Telescope Results. I. The Shadow of the Supermassive Black Hole". In: ApJ 875.1, L1, p. L1. DOI: 10.3847/2041-8213/ab0ec7. arXiv: 1906.11238 [astro-ph.GA].

Fritz, T. K. et al. (2010). "GC-IRS13E—A Puzzling Association of Three Early-type Stars". In: ApJ 721.1, pp. 395–411. DOI: 10.1088/0004-637X/721/1/395. arXiv: 1003.1717 [astro-ph.GA].

Genzel, R., D. Hollenbach, and C. H. Townes (1994). "The nucleus of our Galaxy". In: *Reports on Progress in Physics* 57.5, pp. 417–479. DOI: 10.1088/0034-4885/57/5/001.

Genzel, R. et al. (1997). "On the nature of the dark mass in the centre of the Milky Way". In: MNRAS 291.1, pp. 219–234. DOI: 10.1093/mnras/291.1.219.

Genzel, Reinhard, Frank Eisenhauer, and Stefan Gillessen (2010). "The Galactic Center massive black hole and nuclear star cluster". In: *Reviews of Modern Physics* 82.4, pp. 3121–3195. DOI: 10.1103/RevModPhys.82.3121. arXiv: 1006.0064 [astro-ph.GA].

Ghez, A. M. et al. (1998). "High Proper-Motion Stars in the Vicinity of Sagittarius A*: Evidence for a Supermassive Black Hole at the Center of Our Galaxy". In: ApJ 509.2, pp. 678–686. DOI: 10.1086/306528. arXiv: astro-ph/9807210 [astro-ph].

Ghez, A. M. et al. (2008). "Measuring Distance and Properties of the Milky Way's Central Supermassive Black Hole with Stellar Orbits". In: ApJ 689.2, pp. 1044–1062. DOI: 10.1086/592738. arXiv: 0808.2870 [astro-ph].

Gillessen, S. et al. (2009a). "Monitoring Stellar Orbits Around the Massive Black Hole in the Galactic Center". In: ApJ 692.2, pp. 1075–1109. DOI: 10.1088/0004-637X/692/2/1075. arXiv: 0810.4674 [astro-ph].

Gillessen, S. et al. (2009b). "The Orbit of the Star S2 Around SGR A* from Very Large Telescope and Keck Data". In: ApJ 707.2, pp. L114–L117. DOI: 10.1088/0004-637X/707/2/L114. arXiv: 0910.3069 [astro-ph.GA].

Gillessen, S. et al. (2012). "A gas cloud on its way towards the supermassive black hole at the Galactic Centre". In: Nature 481.7379, pp. 51–54. DOI: 10.1038/nature10652. arXiv: 1112.3264 [astro-ph.GA].

Gillessen, S. et al. (2013a). "New Observations of the Gas Cloud G2 in the Galactic Center". In: ApJ 763.2, 78, p. 78. DOI: 10.1088/0004-637X/763/2/78. arXiv: 1209.2272 [astro-ph.GA].

Gillessen, S. et al. (2013b). "Pericenter Passage of the Gas Cloud G2 in the Galactic Center". In: ApJ 774.1, 44, p. 44. DOI: 10.1088/0004-637X/774/1/44. arXiv: 1306.1374 [astro-ph.GA].

Gillessen, S. et al. (2017). "An Update on Monitoring Stellar Orbits in the Galactic Center". In: ApJ 837.1, 30, p. 30. DOI: 10.3847/1538-4357/aa5c41. arXiv: 1611.09144 [astro-ph.GA].

Gillessen, S. et al. (2019). "Detection of a Drag Force in G2's Orbit: Measuring the Density of the Accretion Flow onto Sgr A* at 1000 Schwarzschild Radii". In: ApJ 871.1, 126, p. 126. DOI: 10.3847/1538-4357/aaf4f8.

Godunov, S.K. (1959). "A difference method for numerical calculation of discontinuous solutions of the equations of hydrodynamics". In: *Mat. Sb. (N.S.)* 47(89).3, pp. 271–306.

Goldwurm, A. (2011). "An Overview of the High-Energy Emission from the Galactic Center". In: *The Galactic Center: a Window to the Nuclear Environment of Disk Galaxies*. Ed. by M. R. Morris, Q. D. Wang, and F. Yuan. Vol. 439. Astronomical Society of the Pacific Conference Series, p. 391. arXiv: 1007.4174 [astro-ph.HE].

Gravity Collaboration et al. (2018). "Detection of the gravitational redshift in the orbit of the star S2 near the Galactic centre massive black hole". In: A&A 615, L15, p. L15. DOI: 10.1051/0004-6361/201833718. arXiv: 1807.09409 [astro-ph.GA].

Gravity Collaboration et al. (2019). "A geometric distance measurement to the Galactic center black hole with 0.3% uncertainty". In: A&A 625, L10, p. L10. DOI: 10.1051/0004-6361/201935656.

Guillochon, James et al. (2014). "Possible Origin of the G2 Cloud from the Tidal Disruption of a Known Giant Star by Sgr A*". In: ApJ 786.2, L12, p. L12. DOI: 10.1088/2041-8205/786/2/L12. arXiv: 1401.2990 [astro-ph.HE].

Habibi, M. et al. (2017). "Twelve Years of Spectroscopic Monitoring in the Galactic Center: The Closest Look at S-stars near the Black Hole". In: ApJ 847.2, 120, p. 120. DOI: 10.3847/1538-4357/aa876f. arXiv: 1708.06353 [astro-ph.SR].

Haggard, Daryl et al. (2014). "2014 Chandra X-ray Monitoring of Sgr A*/G2 and SGR J1745-29". In: *The Astronomer's Telegram* 6242, p. 1.

Haller, Joseph W. et al. (1996). "Stellar Kinematics and the Black Hole in the Galactic Center". In: ApJ 456, p. 194. DOI: 10.1086/176640.

Jackson, J. M. et al. (1993). "Neutral Gas in the Central 2 Parsecs of the Galaxy". In: ApJ 402, p. 173. DOI: 10.1086/172120.

Klein, Richard I., Christopher F. McKee, and Philip Colella (1994). "On the Hydrodynamic Interaction of Shock Waves with Interstellar Clouds. I. Nonradiative Shocks in Small Clouds". In: ApJ 420, p. 213. DOI: 10.1086/173554.

Koyama, Katsuji et al. (1996). "ASCA View of Our Galactic Center: Remains of Past Activities in X-Rays?" In: PASJ 48, pp. 249–255. DOI: 10.1093/pasj/48.2.249.

Lacy, J. H. et al. (1980). "Observations of the motion and distribution of the ionized gas in the central parsec of the Galaxy. II." In: ApJ 241, pp. 132–146. DOI: 10.1086/158324.

LeVeque, R.J. (1992). *NumericalMethods for Conservation Laws*. Basel: Birkhäuser-Verlag. ISBN: 9783034886291. DOI: 10.1007/978-3-0348-8629-1. URL: https://www.springer.com/gp/book/9783764327231.

Levin, Yuri and Andrei M. Beloborodov (2003). "Stellar Disk in the Galactic Center: A Remnant of a Dense Accretion Disk?" In: ApJ 590.1, pp. L33–L36. DOI: 10.1086/376675. arXiv: astro-ph/0303436 [astro-ph].

Lu, J. R. et al. (2009). "A Disk of Young Stars at the Galactic Center as Determined by Individual Stellar Orbits". In: ApJ 690.2, pp. 1463–1487. DOI: 10.1088/0004-637X/690/2/1463. arXiv: 0808.3818 [astro-ph].

Lu, J. R. et al. (2013). "Stellar Populations in the Central 0.5 pc of the Galaxy. II. The Initial Mass Function". In: ApJ 764.2, 155, p. 155. DOI: 10.1088/0004-637X/764/2/155. arXiv: 1301.0540 [astro-ph.SR].

Macquart, Jean-Pierre et al. (2006). "The Rotation Measure and 3.5 Millimeter Polarization of Sagittarius A*". In: ApJ 646.2, pp. L111–L114. DOI: 10.1086/506932. arXiv: astro-ph/0606381 [astro-ph].

Maillard, J. P. et al. (2004). "The nature of the Galactic Center source IRS 13 revealed by high spatial resolution in the infrared". In: A&A 423, pp. 155–167. DOI: 10.1051/0004-6361:20034147. arXiv: astro-ph/0404450 [astro-ph].

Maloney, P. R., D. J. Hollenbach, and C. H. Townes (Dec. 1992). "Heating of H II regions with application to the Galactic center". In: ApJ 401, pp. 559–573. DOI: 10.1086/172086.

Maoz, Eyal (1998). "Dynamical Constraints on Alternatives to Supermassive Black Holes in Galactic Nuclei". In: ApJ 494.2, pp. L181–L184. DOI: 10.1086/311194. arXiv: astro-ph/9710309 [astro-ph].

Mapelli, Michela and Alessia Gualandris (2016). "Star Formation and Dynamics in the Galactic Centre". In: *Astrophysical Black Holes, Lecture Notes in Physics, Volume 905. ISBN 978-3-319-19415-8. Springer International Publishing Switzerland, 2016, p. 205*. Ed. by Francesco Haardt et al. Vol. 905, p. 205. DOI: 10.1007/978-3-319-19416-5_6.

Mapelli, Michela and Emanuele Ripamonti (2015). "Signatures of Planets and Protoplanets in the Galactic Center: A Clue to Understanding the G2 Cloud?" In: ApJ 806.2, 197, p. 197. DOI: 10.1088/0004-637X/806/2/197. arXiv: 1504.04624 [astro-ph.GA].

Marrone, Daniel P. et al. (2006). "Interferometric Measurements of Variable 340 GHz Linear Polarization in Sagittarius A*". In: ApJ 640.1, pp. 308–318. DOI: 10.1086/500106. arXiv: astro-ph/0511653 [astro-ph].

— (2007). "An Unambiguous Detection of Faraday Rotation in Sagittarius A*". In: ApJ 654.1, pp. L57–L60. DOI: 10.1086/510850. arXiv: astro-ph/0611791 [astro-ph].

Martins, F. et al. (2006). "GCIRS 16SW: A Massive Eclipsing Binary in the Galactic Center". In: ApJ 649.2, pp. L103–L106. DOI: 10.1086/508328. arXiv: astro-ph/0608215 [astro-ph].

Martins, F. et al. (2007). "Stellar and wind properties of massive stars in the central parsec of the Galaxy". In: A&A 468.1, pp. 233–254. DOI: 10.1051/0004-6361:20066688. arXiv: astro-ph/0703211 [astro-ph].

McGinn, M. T. et al. (1989). "Stellar Kinematics in the Galactic Center". In: ApJ 338, p. 824. DOI: 10.1086/167239.

Melia, Fulvio (1992). "An Accreting Black Hole Model for Sagittarius A *". In: ApJ 387, p. L25. DOI: 10.1086/186297.

Mezger, Peter G., Wolfgang J. Duschl, and Robert Zylka (1996). "The Galactic Center: a laboratory for AGN?" In: A&A Rev. 7.4, pp. 289–388. DOI: 10.1007/s001590050007.

Miralda-Escudé, Jordi (2012). "A Star Disrupted by a Stellar Black Hole as the Origin of the Cloud Falling toward the Galactic Center". In: ApJ 756.1, 86, p. 86. DOI: 10.1088/0004-637X/756/1/86. arXiv: 1202.5496 [astro-ph.GA].

Montero-Castaño, María, Robeson M. Herrnstein, and Paul T. P. Ho (2009). "Gas Infall Toward Sgr A* from the Clumpy Circumnuclear Disk". In: ApJ 695.2, pp. 1477–1494. DOI: 10.1088/0004-637X/695/2/1477. arXiv: 0903.0886 [astro-ph.GA].

Morris, Mark R., Leo Meyer, and Andrea M. Ghez (2012). "Galactic center research: manifestations of the central black hole". In: *Research in Astronomy and Astrophysics* 12.8, pp. 995–1020. DOI: 10.1088/1674-4527/12/8/007. arXiv: 1207.6755 [astro-ph.GA].

Muno, M. P. et al. (2007). "Discovery of Variable Iron Fluorescence from Reflection Nebulae in the Galactic Center". In: ApJ 656.2, pp. L69–L72. DOI: 10.1086/512236. arXiv: astro-ph/0611651 [astro-ph].

Murray-Clay, Ruth A. and Abraham Loeb (2012). "Disruption of a proto-planetary disc by the black hole at the milky way centre". In: *Nature Communications* 3, 1049, p. 1049. DOI: 10.1038/ncomms2044. arXiv: 1112.4822 [astro-ph.GA].

Novak, G. et al. (2000). "Submillimeter Polarimetric Observations of the Galactic Center". In: ApJ 529.1, pp. 241–250. DOI: 10.1086/308231.

Paumard, T., J. P. Maillard, and M. Morris (2004). "Kinematic and structural analysis of the <ASTROBJ>Minispiral</ASTROBJ> in the Galactic Center from BEAR spectro-imagery". In: A&A 426, pp. 81–96. DOI: 10.1051/0004-6361:20034209. arXiv: astro-ph/0405197 [astro-ph].

Paumard, T. et al. (2006). "The Two Young Star Disks in the Central Parsec of the Galaxy: Properties, Dynamics, and Formation". In: ApJ 643.2, pp. 1011–1035. DOI: 10.1086/503273. arXiv: astro-ph/0601268 [astro-ph].

Pfuhl, O. et al. (2014). "Massive Binaries in the Vicinity of Sgr A*". In: ApJ 782.2, 101, p. 101. DOI: 10.1088/0004-637X/782/2/101. arXiv: 1307.7996 [astro-ph.GA].

Pfuhl, Oliver et al. (2015). "The Galactic Center Cloud G2 and its Gas Streamer". In: ApJ 798.2, 111, p. 111. DOI: 10.1088/0004-637X/798/2/111. arXiv: 1407.4354 [astro-ph.GA].

Phifer, K. et al. (2013). "Keck Observations of the Galactic Center Source G2: Gas Cloud or Star?" In: ApJ 773.1, L13, p. L13. DOI: 10.1088/2041-8205/773/1/L13. arXiv: 1304.5280 [astro-ph.GA].

Plewa, P. M. et al. (2017). "The Post-pericenter Evolution of the Galactic Center Source G2". In: ApJ 840.1, 50, p. 50. DOI: 10.3847/1538-4357/aa6e00. arXiv: 1704.05351 [astro-ph.GA].

Ponti, G. et al. (2010). "Discovery of a Superluminal Fe K Echo at the Galactic Center: The Glorious Past of Sgr A* Preserved by Molecular Clouds". In: ApJ 714.1, pp. 732–747. DOI: 10.1088/0004-637X/714/1/732. arXiv: 1003.2001 [astro-ph.HE].

Prodan, Snezana, Fabio Antonini, and Hagai B. Perets (2015). "Secular Evolution of Binaries near Massive Black Holes: Formation of Compact Binaries, Merger/Collision Products and G2-like Objects". In: ApJ 799.2, 118, p. 118. DOI: 10.1088/0004-637X/799/2/118. arXiv: 1405.6029 [astro-ph.GA].

Quataert, Eliot (2002). "A Thermal Bremsstrahlung Model for the Quiescent X-Ray Emission from Sagittarius A*". In: ApJ 575.2, pp. 855–859. DOI: 10.1086/341425. arXiv: astro-ph/0201395 [astro-ph].

— (2004). "A Dynamical Model for Hot Gas in the Galactic Center". In: ApJ 613.1, pp. 322–325. DOI: 10.1086/422973. arXiv: astro-ph/0310446 [astro-ph].

Quataert, Eliot and Andrei Gruzinov (2000). "Convection-dominated Accretion Flows". In: ApJ 539.2, pp. 809–814. DOI: 10.1086/309267. arXiv: astro-ph/9912440 [astro-ph].

Ressler, S. M., E. Quataert, and J. M. Stone (2018). "Hydrodynamic simulations of the inner accretion flow of Sagittarius A* fuelled by stellar winds". In: MNRAS 478.3, pp. 3544–3563. DOI: 10.1093/mnras/sty1146. arXiv: 1805.00474 [astro-ph.HE].

Roberts, D. A. and W. M. Goss (1993). "Multiconfiguration VLA H92 alpha Observations of Sagittarius A West at 1 Arcsecond Resolution". In: ApJS 86, p. 133. DOI: 10.1086/191773.

Roe, P. L. (1986). "Characteristic-based schemes for the Euler equations". In: *Annual Review of Fluid Mechanics* 18, pp. 337–365. DOI: 10.1146/annurev.fl.18.010186.002005.

Russell, Christopher M. P., Q. Daniel Wang, and Jorge Cuadra (2017). "Modelling the thermal X-ray emission around the Galactic Centre from colliding Wolf-Rayet winds". In: MNRAS 464.4, pp. 4958–4965. DOI: 10.1093/mnras/stw2584. arXiv: 1607.01562 [astro-ph.HE].

Schödel, R. et al. (2002). "A star in a 15.2-year orbit around the supermassive black hole at the centre of the Milky Way". In: Nature 419.6908, pp. 694–696. DOI: 10.1038/nature01121. arXiv: astro-ph/0210426 [astro-ph].

Schödel, R. et al. (2003). "Stellar Dynamics in the Central Arcsecond of Our Galaxy". In: ApJ 596.2, pp. 1015–1034. DOI: 10.1086/378122. arXiv: astro-ph/0306214 [astro-ph].

Scoville, N. and A. Burkert (2013). "The Galactic Center Cloud G2—a Young Low-mass Star with a Stellar Wind". In: ApJ 768.2, 108, p. 108. DOI: 10.1088/0004-637X/768/2/108. arXiv: 1302.6591 [astro-ph.HE].

Sellgren, K. et al. (1990). "Velocity Dispersion and the Stellar Population in the Central 1.2 Parsecs of the Galaxy". In: ApJ 359, p. 112. DOI: 10.1086/169039.

Serabyn, E. et al. (1997). "High-Frequency Measurements of the Spectrum of Sagittarius A*". In: ApJ 490.1, pp. L77–L81. DOI: 10.1086/311010.

Sunyaev, R. A., M. Markevitch, and M. Pavlinsky (1993). "The Center of the Galaxy in the Recent Past: A View from GRANAT". In: ApJ 407, p. 606. DOI: 10.1086/172542.

Teyssier, R. (2002). "Cosmological hydrodynamics with adaptive mesh refinement. A new high resolution code called RAMSES". In: A&A 385, pp. 337–364. DOI: 10.1051/0004-6361:20011817. arXiv: astro-ph/0111367 [astro-ph].

Teyssier, Romain (2015). "Grid-Based Hydrodynamics in Astrophysical Fluid Flows". In: ARA&A 53, pp. 325–364. DOI: 10.1146/annurev-astro-082214-122309.

Tsuboi, Masato et al. (2017). "The Second Galactic Center Black Hole? A Possible Detection of Ionized Gas Orbiting around an IMBH Embedded in the Galactic Center IRS13E Complex". In: ApJ 850.1, L5, p. L5. DOI: 10.3847/2041-8213/aa97d3. arXiv: 1711.00612 [astro-ph.GA].

Valencia-S., M. et al. (2015). "Monitoring the Dusty S-cluster Object (DSO/G2) on its Orbit toward the Galactic Center Black Hole". In: ApJ 800.2, 125, p. 125. DOI: 10.1088/0004-637X/800/2/125. arXiv: 1410.8731 [astro-ph.GA].

van Leer, B. (1976). "MUSCL, a new approach to numerical gas dynamics." In: *Computing in Plasma Physics and Astrophysics*.

— (1977). "Towards the ultimate conservative difference scheme III. Upstream-centered finite-difference schemes for ideal compressible flow". In: *Journal of Computational Physics* 23.3, pp. 263–275. ISSN: 0021-9991. DOI: https://doi.org/10.1016/0021-9991(77)90094-8. URL: http://www.sciencedirect.com/science/article/pii/0021999177900948.

— (1979). "Towards the ultimate conservative difference scheme. V. A second-order sequel to Godunov's method". In: *Journal of Computational Physics* 32.1, pp. 101 –136. ISSN: 0021-9991. DOI: https://doi.org/10.1016/0021-9991(79)90145-1. URL: http://www.sciencedirect.com/science/article/pii/0021999179901451.

Witzel, G. et al. (2014). "Detection of Galactic Center Source G2 at 3.8 μm during Periapse Passage". In: ApJ 796.1, L8, p. L8. DOI: 10.1088/2041-8205/796/1/L8. arXiv: 1410.1884 [astro-ph.HE].

Witzel, G. et al. (2017). "The Post-periapsis Evolution of Galactic Center Source G1: The Second Case of a Resolved Tidal Interaction with a Supermassive Black Hole". In: ApJ 847.1, 80, p. 80. DOI: 10.3847/1538-4357/aa80ea. arXiv: 1707.02301 [astro-ph.GA].

Wollman, E. R. et al. (1977). "Ne II 12.8 micron emission from the galactic center. II." In: ApJ 218, pp. L103–L107. DOI: 10.1086/182585.

Xu, Ya-Di et al. (2006). "Thermal X-Ray Iron Line Emission from the Galactic Center Black Hole Sagittarius A*". In: ApJ 640.1, pp. 319–326. DOI: 10.1086/499932. arXiv: astro-ph/0511590 [astro-ph].

Yelda, S. et al. (2014). "Properties of the Remnant Clockwise Disk of Young Stars in the Galactic Center". In: ApJ 783.2, 131, p. 131. DOI: 10.1088/0004-637X/783/2/131. arXiv: 1401.7354 [astro-ph.GA].

Yu, Yun-Wei et al. (2011). "A past capture event at Sagittarius A* inferred from the fluorescent X-ray emission of Sagittarius B clouds". In: MNRAS 411.3, pp. 2002–2008. DOI: 10.1111/j.1365-2966.2010.17826.x. arXiv: 1010.1312 [astro-ph.HE].

Yuan, Feng, Eliot Quataert, and Ramesh Narayan (2003). "Nonthermal Electrons in Radiatively Inefficient Accretion Flow Models of Sagittarius A*". In: ApJ 598.1, pp. 301–312. DOI: 10.1086/378716. arXiv: astro-ph/0304125 [astro-ph].

Yusef-Zadeh, F. and Mark Morris (1987). "Structural Details of the Sagittarius A Complex: Evidence for a Large-Scale Poloidal Magnetic Field in the Galactic Center Region". In: ApJ 320, p. 545. DOI: 10.1086/165572.

Zhao, Jun-Hui et al. (2009). "Dynamics of Ionized Gas at the Galactic Center: Very Large Array Observations of the Three-dimensional Velocity Field and Location of the Ionized Streams in Sagittarius A West". In: ApJ 699.1, pp. 186–214. DOI: 10.1088/0004-637X/699/1/186. arXiv: 0904.3133 [astro-ph.GA].

Zhao, Jun-Hui et al. (2010). "The High-density Ionized Gas in the Central Parsec of the Galaxy". In: ApJ 723.2, pp. 1097–1109. DOI: 10.1088/0004-637X/723/2/1097. arXiv: 1009.1401 [astro-ph.GA].

2

The Galactic Centre source G2 was unlikely born in any of the known massive binaries

The source G2 has already completed its pericentre passage around Sgr A*, the supermassive black hole in the centre of our Galaxy. Although it has been monitored for 15 years, its astrophysical nature and origin still remain unknown. In this work, we aim to test the hypothesis of G2 being the result of a stellar wind collision. To do so, we study the motion and final fate of gas clumps formed as a result of collisions of stellar winds in massive binaries. Our approach is based on a test-particle model in order to describe the trajectories of such clumps. The model takes into account the gravitational field of Sgr A*, the interaction of the clumps with the interstellar medium as well as their finite lifetimes. Our analysis allows us to reject the hypothesis based on four arguments: *i*) if G2 has followed a purely Keplerian orbit since its formation, it cannot have been produced in any of the known massive binaries since their motions are not consistent; *ii*) in general, gas clumps are evaporated through thermal conduction on very short timescale (< 100 yr) before getting close enough to Sgr A*; *iii*) IRS 16SW, the best candidate for the origin of G2, cannot generate clumps as massive as G2; and *iv*) clumps ejected from IRS 16SW describe trajectories significantly different to the observed motion of G2.

D. Calderón, J. Cuadra, M. Schartmann, A. Burkert, P. Plewa, F. Eisenhauer, M. Habibi, MNRAS, **Volume 478**, *3494 (2018)*

2.1 Introduction

Gillessen et al. (2012) discovered an enigmatic source traveling on a nearly radial orbit to the super-massive black hole (SMBH) of our Galaxy, Sgr A*. Several groups have been monitoring the so-called G2 object since then, aiming to capture its interaction with Sgr A* as well as to understand its astrophysical nature (Witzel et al., 2014; Valencia-S. et al., 2015; Plewa et al., 2017). The possibility of observing a tidal disruption event in the Galactic Centre is a unique opportunity to investigate accretion physics and constrain the properties of the accretion flow. L'-band observations with aid of adaptive optics show G2 as a dusty, unresolved source before and after pericentre passage (Gillessen et al., 2012; Witzel et al., 2014). On the other hand, SINFONI/VLT Br-γ and He I line observations revealed an extended source of ionised gas being affected by tidal shearing due to Sgr A*'s strong gravitational pull (Gillessen et al., 2013a; Gillessen et al., 2013b; Pfuhl et al., 2015). The latest observations complete 15 years of monitoring its orbit, including its recent pericentre passage (Plewa et al., 2017)[1].

Since its discovery there has been an interesting debate regarding G2's nature. The proposed scenarios can be broadly divided in two groups: the compact source and the purely gaseous cloud. The former refers to hypotheses that consider there is/was an object such as a star or a planet within G2. On the contrary, the latter refers to models in which G2 is a purely gaseous and dusty object. Among compact source scenario explanations are an evaporating circumstellar disc Murray-Clay and Loeb (2012) and Miralda-Escudé (2012) or proto-planet (Mapelli and Ripamonti, 2015), a star with a gaseous and dusty envelope (Ballone et al., 2013; De Colle et al., 2014; Valencia-S. et al., 2015; Ballone et al., 2016), and the result of the merger of a binary system (Witzel et al., 2014). On the other hand, if G2 is solely made out of gas and dust it might have originated from the slow stellar wind (300–600 km s^{-1}) of a luminous blue variable (Burkert et al., 2012), as the result of a partial tidal disruption of a late-type giant star by the action of the SMBH (Guillochon et al., 2014), or due to a recent

[1] This was valid at the time of publication but not anymore since Gillessen et al. (2019) reported newer observations.

nova outburst that ejected a ring-like shell of gas (Meyer and Meyer-Hofmeister, 2012). An additional explanation is that the source is part of a clumpy larger stream of gas formed in a stellar wind collision (Burkert et al., 2012; Gillessen et al., 2012; Schartmann et al., 2012; Calderón et al., 2016). This hypothesis is supported by the presence of another object, called G1, that shares similar characteristics with G2, including almost the same orbit but 13 years forward in time (Pfuhl et al., 2015). Moreover, the same study showed the presence of a structure of material trailing G2 on a slightly different orbit. Recently, Plewa et al. (2017) showed that this “tail" of G2 is actually following G2. Tracing back its motion it seems to be coming from the massive binary IRS 16SW which suggests a possible origin. Furthermore, the alignment of G2 and IRS 16SW orbits supports this idea (Gillessen et al., 2012; Burkert et al., 2012). Another argument in favour of this scenario was shown in Calderón et al. (2016). In that study we analysed stellar wind collisions of all possible pairs of mass-losing stars in the Galactic Centre to see whether clump formation could take place or not. There, we found that wind collisions of massive binary systems, and not of encounters between single stars, satisfied the requirements to generate such gas clumps. Specifically, we concluded that IRS 16SW is the best candidate to produce clumps based on its binary and stellar wind properties.

In this work, we aim to test whether a massive binary system, like IRS 16SW, can indeed create and place G2 on its observed orbit assuming a purely gaseous nature. The best way of testing this hypothesis would be to run a self-consistent hydrodynamical simulation of the wind-emitting binary orbiting Sgr A*. However, the scales that need to be covered in space and time span at least 5 and 7 order of magnitudes, respectively, which makes the problem an overwhelming computational challenge. Therefore, in this study we opt for analysing the observed motion of G2 and study whether it is consistent with an origin in a massive binary. Furthermore, we attempt to reproduce G2’s motion by clumps produced in IRS 16SW. To do so, we set up and run several test-particle simulations in order to quantify the probability of ejecting a clump that mimics the trajectory of G2.

This chapter is divided as follows: Section 2.2 describes the clump formation process

in colliding wind binaries. In Section 2.3, we introduce the hypothesis of G2 being formed in IRS 16SW and discuss whether it is consistent with the current knowledge of these objects. Section 2.4 introduces and describes our test-particle simulations of IRS 16SW ejecting clumps while orbiting Sgr A*. In Section 2.4.2, we present the results of our simulations. Section 4.4 compares the results of our model with G2's motion and discusses the limitations of our model. Finally, in Section 2.6 we close with some final remarks and present the conclusions of this work.

2.2 Clump formation in colliding wind binaries

A colliding wind binary is a system of two gravitationally bound stars, whose winds collide between them. This collision creates a hot slab filled with shocked material reaching temperatures of 10^6–10^7 K in the case of Wolf-Rayet (WR) stars. If the material can radiate its energy rapidly enough, the slab becomes thinner and denser. If perturbed, the slab is prone to suffer *thin-shell instabilities* (Vishniac, 1983; Vishniac, 1994). These mechanisms are excited due to the misalignment between the wind ram-pressure and the thermal pressure within the slab. Furthermore, the velocity difference between both winds can excite the Kelvin-Helmholtz instability which can act simultaneously with other instabilities. However, Lamberts, Fromang, and Dubus (2011) showed that the *non-linear thin shell instability* (NTSI Vishniac, 1994) is the one that dominates the long-term evolution of the slab due to its large-scale perturbations. Therefore, we expect this mechanism to produce clumps which then are ejected to the interstellar medium (ISM).

Recently, we conducted a study aiming to estimate analytically the clump masses formed through the NTSI in the Galactic Centre (Calderón et al., 2016). We showed that Earth mass clumps can be produced for certain combinations of wind speed and stellar separation, for stars with strong outflows. Moreover, given the known stellar population in the GC, we found that massive binary systems are the most promising clump sources within the inner parsec.

2.2.1 Massive binaries orbiting Sgr A*

The inner parsec of our Galaxy hosts about 30 WR stars. Photometric and spectroscopic studies have provided valuable information of their orbits and stellar winds. Years of monitoring allowed to identify three binary systems among this sample (Martins et al., 2006; Pfuhl et al., 2014). However, there are other four sources considered as binary candidates (see Pfuhl et al., 2014). Although some of them showed changes on either brightness or radial velocity, there are not enough observations to confirm their binarity. Furthermore, only two of them are within half a parsec from Sgr A*. The other two are at ~1.5 pc, so latest surveys did not include them. Therefore, throughout this work we focus uniquely on systems already confirmed as binaries.

As we stated previously, there are three confirmed massive binaries inside the central parsec of the Galaxy. The first one, IRS 16SW, was identified as an eclipsing binary with a period of 19.5 days by Martins et al. (2006). Its symmetric light curve indicates it is composed of equally massive stars. Their mass was derived from its dynamics to be about ~50 $M_\odot$ for each star. The spectrum is consistent with the presence of strong outflows (~10^{-5} $M_\odot$ yr^{-1}) whose terminal velocity is ~600 km s^{-1} (Martins et al., 2007; Cuadra, Nayakshin, and Martins, 2008). More recently, Pfuhl et al. (2014) identified two new OB/WR binaries: IRS 16NE, a long-period Ofpe/WN9 binary with a period of 224 days, and E60, an eclipsing WR binary with a period of 2.3 days. The most relevant properties of these massive binaries are summarised in Table 2.1.

In Figure 2.1, we show the sky-projected orbits of the known binaries around Sgr A*. Throughout this work we used the most recent orbital data available in the literature for the binaries as well as for G2 (Gillessen et al., 2017; Plewa et al., 2017). Nevertheless, it is important to remark that only IRS 16SW's orbit is completely determined (i.e. observed sky-positions, proper motions, radial velocity, and sky-acceleration). The orbits of the other two binaries have not been entirely constrained yet, as no acceleration has been detected so far. The orbits shown in the figure were chosen by iterating over the unknown position along the

Table 2.1: Properties of massive binaries in the vicinity of Sgr A*.

Name (1)	Type (2)	$a \sin i$ (au) (3)	Eccentricity (4)	Period (d) (5)	$\dot{M}_w$ ($M_\odot$ yr^{-1}) (6)	V_w (km s^{-1}) (7)	r_p (arcsec) (8)
IRS 16SW	Ofpe/WN9	0.3	~0	19.5	$\sim 10^{-5}$	600	1.5
IRS 16NE	Ofpe/WN9	1.2	~0	224	$\sim 2 \times 10^{-5}$	650	> 2.8
E60	WR binary	0.1	0.3	2.3	$\sim 5 \times 10^{-6}$	750	> 2.3

Notes. Column 1: binary system ID. Column 2: Spectral classification (if available; Martins et al., 2007). Column 3: binary semi-major axis. Column 4: binary eccentricity. Column 5: binary period. Binary orbital properties were taken from Martins et al. (2006) and Pfuhl et al. (2014). Column 6: stellar wind mass loss rate. Column 7: stellar wind terminal velocity. Stellar wind properties were obtained from Martins et al. (2007) and Cuadra, Nayakshin, and Martins (2008). Column 8: pericentre distance of the binary system around Sgr A* constrained from the observed sky-projected positions, proper motions and line-of-sight velocity (Paumard et al., 2006; Gillessen et al., 2017).

line of sight, and minimising the resulting orbital eccentricity. Also, by the same procedure we have calculated lower limits for their pericentre distances (see Table 2.1). Notice that the *actual* pericentre distance of IRS 16SW around Sgr A* is shorter by ~2/3 than the *minimum possible* pericentre of either of the other binaries. For them, the free-fall timescale is significantly longer than the typical clump lifetime. Then, it is not possible for clumps created in those binaries to get close to Sgr A* (see Section 2.3.3). Therefore, in this work we focus our study on clumps ejected from IRS 16SW.

It is important to highlight that the apocentre of G2's orbit roughly coincides with IRS 16SW orbit (see Figure 2.1). This fact also gives us a hint of the possible origin of G2 from this binary.

2.3 G2 as a gas clump from IRS 16SW

There are three pieces of evidence pointing to IRS 16SW as G2's origin. Firstly, the cloud orbit is coplanar with the so-called clockwise disc, which includes the binary (Gillessen et al., 2012; Pfuhl et al., 2015). Secondly, G2's apocentre lies roughly on the orbit of IRS 16SW (see Figures 2.1 and 2.2). Finally, the gas stream following G2 seems to have been originated in

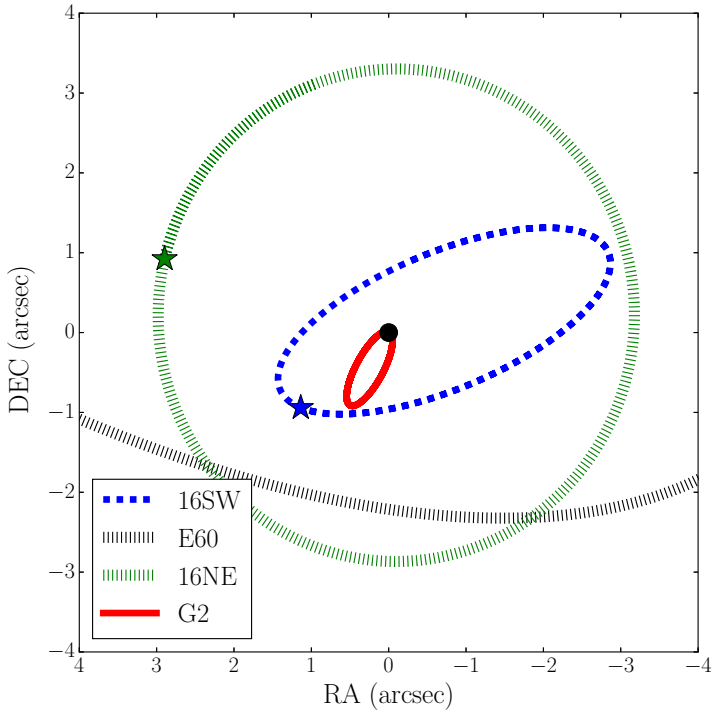

Figure 2.1: Sky-projected orbits of the massive binary systems and G2 around Sgr A*. The dash-dotted black, dash-dotted green and dashed blue lines show the trajectories of IRS 16SW, IRS 16NE and E60, respectively. Star symbols stand for their current positions. E60's current position is outside of this region. Notice that G2's apocentre roughly matches with the orbit of IRS 16SW.

IRS 16SW (Plewa et al., 2017). In this section, we study if this hypothesis is consistent with G2's motion and the expected lifetime of gas clumps in this region.

2.3.1 The Keplerian orbit

Observations of G2's orbit currently span around 12 years, reaching its pericentre. These data can be well described with a Keplerian orbit (Gillessen et al., 2012; Gillessen et al., 2013a; Gillessen et al., 2013b; Pfuhl et al., 2015; Valencia-S. et al., 2015; Plewa et al., 2017), i.e. within

the error bars there is no apparent deviation from a ballistic motion[2]. Let us consider G2 has moved on this orbit since it was formed. This assumption allows us to draw conclusions from the analysis of G2 and IRS 16SW observed orbits. In Figure 2.2, we show sky-projected possible orbits of G2 (solid black lines) and the binary (dotted blue line) around the SMBH. We highlighted positions at $t = 1816, 1916, 2016$ yr, the latter being the epoch of the latest G2 observations. Notice that the positions of IRS 16SW and G2 do not coincide in any time shown. At a given epoch t both sources are separated by at least ~0.25 arcsec (2000 au, even taking into account the uncertainties associated to their inferred orbits (see Figure 2.2)[3]. Thus, G2 cannot have been created in IRS 16SW. However, we have to be careful with this conclusion. We have to bear in mind that in this analysis we have not considered systematic uncertainties on G2's orbit. As the source has been monitored solely around its pericentre passage the pericentre time and distance are well constrained. On the contrary, the apocentre is very uncertain. In the previous analysis we just extrapolated the observational data based on the Keplerian orbit assumption. Then, although this suggests the hypothesis is not feasible we cannot quantify the robustness of this conclusion with the available data.

2.3.2 Clump lifetimes

A critical constraint to conceive G2 as a gas clump is the lifetime of such a clump. Once formed, clumps are immediately ejected into the ISM that close to Sgr A* is a very hostile environment. The region is dominated by shocked stellar winds blown by tens of WR stars. Therefore, the ISM is composed by very hot, diffuse plasma. The properties of the medium are very different compared to the ones of clumps. Typically, the medium is at a temperature of $\sim 10^7$ K while clumps are kept at $\sim 10^4$ K by the strong ultraviolet (UV) radiation from the

[2]At the time of publication this was valid, although Gillessen et al. (2019) reported deviations from Keplerian motions. In Section 2.6, we discuss the implications

[3]The uncertainty on IRS 16SW's position in 1916 was calculated by simple error propagation from its currently measured position and velocity. Given that the time interval considered is much shorter than its orbital period, no further analysis is needed

young stars present in the region. As we know, cold gas clumps embedded in a hot, diffuse medium can be seriously affected by thermal conduction. The rate of evaporation due to this process depends on the ratios of density and temperature between the clumps and the medium.

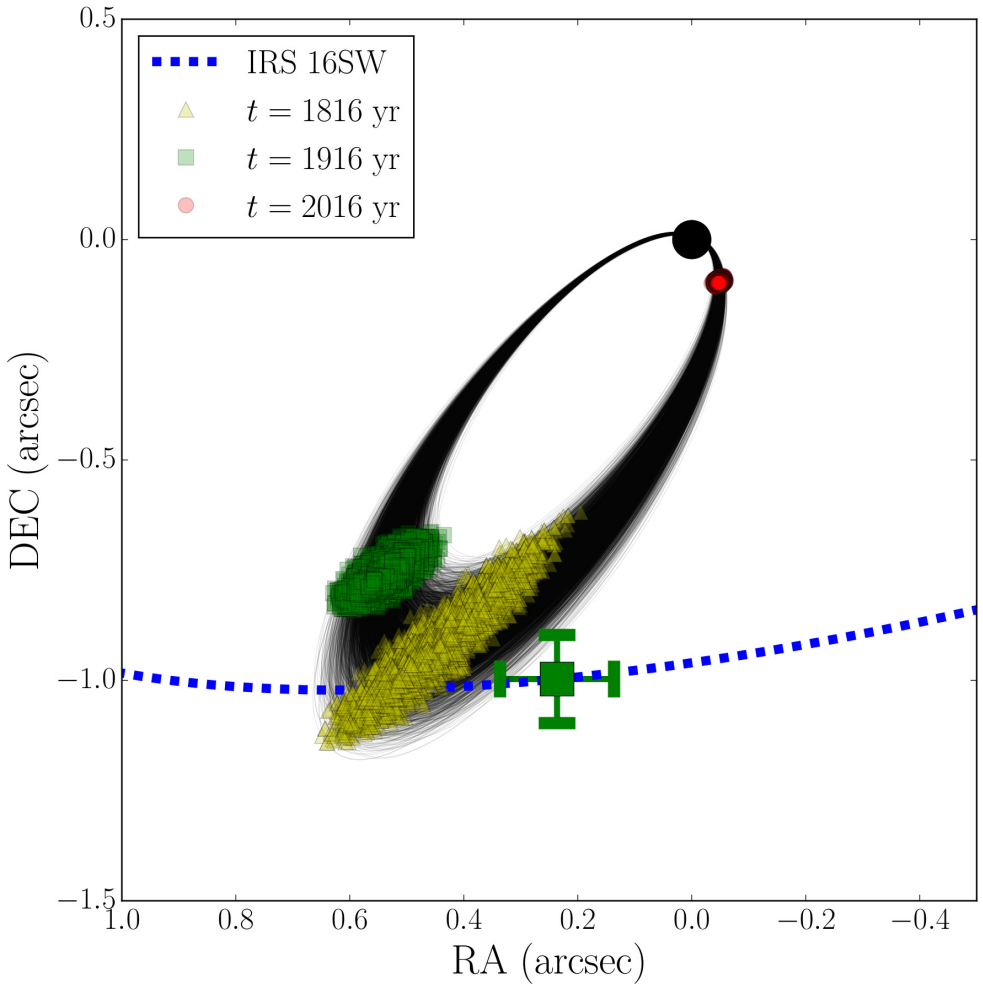

Figure 2.2: Sky-projection of the best fit orbit to G2's motion plotted with 3σ errors (Plewa et al., 2017) shown as solid black lines. Part of the orbit of IRS 16SW is also shown as dashed blue line. Coloured symbols represent positions at different epochs: t = 1816 *yr* (yellow triangles), t = 1916 yr (green squares), t = 2016 (red circles). The error on the projected orbit of IRS 16SW in t = 1916 is ~0.1 arcsec. The big black dot at the origin represents Sgr A*. Notice that G2's apocentre passage is overlaid on IRS 16SW's orbit within the errors.

Based on Cowie and McKee (1977) and Burkert et al. (2012), the mass-loss rate due to thermal conduction of a cloud with a given mass m_c and distance from Sgr A* r can be estimated through the expression

$$\dot{M}_{\rm evap} \approx 1.25 \times 10^{-2}\ {\rm M}_\oplus\ {\rm yr}^{-1} (\alpha+1)^{1/6} \left(\frac{n_0}{100\ {\rm cm}^{-3}}\right)^{1/3} \left(\frac{m_c}{1\ {\rm M}_\oplus}\right)^{2/3} \left(\frac{1.7\times10^{17}\ {\rm cm}}{r}\right)^{(2\alpha-1)/6}, \tag{2.1}$$

where n_0 and α are the normalization and power-law of the medium density profile, respectively; i.e. $n(r) = n_0(r_0/r)^\alpha$, which were chosen to reproduce the X-ray observations of the region (see Appendix 2.A). Notice that this expression was derived in the saturation limit, therefore, it is not very sensitive to the presence of magnetic fields (Cowie and McKee, 1977).

Then, the evaporation timescale is

$$\tau_{\rm evap} \approx \frac{80\ {\rm yr}}{(\alpha+1)^{1/6}} \left(\frac{100\ {\rm cm}^{-3}}{n_0}\right)^{1/3} \left(\frac{m_c}{1\ {\rm M}_\oplus}\right)^{1/3} \left(\frac{r}{1.7\times10^{17}\ {\rm cm}}\right)^{(2\alpha-1)/6}. \tag{2.2}$$

Both expressions were obtained under the assumption of hydrostatic equilibrium of the medium. Thus, the temperature profile follows $T(r) \propto r^{-1}$.

In Figure 2.3, we show the evaporation timescale as a function of the distance from Sgr A* for different clump masses (solid black lines). Also, we plotted the free-fall timescale (dashed blue lines), and the pericentre and apocentre distances of IRS 16SW (green vertical lines). In the left panel, we present the case with $\alpha = 0.5$ (shallow density profile) which describes an outflow solution for the accretion flow as suggested by Wang et al. (2013). In the right panel, we show the case with $\alpha = 1.5$ (steep density profile) which represents a Bondi accretion flow environment. Despite having different dependences on r the values of the evaporation timescale are very similar at the orbit of IRS 16SW. This is a direct consequence of both density models being scaled at the Bondi radius $r_b \approx 1.4$ arcsec, which corresponds to the typical distance between the binary and Sgr A*. Thus, at this separation both density profiles must converge. On the contrary, approaching the SMBH models start to differ. The steep profile ($\alpha = 1.5$) makes thermal conduction twice more efficient at 0.1 arcsec from Sgr A*

when comparing to the shallow profile ($\alpha = 0.5$). This is the result of the medium becoming denser more rapidly as r decreases in the case of the steep profile. Finally, notice that light clumps ($\lesssim 1$ $M_\oplus$) will evaporate very rapidly but more massive ones ($\gtrsim 1$ $M_\oplus$) may survive for decades, and even centuries; regardless of the ISM profile.

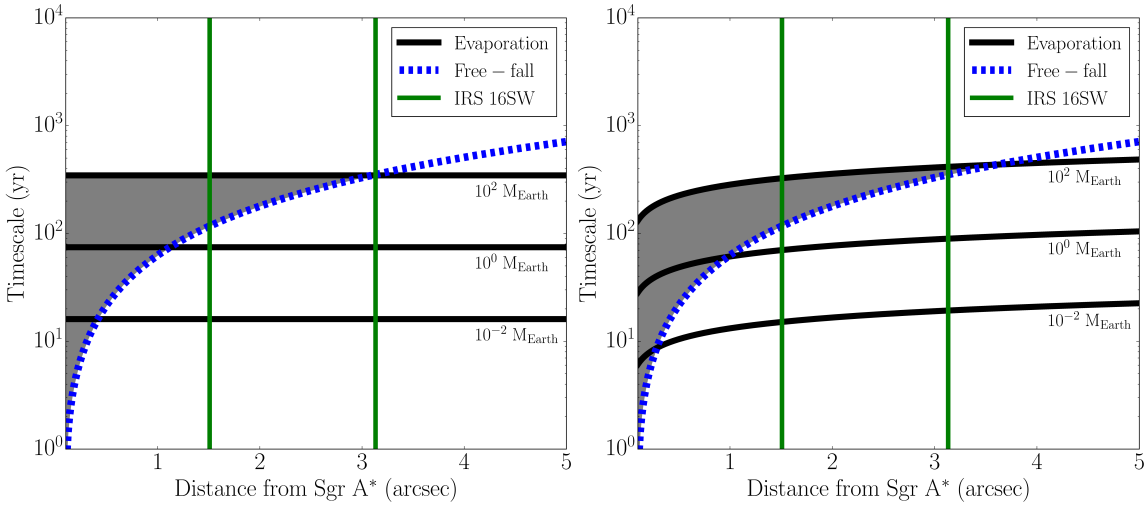

Figure 2.3: Relevant timescales as a function of distance from Sgr A*. The solid black lines show the evaporation timescale, i.e. lifetime, of gas clumps of a given mass embedded in a hot medium. The dashed blue line represents the free-fall timescale. The grey area shows the region where clumps of $M < 100$ $M_\oplus$ need to be produced in order they could be captured. The vertical solid green lines show the pericentre and apocentre distances of IRS 16SW orbit around Sgr A*. The left panel shows estimations using a radial density profile with $\alpha = 0.5$, while the right panel uses $\alpha = 1.5$.

In Figure 2.3, we can observe it is not possible for light clumps (< 1 $M_\oplus$) created by IRS 16SW to reach the SMBH indicated by the black solid lines being below the dashed blue line at distance of the orbit of IRS 16SW. This means that the free-fall timescale is longer than the typical lifetime of the light clumps. Then, they will be evaporated very quickly without having chances of approaching to the SMBH. Only fairly massive clumps ($\gtrsim 3$ $M_\oplus$) live long enough to fall onto Sgr A*. Therefore, only clumps roughly in the range 1–100 $M_\oplus$ can achieve short distances to the central black hole. However, as we will discuss it is not likely

for a binary like IRS 16SW to form such massive clumps (see Section 2.3.3).

Gillessen et al. (2012) estimated the gas mass of G2 from its Br-γ emission to be ~3 $M_\oplus$ assuming it is being kept at 10^4 K. As clumps are evaporated constantly during their lives G2's initial mass had to be larger. Then, from the analysis of clump lifetimes it is still possible for G2 to be one of these gas clumps. However, this also puts strong constraints on the initial mass and the position where clumps have to be ejected from in order to mimic G2 observations.

2.3.3 Clump masses

Here we will constrain the mass of clumps produced in a colliding wind binary. In principle, it is hard to predict the mass of clumps formed in a stellar wind collision. This is due to the fact that we need to derive their size to do so. In Calderón et al. (2016) we overcame this issue by using the unstable wavelength criteria of the NTSI as clump radius proxy. Nevertheless, such an approach can only be used when we can ignore wind acceleration, stellar gravity and radiation pressure. In the case of IRS 16SW we cannot neglect those processes given the very short stellar separation of the binary of ~0.7 au. This is why here we follow a simpler but more appropriate approach instead.

Let us start by considering a system formed by two identical stars. Each of them blows a smooth, isotropic stellar wind whose density and terminal velocity are $\rho_w(r)$ and V_w, respectively (see Figure 2.4). Then, the stellar wind density will be given by

$$\rho_w(r) = \frac{1}{4\pi}\frac{\dot{M}_w}{V_w r^2}, \tag{2.3}$$

where r is the distance to the star and $\dot{M}_w$ its wind mass loss rate. Once winds collide, a slab of shocked material will be formed in the midpoint between the stars. Let us call the distance between a star and the slab D, i.e. the stellar separation is $2D$. The slab will be confined by the ram pressure of the two winds. Assuming the gas within the slab cools down faster than

it can escape from the system its density ρ_s can be estimated by

$$P_s = P_w \Rightarrow \rho_s = \frac{V_w^2}{c_s^2}\rho_w, \tag{2.4}$$

where P_s is the thermal pressure within the slab, P_w is the ram pressure of the wind, and c_s is the slab sound speed.

As clumps are formed out of slab material their mass will be given by $m_c \approx \rho_s L^3$, where L is the size of the clump. Combining the previous expressions we can estimate the mass of the clumps as

$$m_c \approx \frac{1}{4\pi}\frac{\dot{M}_w V_w D}{c_s^2}\left(\frac{L}{D}\right)^3. \tag{2.5}$$

Notice that physically motivated clumps will satisfy $L/D < 1$. Otherwise, the clumps would overlap with the stars. Therefore, we refer to clumps with $L > D$ as not physically motivated objects. Based on this, the maximum clump mass possible will be given when $L/D \approx 1$, i.e.

$$m_c < 3\ \mathrm{M}_\oplus \left(\frac{\dot{M}_w}{10^{-5}\ \mathrm{M}_\odot\ \mathrm{yr}^{-1}}\right)\left(\frac{V_w}{600\ \mathrm{km\ s}^{-1}}\right)\left(\frac{D}{0.3\ \mathrm{au}}\right), \tag{2.6}$$

where the sound speed within the slab was set to 10 km s^{-1}. This corresponds to the sound speed of an ionised ideal gas at 10^4 K. This value is the temperature floor set by the UV radiation of the massive stars. The other quantities were scaled by the values of the binary IRS 16SW (Martins et al., 2006; Cuadra, Nayakshin, and Martins, 2008). It is important to remark that our assumptions are valid for this binary: identical stars with radiative winds (Martins et al., 2006; Calderón et al., 2016).

Thus, this result shows that massive clumps cannot be produced in IRS 16SW. In reality, it is possible that this limit is even smaller. The short stellar separation of the binary (about 0.7 au) is such that it is probable stellar winds do not reach terminal velocity before they collide. As a consequence, the actual upper limit will be only a fraction of our estimate, making the formation of a clump as massive as G2 less likely.

In principle, this result rules out the possibility of a G2-like clump to be produced in IRS 16SW. The fact that clumps are constantly losing mass through thermal conduction will reduce their initial mass since the moment they are born. Currently, G2's observed gas mass is very similar to the maximum clump mass produced in IRS 16SW. Therefore, for G2 to have been born in the binary it should not have lost mass through its life. This statement is very unlikely due to the large temperature difference between G2 and the ISM. However, the process of clump formation in colliding wind binaries is not well studied yet. It still remains as an option that a collection of smaller clumps were ejected and traveled together to Sgr A*. If this is the case they could be observed as a single larger clump (see Section 2.3.4).

In the case of the other binaries in the region, we can use Equation 2.6 to calculate the most massive clump they could create. From this, we obtain that IRS 16NE could generate at most clumps with a mass of 30 $M_\oplus$. Although this is ten times larger than IRS 16SW clumps, the fact that the system is roughly twice as far from Sgr A* makes it impossible for clumps to survive until reaching the SMBH (see Figure 2.3). The scenario is not favourable to E60 either. Its clumps are expected to be at most 0.7 $M_\oplus$. As this binary is further away than IRS 16SW, clumps cannot survive for long enough to fall into the very centre. Thus, clumps produced in these systems are less likely to reproduce the G2 source.

2.3.4 The clump ejection rate of IRS 16SW

In this section we proceed to estimate the amount of clumps a colliding wind binary can create given its properties. We start assuming clumps are exclusively created through the NTSI. This assumption is justified as numerical simulations have shown this instability dominates over others on long timescales (Lamberts, Fromang, and Dubus, 2011). In this context, clumps are formed very close to the line connecting both stars. Therefore, calculating the amount of material flowing into this region we can constrain the mass that could be transformed into clumps per unit of time. In order to delimitate this area we will make use of the length scale of the system, i.e. the stellar separation. So, we will assume clumps are

formed in a portion of the slab of length $2D$ as shown in Figure 2.4. Then, we proceed to estimate the mass flux that goes into a solid angle subtended by D observed from the position of one of the stars (and assuming azimuthal symmetry).

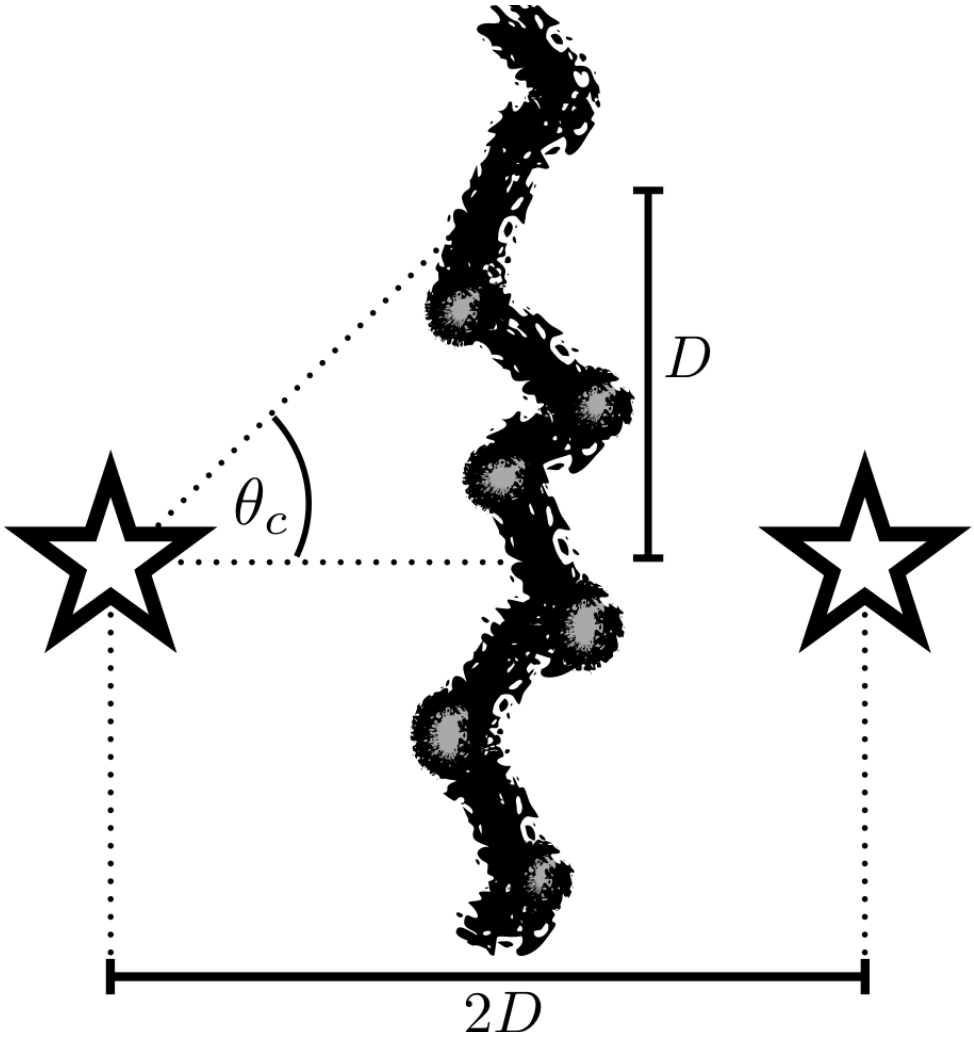

Figure 2.4: Schematic representation of an unstable colliding wind system. A gas slab is formed after the wind collision which is illustrated as the vertical thick sinusoidal line. If it becomes unstable clumps will be created. Clumps are represented as grey knots located in the slab. Overdensities formed as a result of the NTSI are expected to be formed close to the line connecting the two stars. The vertical length D is shown to illustrate the region where we consider clumps are created.

Let us define θ_c as the polar angle as shown in Figure 2.4. Its value can be easily calculated if we assume both stellar winds are identical. Therefore, the slab will be located exactly in the midpoint between the stars. Thus, $\theta_c = \arctan(1) = \pi/4$. Now, we take the ratio of the solid angle covered by a patch on sky of one of the stars described by $0 \leq \theta \leq \theta_c$ and $0 \leq \phi \leq 2\pi$, and the whole sky. Then,

$$\frac{S_c}{S_{\text{sky}}} = \frac{1}{4\pi} \int_0^{2\pi} \int_0^{\theta_c} \sin(\theta) d\theta d\phi \approx 15\%. \tag{2.7}$$

This means that clumps would be formed within 15% of the sky of each star. From spectral analysis we know that the mass loss rate of IRS 16SW is 10^{-5} $M_\odot$ yr^{-1} (Cuadra, Nayakshin, and Martins, 2008). Thus, about 10^{-6} $M_\odot$ yr^{-1} will be transformed into clumps according to our estimate. Then, the rate at which clumps will be formed is $\dot{M}_{\text{clump}} \approx 0.4$ $M_\oplus$ yr^{-1}. This means it would take about eight years to create 3-$M_\oplus$ in clumps. If the whole mass can go into a single clump the binary would need ~140 binary periods to create such a clump. This is not realistic because it is significantly longer than the dynamical timescale of the system. Even in the extreme case in which the complete mass loss rate goes into clumps it would take about 14 binary periods to form a single G2-mass clump. Thus, it is very hard to reconcile the idea of creating a clump with G2's mass.

2.4 Clump ejection along IRS 16SW orbit and simulation setup

Up to now we have investigated properties of clumps formed in wind collisions. However, to be able to test more quantitatively whether G2 could be one of such clumps we need to compare its observations (positions and velocities) with the output of our model. Specifically, here we study if G2's dynamics can be reproduced with a clump ejected from IRS 16SW.

Our approach consists in describing the motion of clumps ejected from IRS 16SW while orbiting the SMBH. Specifically, we compute their trajectories in the presence of the gravitational field of Sgr A*, and the drag force exerted by the ISM. Furthermore, we considered

clump initial velocities and their finite lifetimes given by thermal conduction effects previously discussed. Firstly, we describe our model and describe the impact of different input parameters. In the next Section, we present the results of this analysis.

2.4.1 Clump equation of motion and simulation setup

We start considering IRS 16SW ejects clumps isotropically while it is orbiting around Sgr A* (see Figure 2.5). Every single clump ejected will have an initial velocity with a random orientation. We discuss the impact of this assumption in Section 2.5.1.

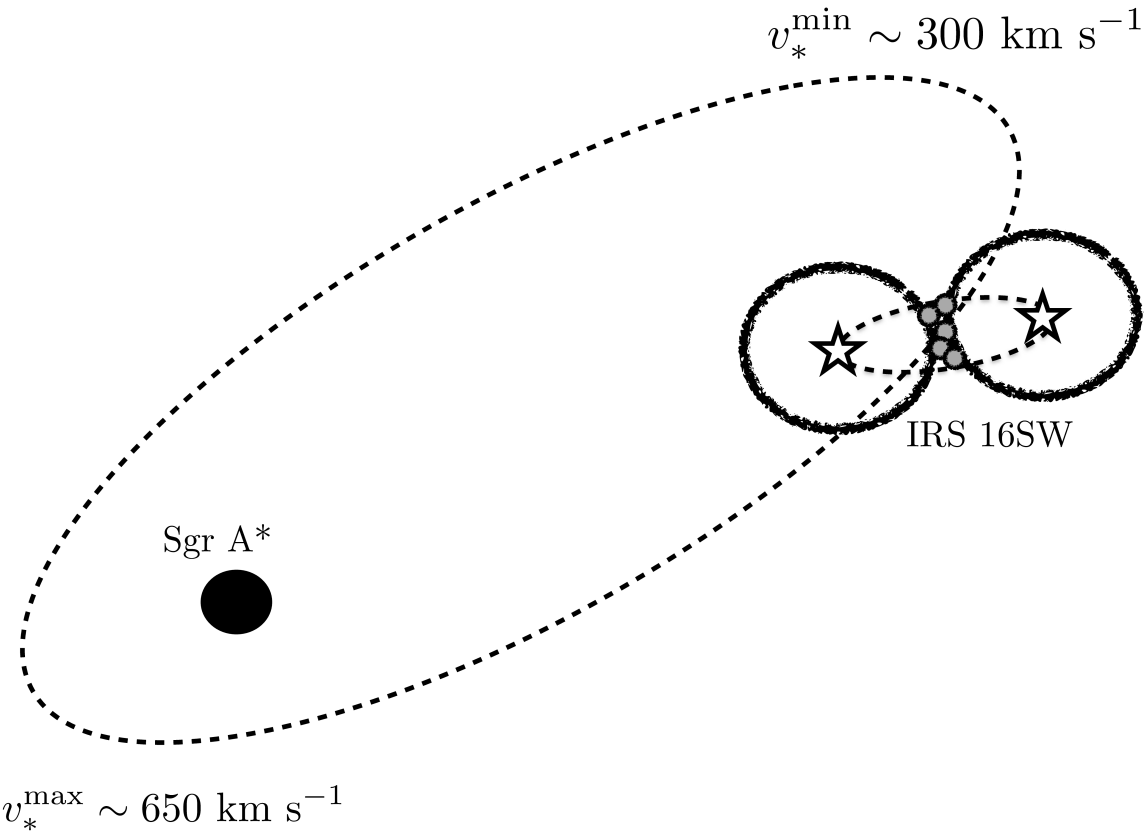

Figure 2.5: Schematic representation of the binary system IRS 16SW orbiting Sgr A*. The stellar components of the binary are expected to blow strong winds. In the collision region of such outflows clump formation takes place.

Immediately after being ejected clumps are subject to the gravitational pull of the SMBH. In principle, this causes clumps to move on Keplerian orbits. However, we included the presence of drag exerted by the ISM that will cause deviations from such Keplerian motion. We modelled this interaction as ram pressure considering the relative motion of the medium and the gas clump. Then, the equation of motion of each clump will be given by

$$\frac{d^2\mathbf{r}}{dt^2} = -\frac{GM_{\rm BH}}{r^2}\hat{\mathbf{r}} - \frac{\sigma_{\rm c}(t)}{m_{\rm c}(t)}\rho_{\rm ISM}(r)\left|\frac{d\mathbf{r}}{dt}\right|^2\hat{\mathbf{v}}, \tag{2.8}$$

where G is the gravitational constant, $M_{\rm BH}$ is the mass of Sgr A*, $\rho_{\rm ISM}$ is the density of the ISM, $\hat{\mathbf{r}}$ is the unit vector in the radial direction, $\hat{\mathbf{v}}$ is the unit vector in the velocity direction, $m_{\rm c}$ and $\sigma_{\rm c}$ are the clump mass and cross section, respectively.

The initial conditions will be given by

$$\frac{d\mathbf{r}}{dt}(t=0) = \mathbf{v}_* + \mathbf{v}_{\rm ej}, \tag{2.9}$$

$$\mathbf{r}(t=0) = \mathbf{r}_*, \tag{2.10}$$

where $\mathbf{v}_{\rm ej}$ is the initial velocity kick whose direction is random, $\mathbf{r}_*$ and $\mathbf{v}_*$ are the binary system position and velocity vectors, respectively.

Furthermore, we included the clump mass loss due to thermal conduction which is the main constraint on clump lifetimes. This can be expressed by

$$\frac{dm_{\rm c}}{dt} = -\dot{M}_{\rm evap}(m_{\rm c}, r), \tag{2.11}$$

where $\dot{M}_{\rm evap}(m_{\rm c}, r)$ is given in Equation 2.1

The model has four input parameters: initial clump mass $m_{\rm c}(t=0)$, ejection rate (number of clumps ejected per time unit), the clump initial kick velocity $\mathbf{v}_{\rm ej}$, and the density profile power law α. Once we set those parameters we compute the trajectory of every single clump solving Equation 2.8. It is important to remark that in our model clump ejection occurs while

IRS 16SW orbits around Sgr A*. This means clumps are ejected from different locations on the binary orbit.

Our simulations are run for a period of 300 yr which is longer than the lifetime of any clump IRS 16SW can create (see Section 2.3.3). Therefore, simulations start and finish in t = 1716 yr and t = 2016 yr, respectively. Finally, from every run we registered clumps whose mass is at least 10% of Earth's at the present, i.e. $m_c(t = 2016\ \mathrm{yr}) \geq 0.1\ \mathrm{M}_\oplus$. Then, we can get an estimate of the spatial distribution of gas clumps present in the region.

In order to avoid undesired statistical noise we consider a very large clump ejection rate. Then, we normalise the number of counts output over the total number of clumps ejected. Therefore, the outputs of the model are *clump fractions* f, i.e. number of clumps whose $m_c > 0.1\ \mathrm{M}_\oplus$ divided by the total number of ejected clumps. However, we are mostly interested only in clumps that could reproduce G2's motion. Thus, we define the *G2 candidate fraction* f_{G2} as the number of clumps that satisfy $m_c > 0.1\ \mathrm{M}_\oplus$ and $r(t = 2016\ \mathrm{yr}) \leq 0.5$ arcsec divided by the total number of clumps ejected. Then, to obtain an absolute value out of this we used the mass in clumps created calculated in Section 2.3.4.

Before jumping to the results, let us bear in mind that the model had three input parameters: clump mass m_c, ejection speed v_{ej}, and ISM density profile power-law α. The choice of a very large value of the clump ejection rate allowed us to reduce the number of parameters. Furthermore, instead of using a single clump mass value, we considered a clump mass function as a semi-log distribution. Here, the mean and standard deviation need to be specified. Although we modelled different mean values, the standard deviation was fixed to 0.1 dex in all simulations. This choice is inspired by our forthcoming work based on numerical hydrodynamical simulations of clump formation in stellar wind collisions (Calderón et al.; in preparation)[4].

The trajectory of IRS 16SW between years 1716 and 2016 was sampled using one thousand points evenly spaced in time. On each of those points 2048 clumps are ejected isotrop-

[4]At the time of publication this reference was in preparation but refers to preliminary work that led to Calderón et al. (2019)

ically with a speed v_{ej} (in the reference frame of the binary). The ejection speed values used are fractions of the terminal velocity of the stellar wind of IRS 16SW. All these values are within the range of the orbital speed of the binary around Sgr A*, i.e. 300–650 km s^{-1}. The orbital sampling and clump ejection number were selected in order that the statistical noise of the G2 candidate fraction f_{G2} was kept to less than 5%. In the following section we present the G2 candidate fraction of each set of simulations, the trajectories of such clumps, the role of the drag force on such trajectories, and the expected clump mass distribution.

2.4.2 Simulation results

2.4.2.1 G2 candidate fraction

In Table 2.2, we present the parameters used in our simulations, as well as diagnostics of their results. Runs with clump mass functions whose mean mass was smaller than a tenth of an Earth-mass did not register any G2 candidate, i.e. $f_{G2} = 0$, as expected from our analytical estimates. Different ejection speeds or density profiles did not change this result. Basically, those clumps have lifetimes that are too short for being able to travel close to Sgr A*. Only clumps with initial masses higher than a single Earth-mass have chances of being captured regardless of the ejection speed and density profile (see Figure 2.3).

In the next set of simulations we used a mean clump mass of $\bar{m}_c = 3\ M_\oplus$. This is the highest physical mass a clump produced in IRS 16SW can have (see Section 2.3.3). As we expect more massive clumps to live for longer, this choice should maximise the G2 candidate fraction. The results are also shown in Table 2.2. Here, we observe that G2 candidate fractions are in all cases in the range 1.0–1.3%, with a shallow maximum for ejection speeds 350–400 km s^{-1}. Higher ejection speeds make clumps more likely to get on unbound orbits. On the contrary, a slower initial speed would keep more clumps bound to the SMBH. However, decreasing the initial speed also causes clumps to retain more angular momentum making infall less likely to occur. Although the drag could eventually place them on more radial orbits, their limited lifetimes do not allow this to happen very easily.

Table 2.2: Input parameters and results of simulation runs. In all simulations $\sim 2 \times 10^6$ clumps were ejected per orbit. Also, the clump mass function standard deviation was fixed to 0.1 dex. Notice that no clumps were captured in the low mass clump runs.

Name	$\bar{m}_c$ ($M_\oplus$)	$\lvert v_{ej} \rvert$ (km s^{-1})	α	f_{G2}	min($\chi^2_{d.o.f.}$)
(1)	(2)	(3)	(4)	(5)	(6)
Low mass	< 0.1	any	any	0	–
M1	1	any	any	$< 0.1\%$	–
M_G2_v300_a05	3	300	0.5	1.2%	2351
M_G2_v300_a15	3	300	1.5	1.1%	2101
M_G2_v350_a05	3	350	0.5	1.3%	815
M_G2_v350_a15	3	350	1.5	1.2%	715
M_G2_v400_a05	3	400	0.5	1.3%	253
M_G2_v400_a15	3	400	1.5	1.2%	340
M_G2_v450_a05	3	450	0.5	1.2%	411
M_G2_v450_a15	3	450	1.5	1.2%	376
M_G2_v500_a05	3	500	0.5	1.1%	633
M_G2_v500_a15	3	500	1.5	1.0%	566

Notes. Column 1: model ID. Column 2: mean mass of the initial clump mass function. Column 3: clump ejection speed (in the reference frame of the binary). Column 4: power-law of the density profile of the medium. Column 5: G2 candidate fraction, i.e. fraction of clumps whose mass satisfies $m_c(t = 2016 \text{ yr}) > 0.1$ $M_\oplus$ and are located within half arcsecond from Sgr A*. Column 6: reduced chi-square value of the clump that is the best-fit to G2 observations.

We see no difference in the results when using different density profiles for the medium. In principle, this is expected due to the similarity between both profiles at the distance of the orbit of IRS 16SW, specially on the effects of thermal conduction (see Figure 2.3). If we consider a clump ejection rate of 0.4 $M_\oplus$ yr^{-1} (see Section 2.3.4) the ejection rate of 3-$M_\oplus$ clumps will be 0.13 yr^{-1}. Thus, in 300 years ~40 clumps should be ejected. As ~1% of them are G2 candidates, we should expect none, or at most one. Could G2 then correspond to a clump created in this way? Our simulations can give us more information, from a dynamical point of view. In the next section we will check if the trajectory of such clumps can mimic the observed motion of G2.

2.4.2.2 Captured clump trajectories

In our simulations we computed the trajectories of clumps up to the epoch of the latest G2 observations available in the literature (Plewa et al., 2017). It is important to remark that we excluded clumps whose positions at $t = 2016$ yr are further than half arcsecond from Sgr A*. Then, we registered state vectors of clumps, i.e. position and velocity vectors at the same time at which observations took place. With this information we computed a Keplerian orbit for each clump. From this we compared the observed positions on the sky and line-of-sight velocities at the same epochs of the observations of G2[5]. Thus, we estimated the $\chi^2_{\rm d.o.f.}$ for each captured clump.

Figure 2.6 shows histograms of the $\chi^2_{\rm d.o.f.}$ distribution for two of our simulations: models M_G2_a05_v400 and M_G2_a15_v400. They correspond to models with ($\alpha = 0.5$, $v_{\rm ej} = 400$ km s^{-1}), and ($\alpha = 1.5$, $v_{\rm ej} = 400$ km s^{-1}), respectively. We do not show histograms of other runs because in those cases the minimum $\chi^2_{\rm d.o.f.}$ was even larger (see Table 2.2). Notice that in both cases the $\chi^2_{\rm d.o.f.}$ values are significantly higher than unity. Thus, all G2 candidates

[5]Observational data points were obtained sampling the posterior distribution of the model of Plewa et al. (2017) which reproduces extremely well the G2 dynamics. We also made the analysis using the previously published data points (Pfuhl et al., 2015) plus the latest epochs taken from the posteriors and found no significant differences.

are far from reproducing G2 observed properties.

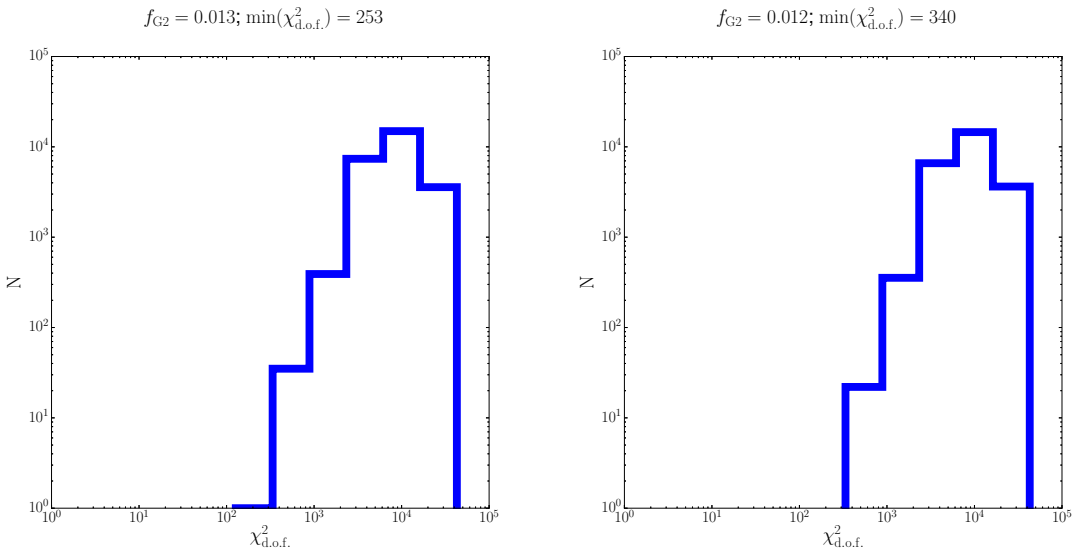

Figure 2.6: Histograms of the $\chi^2_{\rm d.o.f.}$ calculated for each G2 candidate using sky-positions and the line-of-sight velocities. Left and right panels show the results of models M_G2_v400_a05 and M_G2_v400_a15, respectively. The minimum $\chi^2_{\rm d.o.f.}$ value is shown on top of each plot along with f_{G2}.

In each panel of Figure 2.7, we show the orbit of G2 (dashed red line) and the clump whose $\chi^2_{\rm d.o.f.}$ is the minimum (solid black line) from M_G2_a05_v400 and M_G2_a15_v400. Furthermore, the figure includes sky position measurements of G2 with their respective error bars (blue circles). As comparison we show clump positions on the sky at the epochs of the observations (black squares). The inset of each panel shows the line-of-sight velocity measurements of G2 (blue circles) and the clump (black squares). We also show the clump Keplerian orbit computed from its most recent state vector (solid black line). This allows us to visualise deviations of the clump orbits from Keplerian motion, since at earlier epochs the clump position does not follow exactly the Keplerian orbit.

From the analysis of Figure 2.7, it is clear that G2 observations differ significantly from our models. Although some points fall within the error bars of the observations most of

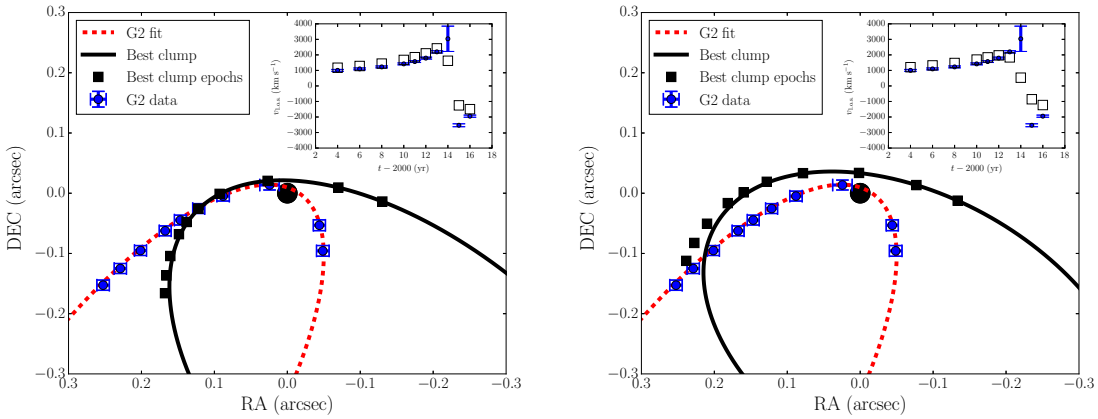

Figure 2.7: Sky projected positions and orbital fits for G2 and the clump whose $\chi^2_{\text{d.o.f.}}$ is the smallest in a given model. Left and right panels show the results of models M_G2_v400_a05 and M_G2_v400_a15, respectively. Blue circles with error bars are the observed positions of G2. Black rectangles show the positions of the best-fit clump at the same epochs as the G2 observations. The dashed red and solid black lines stand for the Keplerian orbital fits to G2 data and to the last epoch of the modelled clump, respectively. The inset graphs show the line-of-sight velocity as a function of time, where symbols retain their meaning, i.e. blue circles and black squares stand for G2 observations and best clump model, respectively.

them display significant deviations from the data. The main differences seem to be on the orientation where the ellipse is pointing. Thus, observations already constrain strongly the direction from where G2 seems to be coming from. None of IRS 16SW clumps can mimic this constraint. This issue was discussed previously in Section 2.3.1. However, in the present analysis we did not specify any orbital fit to G2. Instead we compared a set of data points, and we ended up reaching the same conclusion. Thus, the observed motion of IRS 16SW and G2 are not consistent with the cloud originating from the binary.

2.4.2.3 Role of the drag force

In order to understand the impact of the drag force on clump trajectories we ran an extra set of simulations without including it. We made the same analysis of the outputs, i.e.

register G2 candidates and check if their trajectories fit observations. The results do not show differences on the fraction of G2 candidates f_{G2}. Although some differences were obtained when comparing clump and G2 motions they are not relevant as the $\chi^2_{\text{d.o.f.}}$ did not change significantly. To quantify the effect of the drag we compared the final binding energy of clumps in simulations with and without the presence of the drag force.

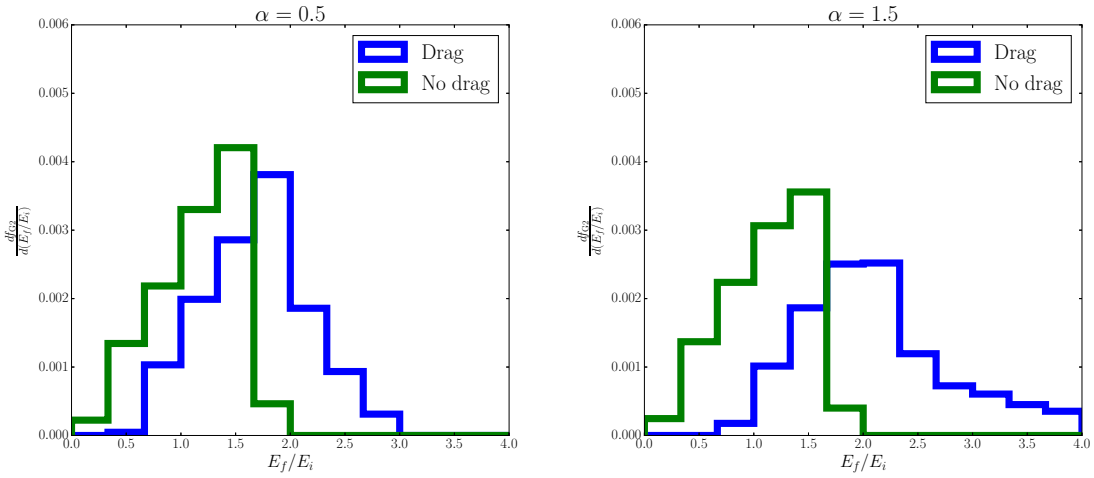

Figure 2.8: Histograms of the final binding energy of G2 candidates scaled by the orbital energy of IRS 16SW, i.e. E_i. Counts were normalised by the total number of clumps ejected. Left and right panels show the results of models M_G2_v400_a05 and M_G2_v400_a15, respectively.

In Figure 2.8, we present histograms of the final binding energy of G2 candidates scaled by the orbital energy of IRS 16SW. Left and right panels present the outputs of models M_G2_v400_a05 and M_G2_v400_a15, respectively. Although we did not consider the presence of the drag force the power law of the ISM does affect the lifetime of clumps. Notice that in both plots the presence of a drag force shifts the distribution towards larger binding energy ratios as we would expect (green and blue histograms). The drag acts subtracting kinetic energy making clumps to switch to more bound orbits, i.e. larger E_f/E_i values. The effect is stronger when we consider a steep density profile ($\alpha = 1.5$) as we observe a longer tail in the blue histogram of the right panel of Figure 2.8. This makes sense as the density

increases more rapidly which translates into a stronger hydrodynamical interaction between clumps and the medium. In principle, this shows the drag effects are not negligible in our model. Nevertheless, despite it is significant we cannot distinguish whether or not they improve chances of reproducing G2 observations. Thus, the drag effect simply does not help clumps to mimic G2's motion close to Sgr A*.

2.4.2.4 Final clump masses

As we have discussed clumps experience mass losses during their lives due to thermal conduction. Here, we refer as "final mass" to the mass a clump would have at the present, i.e. $t = 2016$ yr. In Figure 2.9, we show the final mass of simulations with $\bar{m}_c = 3$ $M_\oplus$ as a function of the ejection velocity v_{ej} of each run. It is important to keep in mind that this analysis includes all clumps that have not been evaporated, and not only G2 candidates. The density profile power-law is colour coded being $\alpha = 0.5$ and $\alpha = 1.5$, blue circles and green triangles, respectively. Each point represents the median of the final masses while the error bars stand for percentiles 34th and 68th, respectively. In all models shown clumps had initial masses of $3^{+2}_{-1} M_\oplus$ following a semi-log distribution. Notice that in all cases shown we see they have lost a significant fraction of their masses. Specifically, they have lost at least 50% of their initial mass. Within the error bars both sets of simulations give exactly the same result. This means the choice of the ejection speed or the power-law of the density profile does not determine the amount of mass clumps lose. Instead this is more likely given by the period of time between the ejection and the end of the simulation.

Overall, clumps lose a significant fraction of their mass before being captured. Even the most massive clumps IRS 16SW can produce would lose 50% of their mass. This means if a G2-mass clump was created by the binary, today we would observe it with at least half of its mass. Thus, G2's initial mass should have been at least 6 $M_\oplus$. But our analytical estimates shows this is not feasible. IRS 16SW is not capable of creating such massive clump given its wind properties.

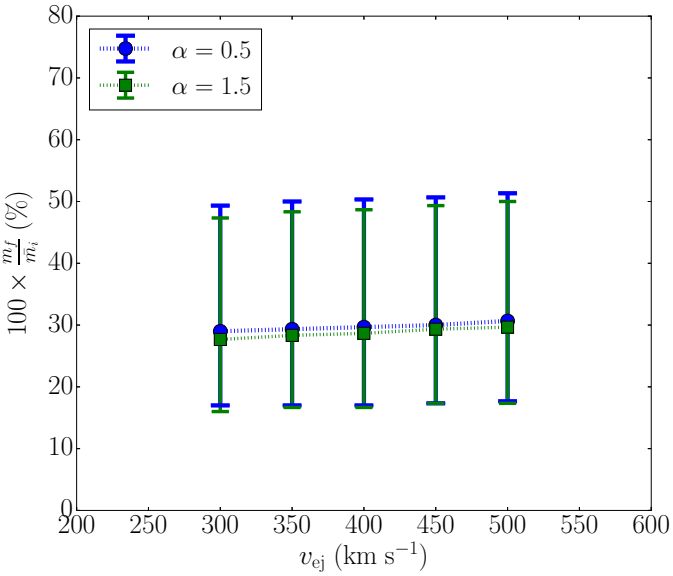

Figure 2.9: Median of the final clump mass distribution as a function of the ejection speed parameter. Error bars represent percentiles 34th and 68th. Final masses are expressed as percentages of the mean clump mass of the initial clump mass function which in these cases was set to $\bar{m} = 3$ M$_\oplus$. Each point corresponds to a single simulation whose ejection speed is specified in the x-axis, and the density profile is colour coded. Blue circles and green squares stand for the use of a shallow ($\alpha = 0.5$) and a steep ($\alpha = 1.5$) density profile, respectively. Notice there is no statistical difference among the choice of different model parameters.

2.5 Discussion

Our analytical and numerical results point that it is hard to conceive the origin of G2 in IRS 16SW, or in any other known massive binary. Nevertheless, we have to be aware that there are some uncertainties our model did not take into account. Here, we discuss the possible effect of such uncertainties. Also, we comment on the detectability of gas clumps we expect IRS 16SW produces.

2.5.1 Limitations and uncertainties in the model

In our model we made two assumptions that could affect part of our results: the isotropic ejection of clumps, and not considering magnetic field effects.

2.5.1.1 Clump ejection isotropy

State-of-the-art numerical simulations of colliding wind binaries show that clumps are not ejected isotropically (Pittard, 2009). Instead, they are more likely launched perpendicularly to the binary orbital plane in some sort of cones upwards and downwards. Bear in mind that clumps are not uniquely ejected in these cones but preferably. Unfortunately, in the case of IRS 16SW it is not possible to estimate the inclination angle between the plane of the binary and the orbit around Sgr A*. Thus, we just cannot constrain the direction of ejection. However, in this scenario (in general) it is less likely for clumps to travel close to Sgr A* compared to the isotropic case. This is due to the fact that clumps need to be ejected on a given direction to get rid of most of their angular momentum, so they can fall into the SMBH. Therefore, if clump ejection occurs preferably on some sort of cones the chances of both directions to be aligned is smaller, the less isotropic the ejection takes place. Based on this, the isotropy is the most sensible assumption to study this problem as it shows us the most optimistic situation.

2.5.1.2 Magnetic fields

Our approach does not include any effect of possible magnetic field present in the region. As thermal conduction was considered in the saturation limit we do not expect the presence of a magnetic field affects it much. However, the drag force could be modified by the action of magnetic fields. McCourt et al. (2015) showed that a magnetic field in a hot wind can enhance the drag force exerted on a cloud traveling through it. The increment is in a factor $(1 + v_A^2/v^2)$, where $v_A = B/\sqrt{4\pi\rho}$ is the Alfvén speed and v the relative speed between the cloud and the wind. Notice the strong dependence on the strength of the magnetic field.

Thus, in this case the drag force has to be replaced by

$$F_{\rm drag}^{\rm mag} = F_{\rm drag}\left(1 + \frac{2}{\beta\mathcal{M}^2}\right), \tag{2.12}$$

where $\mathcal{M}$ is the Mach number, and $\beta = 8\pi P_{\rm thermal}/B^2$ is the ratio of thermal to magnetic pressure of the wind. Typically, at $r = 1.4$ arcsec the temperature of the medium is 10^7 K and clumps can reach speeds of 2000 km s^{-1}, then $\mathcal{M} \approx 3$. Therefore, in order for the drag to be enhanced by a factor two the beta parameter needs to be $\beta \approx 0.1$ (see Section 2.4.2.3), i.e. a magnetic field of $B \approx 10$ mG. In this region the only constraint on the magnetic field strength is given by the observations of the Galactic Centre magnetar (Eatough et al., 2013). This suggests a magnetic field consistent with $\beta \approx 1$ at ~0.1 pc (2.5 arcsec) from Sgr A*. Since we do not expect B to depend strongly on r based on most accretion models that assume equipartion (see Eatough et al., 2013), the drag could be enhanced in a factor of two at most which is too small to have an impact on our results.

2.5.2 Clump detectability

Regardless of whether G2 was created by IRS 16SW or not, we do expect clumps to be formed in the binary. But, should we observe such clumps with our current observational facilities? In this section we proceed to analyse if we could detect such objects. In this way, we make sure that our description of IRS 16SW producing clumps is not in tension with observations. To do so we study the Br-γ luminosity a clump would radiate in this environment. We calculate the Br-γ emissivity following case B recombination theory, i.e.

$$j_{\rm Br\gamma} = 3.44 \times 10^{-27}\left(\frac{T_{\rm c}}{10^4\ {\rm K}}\right)^{-1.09} n_{\rm p} n_{\rm e}\ {\rm erg\ s^{-1}\ cm^3}, \tag{2.13}$$

where $n_{\rm p}$ and $n_{\rm e}$ are the proton and electron number density, respectively. As discussed in Appendix 2.A, it is reasonable to assume the temperature of the clump $T_{\rm c}$ to be 10^4 K.

In order to constrain the physical size of the clump in this environment we will assume it is in pressure equilibrium. We are aware that a clump could be subject to tidal forces by

the SMBH (e.g. Chen, Amaro-Seoane, and Cuadra, 2016). However, we opted for studying the luminosity of the clump only at distances close to IRS 16SW. At this location the thermal pressure of the environment dominates over the tidal forces on clumps whose masses are of the order of Earth's. We estimated the role of the medium pressure and tidal force, and found out that at radius of ~1 arcsec or shorter, the tidal force starts to dominate over the thermal pressure.

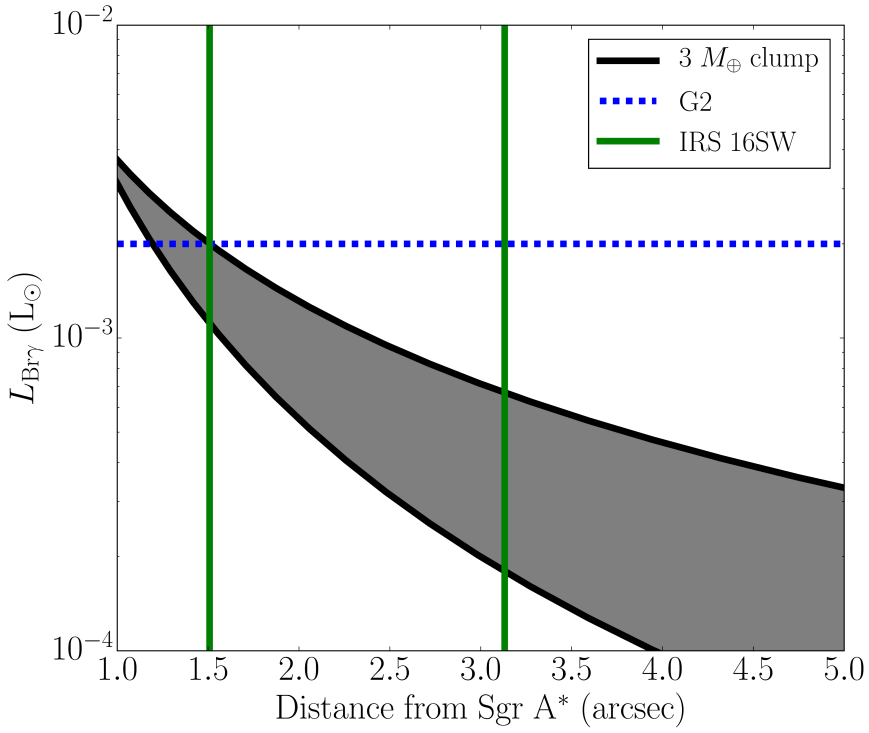

Figure 2.10: Br-γ luminosity of a 3-$M_\oplus$ clump as a function of distance from Sgr A* (solid black line) estimated from our simple model. The observed Br-γ luminosity of G2 is shown as a horizontal dashed blue line. Solid green vertical lines represent pericentre and apocentre of IRS 16SW around Sgr A*

In Figure 2.10, we show the Br-γ luminosity $L_{\mathrm{Br}\gamma}$ of a 3-$M_\oplus$ clump as a function of distance from Sgr A*. Solid black lines show the luminosity estimated when assuming a density power-law $a = 0.5$ (lower limit) and $a = 1.5$ (upper limit). As comparison we show the Br-γ luminosity of G2 constrained by observations to be $L_{\mathrm{Br}\gamma} = 2 \times 10^{-3} L_\odot$ (dotted blue line).

Vertical solid green lines stand for pericentre and apocentre distances of IRS 16SW. Notice that the maximum luminosity of clumps is on the pericentre of the binary, where it is very similar to G2's. Further from this point the luminosity can only be of a fraction of G2's luminosity, so less likely to be detected. If we consider less massive clumps they will be even fainter. Then, only clumps that manage to travel towards Sgr A*, and are about 3-$M_\oplus$, could radiate as much as G2. Unfortunately, we expect that most clumps ejected by IRS 16SW not to be detected. The reasons behind this are that only few of them will be massive enough and, at the same time, launched in the direction of Sgr A*. Thus, our model and results are consistent with current observations.

2.6 Conclusions

Our analytical and test-particle simulation results show that we cannot reconcile the hypothesis of G2 being a gas clump formed in any known massive binary system with its observed motion. The results that support this conclusion are the following

1. *G2 orbital fit is not consistent with an origin in IRS 16SW.* It is not possible to match IRS 16SW and G2 positions on the sky if we trace their orbits back in time. Their projected separation (lower limit of the physical separation) always remains larger than ~0.2 arcsec.

2. *Cold gas clumps do not live long enough.* The hot environment close to Sgr A* evaporates cold clumps very rapidly via thermal conduction. At the orbit of IRS 16SW, massive clump lifetimes and the free-fall timescale are comparable (~200 yr). Therefore, only the most massive of them would live long enough to reach the vicinity of Sgr A*.

3. *IRS 16SW cannot produce massive enough clumps.* Given its orbital and stellar wind parameters, we can expect it to create clumps with *initial* masses of at most 3 Earth

masses. Roughly half of that mass would be lost before reaching Sgr A*, in disagreement with the observed G2 mass.

4. *Our test-particle simulations cannot reproduce G2 observations.* A model based on IRS 16SW ejecting clumps along its orbit is not capable of producing any clump that matches the observed G2 positions on the sky and radial velocity measurements.

These results, together with our previous work on encounters between single stars (Calderón et al., 2016), reject the idea of G2 being created in a stellar wind collision. However, our work does not rule out the "purely gaseous cloud" scenario in general. Other gas cloud models remain as possible explanations. In order to reject those, following a procedure similar to the one presented in this paper, it would be necessary to first identify candidate progenitors, e.g. a star recently going through a nova outburst, or being partially disrupted.

Acknowledgments

We thank the anonymous referee for useful comments. We also thank G. Hajdu and A. Ballone for very helpful discussions. This work was partially developed while JC was on sabbatical leave at MPE. DC and JC acknowledge the kind hospitality of MPE, and funding from the Max Planck Society through a "Partner Group" grant. We acknowledge support from CONICYT-Chile through FONDECYT (1141175) and Basal (PFB0609) grants. DC is supported by CONICYT-PCHA/Doctorado Nacional (2015-21151574).

References

Ballone, A. et al. (2013). "Hydrodynamical Simulations of a Compact Source Scenario for the Galactic Center Cloud G2". In: ApJ 776.1, 13, p. 13. DOI: 10.1088/0004-637X/776/1/13. arXiv: 1305.7238 [astro-ph.GA].

Ballone, A. et al. (2016). "The G2+G2t Complex as a Fast and Massive Outflow?" In: ApJ 819.2, L28, p. L28. DOI: 10.3847/2041-8205/819/2/L28. arXiv: 1602.07305 [astro-ph.GA].

Burkert, A. et al. (2012). "Physics of the Galactic Center Cloud G2, on Its Way toward the Supermassive Black Hole". In: ApJ 750.1, 58, p. 58. DOI: 10.1088/0004-637X/750/1/58. arXiv: 1201.1414 [astro-ph.GA].

Calderón, D. et al. (2016). "Clump formation through colliding stellar winds in the Galactic Centre". In: MNRAS 455.4, pp. 4388–4398. DOI: 10.1093/mnras/stv2644. arXiv: 1507.07012 [astro-ph.GA].

Calderón, Diego et al. (2019). "3D simulations of clump formation in stellar wind collisions". In: *arXiv e-prints*, arXiv:1906.04181, arXiv:1906.04181. arXiv: 1906.04181 [astro-ph.GA].

Chen, Xian, Pau Amaro-Seoane, and Jorge Cuadra (2016). "Stability of Gas Clouds in Galactic Nuclei: An Extended Virial Theorem". In: ApJ 819.2, 138, p. 138. DOI: 10.3847/0004-637X/819/2/138. arXiv: 1506.08196 [astro-ph.GA].

Cowie, L. L. and C. F. McKee (1977). "The evaporation of spherical clouds in a hot gas. I. Classical and saturated mass loss rates." In: ApJ 211, pp. 135–146. DOI: 10.1086/154911.

Cuadra, Jorge, Sergei Nayakshin, and Fabrice Martins (2008). "Variable accretion and emission from the stellar winds in the Galactic Centre". In: MNRAS 383.2, pp. 458–466. DOI: 10.1111/j.1365-2966.2007.12573.x. arXiv: 0705.0769 [astro-ph].

De Colle, Fabio et al. (2014). "A Stellar Wind Origin for the G2 Cloud: Three-dimensional Numerical Simulations". In: ApJ 789.2, L33, p. L33. DOI: 10.1088/2041-8205/789/2/L33. arXiv: 1406.1188 [astro-ph.GA].

Eatough, R. P. et al. (2013). "A strong magnetic field around the supermassive black hole at the centre of the Galaxy". In: Nature 501.7467, pp. 391–394. DOI: 10.1038/nature12499. arXiv: 1308.3147 [astro-ph.GA].

Gillessen, S. et al. (2012). "A gas cloud on its way towards the supermassive black hole at the Galactic Centre". In: Nature 481.7379, pp. 51–54. DOI: 10.1038/nature10652. arXiv: 1112.3264 [astro-ph.GA].

Gillessen, S. et al. (2013a). "New Observations of the Gas Cloud G2 in the Galactic Center". In: ApJ 763.2, 78, p. 78. DOI: 10.1088/0004-637X/763/2/78. arXiv: 1209.2272 [astro-ph.GA].

Gillessen, S. et al. (2013b). "Pericenter Passage of the Gas Cloud G2 in the Galactic Center". In: ApJ 774.1, 44, p. 44. DOI: 10.1088/0004-637X/774/1/44. arXiv: 1306.1374 [astro-ph.GA].

Gillessen, S. et al. (2017). "An Update on Monitoring Stellar Orbits in the Galactic Center". In: ApJ 837.1, 30, p. 30. DOI: 10.3847/1538-4357/aa5c41. arXiv: 1611.09144 [astro-ph.GA].

Gillessen, S. et al. (2019). "Detection of a Drag Force in G2's Orbit: Measuring the Density of the Accretion Flow onto Sgr A* at 1000 Schwarzschild Radii". In: ApJ 871.1, 126, p. 126. DOI: 10.3847/1538-4357/aaf4f8.

Guillochon, James et al. (2014). "Possible Origin of the G2 Cloud from the Tidal Disruption of a Known Giant Star by Sgr A*". In: ApJ 786.2, L12, p. L12. DOI: 10.1088/2041-8205/786/2/L12. arXiv: 1401.2990 [astro-ph.HE].

Lamberts, A., S. Fromang, and G. Dubus (2011). "High-resolution numerical simulations of unstable colliding stellar winds". In: MNRAS 418.4, pp. 2618–2629. DOI: 10.1111/j.1365-2966.2011.19653.x. arXiv: 1109.1434 [astro-ph.SR].

Mapelli, Michela and Emanuele Ripamonti (2015). "Signatures of Planets and Protoplanets in the Galactic Center: A Clue to Understanding the G2 Cloud?" In: ApJ 806.2, 197, p. 197. DOI: 10.1088/0004-637X/806/2/197. arXiv: 1504.04624 [astro-ph.GA].

Martins, F. et al. (2006). "GCIRS 16SW: A Massive Eclipsing Binary in the Galactic Center". In: ApJ 649.2, pp. L103–L106. DOI: 10.1086/508328. arXiv: astro-ph/0608215 [astro-ph].

Martins, F. et al. (2007). "Stellar and wind properties of massive stars in the central parsec of the Galaxy". In: A&A 468.1, pp. 233–254. DOI: 10.1051/0004-6361:20066688. arXiv: astro-ph/0703211 [astro-ph].

McCourt, Michael et al. (2015). "Magnetized gas clouds can survive acceleration by a hot wind". In: MNRAS 449.1, pp. 2–7. DOI: 10.1093/mnras/stv355. arXiv: 1409.6719 [astro-ph.GA].

Meyer, F. and E. Meyer-Hofmeister (2012). "A nova origin of the gas cloud at the Galactic center?" In: A&A 546, L2, p. L2. DOI: 10.1051/0004-6361/201220145. arXiv: 1208.6514 [astro-ph.SR].

Miralda-Escudé, Jordi (2012). "A Star Disrupted by a Stellar Black Hole as the Origin of the Cloud Falling toward the Galactic Center". In: ApJ 756.1, 86, p. 86. DOI: 10.1088/0004-637X/756/1/86. arXiv: 1202.5496 [astro-ph.GA].

Murray-Clay, Ruth A. and Abraham Loeb (2012). "Disruption of a proto-planetary disc by the black hole at the milky way centre". In: *Nature Communications* 3, 1049, p. 1049. DOI: 10.1038/ncomms2044. arXiv: 1112.4822 [astro-ph.GA].

Paumard, T. et al. (2006). "The Two Young Star Disks in the Central Parsec of the Galaxy: Properties, Dynamics, and Formation". In: ApJ 643.2, pp. 1011–1035. DOI: 10.1086/503273. arXiv: astro-ph/0601268 [astro-ph].

Pfuhl, O. et al. (2014). "Massive Binaries in the Vicinity of Sgr A*". In: ApJ 782.2, 101, p. 101. DOI: 10.1088/0004-637X/782/2/101. arXiv: 1307.7996 [astro-ph.GA].

Pfuhl, Oliver et al. (2015). "The Galactic Center Cloud G2 and its Gas Streamer". In: ApJ 798.2, 111, p. 111. DOI: 10.1088/0004-637X/798/2/111. arXiv: 1407.4354 [astro-ph.GA].

Pittard, J. M. (2009). "3D models of radiatively driven colliding winds in massive O+O star binaries - I. Hydrodynamics". In: MNRAS 396.3, pp. 1743–1763. DOI: 10.1111/j.1365-2966.2009.14857.x. arXiv: 0904.0164 [astro-ph.SR].

Plewa, P. M. et al. (2017). "The Post-pericenter Evolution of the Galactic Center Source G2". In: ApJ 840.1, 50, p. 50. DOI: 10.3847/1538-4357/aa6e00. arXiv: 1704.05351 [astro-ph.GA].

Roberts, Shawn R. et al. (2017). "Towards self-consistent modelling of the Sgr A* accretion flow: linking theory and observation". In: MNRAS 466.2, pp. 1477–1490. DOI: 10.1093/mnras/stw2995. arXiv: 1611.00118 [astro-ph.HE].

Schartmann, M. et al. (2012). "Simulations of the Origin and Fate of the Galactic Center Cloud G2". In: ApJ 755.2, 155, p. 155. DOI: 10.1088/0004-637X/755/2/155. arXiv: 1203.6356 [astro-ph.GA].

Valencia-S., M. et al. (2015). "Monitoring the Dusty S-cluster Object (DSO/G2) on its Orbit toward the Galactic Center Black Hole". In: ApJ 800.2, 125, p. 125. DOI: 10.1088/0004-637X/800/2/125. arXiv: 1410.8731 [astro-ph.GA].

Vishniac, E. T. (1983). "The dynamic and gravitational instabilities of spherical shocks". In: ApJ 274, pp. 152–167. DOI: 10.1086/161433.

Vishniac, Ethan T. (1994). "Nonlinear instabilities in shock-bounded slabs". In: ApJ 428.1, pp. 186–208. DOI: 10.1086/174231. arXiv: astro-ph/9306025 [astro-ph].

Wang, Q. D. et al. (2013). "Dissecting X-ray-Emitting Gas Around the Center of Our Galaxy". In: *Science* 341.6149, pp. 981–983. DOI: 10.1126/science.1240755. arXiv: 1307.5845 [astro-ph.HE].

Witzel, G. et al. (2014). "Detection of Galactic Center Source G2 at 3.8 μm during Periapse Passage". In: ApJ 796.1, L8, p. L8. DOI: 10.1088/2041-8205/796/1/L8. arXiv: 1410.1884 [astro-ph.HE].

Yuan, Feng, Eliot Quataert, and Ramesh Narayan (2003). "Nonthermal Electrons in Radiatively Inefficient Accretion Flow Models of Sagittarius A*". In: ApJ 598.1, pp. 301–312. DOI: 10.1086/378716. arXiv: astro-ph/0304125 [astro-ph].

Appendix 2.A Ambient medium model and clump sizes

In order to estimate the mass loss through thermal conduction and to include the effects of the drag force in our simulations we need to specify density and temperature profiles for the environment. In this work we consider the same approach used by Burkert et al. (2012). We used the model described by Yuan, Quataert, and Narayan (2003) that reproduces CHANDRA X-ray observations assuming a completely ionised gas and solar metallicity. This model is consistent with state-of-the-art modelling of these observations by Roberts et al. (2017). Thus, the density profile of the medium is given by

$$\rho_{\rm ISM}(r) = 10^{-22}\left(\frac{1.7\times10^{17}{\rm cm}}{r}\right)^{\alpha}\ {\rm g\ cm^{-3}}. \tag{2.14}$$

To compute a temperature profile we assume hydrostatic equilibrium between the hot ISM and the gravitational potential of Sgr A* (Burkert et al., 2012). Therefore,

$$T_{\rm ISM}(r) = \frac{2.4\times10^{7}}{\alpha+1}\left(\frac{1.7\times10^{17}{\rm cm}}{r}\right)\ {\rm K}. \tag{2.15}$$

With a thermodynamic description of the ISM we can estimate clump sizes. To do so, we consider that clumps are completely ionised, and have a temperature of $T_{\rm c} = 10^4$K. Both assumptions are justified because of the presence of strong UV field radiated by the massive stars in the inner parsec. Also, we assume pressure equilibrium between the thermal pressure of the ISM and the clumps, i.e. $\rho_{\rm c} = \rho_{\rm ISM}T_{\rm ISM}/T_{\rm c}$. Considering clumps with a given mass, uniform density and spherical symmetry, obtaining their radius is straightforward.

3

3D simulations of unstable stellar wind collisions

The inner parsec of our Galaxy contains tens of Wolf-Rayet stars whose powerful outflows are constantly interacting while filling the region with hot, diffuse plasma. Theoretical models have shown that, in some cases, the collision of stellar winds can generate cold, dense material in the form of clumps. However, their formation process and properties are not well-understood yet. In this work we present, for the first time, a statistical study of the clump formation process in unstable wind collisions. We study systems with dense outflows ($\sim 10^{-5}$ $M_\odot$ yr^{-1}), wind speeds of 500–1500 km s^{-1}, and stellar separations of ~20–200 au. We develop 3D high resolution hydrodynamical simulations of stellar wind collisions with the adaptive-mesh refinement grid-based code Ramses. We aim to characterise the initial properties of clumps that form through hydrodynamic instabilities, mostly via the non-linear thin shell instability (NTSI). Our results confirm that more massive clumps are formed in systems whose winds are close to the transition between the radiative and adiabatic regimes. Increasing either the wind speed or the degree of asymmetry increases the dispersion of the clump mass and ejection speed distributions. Nevertheless, the most massive clumps are very light ($\sim 10^{-3}$–10^{-2} $M_\oplus$), about three orders of magnitude less massive than theoretical upper limits. Applying these results to the Galactic Centre we find that clumps formed through the NTSI should not be heavy enough neither to affect the thermodynamic state of the region nor to survive for long enough to fall onto the central super-massive black hole.

D. Calderón, J. Cuadra, M. Schartmann, A. Burkert, J. Prieto, C. M. P. Russell, MNRAS, **Submitted** *(2019), arXiv:1906.04181*

3.1 Introduction

Massive stars experience strong mass-loss episodes during their lives. Their powerful outflows have mass-loss rates that can reach up to $\sim 10^{-4}$ $M_\odot$ yr^{-1} and velocities that can exceed 2000 km s^{-1} (Puls, Vink, and Najarro, 2008). This kind of activity occurs mainly during the Wolf-Rayet (WR) and Luminous Blue Variable (LBV) stages. It has been observed that in binary systems such winds collide producing very energetic signatures such as particle acceleration, X-ray and γ-ray emission (Abdo et al., 2010; Hamaguchi et al., 2016; Hamaguchi et al., 2018; Panagiotou and Walter, 2018). In this case the material launched at supersonic speeds on opposite directions collides generating dense shells of compressed shocked material at temperatures typically in the range $\sim 10^6$–10^7 K. However, binaries are not the only environments where stellar winds interact leaving energetic observational signatures. Crowded stellar systems like the nuclear star clusters in the centre of the Milky Way are a clear example. The immediate vicinity of the central super-massive black hole (SMBH), Sgr A*, is populated by hundreds of massive O, B, and evolved stars (see Genzel, Eisenhauer, and Gillessen, 2010, for a review). Out of them 30 have been spectroscopically identified as WR stars. They have significant mass loss rates ($\gtrsim 10^{-5}$ $M_\odot$ yr^{-1}) in the form of stellar winds at very high speeds (500–2500 km s^{-1}; Martins et al., 2007). It is thought that these outflows are responsible for filling the region with hot ($\sim 10^7$ K), diffuse plasma ($n \approx 10$ cm^{-3}; Baganoff et al., 2003) that irradiates in X-ray (Roberts et al., 2017). On top of this, it is reasonable to argue that a fraction of this material might fall onto the SMBH. However, the amount and way the gas flows towards Sgr A* or escape from the environment outwards is not well-understood yet (Wang et al., 2013).

In the last decades several groups have been monitoring the stars located within the inner parsec. This has made it possible to infer the physical properties of the stars and their winds, and, in some cases, determine their orbital motion around the SMBH with high precision (Paumard et al., 2006; Yelda et al., 2014; Gillessen et al., 2017). Therefore, modelling the hydrodynamics of this environment is a unique opportunity to study the gas dynamics at small

distances from a SMBH, and also the multiple stellar wind interactions that are constantly taking place in this region. Cuadra et al. (2005), Cuadra et al. (2006), Cuadra, Nayakshin, and Martins (2008), and Cuadra, Nayakshin, and Wang (2015) developed hydrodynamics simulations of the complete system of WR stars moving on the observed orbits around Sgr A*. Simultaneously, the stars were feeding their environment via stellar winds.

Lützgendorf et al. (2016) conducted a similar work but studied another stellar component, the so-called S-stars. These objects correspond to B-type stars which are orbiting around the SMBH more closely compared to the WR stars. The wind properties of the S-stars have not been constrained accurately yet, but their winds are certainly not as dense as the WR stars. Specifically, their mass-loss rates are about two orders of magnitude lower. Although both works have managed to model very complex systems they have not been able to obtain reliable estimates of the amount of cold, low-angular momentum material, i.e. material that is more likely to be accreted by Sgr A*. This is a direct consequence of the use of the traditional Smoothed-Particle Hydrodynamics (SPH), which presents problems when simulating strong shocks, discontinuities, and two-phase medium. In some cases, this fact can produce artificial clumping instead of describing the expected filamentary structure properly (Hobbs et al., 2013). For instance, the simulations of Cuadra, Nayakshin, and Martins (2008) show that stellar wind collisions constantly generate dense, cold, clumpy material. However, our analytical study showed that clump formation should not be as frequent as seen in such simulations (Calderón et al., 2016). Therefore, there is a need for describing these processes in detail with more appropriate computational tools, especially in this environment.

Very recently, Ressler, Quataert, and Stone (2018) modelled the WR outflows in the Galactic Centre with a grid-based hydrodynamical code. This approach is significantly better suited to simulate shocks and a two-phase medium. As a result, they did not observe cold, dense clumps as originating from the stellar wind collisions. However, this was not the focus of their study. Their models were optimised to resolve the inner region as accurately as possible, and not necessarily for modelling the wind collisions in detail. Thus, despite the efforts of several works dedicated to studying how stellar winds feed Sgr A*, the wind interactions

themselves have not been the focus of any previous study yet.

In this context, it is important to remark that the thermodynamic state of the gas in the inner parsec can have a significant impact on the accretion rate onto the central black hole. For example if cold material can be formed and survive long enough to fall onto the SMBH it could cause variability in the accretion activity. Cuadra, Nayakshin, and Martins (2008) showed how the accretion of gas clumps can cause variability episodes on timescales of hundreds of years on the activity of Sgr A*. Theoretically, the accretion of a single clump of large enough mass could be responsible for the more active past of the SMBH inferred from observations of X-ray echoes (Sunyaev, Markevitch, and Pavlinsky, 1993; Sunyaev and Churazov, 1998; Ponti et al., 2010). In addition, the question arises whether the cold, small gas cloud G2 on a tight orbit around the central SMBH could be a result of wind interactions (Gillessen et al., 2012; Burkert et al., 2012; Calderón et al., 2016; Calderón et al., 2018). Therefore, in order to understand the current and past activity of the Galactic Centre, it is necessary to describe its stellar-wind collisions, more specifically the potential formation and evolution of gas clumps.

In general, studies of stellar wind collisions have focused on binary systems, a.k.a. colliding wind binaries. Early work was done by Stevens, Blondin, and Pollock (1992) studying unstable wind collisions through numerical 2D simulations. Pittard (2009) developed sophisticated 3D simulations of binary systems aiming to describe the hydrodynamics of wind interactions. These models included many physical ingredients such as gravity, wind acceleration, radiative cooling, and orbital motion. Within their findings they showed that clumps could be formed and, in some cases, they could live for long enough to escape from the system. Lamberts, Fromang, and Dubus (2011) revisited 2D models with the aid of the adaptive-mesh refinement (AMR) technique in order to simulate unstable wind collisions with high resolution. In this study, they formally identified that the so-called non-linear thin shell instability dominates the shape of unstable slabs over long timescales. Also, they warned about the tremendous computational challenge that one faces when modelling these systems. van Marle, Keppens, and Meliani (2011) presented 3D simulations of colliding wind

binaries to study the shape and structure of the slabs formed in wind collisions. Later, they also explored the structure of shells formed from the interaction of WR winds with material previously ejected by the same star during earlier stages of its life (van Marle and Keppens, 2012). In this study, they found that such interactions can create very complex structures through the development of different thin-shell instabilities depending on the radiative properties of the WR wind shock. If the material swept-up was dense enough, it could lose its thermal support becoming unstable very easily and creating very distinctive small scale patterns. Kee, Owocki, and ud-Doula (2014) studied the effects of the non-linear thin shell instability on X-ray emission through numerical 2D simulations. Hendrix et al. (2016) carried out 3D simulations with extremely high-resolution and dust formation, aiming to reproduce infrared observations of the spiral patterns created by the interaction of the winds combined with binary orbital motion.

Up to now there has not been any detailed quantitative study of the cold gas, sometimes in the form of clumps, produced in stellar wind collisions. In this work we present, for the first time, a statistical analysis of the clump formation process in such systems. Motivated by the WR in the Galactic Centre, we study systems with dense outflows ($\sim 10^{-5}$ $M_\odot$ yr^{-1}), speeds of 500–1500 km s^{-1}, and stellar separations of ~20–200 au. In general, these systems are wider than typical colliding wind binaries studied in the literature. We use the code Ramses (Teyssier, 2002) to run 3D hydrodynamic simulations of unstable wind collisions. The code includes an AMR module for reaching higher resolution without increasing the computational cost significantly. We do not focus on modelling specific colliding wind binary systems. Instead, we explore a rather specific set of parameters, suited for the WR stellar system in the Galactic centre in order to: *i*) understand the process of clump formation, *ii*) determine the initial clump physical properties and characterise their dependence on system parameters, and *iii*) compare the results with previous theoretical estimates of clump formation in the Galactic Centre.

This chapter is structured as follows. In Section 3.2, we describe the physics involved in stellar wind collisions. Also, we briefly review the physical mechanisms responsible for

clump formation and discuss relevant parameters. Then, we present the numerical setup of our simulations in Section 3.3. Here, we include a description of the models explored. The results of our study are shown in Section 3.4, where we describe the hydrodynamics of each model, as well as the characteristics of the clumps that form. Then, we compare our results with previous analytical work, study the impact of resolution, and discuss implications on the hydrodynamics state of the Galactic Centre in Section 3.5. Finally, we present our conclusions and future work guidelines in Section 3.6.

3.2 Stellar wind collisions

3.2.1 Structure of the interaction zone

In general, stellar winds of massive stars propagate with supersonic speeds and therefore their collision develops shock waves that compress material in shells behind their fronts. The shape and physical properties of such shells depend strongly on the nature of the shocks, in particular the ability of the shocked material to radiate away its thermal energy. Accordingly, there are two regimes into which shocks fall: radiative and adiabatic. In the former, the compressed material radiates its thermal energy rapidly and forms thin shells of cold, dense material just behind the shock front. For the latter, the compressed material predominantly loses energy through adiabatic expansion, leaving the layer hot and thick. Naturally there is also an intermediate case where the energy losses through radiation and adiabatic expansion are complimentary, and in a binary system the two shocks can have different properties.

In their seminal work, Stevens, Blondin, and Pollock (1992) introduced the parameter χ to characterise the radiative nature of a stellar wind such that we can interpret in advance if it is associated to a radiative or an adiabatic shock. The *cooling parameter* χ is defined as the ratio of the cooling timescale $t_{\rm cool}$ to the adiabatic expansion timescale $t_{\rm ad}$ for the shocked

material:

$$\chi = \frac{t_{\rm cool}}{t_{\rm ad}} \approx \frac{V_{\rm w,8}^4 d_{12}}{\dot{M}_{-7}}, \tag{3.1}$$

where $V_{\rm w,8}$ is the wind speed in units of 1000 km s^{-1}, d_{12} is the distance from the star to the contact discontinuity in units of 10^{12} cm, $\dot{M}_{-7}$ is the wind mass-loss rate in units of 10^{-7} M$_\odot$ yr^{-1}. Originally, this expression was obtained under the assumption of solar abundances; however we modified it in order to account for different values of metallicity by introducing a factor $(Z/Z_\odot)^{-1}$, where Z is the mass fraction in metals. Based on this definition, if $\chi < 1$ the wind is radiative while if $\chi > 1$ the wind is adiabatic.

In the case where both winds are adiabatic, the resulting slab is smooth, thick and hot and held up by thermal pressure on both sides (see left panel of Figure 3.1). If one wind is adiabatic while the other is radiative, the radiative shock is supported by its ram pressure and a thin shell of cold material forms (see central panel of Figure 3.1). Such a thin shell can become unstable very easily; however, the thermal pressure of the adiabatic shock acts as a dampener of such instabilities. This is the so-called Vishniac instability (Vishniac, 1983). Finally, if both winds are radiative, a dense and cold slab is formed, confined by ram-pressure on both sides. If it is perturbed, the non-linear thin shell instability (NTSI; Vishniac, 1994) can be excited. This mechanism is caused by the misbalance of the thermal pressure inside the cold slab with respect to the ram-pressure of the winds. Consequently, material tends to accumulate on the knots of the perturbation of the slab (gray regions in right panel of Figure 3.1). It is important to remark that in the case where the winds have different speeds, regardless of the radiative nature of the winds, the Kelvin-Helmholtz instability (KHI) can be excited. However, high-resolution numerical models of unstable wind collisions have shown that, if excited, the NTSI tends to dominate over other instabilities. Specifically, it is the main shaper of the slab structure due to its large-scale perturbations (Lamberts, Fromang, and Dubus, 2011).

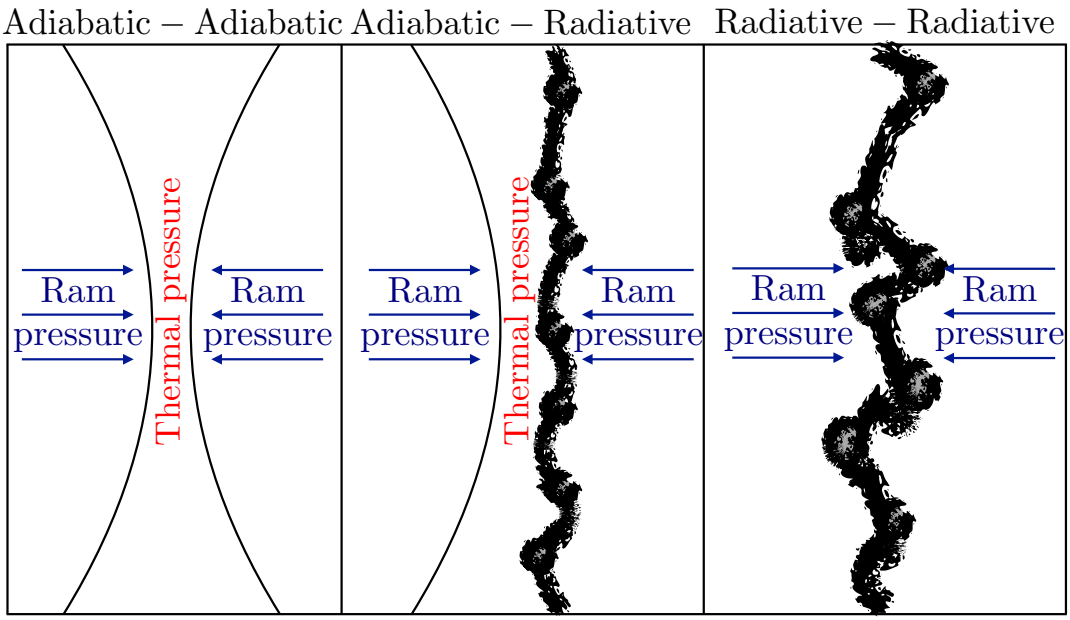

Figure 3.1: Schematic representation of different types of stellar wind collisions according to radiative properties. Left panel shows the result of a collision of two adiabatic winds: a thick, hot slab of shocked material. The middle panel contains the outcome of a radiative wind colliding with an adiabatic wind: a dense, thin shell of cold material subject to the Vishniac's instability. Right panel illustrates the result of a collision of two radiative winds: a dense, thin shell of cold material subject to the NTSI. It is important to remark that in case the winds have different speeds the KHI can be excited in any case.

3.2.2 Clump formation

Theoretically, only a limited range of wavelengths can excite the NTSI. Vishniac (1994) showed that the unstable wavelengths should be at least of the width of the slab. Otherwise, such shells could not be effectively corrugated. On the other side, the upper limit is given by the sound crossing length[1], so

$$l_{\rm slab} \lesssim \lambda_{\rm NTSI} \lesssim l_{\rm s}. \tag{3.2}$$

This analytical description assumes an isothermal equation of state, i.e. infinitely efficient cooling. However, in reality we expect cooling to occur on a finite amount of time. Within the ideal gas assumption the sound speed is proportional to the square root of the temperature of the gas, i.e. $c_{\rm s} \propto \sqrt{T}$. Thus, a longer cooling timescale implies also a longer unstable wavelength upper limit, which potentially means that larger clumps could be formed. Nevertheless, let us bear in mind that still it is a necessary condition of having a thin, cold slab. The largest clumps will form whenever radiative cooling is efficient but takes place as slow as possible. Therefore, winds whose χ approaches unity should generate the largest and most massive clumps (Calderón et al., 2016). Simply by assuming a geometry and using the value of the density in the slab we can estimate the approximate clump masses.

3.3 Numerical simulations

3.3.1 Equations

Our numerical simulations are carried out with the adaptive-mesh refinement hydrodynamics code Ramses (Teyssier, 2002). The code solves the Euler equations in their conservative form, i.e.

[1] Defined as the distance a sound wave travels in a given timescale, i.e. $l_{\rm s} = c_{\rm s}\Delta t$

$$\frac{\partial \rho}{\partial t} + \nabla \cdot (\rho \mathbf{u}) = 0, \tag{3.3}$$

$$\frac{\partial}{\partial t}(\rho \mathbf{u}) + \nabla \cdot (\rho \mathbf{u} \otimes \mathbf{u}) = \rho \mathbf{f}(\mathbf{x}) - \nabla P, \tag{3.4}$$

$$\frac{\partial}{\partial t}(\rho e) + \nabla \cdot \left[\rho \mathbf{u} \left(e + \frac{P}{\rho}\right)\right] = -\frac{\rho^2}{(\mu m_{\rm H})^2}\Lambda(T), \tag{3.5}$$

where ρ, $\mathbf{u}$ and P are the mass density, velocity, and pressure of the fluid, respectively; $\mathbf{f}$ is the gravitational force per mass unit and e the total specific energy density which is given by

$$e = \frac{1}{2}\mathbf{u} \cdot \mathbf{u} + \frac{P}{(\gamma - 1)\rho}, \tag{3.6}$$

where γ is the adiabatic index that is set to $5/3$ for adiabatic gases. Furthermore, μ is the mean molecular weight, $m_{\rm H}$ is the proton mass, T is the temperature of the gas, and $\Lambda(T)$ is the energy losses due to optically thin radiative cooling. Additionally, we included a prescription for the stellar wind generation which is presented in Section 3.3.3.

3.3.2 Numerical setup

We run 3D simulations on a Cartesian grid making use of the adaptive-mesh refinement technique, such that the resolution is enhanced in regions of the domain where specified physical criteria are met. Every side of our cubic domain has an outflow boundary condition. The domain is a cube of side length $2a$ where a is the stellar separation of the system.

The setup was chosen in order to capture the development of instabilities in the wind interactions as accurate as possible. We follow the guidelines provided by Lamberts, Fromang, and Dubus (2011) in their extensive 2D study. We used an exact Riemann solver with a MinMod flux limiter. These choices avoid the quenching of instabilities by numerical diffusion. The refinement strategy is set to be based on density gradients, thus the resolution increases mostly in shocks and discontinuities. The coarse grid resolution of our simulations is 64^3 cells, and there are four levels of refinement (standard resolution),

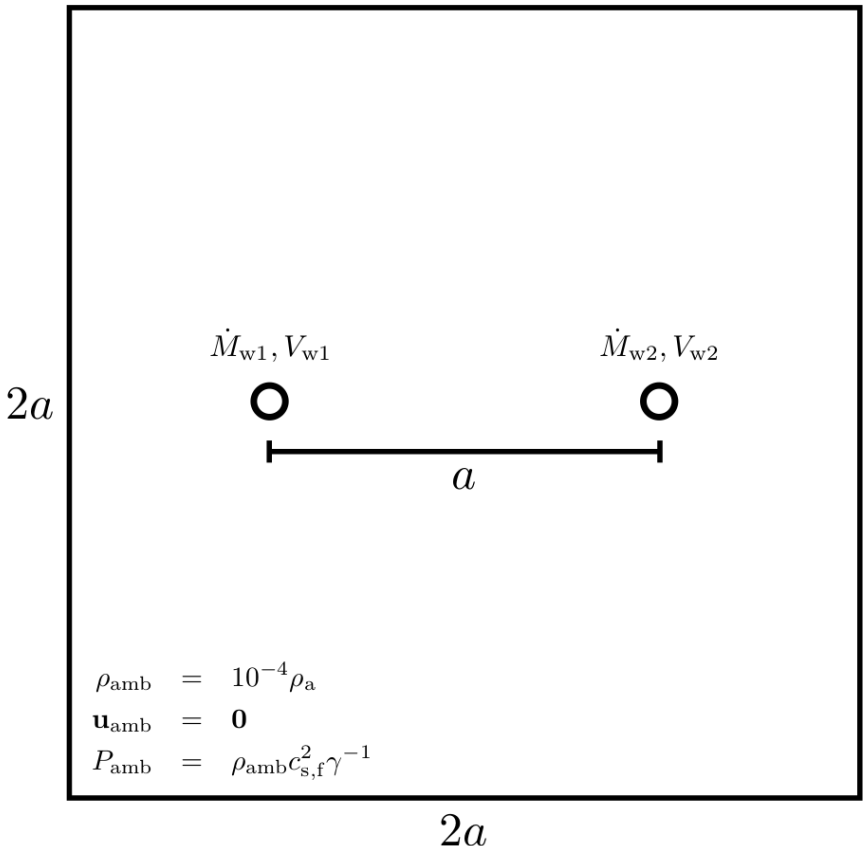

Figure 3.2: Schematic representation of the initial conditions of simulations at proportional scale. The domain is a cubic box with a side length of $2a$, hence volume $8a^3$. The hydrodynamic variables of the ambient medium initially are set to $\rho_{\rm amb} = 10^{-4}\rho_a$, $\mathbf{u}_{\rm amb} = \mathbf{0}$, $P_{\rm amb} = \rho_{\rm amb} c^2_{\rm s,f} \gamma^{-1}$. Two stars blowing stellar winds are fixed at $\mathbf{r}_{\rm w,1} = (-0.5a, 0, 0)$ and $\mathbf{r}_{\rm w,2} = (+0.5a, 0, 0)$, i.e. their separation is a. The stellar winds are generated in spherical regions of radius $a_{\rm w} = 0.04a$ centred at those locations. Each stellar wind is characterised by its mass loss rate $M_{\rm w,i}$ and terminal velocity $V_{\rm w,i}$.

creating an effective resolution of 1024^3 cells. Therefore, each resolution element reaches a length of $a/512 \approx 0.002a$. Each simulation in this work consists of the hydrodynamics evolution of two stellar winds that are being blown from stars fixed in space from positions $\mathbf{r}_{\rm w,1} = (-0.5a, 0, 0)$ and $\mathbf{r}_{\rm w,2} = (+0.5a, 0, 0)$ in a cubic volume of length $2a$. The domain size is chosen in order to maximise the resolution in the region where clumps are formed which

is the main scope of this work. The environment is initialised at low density, specifically, four orders of magnitude smaller than the wind density at the distance that it is blown $\rho_{\rm amb} = 10^{-4}\rho_{\rm a}$. The medium is set at rest $\mathbf{u} = \mathbf{0}$, and at the lowest temperature allowed $P_{\rm amb} = \rho_{\rm amb} c_{\rm s,f}^2 \gamma^{-1}$, where $c_{\rm s,f}$ is the sound speed at the temperature floor. These specifications allow the stellar winds to flow freely, filling the domain without difficulties until they collide.

Figure 3.2 shows a 2D schematic representation at $z = 0$ of the setup and initial conditions. We ran each simulation for at least five wind crossing timescales, defined as the time the slowest wind takes to cross the domain, i.e. $t_{\rm cross} = 2a/V_{\rm w,1}$. The simulation time of each model corresponds to a small fraction of the orbital period in case the stars were in a binary system. However, the orbital speed of such a system would be $\lesssim 10\%$ of the stellar wind velocity, which justifies our choice of considering motionless stars.

We consider that the gas has a metallicity of $Z = 3Z_{\odot}$. This choice is inspired by our motivation to apply the results to the Galactic Centre environment. Although metallicity is not strongly constrained for such stars, this is the value typically assumed in theoretical studies of the region (Cuadra, Nayakshin, and Martins, 2008; Calderón et al., 2016; Ressler, Quataert, and Stone, 2018).

3.3.3 Stellar wind generation

The setup includes a module to generate stellar winds, largely inspired by the approach of Lemaster, Stone, and Gardiner (2007). Specifically, it consists of resetting the hydrodynamic variables to the 1D free-wind solutions inside a spherical region of the domain (hereafter "masked region") after every time step. Here we assumed that the winds are instantaneously accelerated up to their terminal speeds, which is justified as we study models whose stellar separations are significantly larger than the stellar radius of the stars ($a \gg R_*$). In order to capture the spherical symmetry of the wind model, we forced the masked region to be refined up to the maximum level. Each stellar wind in our simulations is determined by three parameters: mass loss rate $\dot{M}_{\rm w,i}$, terminal velocity $V_{\rm w,i}$, and mask radius $a_{\rm w}$. Therefore, the

(primitive) hydrodynamic variables within the mask are kept fixed in time with the following values:

$$\rho(|\mathbf{x}-\mathbf{r}_{\mathrm{w,i}}|^2 < a_{\mathrm{w}}^2) = \rho_a \left(\frac{a_{\mathrm{w}}}{|\mathbf{x}-\mathbf{r}_{\mathrm{w,i}}|}\right)^2, \tag{3.7}$$

$$\mathbf{u}(|\mathbf{x}-\mathbf{r}_{\mathrm{w,i}}|^2 < a_{\mathrm{w}}^2) = V_{\mathrm{w,i}} \left(\frac{\mathbf{x}-\mathbf{r}_{\mathrm{w,i}}}{|\mathbf{x}-\mathbf{r}_{\mathrm{w,i}}|}\right), \tag{3.8}$$

$$P(|\mathbf{x}-\mathbf{r}_{\mathrm{w,i}}|^2 < a_{\mathrm{w}}^2) = P_a \left(\frac{a_{\mathrm{w}}}{|\mathbf{x}-\mathbf{r}_{\mathrm{w,i}}|}\right)^{10/3}, \tag{3.9}$$

$$\rho_a = \frac{1}{4\pi a_{\mathrm{w}}^2}\frac{\dot{M}_{\mathrm{w,i}}}{V_{\mathrm{w,i}}}, \tag{3.10}$$

$$P_a = \frac{1}{\gamma}\rho_a c_{\mathrm{s,f}}^2, \tag{3.11}$$

where the subscript $\mathrm{i} = 1, 2$ is the label of each wind in the simulation. The sound speed $c_{\mathrm{s,f}}$ is obtained by choosing the temperature of the wind. We set $T_{\mathrm{w}} = 10^4$ K for the winds at $|\mathbf{x}-\mathbf{r}_{\mathrm{w,i}}| = a_{\mathrm{w}}$, which implies $c_{\mathrm{s,f}} \approx 10$ km s^{-1}. This temperature also corresponds to the floor temperature set in the simulations. In reality we expect the strong UV radiation field of the massive stars to be the responsible for setting this floor. The size of the computational region where winds are generated was chosen to be of radius $a_{\mathrm{w}} = 0.04a$. With this choice, the free wind region profile agrees to 1% with the analytical density profile. The size of this masked region is the same for both stars in every run.

3.3.4 Models

Figure 3.3 presents the cooling parameter χ of a stellar wind computed from Equation 3.1 as a function of its wind speed and distance to the contact discontinuity for the metallicity chosen in this work. The solid black line corresponds to $\chi = 1$, i.e. the transition from the radiative ($\chi \lesssim 1$) to the adiabatic ($\chi \gtrsim 1$) regime. In this diagram the mass-loss rate is $\dot{M}_{\mathrm{w}} = 10^{-5}$ M$_\odot$ yr^{-1}, which is a typical value for WR stars. However, their wind terminal

velocities span a very wide range (500–2500 km s^{-1}; Martins et al., 2007). Based on this, winds can be radiatively efficient if their speeds are slow, and/or if the position of the wind interaction region is very close to one of the stars (see Figure 3.3). The former condition can be satisfied for some types of WR stars, for example by the Ofpe/WN9 class whose winds are relatively slow of about 400–600 km s^{-1} (Crowther and Willis, 1993; Martins et al., 2007; Vink and Harries, 2017). The latter can occur in close encounters of single stars, including the case when stars with very different momentum flux in their winds are involved. In such a case, the stronger wind "pushes" the weaker one to remain closer to its star and, in some cases, can force it to be radiative.

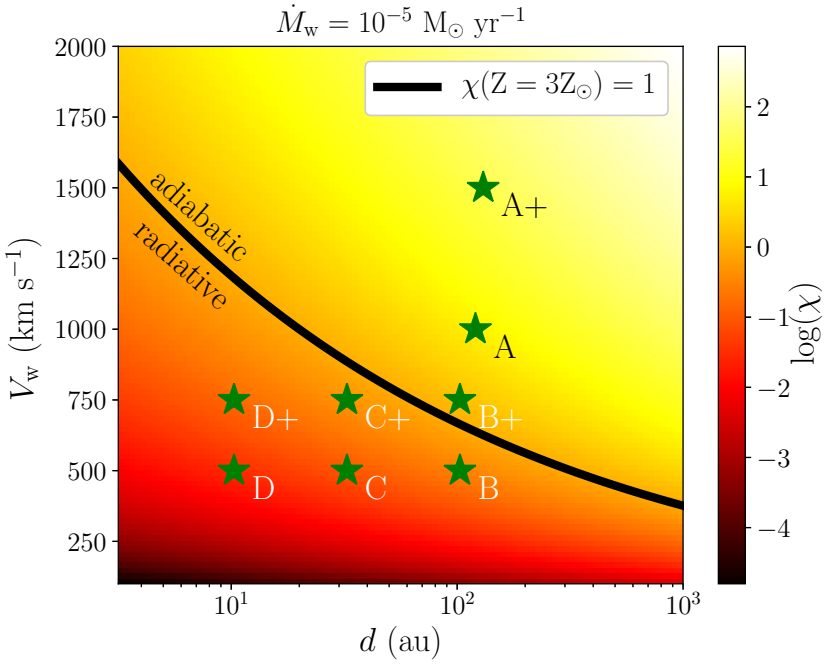

Figure 3.3: The cooling parameter χ computed from Equation 3.1 for a fixed mass-loss rate as a function of wind speed and distance to the contact discontinuity. The solid black line stands for $\chi = 1$ which divides the radiative and adiabatic regime. Green stars represent the wind of each star from each model studied.

In this work we fixed the mass-loss rate of the stars to $\dot{M}_w = 10^{-5}$ M$_\odot$ yr^{-1}, therefore, the

stellar separation a and the wind terminal speed of each star $V_{\rm w,i}$ are the free parameters of each model. We refer to models of two identical stars, i.e. with identical winds, as *symmetric systems*. On the other hand, models whose stars have winds with different terminal velocities are referred to as *asymmetric systems*. In order to quantify the degree of asymmetry in the wind interaction we use the ratio of wind momentum fluxes η which can be calculated by

$$\eta = \frac{\dot{M}_{\rm w,1} V_{\rm w,1}}{\dot{M}_{\rm w,2} V_{\rm w,2}}, \tag{3.12}$$

where subscripts 1 and 2 represent the weaker and the stronger wind, respectively (Lebedev and Myasnikov, 1990). Thus, it is satisfied that $\eta \leq 1$. As the mass-loss rates are fixed, the momentum flux ratio is determined by the terminal velocity ratio, i.e. $\eta = V_{\rm w,1}/V_{\rm w,2}$.

Calderón et al. (2016) conducted an analytic study in order to predict the mass of clumps formed in unstable stellar wind collisions. That study focused on models whose parameters were motivated by the WR stars present in the Galactic Centre. Here, we study a subsample of those models in order to make a direct comparisons between the simulations and that work. Table 3.1 presents the parameters of every model explored in this work. In total, we simulate six symmetric models with three different stellar separations $a = 210, 66, 21$ au, and two wind speeds $V_{\rm w} = 500, 750$ km s^{-1}. Furthermore, we studied two asymmetric models by fixing the stellar separation and the weaker wind speed to $a = 210$ au and $V_{\rm w,1} = 500$ km s^{-1}, and using $V_{\rm w,2} = 1000, 1500$ km s^{-1} for the stronger wind ($\eta = 0.5, 0.33$). Finally, we ran two more simulations, one with one level less and another with an extra level of refinement (up to three and five levels, respectively), for analysing the impact of resolution and convergence. Figure 3.3 highlights the position of every wind in our models in the parameter space in order to get an idea of their radiative nature. Most of them are below the $\chi = 1$ line, which means they correspond to radiative winds. The fastest winds, A and A+, are located well above the transition line in the adiabatic regime. Although the B+ wind is in the adiabatic wind region, the transition is not sharply defined, thus it is more accurate to refer to this region as a transition zone.

Table 3.1: Parameters of each model.

Name	η	$V_{w,1}, V_{w,2}$ (km s^{-1})	a (au)	t_{cross} (yr)	χ	Max. Res. (cells)
B10	1.0	500, 500	210	4.0	0.321	1024^3
B+10	1.0	750, 750	210	2.67	1.627	1024^3
C10	1.0	500, 500	66	0.6	0.032	1024^3
C+10	1.0	750, 750	66	0.4	0.163	1024^3
D10	1.0	500, 500	21	0.2	0.003	1024^3
D+10	1.0	750, 750	21	0.13	0.016	1024^3
B9	1.0	500, 500	210	4.0	0.321	512^3
B11	1.0	500, 500	210	4.0	0.321	2048^3
BA10	0.5	500, 1000	210	2.0	6.069	1024^3
BA+10	0.33	500, 1500	210	1.33	32.805	1024^3

Notes. The mass loss rate of the stars is set to $\dot{M}_w = 10^{-5}$ M$_\odot$ yr^{-1} in every model. Column 1: ID of a single simulation run. Column 2: ratio of the momentum fluxes of the winds. Column 3: stellar wind speed of each star in km s^{-1}. Column 4: stellar separation in astronomical units. Column 5: wind crossing timescale defined as $t_{cross} = 2a/V_{w,1}$ in years. Column 6: cooling parameter calculated from Equation 3.1. Column 7: maximum effective resolution of the simulation in number of cells.

3.4 Results

In this section we present and analyse each model. Firstly, we give a description of each run and highlight differences among them. Then, we present a quantitative analysis and characterisation of the structures formed in wind collisions.

3.4.1 Hydrodynamics

As we described previously, our simulations can be divided in two groups: symmetric ($\eta = 1$); and asymmetric ($\eta < 1$) wind collisions. The overall structure of the slabs formed and mechanisms acting can differ significantly between them (see Section 3.2.1), thus we present the results of the symmetric and asymmetric models separately in the following sections.

3.4.1.1 Symmetric models

In order to describe the evolution of these systems, we use as reference the model B10, which resembles very well the general behaviour of the symmetric models. Immediately after the winds collide a thick slab of compressed and hot material is formed (see Figure 3.4a). Given that the winds are radiative (by construction) the material cools down very rapidly. As a consequence, the slab loses its thermal pressure support, so it becomes thinner and denser as shown in Figure 3.4b. In general, such a thin slab can be easily perturbed from its rest position. In this case numerical noise is enough to seed instabilities in the shell. Thus, wiggles appear on the slab and are located away from the apex[2]. They can be clearly observed in Figures 3.4b and 3.4c, though they are quickly advected out of the domain. Meanwhile, close to the apex a roughly sinusoidal displacement of the slab starts to grow in amplitude (see Figure 3.4c). Now, in this region winds are no longer colliding completely perpendicular to the slab anymore. As a result, the slab becomes slightly wider (and less dense) while material seems to concentrate on the extremities of the perturbation. The density enhancement can

[2]In the context of stellar wind collisions, the apex is defined as the intersection point between the slab and the line connecting both stars.

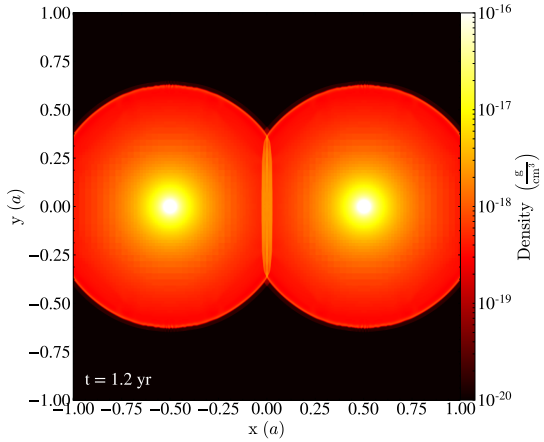

(a) Model B10: density at $z = 0$ and $t = 1.2$ yr

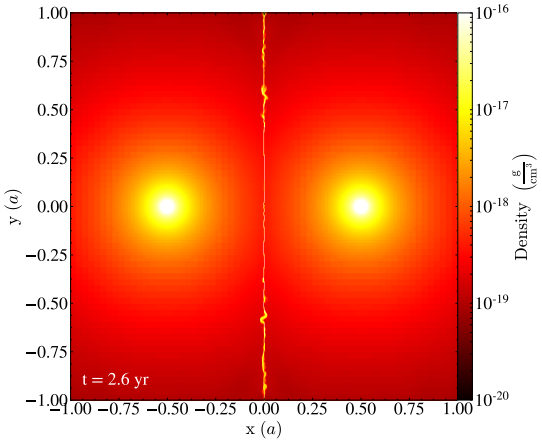

(b) Model B10: density at $z = 0$ and $t = 2.6$ yr

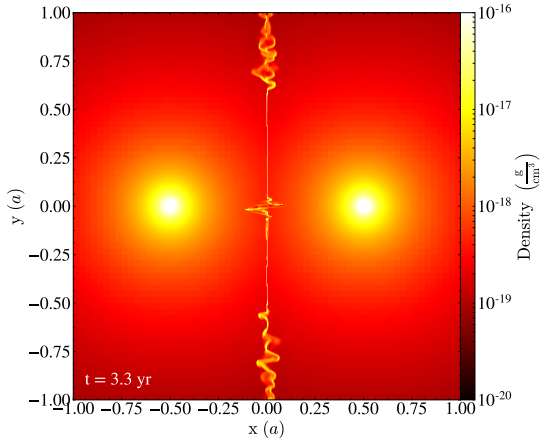

(c) Model B10: density at $z = 0$ and $t = 3.3$ yr

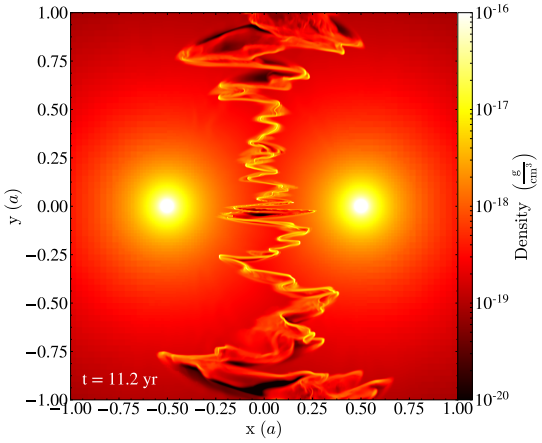

(d) Model B10: density at $z = 0$ and $t = 11.2$ yr

Figure 3.4: Density maps of cuts along $z = 0$ plane of model B10. Each panel shows different stages in the simulation. Panel (a) shows the model at $t = 1.2$ yr (0.3 $t_{\rm cross}$) when the initial wind collision creates a thick dense, hot slab. Panel (b) contains the system at $t = 2.6$ yr (0.65 $t_{\rm cross}$) highlighting the dense thin-shell formed after the slab cooled down. Here it is also possible to spot the first wiggles observed off-axis. Panel (c) shows the simulation at $t = 3.3$ yr (0.83 $t_{\rm cross}$) when a roughly sinusoidal perturbation appears near the apex. This perturbation starts to shape the entire slab. Panel (d) illustrates the system at $t = 11.2$ yr (2.8 $t_{\rm cross}$). At this point, the system is already in stationary state. Notice that the slab is completely unstable. This Figure has an associated animation attached (Figure4_B10_density_slice_z.mov).

be observed already in Figure 3.4c. Then, the central displacement of the slab starts to be advected away from the apex, which moves the sinusoidal perturbation to the rest of the slab. Simultaneously, more modes are excited, especially after the perturbation propagated across the whole slab. Approximately after two wind crossing timescales, the slab is completely shaped by the instability (see Figure 3.4d). Here, it is even clearer that the density enhancements (clumps) occur on the most displaced regions of slab. Beyond this point the system is in an approximately stationary state, at least until the end of the simulation, which is a minimum of four wind crossing timescales for the standard resolution runs.

The general behaviour of the symmetric models described so far resembles very well the evolution observed in the 2D isothermal models by Lamberts, Fromang, and Dubus (2011). Since these simulations are 3D, we can move beyond just analyzing the simulations in the $z = 0$ plane. However, in 3D space the evolution of the system and the shape of the slab is harder to study due to its complexity. Figure 3.5 contains projected density maps along the z- and x-axes across the entire computational domain weighed by density [3] in the left and right panels, respectively. Figure 3.5a shows once again that the densest regions of the interaction are the most displaced extremities of the slab, while Figure 3.5b demonstrates how complex the structure can be with all the small-scale, filamentary, dense structure generated due to the radiative wind collision. Section 3.4.2 presents the study of the physical properties of such overdensities.

The most relevant consequence of considering models with faster winds is the increase of the cooling timescale of the shocked gas. There are two independent factors that contribute to this: firstly, as the density of a stellar wind is inversely proportional to its terminal speed, the density decreases by having a faster wind. Then, as the cooling is proportional to ρ^2, its efficiency is reduced. Secondly, a faster wind leads to a higher temperature reached by the shocked material. For typical temperature values of shocked material in stellar winds ($\sim 10^6$–10^7K), at higher temperature the cooling is less efficient.

[3] This quantity is $\int \rho^2 dz / \int \rho dz$, and helps to highlight the dense gas, which corresponds to the most refined regions of the domain.

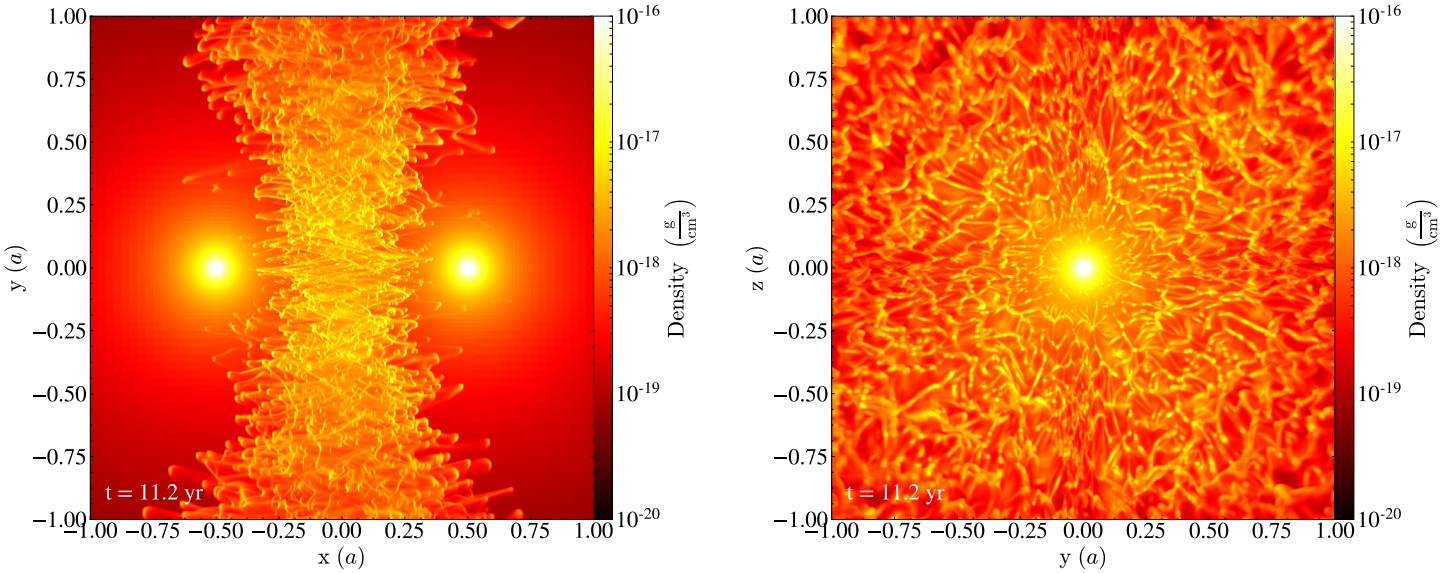

(a) Model B10: density integrated along z-axis at t = 11.2 yr

(b) Model B10: density integrated along x-axis at t = 11.2 yr

Figure 3.5: Density projection maps of model B10 at t = 11.2 yr (2.8 $t_{\rm cross}$). Each panel corresponds to projections along the z- and x-axis, respectively. The column density was calculated using the density field as weight, i.e. $\int \rho^2 dl / \int \rho dl$. This quantity helps to highlight the dense gas, which correspond to the most refined regions of the domain. Notice that the simulation time is the same as in Figure 3.4d. Panel (b) has an associated animation attached (Figure5b_B10_density_projection_x.mov).

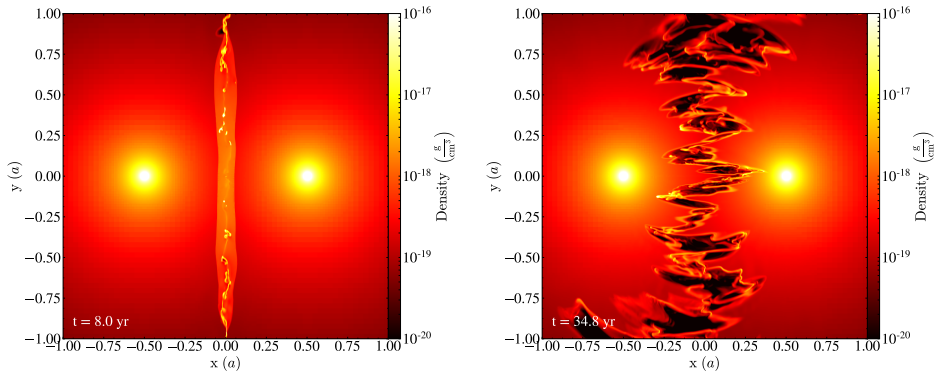

(a) B+10: t = 8 yr (b) B+10: t = 34.8 yr

Figure 3.6: Density maps on the $z = 0$ plane of model B+10. Notice that the left panel shows the evolution of the system at similar time compared to Figure 3.4d ($t \approx 3\ t_{\rm cross}$). However, given that in this case the winds are faster the slab has not cooled down yet. The right panel presents the evolution of the system at t=34.8 yr (13 $t_{\rm cross}$) Notice that in this case the instability looks more violent compared to the model B10. In particular, the density contrast in this model is starker. This Figure has an associated animation attached (Figure6_B+10_density_slice_z.mov).

Thus, the slab formed in wind collisions cools down more slowly if we consider faster winds. This is exactly what happens in the case of the model B+10, seen by comparing the density at $z = 0$ of model B+10 in Figure 3.6a to model B10 in Figure 3.4c. Here, the slab remains thick, i.e. supported by thermal pressure, for longer compared to the case of model B10. The model B10 at t = 3.3 yr (0.83 $t_{\rm cross}$) shows that the slab has already cooled down and that it is starting to become unstable. On the contrary, in model B+10 even at t = 8.0 yr (3 $t_{\rm cross}$) the slab is still thick and hot. Although condensation is observed in its inner part probably due to thermal instabilities, overall the slab remains thick, which means that it has not radiated its thermal energy yet. Only after about ten years, the slab ends up collapsing initially at the centre and, at the same time, the instability starts to develop. Figure 3.6b presents the state of the model B+10 at t = 34.8 (13 $t_{\rm cross}$), which corresponds to the end of the simulation. It is important to remark that in this case the system was

not completely radiative or adiabatic, instead it was in the transition of both regimes, i.e. $\chi \approx 1$ (see Figure 3.3). This is why the slab does not cool down easily, but with the help of thermal instabilities it manages to radiate its energy to become thin and, therefore, subject to more violent instabilities. Furthermore, notice that in this model once the slab is completely unstable, its structure looks more violent compared to model B10. From a theoretical point of view this is expected because the Mach number is larger in this case ($\mathcal{M} \approx 75$) compared to the model B10 ($\mathcal{M} \approx 50$). This means that the fluid can become more turbulent and, therefore, the density contrast is larger (Parkin and Gosset, 2011). Such behaviour will also be present when studying in detail the structure of the unstable slab.

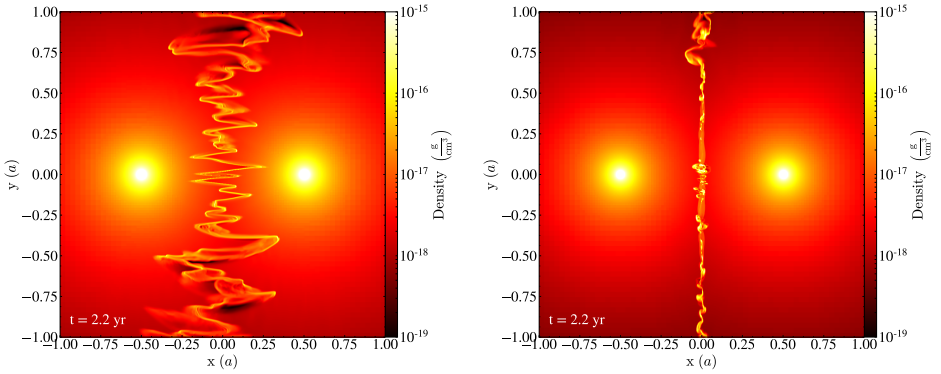

(a) C10: $t = 2.2$ yr (b) C+10: $t = 2.2$ yr

Figure 3.7: Density maps at $z = 0$ plane of models C10 and C+10 in panels (a) and (b), respectively. Both show the state of the system at exactly the same simulation time $t = 2.2$ yr. Notice that in the model C10 the instability has already developed in the entire slab. Meanwhile, in the model C+10 the instability is developing but has not reached stationary state yet.

In models with smaller stellar separations (and also smaller domains), faster winds do not produce differences as significant as in the B models . This is due to the cooling efficiency not changing as dramatically between C10 and C+10 compared to the B10 and B+10 models. The winds of both models C10 and C+10 are in the radiative wind regime (see Figure 3.3), thus we expect their slabs to cool down relatively fast. Even though model C+10 considers

a faster wind speed, which makes cooling more inefficient, at the same time the winds are denser at the collision given that the stellar separation is shorter. Figure 3.7 shows a comparison between systems C10 and C+10 at exactly the same simulation time. Here we can observe that the slab of model C10 at $t = 2.2$ yr is already completely unstable (see Figure 3.7a). However, in model C+10 the instability is still growing, even though some parts of the slab have not cooled down yet as they remain thick (see Figure 3.7b). If we consider even shorter stellar separations, namely models D10 and D+10, the differences are even smaller (not shown here). Both systems consider winds which can cool more efficiently compared to C or B models (see Figure 3.3). This is because the winds are denser at the collision due to the shorter stellar separation, which translates into an increase of the cooling efficiency. Increasing the wind from 500 km s^{-1} to 750 km s^{-1} does not seem to be enough for overcoming such effect. Here, in both cases the slabs cool down very rapidly, and they become unstable very easily. Therefore, we do not see significant differences between models D10 and D+10.

3.4.1.2 Asymmetric models

Figure 3.8 presents density maps at $z = 0$ showing the evolution of models B10, BA10, and BA+10 along the upper, central, and lower rows, respectively. Each column contains each system at the same simulation time, specifically, from left to right $t = 1.2, 2.6, 3.3, 11.2$ yr. As the winds are not identical, the slab formed after the collision is not located at the midpoint between the stars. In general, the equilibrium position of the slab is determined by balancing the wind momenta. Based on this, the slab should be at a distance $[a\sqrt{\eta}/(1 + \sqrt{\eta})]$ from the star with the weaker wind (Stevens, Blondin, and Pollock, 1992), which in our case also corresponds to the slower wind located on the left side of the domain . Thus, in models BA10 and BA+10 the slab is centred at $\sim 0.41a$ and $\sim 0.37a$ from the slow wind star, respectively. Although the difference is small compared to the symmetric cases, this causes the slow wind to be denser at the collision and, therefore, being more radiatively efficient.

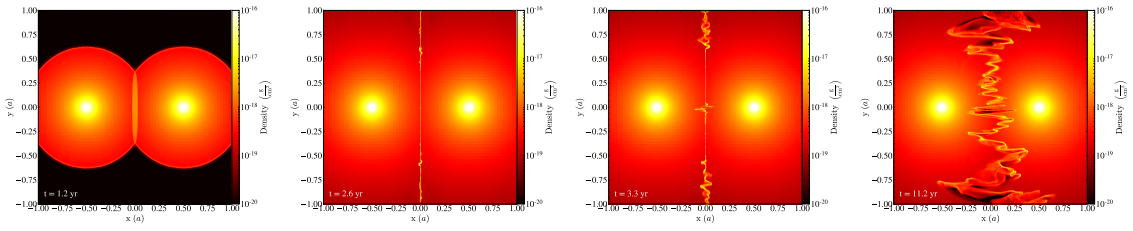

(a) B10: t = 1.2 yr (b) B10: t = 2.6 yr (c) B10: t = 3.3 yr (d) B10: t = 11.2 yr

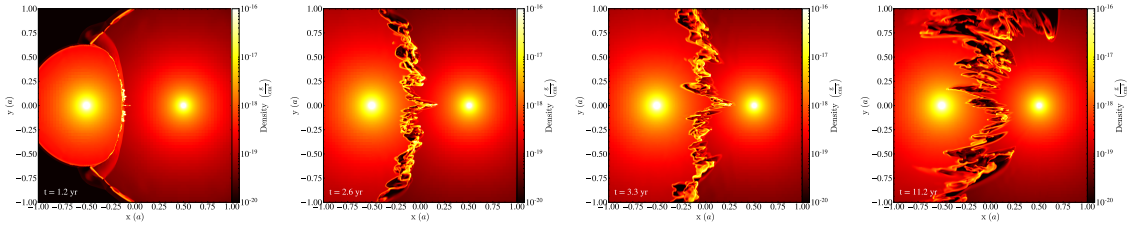

(e) BA10: t = 1.2 yr (f) BA10: t = 2.6 yr (g) BA10: t = 3.3 yr (h) BA10: t = 11.2 yr

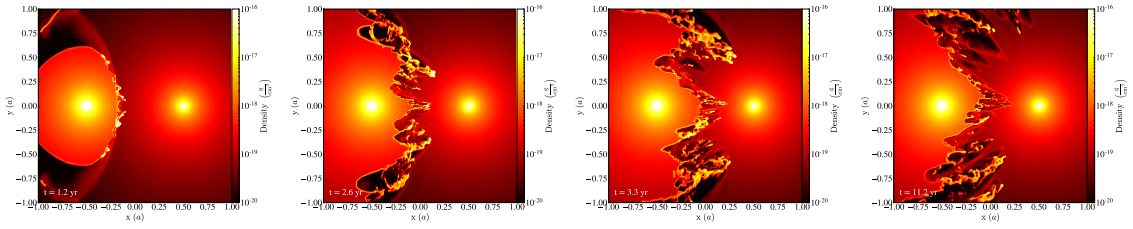

(i) BA+10: t = 1.2 yr (j) BA+10: t = 2.6 yr (k) BA+10: t = 3.3 yr (l) BA+10: t = 11.2 yr

Figure 3.8: Density maps at $z = 0$ of different models at the same simulation time. Rows stand for models B10 (upper), BA10 (central), and BA+10 (lower). It is important to remark that these models consider the same domain size and resolution. From left to right, columns represent simulation times t = 1.2 yr, t = 2.6 yr, t = 3.3 yr, and t = 11.2 yr. Notice that the more different the wind speed is the faster the slab becomes unstable. Furthermore, a large velocity difference produces more violent instabilities excited in the slab. Models B10 (upper row) and BA+10 (lower row) have associated animations attached (Figure6_B10_density_slice_z.mov and Figure8ijkl_BA+10_density_slice_z.mov, respectively).

This picture is even more dramatic when winds collide for the first time in the simulation. Mainly, because the location of such encounter is determined by the speed of the winds which does not necessarily coincide with the equilibrium position of the slab. As in the model BA10

(BA+10) the stronger wind is twice (three times) as fast the initial collision occurs at $\sim 0.33a$ ($0.25a$) from the weak wind star. Notice that both separations are shorter compared to the distance to the slab equilibrium position (see first column of Figure 3.8). Therefore, the weaker wind collides being even denser and the radiative cooling takes place even faster compared to the case when the slab is located on its rest position. On the contrary, the opposite applies for the faster wind, i.e. it is more diluted when it collides for the first time causing the cooling to be less efficient.

The asymmetric models also show that instabilities are triggered at earlier times. Specifically, in less than a year after the initial wind collision, we can visually recognise patterns consistent with the KHI in the interaction region located away from the apex. This is not surprising as Lamberts, Fromang, and Dubus (2011) had already observed such behaviour finding that even very small speed difference between the winds could excite this instability. Nevertheless, in these cases this instability is not necessarily the only one acting like in the adiabatic models of Lamberts, Fromang, and Dubus (2011). Instead, as our models consider radiative cooling it is possible that the slab loses its thermal support, at least partially, so that the KHI can develop simultaneously along with the thin-shell instabilities, most likely with the Vishniac instability (Vishniac, 1983). This is most likely the reason behind the wind interaction becoming even more complex after a couple of years, especially if we compare its evolution with the symmetric model B10 (see second column of Figure 3.8).

There are two more important observations we can infer from the evolutionary sequences of Figure 3.8. Firstly, notice that with decreasing η, i.e. larger wind speed difference, the instabilities seem to grow faster. For instance, the slab of model B10 looks completely unstable only in the last panel of the sequence which is at $t = 11.2$ yr (see Figure 3.8d). On the other side, the slabs of the asymmetric models are already unstable in the second panel of the sequence, i.e. at $t = 2.6$ yr (see Figure 3.8f and 3.8j). Also, the instabilities grow faster in BA+10 than in BA10 (see central and lower rows of Figure 3.8). At $t = 3.3$ yr there are larger amplitude modes excited in BA+10 (see Figure 3.8k) than in BA10 (see Figure 3.8g). Even at earlier times longer wavelength modes seem to be excited in BA+10 (see Figure 3.8j) but

not yet triggered in BA10 (see Figure 3.8f). The KHI is very likely responsible for this as its growth timescale in the linear regime is given by $t_{\rm KHI} = \lambda/(2\pi\Delta v)$, where λ is the wavelength and Δv is the velocity difference between the fluid layers. Thus, a given mode λ grows faster the larger the velocity difference is. As in model BA+10, Δv is twice that of model BA10, so an arbitrary mode should grow twice as fast. Secondly, it is important to remark that once all of the systems reached their stationary state, the slab of model BA+10 shows the largest density constrast compared to the rest. Additionally, the structure of the unstable shell looks more clumpy and less filamentary than BA10 and B10 (see last column of Figure 3.8). The explanation of such features could be the degree of the supersonic nature of winds. In B10, BA10, and BA+10, the faster winds have a Mach number of $\mathcal{M} \approx 50, 100, 150$, respectively. As this quantity reflects the compression of the material of the slab, it is natural to expect higher compression, and therefore a denser slab, with a higher Mach number. Also, let us remember that at lower η the collision takes place closer to one of the stars, which also translates into a higher density in the shell. Therefore, these could explain the larger density contrast observed in the density maps, especially in BA+10.

In order to describe the thermodynamic state of the wind interaction in the asymmetric models, Figures 3.9 and 3.10 present density and temperature maps of models BA10 and BA+10, respectively. The upper row of each figure contains density maps while the lower row presents temperature maps. The left and right columns show maps at the $z = 0$ and $x = x_{\rm slab}$ planes, respectively, where $x_{\rm slab}$ corresponds to the slab rest position of a given model. Analysing the temperature maps, it is possible to observe that most of the domain is kept at low temperatures ($T \lesssim 10^5$K). Bear in mind that mostly these regions correspond to the free-wind regions, which are initially blown at $\sim 10^4$ K. However, there are some regions in the slab that are also at this temperature. Observing carefully it is possible to see that each of these regions corresponds to the densest parts of the slab. Furthermore, notice that they all are surrounded by hotter material due to the presence of the adiabatic shock of the faster winds. As this material cannot cool down efficiently, the condensed regions in the slab must originate solely from the slowest wind.

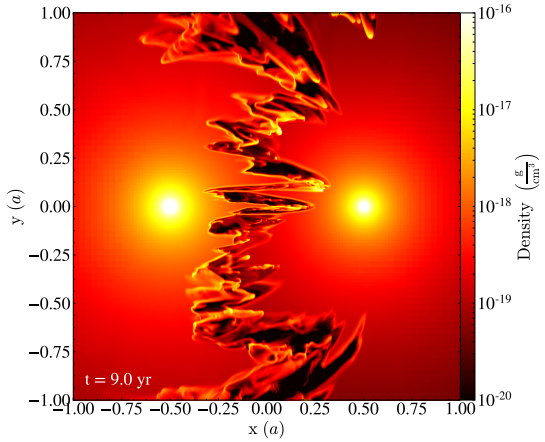

(a) BA10: $\rho(x, y, z = 0)$

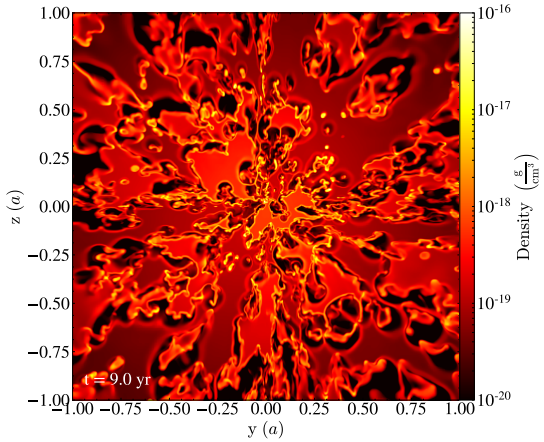

(b) BA10: $\rho(x = -0.09a, y, z)$

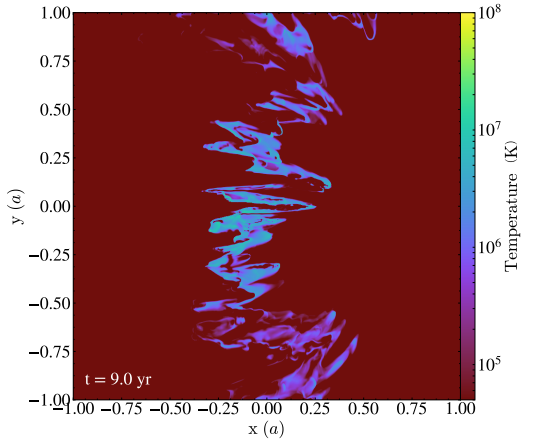

(c) BA10: $T(x, y, z = 0)$

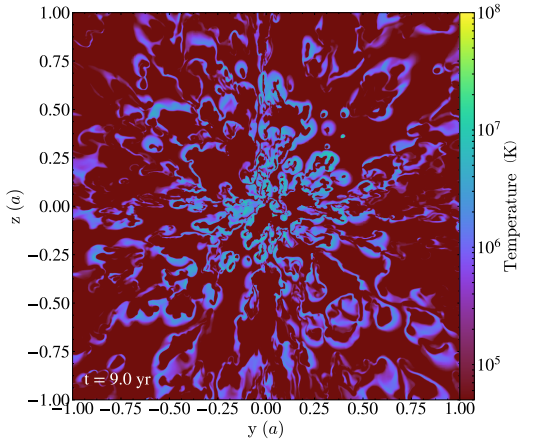

(d) BA10: $T(x = -0.09a, y, z)$

Figure 3.9: Density (upper row) and temperature maps (lower row) of model BA10. The left and right columns contain maps at $z = 0$ and x =–0.09a (slab equilibrium position), respectively. All panels show the state of the system at exactly the same simulation time $t = 9.0$ yr. High temperatures in the slab are due to the compression and inefficient cooling of the fast wind material (blown by the star on the right). Notice that the densest regions in the unstable slab are at low temperatures ($T \lesssim 10^5$ K). Meanwhile lower density regions in the slab are kept at very high temperatures ($T \approx 10^6$–10^7 K).

This description resembles very well the description of the Vishniac instability. Here, the dense slab is confined on one side directly by ram-pressure and on the other by the thermal pressure of the adiabatic shock. This could be the reason why the unstable slab is very different in the asymmetric cases compared to the symmetric models. Let us remember that in our symmetric models both winds were radiatively efficient, by construction, therefore the slab ended up being confined by ram-pressure on both sides. In that case the unstable shell is better described by the NTSI (Vishniac, 1994).

Finally, let us analyse differences between the density and temperature maps of models BA10 and BA+10 (see Figures 3.9 and 3.10). At $x = x_{\rm slab}$ the structures present are denser in model BA+10 (Figure 3.10b) compared to BA10 (Figure 3.9b). This fact is simply explained by the stronger pressure confinement of the winds. On one side the stronger wind is faster, so ram-pressure is larger. On the other side, the slab is being pushed closer to the weaker wind star, so this wind is denser at the collision, which also enhances the ram-pressure strength.

Another important observation is related to the temperature reached in certain regions of the slab. As expected, model BA+10 reaches higher temperatures, in general, than BA10 since the fast wind of the former is 50% larger. More important it is the temperature differences along each of the slabs (see Figures 3.9c and 3.10c). Higher temperatures in the slab are found closer to the apex. This is due to the fact that the shocks are closer to be normal to the slab in this region. Away from the apex, ram-pressure decreases with density and the velocity of the winds is not entirely compressing material; instead it helps to advect the slab away from the domain. On top of this, once the slabs become unstable the shocks do not hit, in general, perpendicular to the slab, so the shocks unlikely generate the maximum compression expected in a plane-parallel setup.

3.4.2 Structure search and characterisation

Now that we have described the general evolution of the systems we proceed to study the properties of the overdensities formed in the slab. Firstly, we describe our structure finder

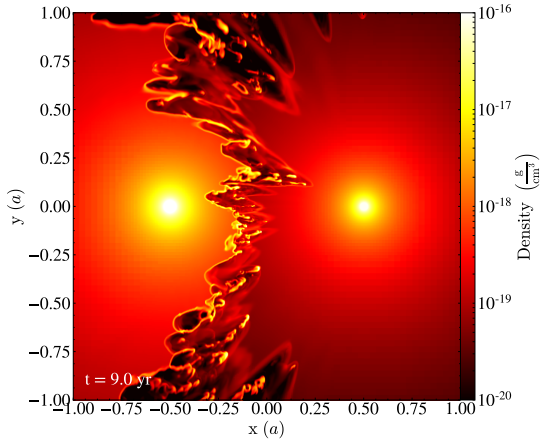

(a) BA+10: $\rho(x, y, z = 0)$

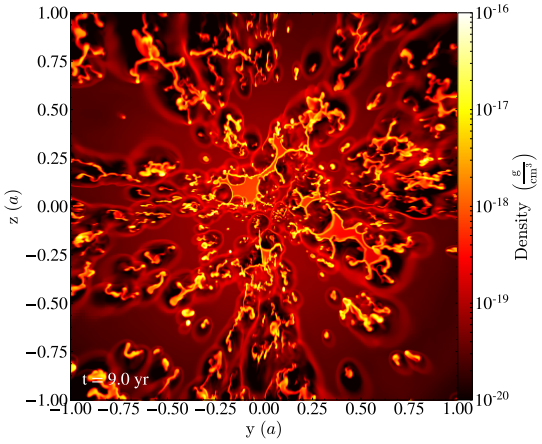

(b) BA+10: $\rho(x = -0.13a, y, z)$

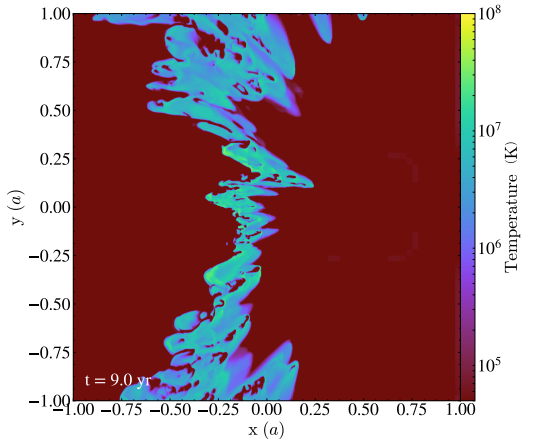

(c) BA+10: $T(x, y, z = 0)$

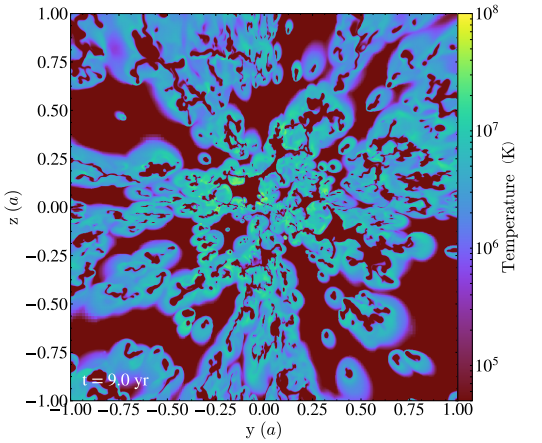

(d) BA+10: $T(x = -0.13a, y, z)$

Figure 3.10: Density and temperature maps of model BA+10. This figure is analogous to Figure 3.9 but for model BA+10. The left and right columns contain maps at $z = 0$ and $x = -0.13a$ (slab equilibrium position), respectively. Notice that density and temperature reached are larger compared to model BA10.

algorithm. Then, we study the physical properties and dynamics of the clumps, and how the wind speed and stellar separation determine such properties.

3.4.2.1 Identification criteria

In each simulation run we searched for overdense regions (clumps). To do so, we made use of a clump finder algorithm that was applied to every single snapshot of the simulations. Typically, these type of algorithms receive (at least) two input parameters: a density threshold $\rho_{\rm tr}$ and a minimum number of cells for defining a clump $N_{\rm cell}$. Here, we used a density threshold of $\rho_{\rm tr} = \bar{\rho} + 5\sigma_{\rho}$, where $\bar{\rho}$ and σ_{ρ} correspond to the mean density and density dispersion, respectively. The value of $\rho_{\rm tr}$ is about $\sim 10^{-17}$ g cm^{-3} in models with a large domain like B10 (see Figure 3.4 as reference). We tested several threshold values, and noticed this value gave the most reasonable result maximising the selection of cells in the slab while minimising the cells of the free wind region. The minimum number of cells for detecting a clump was set to $N_{\rm cell} = 10$ (for the standard resolution runs). Making use of these parameters the algorithm executes the following tasks. Firstly, it applies a density cut on the cells of the snapshot, i.e. it ignores every cell whose density is lower than the threshold. Then, it searches for physically connected structures within the remaining cells. It continues analysing the substructure of each previously identified structure. By doing so, it defines a clump per each density local maximum found. The algorithm iterates until every cell was assigned to a (sub)structure. The output is a list of structures with their associated substructures. For each substructure we extracted its physical properties, such as total mass m, centre-of-mass position $\mathbf{R}_{\rm cm}$, and velocity $\mathbf{v}_{\rm cm}$. For a more detailed description of the algorithm we refer the reader to the Appendix 3.A. It is important to remark that these clumps are not gravitationally bound. As we expect them to have, at most, a mass of the order of the Earth, self-gravity is negligible compared to the wind ram-pressure confinement. Therefore, the clumps correspond to pressure confined overdensities.

An example of the analysis performed by the algorithm is shown in Figure 3.11. It corre-

sponds to the model B10 at time $t = 11.2$ yr. It presents a density projection along the x-axis (weighted by density) but considering only cells above the density threshold. The zoomed-in region marks the centre-of-mass of clumps identified by the algorithm.

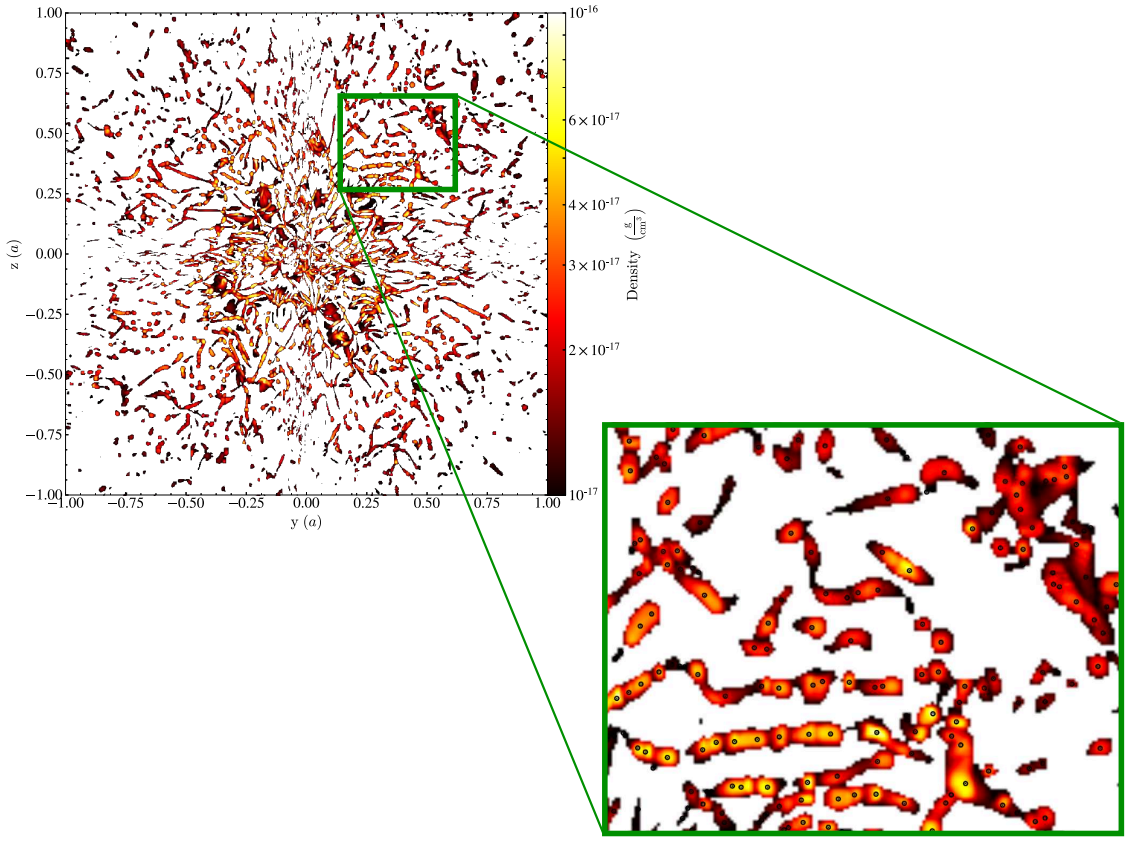

Figure 3.11: Density projection along the x-axis of the model B10 at $t = 11.2$ yr after performing a density cut at $\rho_{\rm tr} = \bar{\rho} + 5\sigma_\rho$, i.e. not considering cells whose $\rho \leq \rho_{\rm tr}$. The zoomed region shows an example of the overdensities our clumpfinder algorithm identifies as clumps. Black circles highlight the centre-of-mass of the identified overdensities. This snapshot analysis corresponds to the same model at the same simulation time as the one shown in Figure 3.5.

3.4.2.2 Clump masses and motion

Now, we proceed to analyse the simulations in order to search and characterise clumps. As we described in Section 3.4.1, in each model there is a point at which the system reaches

an approximate stationary state. Under this regime the slab shape is completely determined by the instabilities. In general, we noticed that this state starts, approximately, after two wind crossing timescales. Based on this, we decided to analyse the simulation only during this self-regulated state, as we aim to characterise the long-term behaviour of the system. Firstly, we describe in detail the analysis of model B10 so that we present a general view of the clump properties and dynamics. Then, we analyse how these results change if we modify the properties of the stellar winds.

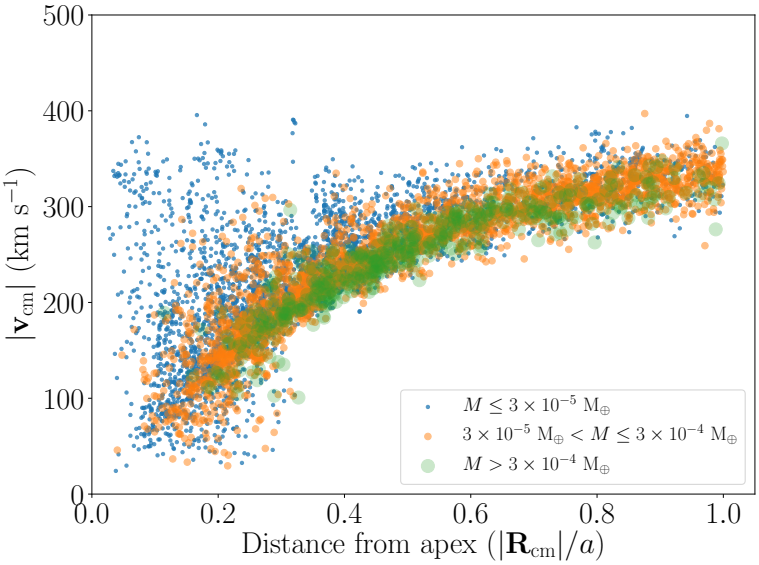

Figure 3.12: Magnitude of the clump centre-of-mass velocity $|\mathbf{v}_{\rm cm}|$ as a function of their 3D distance from the apex (which in symmetric models coincides with the centre of the domain) $|\mathbf{R}_{\rm cm}|$ at $t = 11.2$ yr in model B10. Clumps located further than $|\mathbf{R}_{\rm cm}| = a$ are not shown. Each point represents a single clump. The size and colour encode their mass. The most massive clumps are shown as big green dots. The lightest clumps appear as small blue dots. Notice that clumps tend to follow a clear trend, specially as they move away from the centre.

Figure 3.12 presents the velocity of the clumps as a function of their distance from the apex, which coincides with the centre of the domain in symmetric models. On top of this, clumps are shown as dots (each dot corresponds to a single clump). Their mass are colour-

and size-coded. Larger green dots represent more massive clumps while smaller blue dots stand for lighter clumps. This analysis corresponds to the model B10 at time $t = 11.2$ yr. Overall, notice that the parameter space where most clumps are located is well-defined. The shape of this diagram does not change significantly with time in the stationary regime. This fact points to a sequence that clumps seem to follow since they are formed at small $|\mathbf{R}_{\rm cm}|$ until they leave the domain $|\mathbf{R}_{\rm cm}|/a \rightarrow 1$. Notice that at short distances the scatter on their speed is large. Here, clumps can have almost null speed up to 400 km s^{-1}, which is about 80% of the wind speed. Nevertheless this description does not apply to the most massive clumps given that only few of them are present at $|\mathbf{R}_{\rm cm}|/a < 0.25$. Once the distance goes beyond this value, we can observe that the most massive clumps start to populate the diagram. At longer separations the scatter of the clump speed distribution tends to decrease. Furthermore, as clumps are getting closer to the boundaries of the domain ($|\mathbf{R}_{\rm cm}|/a \rightarrow 1$) their velocity seems to be converging.

In order to analyse this in more detail we divided the velocity and position vectors into components. Such a description is presented in Figure 3.13, where each panel shows the clump velocity as a function of distance along the x-axis (left panel), and within the yz-plane (right panel), bearing in mind that the x-axis is parallel to the line connecting the stars. Here we can clearly observe that the dispersion seen at small $\mathbf{R}_{\rm cm}$ in Figure 3.12 is shown solely in the x-component (left panel of Figure 3.13), and not along the other components. This dispersion seems to be caused by the instability which produces significant displacements of the slab towards one of the stars before the structure has time to be advected away from the domain. Thus, initially overdensities are pushed to either of the stars, and only when they reach certain distance from the centre they start to be accelerated steadily along the x-axis. However, the other components do not show the same behaviour. In the right panel of Figure 3.13, we can observe that the clump speed projected onto the yz-plane increases steadily with distance. This means these components are responsible for driving the clumps away from the system. Furthermore, it is possible to observe that the acceleration decreases with distance, which also implies that the velocity is converging. This is due to the change

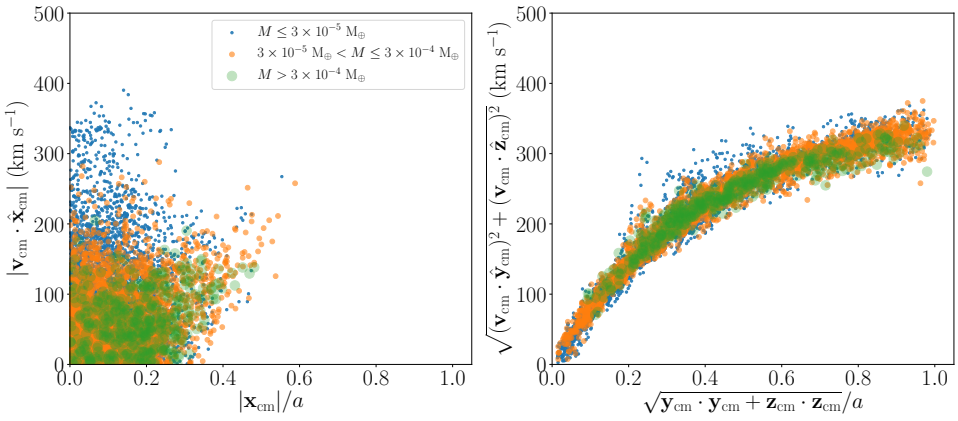

Figure 3.13: Figure analogous to Figure 3.12, however, here each panel shows the components of velocity and position. Left panel shows the velocity and distance component along the x-axis, while the right panel contains the velocity and distance projections onto the yz-plane. Bear in mind that the line connecting both stars is parallel to the x-axis, and the slab is initially located at $x = 0$.

of the stellar wind ram-pressure strength as a function of distance, $P_w \propto r^{-2}$. Unfortunately, our domain size does not allow us to observe what occurs further away. In general, this will depend largely on the environment this system is immersed in. This is why we preferred not to go beyond this range with our models. By doing so, these high-resolution simulations provide a detailed view of the initial properties and behaviour of clumps immediately after being formed.

To conduct a quantitative description of the clump mass and velocity distribution, we divided the clumps located in two groups according to their spatial location: an inner and an outer region. The former is defined as a sphere of radius $0.5a$ centred in the apex of the wind interaction. The latter was defined as a concentric spherical shell whose inner and outer radii are $0.5a$ and a, respectively. Figures 3.14 presents clump mass (left panel) and velocity (right panel) histograms of model B10 at $t = 11.2$ yr.

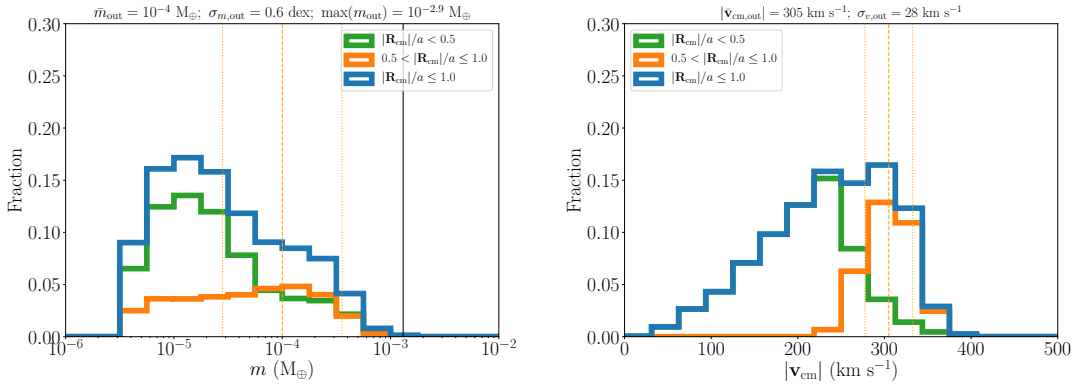

(a) Model B10: clump mass histogram

(b) Model B10: clump velocity histogram

Figure 3.14: Histograms of mass (left panel) and velocity (right panel) of clumps in different regions at t = 11.2 yr in model B10. Counts are shown as fractions (counts divided by the total number of clumps). In both panels, the green and orange lines show clumps located inside a sphere of radius 0.5a (inner region), and a spherical shell delimited by radii 0.5a and a (outer region), respectively. The blue lines represent the sum of the green and orange line histograms, i.e. clumps enclosed within a sphere of radius a. Notice that the x-axis scale is logarithmic on the left panel but linear on the right panel. Both panels also show the mean and standard deviation of the distribution for clumps in the outer region (orange lines) as dashed and dotted orange vertical lines, respectively. The vertical solid black line in the left panel corresponds the mass of the most massive clump. The numerical values plotted with vertical lines are shown on top of each panel.

The counts of each histogram are normalised by the total number of clumps identified, therefore, they are fractions of the total number of clumps. The line colour highlights the region where clumps are located. The green histogram represents clumps enclosed in the sphere of radius 0.5a (inner region). The orange histogram shows objects inside the spherical shell (outer region). The sum of the two is shown as a blue line. Vertical dashed lines stand for the mean value for clumps of the outer region. Meanwhile, vertical dotted lines show the standard deviation of the distributions. Finally, the most massive clump is shown with a vertical

solid black line. In Figure 3.14a notice that most clumps are of fairly low mass $m \approx 10^{-5}$ $M_\oplus$, while only a few of them reach the maximum mass of about $m \approx 10^{-3}$ $M_\oplus$. Here it is important to consider that the lower mass end is a direct consequence of the parameters of our clump finding algorithm: minimum cell size and density threshold. Therefore, we should not interpret it as the physical lower limit of the distribution. On the contrary, the upper mass limit is set purely by the hydrodynamics and radiative properties of the system.

Figure 3.14a also shows that in the inner region the majority of clumps are very light ($m < 5 \times 10^{-5}$ $M_\oplus$). In contrast, in the outer region we do not find as many light clumps. Even looking at the median clump mass we see that it is significantly displaced toward heavier clumps of, at least, an order of magnitude. In stationary state this histogram does not change significantly, therefore we can obtain information analysing why it preserves its shape. A possible explanation for this behaviour is that small clumps are formed in the inner region, some are destroyed while others merge into larger ones. Thus, only about a quarter of them manage to reach the outer region, which now contains less smaller clumps than the inner region. In the case of more massive clumps, we expect that they are being ablated through mass-loss as they lose the ram-pressure confinement while escaping from the system. However, as the number of massive clumps is the same between the inner and the outer region, more massive clumps should be constantly forming. Therefore, on one side clumps are losing mass, and moving to smaller mass bins, while at the same rate lighter clumps are either growing or merging to form more massive ones. Section 3.4.2.3 presents a detailed study tracking the properties of a single clump.

Figure 3.14b shows that clumps in the inner and outer regions have very different speed distributions. In the inner region clumps have lower speeds and also span a wider range of values. On the contrary, the outer region clumps tend to have larger speeds and smaller dispersion. This properties can be easily explained by observing the evolution of the system. Clumps are formed at short distances from the domain center where the wind collision cancels most of their linear momentum. This causes overdensities not to carry much momentum, at least initially. Then the instability growth displaces overdensities towards one of

the stars increasing their speed, specifically, along the x-axis (see left panel of Figure 3.13). Simultaneously, clumps start being advected away from the apex steadily increasing their velocity (see right panel of Figure 3.13). At this point, clumps stop being pushed toward any of the stars, and instead they are only gaining momentum for escaping from the system. After this transition, most clumps already have a well-defined velocity as they have spent roughly the same amount of time being accelerated by the winds. The latter regime corresponds to objects which are already in the outer region where their speed is about ∼60% of the wind speed and its dispersion is only ∼10%.

Recapping, model B10 shows that clumps in the inner region are still being formed, because they are part of the ram-pressure confined slab. Here, there is a larger fraction of lighter clumps, they are being accelerated, and, in general their speeds are small but show a large dispersion. On the contrary, in the outer region there are not as many light clumps due to their destruction and/or merging events. Their acceleration is decreasing given that ram-pressure loses strength with distance. Therefore, they seem to have reached their terminal speed that is about ∼3/5 of the wind speed. Notice that this description only applies to clumps located not further than the length of the stellar separation $|\mathbf{R}_{\rm cm}| = a$. Clump properties can be affected by the medium into which they are ejected.

3.4.2.3 The life of a clump

In our models, we were able to follow the evolution of some of the clumps. We restricted this analysis only to the most massive clumps as the problem of tracking overdensities is not straightforward in Eulerian hydrodynamics. To do so, we developed a criterion based on extrapolating the position of a clump at a given snapshot into the next one, and then performing a search in it based on the predicted position as well as taking into account the mass of the clump. In order to be sure that our algorithm was able to follow the same clump we inspected visually the density maps of its vicinity in order to observe a coherent evolution of the overdensity. Figure 3.15 presents a couple of examples of this analysis performed on

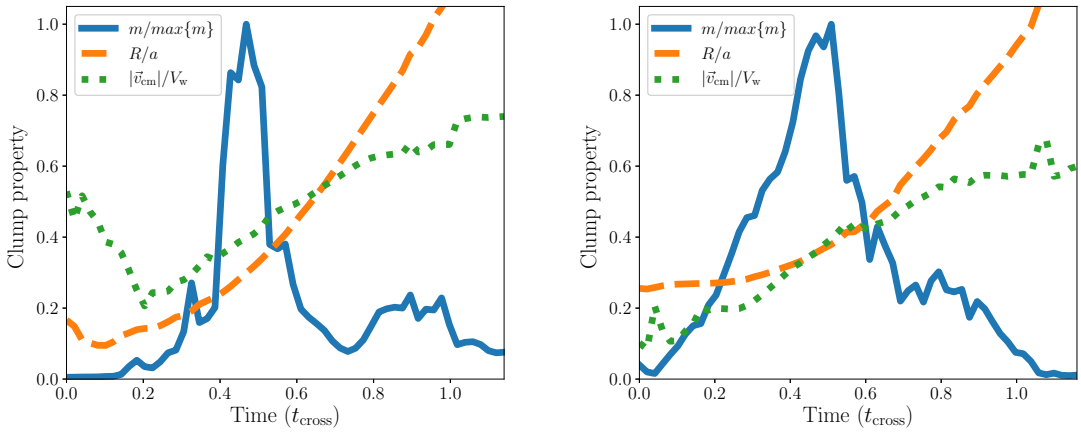

Figure 3.15: Clump evolution as a function of time. Each panel represents a different clump tracked through the simulation. Solid blue, dashed orange, and dotted green lines stand for clump mass, distance from the apex, and velocity magnitude, respectively. Notice that clumps tend to reach their maximum mass close around $|\mathbf{R}_{\rm cm}|/a \approx 0.5$. The process of formation, growth and advection take about one wind crossing timescale.

model B10. Specifically, we showed the clump physical properties; mass (solid blue line), distance from the apex (dashed orange line) and velocity magnitude (dotted green line), as a function of time. Notice that all values were scaled to representative values in order to make a fair comparison between different objects. Let us observe the evolution of the clump mass. The left panel shows that mass can increase relatively fast, which seems to be related with the merging of similarly massive clumps. On the other hand, the right panel shows how mass accumulates in a given object at a lower rate. Both cases show that the maximum mass is reached at a distance of $|\mathbf{R}_{\rm cm}|/a \approx 0.5$ from the apex. After this point, clumps seem be to losing mass constantly and relatively fast. This occurs as the result of the decrease of the ram-pressure confinement of the clumps as they are advected. In particular, there is a transition of the pressure confinement regime around the point where the mass of clumps is maximal. Figure 3.16 shows the ram-pressure of the winds as a function of the distance from the apex, although projected onto the yz-plane. Here we divided the pressure into two

components: compressive and advective. We defined the compression as the component parallel to the x-axis, i.e. perpendicular to the slab at the apex, which causes the slab confinement. Meanwhile, the pressure responsible for the advection of the clumps away from the domain is the component on the yz-plane. Both values were scaled by the value of the wind ram-pressure at the apex, which is given by $P_{\rm w,0} = \dot{M}_{\rm w} V_{\rm w}/(\pi a^2)$. This analysis shows how the compression of the slab decreases with distance and, more specifically, that it starts being smaller than the advection component at about $\sqrt{y^2+z^2}/a \approx 0.5$. After this point the slab, and clumps, lose a significant fraction of their confinement, which results into their mass loss and, in some cases, in their eventual destruction.

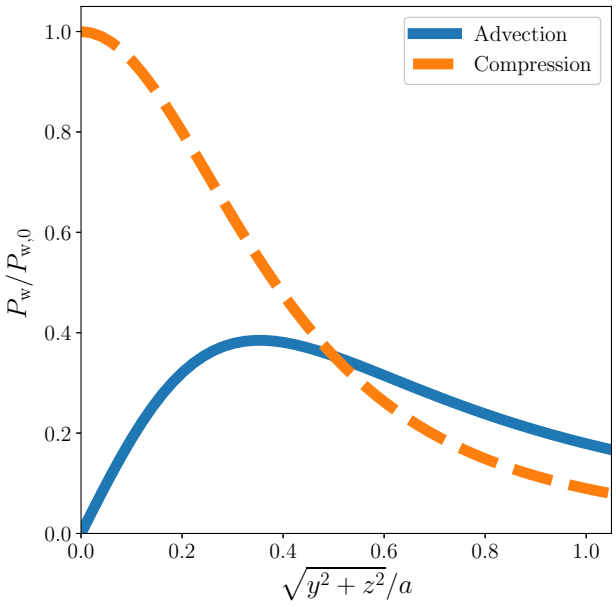

Figure 3.16: Ram-pressure exerted by a single wind in the yz-plane as a function of the projected distance along the plane. In our symmetric models this plane coincides with the rest position of the slab. The pressure was scaled by the ram-pressure at the apex and the distance by the stellar separation. Also, it is divided in two components: the advective which is projected into the yz-plane (solid blue line) and the compressive that is parallel to the x-axis (dashed orange line). Notice that there is a regime transition at $\sqrt{y^2+z^2}/a \approx 0.5$.

Furthermore, the advection strength, although slower, decreases constantly, which also can explain the fact that most of the clump momenta is gained at $|\mathbf{R}_{\rm cm}|/a \lesssim 0.5$. Finally, clumps leave the domain ($|\mathbf{R}_{\rm cm}|/a \approx 1$) at about $t \approx t_{\rm cross}$, which means they travel in average at about half of the wind speed.

3.4.2.4 The effects of wind speed and stellar separation

Although so far we have focused on describing the model B10, the qualitative behaviour of symmetric models is very similar. Hence its description also applies for the rest of those models. Now, we will present the results on how the clump properties are affected by changing the wind speed and/or the stellar separation. Summarised results are shown shown in Table 3.2. Here we included the mean clump mass and velocity, their dispersion and the maximum clump mass of each model studied. In model B+10 we increased the velocity of each wind by 50% compared to B10, by doing so we found that both the clump mass and velocity distributions have a slightly larger dispersion. Notice that this is consistent with the fact that the density maps of this model also showed starker contrasts compared to B10. Nevertheless, the mean values do not seem to change significantly, which might be the net effect of a higher compression and, at the same time, a more diluted wind caused by the presence of faster winds. The clump velocity ejection is also observed to be of ~3/5 of the wind speed. In the case of models with a smaller stellar separation, the mean clump mass decreases by ~0.5 dex in model C10, and becomes slightly smaller than this in C+10 (see Table 3.2). However, the outer clump velocities follow the same previous relations where the mean speed is about 60% of the wind speed and its dispersion is 10% of the mean velocity. If we consider the even smaller stellar separation in models D10 and D+10, we observe the same evolution overall, although clumps are now ~1 dex lighter than B10 and B+10. Furthermore, clumps seem to be accelerated and ejected following the same proportion observed in the other models. In summary, higher speeds cause clump mass and velocity distributions having larger dispersions, while clump masses seem to be correlated with the stellar separation.

Table 3.2: Ejected clump properties.

Name	$\bar{m}_{\rm out}$ $M_\oplus$	$\sigma_{m,\rm out}$ (dex)	$\max(m_{\rm out})$ $M_\oplus$	$\bar{v}_{\rm out}$ (km s^{-1})	$\sigma_{v,\rm out}$ (km s^{-1})
B10	$10^{-4.0}$	0.6	$10^{-2.9}$	300	30
B+10	$10^{-4.1}$	0.7	$10^{-2.7}$	497	59
C10	$10^{-4.5}$	0.6	$10^{-3.5}$	283	25
C+10	$10^{-4.8}$	0.7	$10^{-3.3}$	455	46
D10	$10^{-5.0}$	0.6	$10^{-3.9}$	307	26
D+10	$10^{-5.2}$	0.6	$10^{-4.0}$	411	36
B9	$10^{-3.6}$	0.7	$10^{-2.2}$	296	25
B11	$10^{-4.0}$	0.6	$10^{-3.0}$	303	26
BA10	$10^{-4.1}$	0.9	$10^{-2.7}$	433	89
BA+10	$10^{-4.0}$	1.0	$10^{-2.3}$	438	87

Notes. Summarised results: clump statistical physical properties per model. Column 1: name of simulation run. Column 2: mean clump mass at $0.5 < |\mathbf{R}_{\rm cm}|/a \leq 1$ in Earth masses. Column 3: standard deviation of the clump mass distribution in dex. Column 4: maximum clump mass in Earth masses. Column 5: mean clump speed at $0.5 < |\mathbf{R}_{\rm cm}|/a \leq 1$. Column 6: standard deviation of the clump speed at $0.5 < |\mathbf{R}_{\rm cm}|/a \leq 1$.

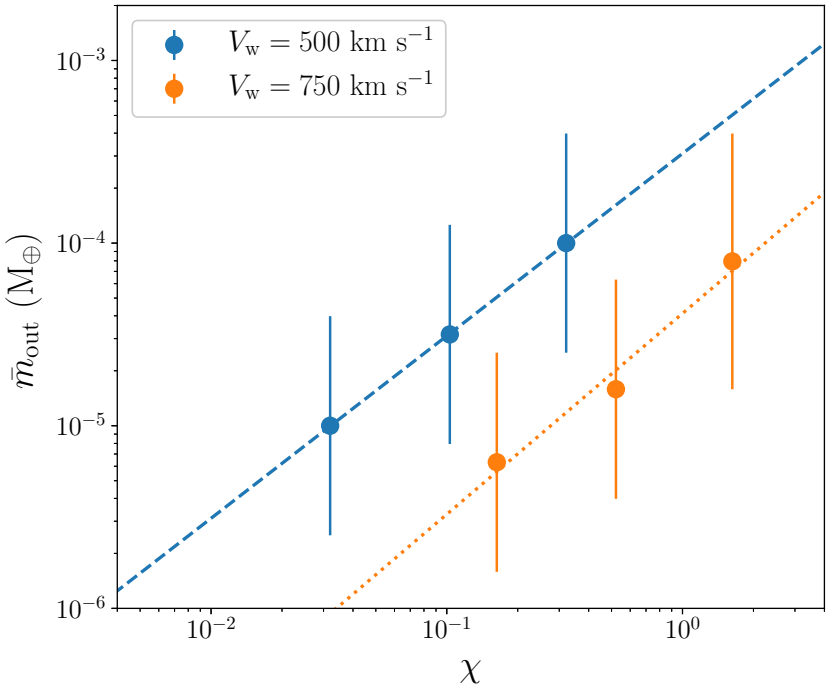

Figure 3.17: Mean mass of ejected clumps $\bar{m}_{out}$ as a function of the cooling parameter χ. Each point represents each symmetric model simulated. Error bars show the standard deviation of the distribution which is about 0.6 dex. Blue and orange points stand for models whose wind speed is 500 and 750 km s^{-1}, respectively. The dashed and dotted lines correspond to the best linear fit to each set of models.

Now we proceed to analyse the systematic differences observed in clump masses with stellar separation. Figure 3.17 shows the clump mean mass of the outer clumps (with their respective dispersion) as a function of the cooling parameter of the winds estimated at the apex of each system. Notice that this analysis only considers the symmetric models. Here we can separate them into two families according to their wind speed. The blue and orange points show models with 500 and 750 km s^{-1}, respectively. We fit the best linear function (in logarithmic scale) to each family of points:

$$\log\left(\frac{\bar{m}_{\rm out}}{\rm M_\oplus}\right) = 1.0\log\chi - 3.5;\ V_{\rm w} = 500\ {\rm km\ s^{-1}}, \quad (3.13)$$

$$\log\left(\frac{\bar{m}_{\rm out}}{\rm M_\oplus}\right) = 1.1\log\chi - 4.4;\ V_{\rm w} = 750\ {\rm km\ s^{-1}}. \quad (3.14)$$

Such relations confirm the fact that the slower the slab cools down the more massive the clumps can be. Recalling the definition of the cooling parameter, we can recover the dependence of the mean mass as a function of the stellar separation. This results in $\bar{m}_{\rm out} \propto a$ for symmetric systems. Thus, as long as the winds are radiative, the mass of the clumps, in general, increases with the stellar separation.

3.4.2.5 Clumps in asymmetric systems

Finally, we present the properties of clumps in the asymmetric models. Figure 3.18 shows histograms of clump mass and speed of model BA+10. Although the mean mass value is roughly the same, the mass distribution spans a larger mass range compared to model B10 (see Figure 3.18a). For instance, the most massive clump formed reaches a significantly higher mass than model B10 of about 1 dex. This feature can be attributed to the higher Mach number of one of the winds, which compresses the material stronger and, at the same time, generates a more turbulent state in the unstable slab. It is also important to notice the differences in the distribution of clump masses. In model BA+10 the mass of clumps in the inner and outer regions are extremely similar, both having peaks at low mass. However, in model B10 the inner and outer clump masses are much more different. Inner clumps are mostly very light, while outer clumps in general are more massive (see Figure 3.14a). The presence of different instability mechanisms could be the explanation of these differences. Let us remember that in asymmetric models the NTSI is acting along with the KHI. Thus, it is possible that the growth of clumps created by the former process is being limited by the latter.

In the case of the velocity distribution, the mean ejection speed of outer clumps is larger

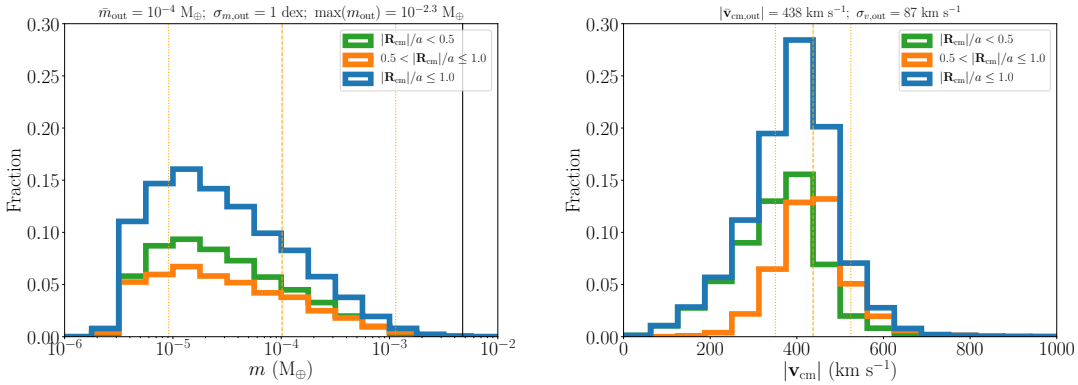

(a) Model BA+10: clump mass histogram

(b) Model BA+10: clump velocity histogram

Figure 3.18: Analogous to Figure 3.14 but for model BA+10. Notice that the dispersion of each distribution is larger in this case compared to B10.

than in symmetric models. For instance, clumps in model BA+10 reach about ~430 km s^{-1}, which is about ~90% of the weaker wind speed. We also notice that the dispersion is larger than in symmetric cases (see Figure 3.18b) being roughly ~20% of the mean speed. Therefore, the stronger (faster) wind contributes to accelerate the material to higher speeds, but the fact that the slab is subject to the KHI also causes larger fluctuations in the velocity field. Although not shown here, the properties of clumps of model BA10 also show differences compared to model B10. The clumps of model BA10 show a larger dispersion in the clump mass and velocity distribution compared to model B10, though not as much as BA+10 (see Table 3.2). This points to the fact that the degree of asymmetry and, more importantly, the wind velocity difference, is the cause behind such differences.

3.5 Discussion

In this section we proceed to compare the results of this work with previous analytical estimates mainly from Calderón et al. (2016). Furthermore, we discuss the choice of the resolution employed in our simulations, and study the convergence of the results. Finally, we

discuss the implications of the results on the Galactic Centre hydro- and thermodynamics.

3.5.1 Comparison with analytical estimates

Calderón et al. (2016) estimated the range of clump masses expected in symmetric wind collisions. For systems like model B10, the analytic estimates show that clumps could have masses up to the order of $\sim M_{\oplus}$. The results of the model B10 hydrodynamic simulations do adhere to this analytical upper limit since clumps are formed with $\sim 10^{-3} M_{\oplus}$ at most (see Table 3.2). However, there is a difference of three order of magnitudes between the theoretical and the numerical clump mass upper limit, and this difference does not change if we analyse other models either. To explain this difference we have to bear in mind that there are differences in the geometry between the analytical and numerical models: *i*) the planar and spherical winds, and *ii*) the "0D" and 3D approaches. Stellar winds are naturally closer to being spherical rather than planar. Thus, in a collision of spherical stellar winds the maximum compression of the slab occurs solely at the apex, and not through the entire slab, which is one of the implications of the planar wind assumption. Furthermore, the density of a spherical wind changes with the distance from the star while in the case of a planar wind it is assumed to be constant. Therefore, if the amplitude of the NTSI increases, it suffers from a damping effect as the ram-pressure is stronger approaching to any of the stars, which does not act in the case of colliding planar flows. Secondly, modelling the complete system with the appropriate geometry in 3D can differ significantly from the simple "0D" approach of considering an infinite slab. The fact that the gas in the slab can be advected away from the apex can affect how the gas can concentrate on the knots of the perturbed shell. As discussed in previous sections, the material is advected quicker as it moves away from the apex due to the acceleration caused by the wind ram-pressure. Thus, it is possible that the idealised geometry of the analytical model could account, at least partially, for the difference in the clump mass upper limits.

3.5.2 Impact of spatial resolution

We have studied the properties of clumps formed in stellar winds collisions namely their initial mass and velocity. In order to follow the clump formation process in detail, ideally we would need to resolve sizes comparable with the unstable wavelengths excited in the slabs. As the shortest wavelength of the NTSI is set by the width of the slab, the challenge is to be able to resolve such lengths as well as possible. In a radiative wind collision once the slab cools down it can become extremely thin, as seen in model B10 (see Figure 3.4b). However, this situation changes rapidly once instabilities are excited in the slab as it becomes slightly wider as compression diminishes because shocks are not strictly perpendicular to the slab anymore. Previously, Lamberts, Fromang, and Dubus (2011) warned about the computational difficulty of resolving wind confined thin shells. In their study, they ensured to have at least eight cells for resolving the slab in order to capture the development of the instabilities, this was possible given that such models considered an isothermal equation of state in 2D, which significantly decreases the computational cost. Unfortunately, in 3D even with the aids of the AMR technique it is difficult to afford such resolution. The main problem is related to the size of the slab which is usually refined up to the maximum level increasing significantly the computational cost of the simulations. Therefore, it is not possible to enhance the resolution much more from our standard setup. Nevertheless, we ran a couple of tests at lower and higher resolution to illustrate how the results could be affected by the resolution used in this study. Specifically, we investigated models B9 and B11, whose effective maximum resolution are 512^3 and 2048^3 cells, respectively.

In Figure 3.19 we present a comparison of models B9 (left column), B10 (central column) and B11 (right column) showing density maps at the $z = 0$ (upper row) and $x = 0$ (lower row) planes. Firstly, focusing on the shape of the slabs at $z = 0$ (see Figures 3.19a, 3.19b and 3.19c), notice that in general the unstable slab seems very similar, though there are differences especially at small scales. More complex substructure appears in the slab as the resolution increases. This is clearer in the maps at $x = 0$ (see Figures 3.19d, 3.19e and 3.19f).

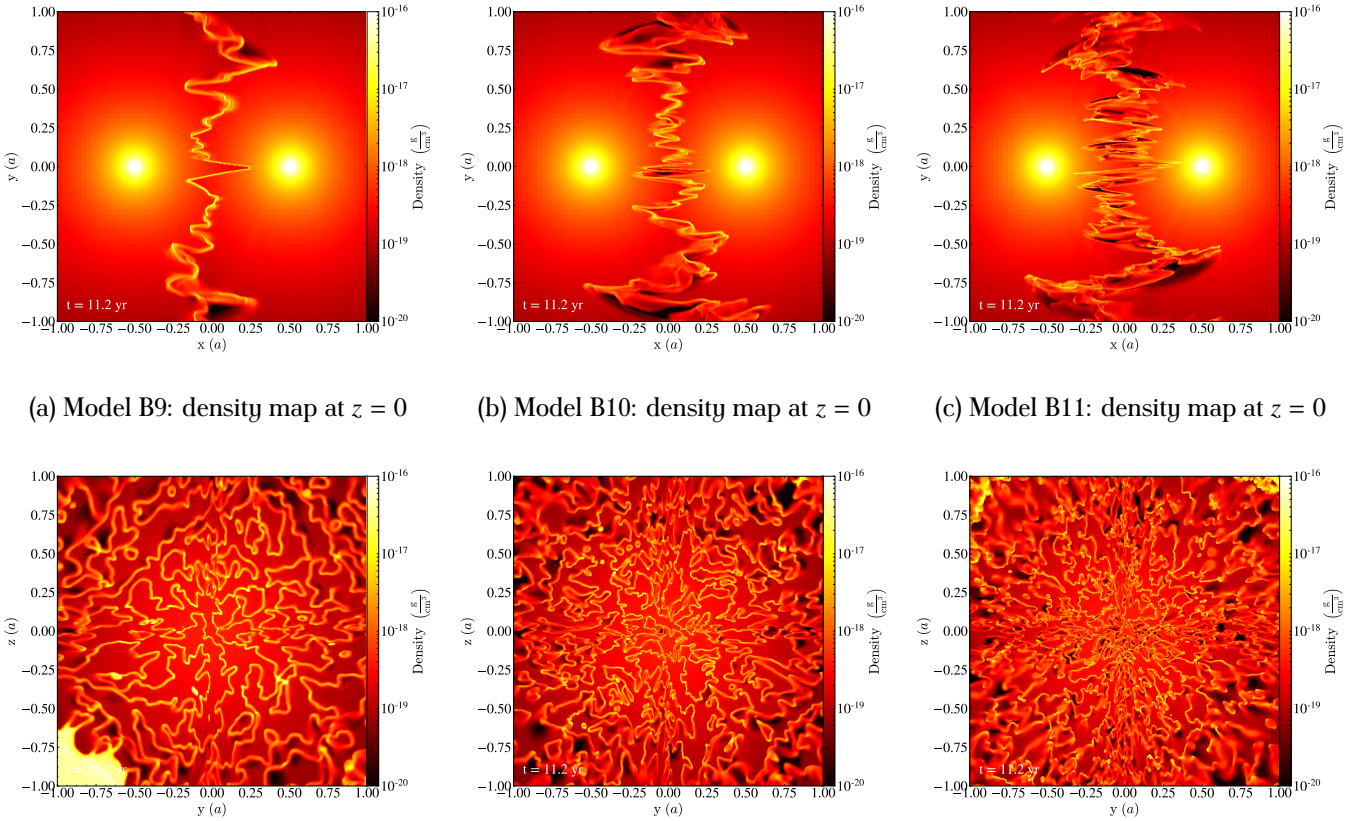

(a) Model B9: density map at $z = 0$

(b) Model B10: density map at $z = 0$

(c) Model B11: density map at $z = 0$

(d) Model B9: density map at $x = 0$

(e) Model B10: density map at $x = 0$

(f) Model B11: density map at $x = 0$

Figure 3.19: Density maps of models B9, B10 and B11 are shown in the left, central and right columns, respectively. The upper row shows maps at $z = 0$ while the lower row does it at $x = 0$. Every map is at simulation time $t = 11.2$ yr. At large scale models look similar, although at smaller scales higher resolution models can resolve shorter modes. The dense feature in the left lower corner of panel (d) corresponds to the wiggles observed away from the apex, which have not been advected away from the domain yet.

The finer structure is very likely due to the excitation of shorter unstable modes, which can be resolved only with high enough resolution. Evidence supporting this idea is related to the time the slab takes to become unstable. It is known that the shorter scale modes of the NTSI grow faster than longer ones (Vishniac, 1994). Therefore, this explains why the instability starts growing at earlier times as the resolution increases, i.e. the slab in B11 becomes unstable faster than B10, and this also applies comparing B10 and B9.

Now, let us analyse the statistical properties of clumps at different resolutions. In order to make a fair comparison between these simulations, we decided to study only clumps above a fixed physical size. To do so, we set the minimum number of cells to define a clump as $N_{\rm cell} = 1, 8, 64$ in runs B9, B10, and B11, respectively. Figure 3.20 shows clump mass and velocity histograms along the upper and lower rows, respectively. Each column represents different resolution models increasing from left to right. The different colour solid lines represent the inner (green) and outer (orange) clumps, and the sum of the two (blue). Firstly, notice that the clump mass histograms change appreciably when changing the resolution. Here, it is important to observe that increasing the numerical resolution the clump mean mass shifts towards lower mass with a difference of 0.4 dex between B9 and B10 as well as comparing B10 and B11. Furthermore, the clump maximum mass is about one order of magnitude different between B9 and B10 but we observe almost no difference comparing B10 and B11. Analysing the clump velocity histograms (see lower panels of Figure 3.20) shows that the distributions to become similar regardless of the resolution. Also, the mean clump speed and the dispersion of the outer clumps is the same. The most important difference is the fast speed tail of the inner clump distribution (green line); it does not span to high speed in the model B9, yet it does in B10 and B11. This means that the velocity dispersion of the inner clumps is smaller. This could be attributed to the fact that inner clumps, and also clumps in general, are more massive in the low resolution run, so it is more difficult for them to reach higher speeds. Meanwhile, at higher resolution the inner clumps that have high speed are typically the least massive ones (see Figure 3.12). Therefore, the fact that inner clumps of model B9 do not reach high speeds is due to the limited spatial resolution. Once more,

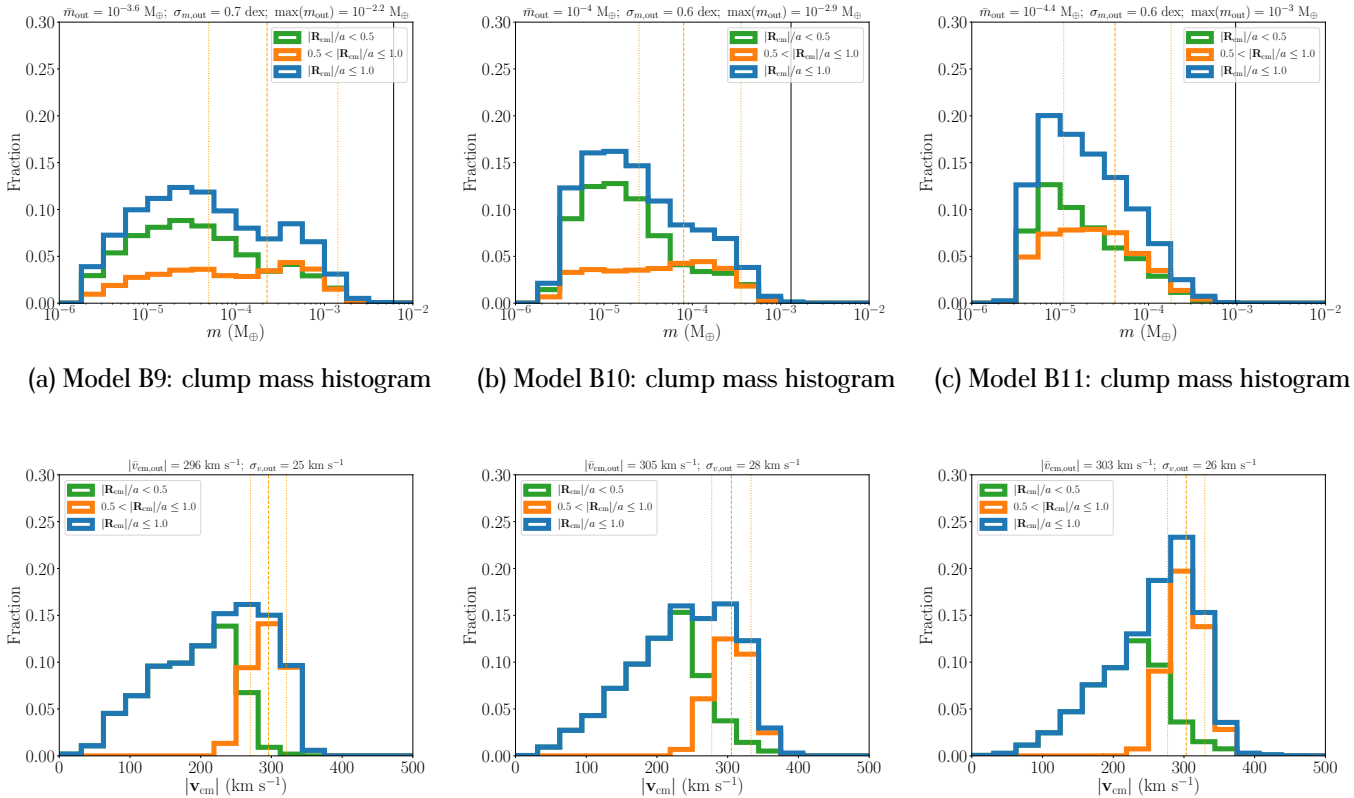

(a) Model B9: clump mass histogram (b) Model B10: clump mass histogram (c) Model B11: clump mass histogram

(d) Model B9: clump velocity histogram (e) Model B10: clump velocity histogram (f) Model B11: clump velocity histogram

Figure 3.20: Histograms of mass and velocity of ejected clumps of models B9, B10, and B11. The upper and lower rows show the mass and velocity histograms, respectively. From left to right, each column contains the analysis of models B9, B10 and B11. In order to make a fair comparison between different resolution models we selected clumps only above a certain physical size.

clumps from models B10 and B11 span the same velocity ranges, although we notice some differences in the shape of the distributions. From this analysis we can conclude that the ranges in mass and velocity covered by the clumps seems to be converging for our standard resolution but the detailed shape of distributions has not. Unfortunately, increasing the resolution of these models is beyond the scope of this work due to the high computational costs.

3.5.3 Implications for the Galactic Centre hydro- and thermodynamic state

As we shown in Calderón et al. (2016) close encounters (< 2000 au) between the WR stars in the Galactic Centre, although not very frequent ($\sim 10^{-3}$ yr^{-1}), can take place. Such encounters, in general, correspond to fairly asymmetric wind collisions. In some cases they have very low η so that the cooling parameter of the weaker wind can become of the order of unity. According to our results, clump formation can take place under these conditions (e.g. model B+10). However, given their low masses ($\lesssim 0.01$ M$_\oplus$) they would be destroyed very rapidly. The fact that they are ejected into a hot, diffuse and dynamic medium makes them susceptible to ablation and, more importantly, to thermal conduction (Burkert et al., 2012). Specifically, for such light clumps they would evaporate in less than 10 years (Calderón et al., 2018). Comparing this timescale with the free-fall timescale of the region, such clumps could be captured by Sgr A* if they were ejected at a distance of $\lesssim 0.004$ pc (0.1 arcsec); however, the WR stars orbits are located at least one order of magnitude further (Paumard et al., 2006). This makes it very unlikely that clumps formed in stellar wind collisions and even in colliding wind binaries, e.g. IRS 16NE, IRS 16SW, E60, have chances of being accreted by the super-massive black hole. Furthermore, these results are an extra piece of evidence against the hypothesis of the dusty G2-like objects (Gillessen et al., 2012) being born in wind collisions (Calderón et al., 2018).

3.6 Conclusions

We present a set of 3D hydrodynamical simulations of stellar wind collisions aiming to characterise the clumps that form as a result of such an interaction. Motivated by the WR stars in the Galactic Centre, we conduct a parameter study of systems of two stars with powerful outflows $\sim 10^{-5}$ $M_\odot$ yr^{-1}, wind terminal speeds of ~500–1500 km s^{-1}, and stellar separations in the range ~20–200 au. We explore models with two identical stellar winds as well as systems with different stellar wind properties. The 3D hydrodynamic evolution of radiative wind collisions confirm the 2D description studied previously (Lamberts, Fromang, and Dubus, 2011). Systems with identical radiative winds create hot slabs of material that cools down very rapidly becoming thinner and denser. The resulting slab is susceptible to the NTSI that quickly manages to shape the whole slab, reaching an approximate stationary state at $t \gtrsim 2\ t_{\rm cross}$. As expected, increasing the radiative efficiency of the stellar winds causes slabs to become unstable quicker. Interestingly, systems whose winds are within the transition between the radiative and adiabatic regimes can also generate unstable slabs. Although initially those systems generate a hot, thick slab, thermal instabilities seem to be excited in the innermost part of the slab, which help to destabilise it allowing thin shell instabilities to grow. However, it can take a significantly longer time for them to reach a stationary state ($t \gtrsim 10\ t_{\rm cross}$). Symmetric models also display an increase in the density contrast with larger Mach numbers of the stellar winds, i.e. with faster stellar winds. This behaviour is caused by the fact that the flow becomes more turbulent.

Asymmetric models show a different behaviour as the wind collisions becomes unstable faster due to the presence of the KHI. The more asymmetric the wind interaction, the faster instabilities are excited and grow. This feature is observed even if only one of the winds is of a radiatively efficient nature. In this case, the cool dense shell and clumps are formed solely of material from the weaker wind while the hot shocked material of the other wind compresses it from the other side of the interaction. Having adiabatic winds with even larger Mach numbers enhances the observed density contrast even more than in the symmetric

models studied.

Overall, the clumps formed in wind interactions through the NTSI have very small masses ($m \lesssim 10^{-2}$ $M_\oplus$). In symmetric models, they are born close to the apex being even lighter ($\sim 10^{-6}$–10^{-5} $M_\oplus$). At this point most of their momentum is parallel to the line connecting both stars, and spans a wide range. As they are moving outwards (away from the apex), they gain mass and the stellar wind ram-pressure accelerates them at the same time. They reach their maximum mass ($\sim 10^{-4}$–10^{-3} $M_\oplus$) while escaping from the system at the point where the advective component of the ram-pressure starts to dominate over the compressive component. At a distance equal to the stellar separation from the apex, the velocity of clumps is about ~60% of the stellar wind speed with a small dispersion. On average, clumps take about $\sim 2\ t_{\rm cross}$ to be ejected once they are formed.

The analysis of clumps in symmetric models confirm the fact that their masses are correlated with the cooling parameter, i.e. the less efficient the cooling in the post shocked material the more massive clumps can be. In asymmetric models, although the mean clump properties are similar when scaled by the wind properties, the range they span is larger. Furthermore, we found that the clump mass distribution close to the apex is approximately the same shape as the one for clumps further away. This might hint to the KHI limiting the growth of the clumps.

Although in agreement with previous analytical estimates, clump masses are found to be significantly smaller (a factor ~1000) than the theoretical upper limit. Having such small masses means it is very unlikely that clumps formed in stellar wind collisions can be accreted by Sgr A*, or have an impact onto the Galactic Centre thermodynamics state, especially considering the hostile environment to which they would be subject to. Yet multiple dusty blobs, likely clumps, are observed to be present close to the powerful WR stars of the IRS 13E cluster (Fritz et al., 2010). If stellar wind collisions cannot generate such massive clouds, is there another mechanism capable of condensing material from the stars? The interaction of multiple stellar winds, or between denser, slower outflows and the ambient medium (e.g. IRS 33E; Martins et al., 2007), are more complex phenomena that are constantly taking place in

the region. These scenarios remain as potential explanations worthy of further investigation, although they require much more computational resources and more physical aspects to incorporate into the models.

Acknowledgments

DC and JC acknowledge the kind hospitality of the Max Planck Institute for Extraterrestrial Physics as well as funding from the Max Planck Society through a "Partner Group" grant. The authors acknowledge support from CONICYT project Basal AFB-170002. DC is supported by CONICYT-PCHA/Doctorado Nacional (2015-21151574). CMPR is supported by FONDECYT grant 3170870. Numerical simulations were run on the HPC systems HYDRA and COBRA of the Max Planck Computing and Data Facility. Data analysis was carried out making use of the PYTHON package YT (Turk et al., 2011).

References

Abdo, A. A. et al. (2010). "Fermi Large Area Telescope Observation of a Gamma-ray Source at the Position of Eta Carinae". In: ApJ 723.1, pp. 649–657. DOI: 10.1088/0004-637X/723/1/649. arXiv: 1008.3235 [astro-ph.HE].

Baganoff, F. K. et al. (2003). "Chandra X-Ray Spectroscopic Imaging of Sagittarius A* and the Central Parsec of the Galaxy". In: ApJ 591.2, pp. 891–915. DOI: 10.1086/375145. arXiv: astro-ph/0102151 [astro-ph].

Burkert, A. et al. (2012). "Physics of the Galactic Center Cloud G2, on Its Way toward the Supermassive Black Hole". In: ApJ 750.1, 58, p. 58. DOI: 10.1088/0004-637X/750/1/58. arXiv: 1201.1414 [astro-ph.GA].

Calderón, D. et al. (2016). "Clump formation through colliding stellar winds in the Galactic Centre". In: MNRAS 455.4, pp. 4388–4398. DOI: 10.1093/mnras/stv2644. arXiv: 1507.07012 [astro-ph.GA].

Calderón, D. et al. (2018). "The Galactic Centre source G2 was unlikely born in any of the known massive binaries". In: MNRAS 478.3, pp. 3494–3505. DOI: 10.1093/mnras/sty1330. arXiv: 1805.05341 [astro-ph.GA].

Crowther, Paul A. and Allan J. Willis (1993). "Observations of the atmospheres and winds of O-stars, LBV's and Wolf-Rayet stars". In: Space Sci. Rev. 66.1-4, pp. 85–103. DOI: 10.1007/BF00771051.

Cuadra, Jorge, Sergei Nayakshin, and Fabrice Martins (2008). "Variable accretion and emission from the stellar winds in the Galactic Centre". In: MNRAS 383.2, pp. 458–466. DOI: 10.1111/j.1365-2966.2007.12573.x. arXiv: 0705.0769 [astro-ph].

Cuadra, Jorge, Sergei Nayakshin, and Q. Daniel Wang (2015). "The role of feedback in accretion on low-luminosity AGN: Sgr A* case study". In: MNRAS 450.1, pp. 277–287. DOI: 10.1093/mnras/stv584. arXiv: 1503.02745 [astro-ph.HE].

Cuadra, Jorge et al. (2005). "Accretion of cool stellar winds on to Sgr A*: another puzzle of the Galactic Centre?" In: MNRAS 360.1, pp. L55–L59. DOI: 10.1111/j.1745-3933.2005.00045.x. arXiv: astro-ph/0502044 [astro-ph].

— (2006). "Galactic Centre stellar winds and Sgr A* accretion". In: MNRAS 366.2, pp. 358–372. DOI: 10.1111/j.1365-2966.2005.09837.x. arXiv: astro-ph/0505382 [astro-ph].

Fritz, T. K. et al. (2010). "GC-IRS13E—A Puzzling Association of Three Early-type Stars". In: ApJ 721.1, pp. 395–411. DOI: 10.1088/0004-637X/721/1/395. arXiv: 1003.1717 [astro-ph.GA].

Genzel, Reinhard, Frank Eisenhauer, and Stefan Gillessen (2010). "The Galactic Center massive black hole and nuclear star cluster". In: *Reviews of Modern Physics* 82.4, pp. 3121–3195. DOI: 10.1103/RevModPhys.82.3121. arXiv: 1006.0064 [astro-ph.GA].

Gillessen, S. et al. (2012). "A gas cloud on its way towards the supermassive black hole at the Galactic Centre". In: Nature 481.7379, pp. 51–54. DOI: 10.1038/nature10652. arXiv: 1112.3264 [astro-ph.GA].

Gillessen, S. et al. (2017). "An Update on Monitoring Stellar Orbits in the Galactic Center". In: ApJ 837.1, 30, p. 30. DOI: 10.3847/1538-4357/aa5c41. arXiv: 1611.09144 [astro-ph.GA].

Hamaguchi, Kenji et al. (2016). "Eta Carinae's Thermal X-Ray Tail Measured with XMM-Newton and NuSTAR". In: ApJ 817.1, 23, p. 23. DOI: 10.3847/0004-637X/817/1/23. arXiv: 1602.01148 [astro-ph.SR].

Hamaguchi, Kenji et al. (2018). "Non-thermal X-rays from colliding wind shock acceleration in the massive binary Eta Carinae". In: *Nature Astronomy* 2, pp. 731–736. DOI: 10.1038/s41550-018-0505-1. arXiv: 1904.09219 [astro-ph.HE].

Hendrix, Tom et al. (2016). "Pinwheels in the sky, with dust: 3D modelling of the Wolf-Rayet 98a environment". In: MNRAS 460.4, pp. 3975–3991. DOI: 10.1093/mnras/stw1289. arXiv: 1605.09239 [astro-ph.SR].

Hobbs, Alexander et al. (2013). "Thermal instabilities in cooling galactic coronae: fuelling star formation in galactic discs". In: MNRAS 434.3, pp. 1849–1868. DOI: 10.1093/mnras/stt977. arXiv: 1207.3814 [astro-ph.GA].

Kee, Nathaniel Dylan, Stanley Owocki, and Asif ud-Doula (2014). "Suppression of X-rays from radiative shocks by their thin-shell instability". In: MNRAS 438.4, pp. 3557–3567. DOI: 10.1093/mnras/stt2475. arXiv: 1401.2063 [astro-ph.SR].

Lamberts, A., S. Fromang, and G. Dubus (2011). "High-resolution numerical simulations of unstable colliding stellar winds". In: MNRAS 418.4, pp. 2618–2629. DOI: 10.1111/j.1365-2966.2011.19653.x. arXiv: 1109.1434 [astro-ph.SR].

Lebedev, M. G. and A. V. Myasnikov (1990). "Interaction of two supersonic radial gas flows". In: *Fluid Dynamics* 25, pp. 629–635.

Lemaster, M. Nicole, James M. Stone, and Thomas A. Gardiner (2007). "Effect of the Coriolis Force on the Hydrodynamics of Colliding-Wind Binaries". In: ApJ 662.1, pp. 582–595. DOI: 10.1086/515431. arXiv: astro-ph/0702425 [astro-ph].

Lützgendorf, N. et al. (2016). "Stellar winds near massive black holes - the case of the S-stars". In: MNRAS 456.4, pp. 3645–3654. DOI: 10.1093/mnras/stv2918. arXiv: 1512.03304 [astro-ph.GA].

Martins, F. et al. (2007). "Stellar and wind properties of massive stars in the central parsec of the Galaxy". In: A&A 468.1, pp. 233–254. DOI: 10.1051/0004-6361:20066688. arXiv: astro-ph/0703211 [astro-ph].

Panagiotou, C. and R. Walter (2018). "The environment of the wind-wind collision region of η Carinae". In: A&A 610, A37, A37. DOI: 10.1051/0004-6361/201731841. arXiv: 1712.01382 [astro-ph.HE].

Parkin, E. R. and E. Gosset (2011). "Investigating the X-ray emission from the massive WR+O binary WR 22 using 3D hydrodynamical models". In: A&A 530, A119, A119. DOI: 10.1051/0004-6361/201016125. arXiv: 1104.2383 [astro-ph.HE].

Paumard, T. et al. (2006). "The Two Young Star Disks in the Central Parsec of the Galaxy: Properties, Dynamics, and Formation". In: ApJ 643.2, pp. 1011–1035. DOI: 10.1086/503273. arXiv: astro-ph/0601268 [astro-ph].

Pittard, J. M. (2009). "3D models of radiatively driven colliding winds in massive O+O star binaries - I. Hydrodynamics". In: MNRAS 396.3, pp. 1743–1763. DOI: 10.1111/j.1365-2966.2009.14857.x. arXiv: 0904.0164 [astro-ph.SR].

Ponti, G. et al. (2010). "Discovery of a Superluminal Fe K Echo at the Galactic Center: The Glorious Past of Sgr A* Preserved by Molecular Clouds". In: ApJ 714.1, pp. 732–747. DOI: 10.1088/0004-637X/714/1/732. arXiv: 1003.2001 [astro-ph.HE].

Puls, Joachim, Jorick S. Vink, and Francisco Najarro (2008). "Mass loss from hot massive stars". In: A&A Rev. 16.3-4, pp. 209–325. DOI: 10.1007/s00159-008-0015-8. arXiv: 0811.0487 [astro-ph].

Ressler, S. M., E. Quataert, and J. M. Stone (2018). "Hydrodynamic simulations of the inner accretion flow of Sagittarius A* fuelled by stellar winds". In: MNRAS 478.3, pp. 3544–3563. DOI: 10.1093/mnras/sty1146. arXiv: 1805.00474 [astro-ph.HE].

Roberts, Shawn R. et al. (2017). "Towards self-consistent modelling of the Sgr A* accretion flow: linking theory and observation". In: MNRAS 466.2, pp. 1477–1490. DOI: 10.1093/mnras/stw2995. arXiv: 1611.00118 [astro-ph.HE].

Stevens, Ian R., John M. Blondin, and A. M. T. Pollock (1992). "Colliding Winds from Early-Type Stars in Binary Systems". In: ApJ 386, p. 265. DOI: 10.1086/171013.

Sunyaev, R. and E. Churazov (1998). "Equivalent width, shape and proper motion of the iron fluorescent line emission from molecular clouds as an indicator of the illuminating source X-ray flux history". In: MNRAS 297.4, pp. 1279–1291. DOI: 10.1046/j.1365-8711.1998.01684.x. arXiv: astro-ph/9805038 [astro-ph].

Sunyaev, R. A., M. Markevitch, and M. Pavlinsky (1993). "The Center of the Galaxy in the Recent Past: A View from GRANAT". In: ApJ 407, p. 606. DOI: 10.1086/172542.

Teyssier, R. (2002). "Cosmological hydrodynamics with adaptive mesh refinement. A new high resolution code called RAMSES". In: A&A 385, pp. 337–364. DOI: 10.1051/0004-6361:20011817. arXiv: astro-ph/0111367 [astro-ph].

Turk, Matthew J. et al. (2011). "yt: A Multi-code Analysis Toolkit for Astrophysical Simulation Data". In: ApJS 192.1, 9, p. 9. DOI: 10.1088/0067-0049/192/1/9. arXiv: 1011.3514 [astro-ph.IM].

van Marle, A. J. and R. Keppens (2012). "Multi-dimensional models of circumstellar shells around evolved massive stars". In: A&A 547, A3, A3. DOI: 10.1051/0004-6361/201218957. arXiv: 1209.4496 [astro-ph.SR].

van Marle, A. J., R. Keppens, and Z. Meliani (2011). "Thin shell morphology in the circumstellar medium of massive binaries". In: A&A 527, A3, A3. DOI: 10.1051/0004-6361/201015517. arXiv: 1011.1734 [astro-ph.GA].

Vink, Jorick S. and Tim J. Harries (2017). "Wolf-Rayet spin at low metallicity and its implication for black hole formation channels". In: A&A 603, A120, A120. DOI: 10.1051/0004-6361/201730503. arXiv: 1703.09857 [astro-ph.SR].

Vishniac, E. T. (1983). "The dynamic and gravitational instabilities of spherical shocks". In: ApJ 274, pp. 152–167. DOI: 10.1086/161433.

Vishniac, Ethan T. (1994). "Nonlinear instabilities in shock-bounded slabs". In: ApJ 428.1, pp. 186–208. DOI: 10.1086/174231. arXiv: astro-ph/9306025 [astro-ph].

Wang, Q. D. et al. (2013). "Dissecting X-ray-Emitting Gas Around the Center of Our Galaxy". In: *Science* 341.6149, pp. 981–983. DOI: 10.1126/science.1240755. arXiv: 1307.5845 [astro-ph.HE].

Yelda, S. et al. (2014). "Properties of the Remnant Clockwise Disk of Young Stars in the Galactic Center". In: ApJ 783.2, 131, p. 131. DOI: 10.1088/0004-637X/783/2/131. arXiv: 1401.7354 [astro-ph.GA].

Appendix 3.A Clump finder algorithm

Here we describe the algorithm we used to identify clumps in our hydrodynamic models. The method was inspired by the approach used in the PYTHON package ASTRODENDRO (http://www.dendrograms.org/). The input parameters, besides a RAMSES output file, are N_σ and $N_{\rm cell}$, where the former defines the density threshold $\rho_{tr} = \bar{\rho} + N_\sigma \times \sigma_\rho$ (being $\bar{\rho}$ the mean density and σ_ρ the density dispersion), and the latter the minimum number of cells to identify a clump.

Algorithm 1 Clumpfinder

procedure FIND_CLUMPS(snapshot,N_σ,$N_{\rm cell}$)
  Read RAMSES snapshot file
  Consider only cells satisfying $\rho \geq \bar{\rho} + N_\sigma \times \sigma_\rho$
  Extract x, y, z, ρ from remaining cells
  Find physically connected regions: structures
  for each structure **do**
    Define a clump per local density maximum
    Assign such cell to each clump
    Assign neighbour cells to corresponding clumps
    while N(unassigned cells)> 0 **do**
      Add neighbour cells recursively to each clump
      as long as the density slope towards the
      maximum is positive or zero
    for each clump in structure **do**
      if N(cells in clump) > $N_{\rm cell}$ **then**
        Calculate clump physical properties:
        $[m, x_{\rm cm}, y_{\rm cm}, z_{\rm cm}, v_{x,\rm cm}, v_{y,\rm cm}, v_{z,\rm cm}]$
        Write clump properties into output file
    Flag structure as analysed

4

Stellar winds pump the heart of the Milky Way

The central super-massive black hole of the Milky Way, Sgr A*, accretes at a very low rate making it a very underluminous galactic nucleus. Despite the tens of Wolf-Rayet stars present within the inner parsec supplying $\sim 10^{-3}$ $M_\odot$ yr^{-1} in stellar winds, only a negligible fraction of this material ($< 10^{-4}$) ends up being accreted onto Sgr A*. The recent discovery of cold gas ($\sim 10^4$ K) in its vicinity raised questions about how such material could settle in the hostile ($\sim 10^7$ K) environment near Sgr A*. In this work we show that the system of mass-losing stars blowing winds can naturally account for both the hot, inefficient accretion flow, as well as the formation of a cold disc-like structure. We run hydrodynamical simulations using the grid-based code Ramses starting as early in the past as possible to observe the state of the system at the present time. Our results show that the system reaches a quasi-steady state in about ~500 yr with material being captured at a rate of $\sim 10^{-6}$ $M_\odot$ yr^{-1} at scales of $\sim 10^{-4}$ pc, consistent with the observations and previous models. However, on longer timescales ($\gtrsim$ 3000 yr) the material accumulates close to the black hole in the form of a disc. Considering the duration of the Wolf-Rayet phase ($\sim 10^5$ yr), we conclude that this scenario likely has already happened, and could be responsible for the more active past of Sgr A*, and/or its current outflow. We argue that the hypothesis of the mass-losing stars being the main regulator of the activity of the black hole deserves further consideration.

D. Calderón, J. Cuadra, M. Schartmann, A. Burkert, C. M. P. Russell, ApJL, **Submitted** *(2019), arXiv:1910.06976*

4.1 Introduction

Murchikova et al. (2019) recently detected cold gas ($\sim 10^4$ K) at short distances ($\sim 10^{-3}$ pc) from the Milky Way central super-massive black hole (SMBH), Sgr A*. The observation of a relatively wide ($\sim$2200 km s^{-1}) double-peaked H30α recombination line suggests the presence of a disc-like structure made out of such material. On the other hand, *Chandra* observations reveal that the innermost parsec of Sgr A* is filled with hot ($\sim 10^7$ K) and diffuse plasma with a mean density of $\sim$10 cm^{-3} (Baganoff et al., 2003; Wang et al., 2013; Russell, Wang, and Cuadra, 2017). This material is constantly being supplied by the powerful outflows of the tens of Wolf-Rayet (WR) stars inhabiting the region at 1–10 arcsec from Sgr A* (Paumard et al., 2006; Yelda et al., 2014)[1]. Additionally, the G2 object (Gillessen et al., 2012), as well as the bright knots in the IRS 13E cluster (Fritz et al., 2010), correspond to cold sources in this region that are observed in the Br-γ recombination line. How such cold gas structure could form in such a hot and hostile environment remains unexplained.

In total, the mass flow rate supplied by the WR stars is estimated to be $\sim 10^{-3}$ M$_\odot$ yr^{-1} (Martins et al., 2007). However, the detection of polarised emission at sub-mm wavelengths has constrained the accretion rate at hundreds of Schwarzschild radii ($\sim 10^{-5}$ pc) to be many orders of magnitude smaller (10^{-9}–10^{-7} M$_\odot$ yr^{-1}; Marrone et al., 2006; Marrone et al., 2007). Although this is a very low accretion rate, it could have been different in the past. Since the early 90s, many authors have argued that Sgr A* was more active in the past, specifically about hundreds of years ago (Sunyaev, Markevitch, and Pavlinsky, 1993; Koyama et al., 1996; Ponti et al., 2010), and even as little as decades ago (Muno et al., 2007). Such hypotheses rely on X-ray light echoes observations of molecular clouds located at hundreds of parsecs from the SMBH. Based on long-exposure X-ray observations of the inner parsec, Wang et al. (2013) ruled out a Bondi (no-outflow) solution for the plasma distribution in the region. Instead, the distribution showed agreement with an outflow solution, supporting the past

[1]Given the mass and distance of Sgr A* (4.3×10^6 M$_\odot$ and 8.3 kpc), 1 arcsec $\approx$ 0.04 pc $\approx 10^5$ Schwarzschild radii.

activity hypothesis.

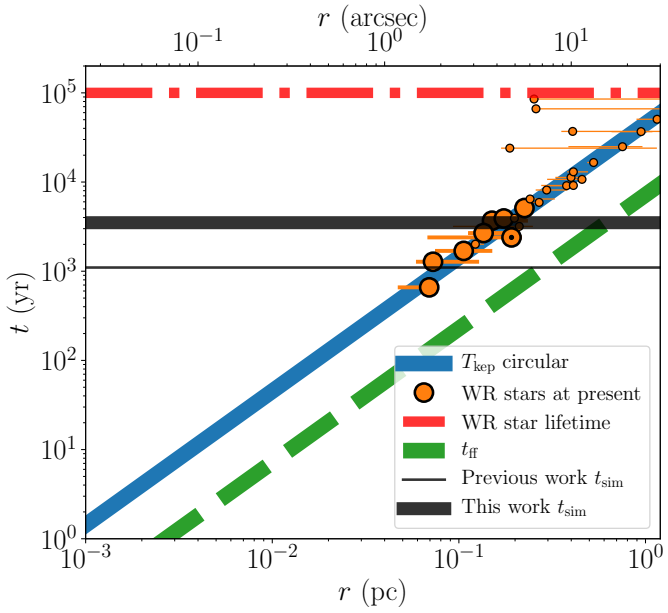

Figure 4.1: Timescales as a function of distance from Sgr A*. The solid blue line represents the circular Keplerian orbital period. The dashed green line shows the free-fall timescale. Orange circles denote the orbital periods of individual WR stars, with the horizontal orange segments indicating the separation change to Sgr A* due to their orbital eccentricity. Smaller symbols represent stars with minimum eccentricity orbits. The circle with a black dot in its centre represents the star IRS 33E. The horizontal dash-dotted red line marks the WR phase duration. The horizontal solid thin and thick black lines indicate the simulation time of previous and current studies, respectively.

Currently, it is hard to conceive this system with a steady-state Bondi model as the material is not being effectively accreted. Thus, it should be either accumulating at the center or expelled outwards as an outflow. Numerical hydrodynamics models of the system of WR stars have been able to reproduce the mass inflow rate at the Bondi radius ($\sim 10^{-6}$ $M_\odot$ yr^{-1}; Cuadra, Nayakshin, and Martins, 2008; Cuadra, Nayakshin, and Wang, 2015; Russell, Wang, and Cuadra, 2017), and even deeper relatively well (Ressler, Quataert, and Stone, 2018). These studies simulated the system starting 1100 yr in the past and evolved it to reach a

quasi-steady state at the present. Nevertheless, this timescale only manages to capture a single complete orbital period of the innermost WR star (see Figure 4.1). Furthermore, it is approximately two orders of magnitude smaller than the typical duration of the WR phase in massive stars of 10–25 $M_\odot$ (~0.1 Myr; Crowther, 2007, for a review). In reality, the WR stellar system will exist for even longer as the stars do not necessarily evolve coordinately in and off the WR phase. Thus, we should not draw strong conclusions of the long-term state of the system based on previous studies.

In this letter, we investigate, for the first time, the evolution of the system of mass-losing stars orbiting Sgr A* for longer timescales. Although we could not afford to simulate the system for timescales comparable to the typical duration of the WR phase (~0.1 Myr), we improve the simulation time of previous works by a factor ~four. This work is presented as follows: Section 4.2 describes the numerical setup, initial conditions and assumptions. Section 4.3 presents the simulation and characterises each phase of the evolution. Finally, in Section 4.4 we discuss implications and present the conclusions.

4.2 Numerical setup

We developed 3D hydrodynamics simulations making use of the adaptive-mesh refinement (AMR) grid-based code RAMSES (Teyssier, 2002). The code uses a second-order Godunov method to solve the equations of hydrodynamics. We consider an adiabatic equation of state, plus optically thin radiative cooling with $Z = 3Z_\odot$, where $Z_\odot$ is the Solar mass fraction in metals (Calderón et al., 2019). We use an exact Riemann solver together with a MonCen slope limiter (e.g. Toro, 2009). The simulation setup considers the system of WR stars blowing stellar winds into the medium while they move under the influence of the gravitational potential of Sgr A* whose mass is 4.3×10^6 $M_\odot$ (Gillessen et al., 2017). For simplicity, we assume that the motion of the stars is completely determined by the gravity of the SMBH. The stars describe Keplerian orbits, which have been constrained through decade-long observational monitoring (Paumard et al., 2006; Gillessen et al., 2017). For the stars whose

orbits have not been completely determined, we used the most likely trajectories expected for the members of the “clockwise disc" (Beloborodov et al., 2006), while the rest were calculated through minimizing their eccentricity (Cuadra, Nayakshin, and Martins, 2008). The stellar wind generation is simulated following the approach of Lemaster, Stone, and Gardiner (2007), and also used in Calderón et al. (2019). The properties of the stellar winds were taken from spectroscopic studies (Martins et al., 2007; Cuadra, Nayakshin, and Martins, 2008), and are shown in Table 4.1 in Appendix 4.A. In order to avoid artificial accumulation of material close to the black hole we set an open boundary of radius $2\sqrt{3}\Delta x$, where Δx is the size of the smallest cell. This sphere in the domain is reset after each time step to low density at rest and low pressure (Ressler, Quataert, and Stone, 2018). The domain of the simulation is a cubic box of side length 1.6 pc (~40 arcsec) with outflow boundary conditions (zero gradients). The coarse resolution corresponds to 64^3 cells, plus four extra refinement levels ($\Delta x \approx 1.6 \times 10^{-3}$ pc). Instead, the stellar wind generation regions allow five extra refinement levels ($\Delta x \approx 7.8 \times 10^{-4}$ pc), while the vicinity of the inner boundary allows eight extra refinement levels ($\Delta x \approx 9.8 \times 10^{-5}$ pc). The initial position and velocity of the WR stars are determined extrapolating the state vectors to the past, so that the simulation evolves the system up to the present epoch (Cuadra, Nayakshin, and Martins, 2008; Cuadra, Nayakshin, and Wang, 2015; Ressler, Quataert, and Stone, 2018). Most stars have periods of the order of $\sim 10^4$ yr and orbit around Sgr A* at a distance of ~0.3 pc (see Figure 4.1). Although at such distances the free-fall timescale (dashed green line) is of the order of hundreds of year, it is not easy for the stellar wind material to shed its angular momentum, so it corresponds to a lower limit of the actual infalling timescale.

In this work, the simulation starts from 3500 yr in the past in order to study whether it is possible for the system to reach, and maintain steady state or not[2]. As a control sample we run a model starting 1100 yr in the past, similar to previous works in the literature (Cuadra, Nayakshin, and Martins, 2008; Cuadra, Nayakshin, and Wang, 2015; Ressler, Quataert, and

[2]Ideally, we would like to start the simulation as early as possible but this incurs a very high computational cost: 3500 yr equates to ~100,000 cpu hours.

Stone, 2018). The domain is initialised at very low density $\rho_{\rm ISM} = 10^{-24}$ g cm^{-3} at rest $\mathbf{u} = \mathbf{0}$, and low pressure $P_{\rm ISM} = \rho_{\rm ISM} c_{\rm s,f}^2 \gamma^{-1}$, where $c_{\rm s,f} = 10$ km s^{-1} is the sound speed of the temperature floor ($T \approx 10^4$ K), and γ is the adiabatic index which is set to 5/3 for an adiabatic gas. This latter value was chosen, assuming that the strong ultraviolet radiation field of the young massive stars keeps the environment at such temperature.

4.3 Hydrodynamics: evolution phases

Figure 4.2 shows density maps illustrating the time evolution of the simulation. Each map corresponds to a density projection of the full domain along the z-axis, which is parallel to the line-of-sight, weighted by density (i.e. $\int \rho^2 dz / \int \rho dz$)[3]. The horizontal and vertical axes are parallel to right ascension and declination, respectively. Panel a) shows the initial condition of the simulation at $t = -3500$ yr. Once the simulation starts, each star blows a wind, which develops a shock that at some point ends up colliding with the others (panel b). Such collisions create dense ($\sim 10^{-22}$ g cm^{-3}), hot material ($\sim 10^7$ K) that fills the entire domain relatively quickly ($\sim$500 yr). Notice how complex structures develop in the gas, e.g. the interaction of stellar winds, instabilities, dense clumps, and bow shocks forming due to the motion of the stars through the medium. In panel c) the system has already attained what appears to be a quasi-steady state like in previous works in which the simulations end after a time comparable to the evolution time of panel d) (Cuadra, Nayakshin, and Martins, 2008; Ressler, Quataert, and Stone, 2018). However, in panel g) it is possible to observe an accumulation of material at the center of the domain. Visually, this material seems to settle into a disc-like structure around Sgr A*, which is confirmed analyzing the central region in detail (see panels g and h). This material mainly arises from the disruption of the strong bow shock generated by the star IRS 33E (panel f). Based on the appearance of the system we divide its evolution in three phases: the transient, quasi-steady, and disc phases.

[3]This quantity helps to highlight the dense gas, which corresponds to the cold material which is most likely to contribute to the disc formation and the most refined regions of the domain.

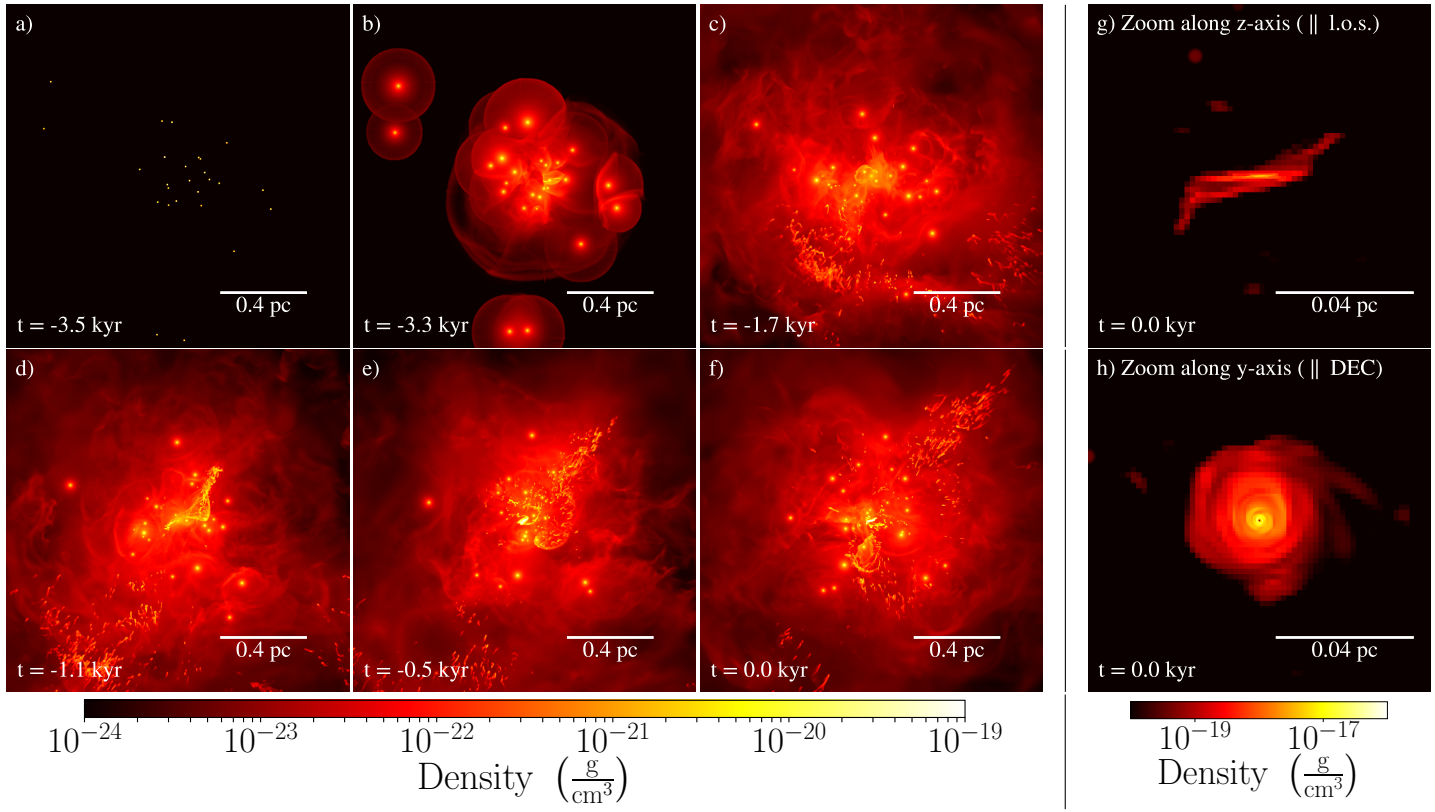

Figure 4.2: Complete evolution of the mass-losing stars orbiting Sgr A*. The panels a)-f) show projected density maps along the z-axis (parallel to the line-of-sight) weighted by density. The horizontal and vertical axes are parallel to right ascension and declination, respectively. Each panel shows the complete simulation domain at different simulation times. Panels g) and f) are zoomed density projection maps at $t = 0$ along the z- and y-axes, respectively, showing the disc-like structure around Sgr A*.

Figure 4.3 shows the mass flow rate across a sphere of radius $\sim 5 \times 10^{-4}$ pc (1.25×10^{-2} arcsec) as a function of time, highlighting the transition between phases. This length scale is about two orders of magnitude smaller than the radius of the disc. In the transient phase the mass inflow rate increases up to $\sim 10^{-6}$ $M_\odot$ yr^{-1} roughly at $t \approx -3000$ yr. Then, in the quasi-steady phase the net mass flow rate $\dot{M}_{\rm net}$ is variable but permanently inflowing and around the same order of magnitude. At $t \approx -800$ yr the system enters into the disc phase, whereby the formation and presence of the disc produces significant changes in both the inflow and outflow mass flow rates. In general, the net flow remains variable, but now its amplitude is about one order of magnitude larger due to the enhancement of the inflow and outflow rates.

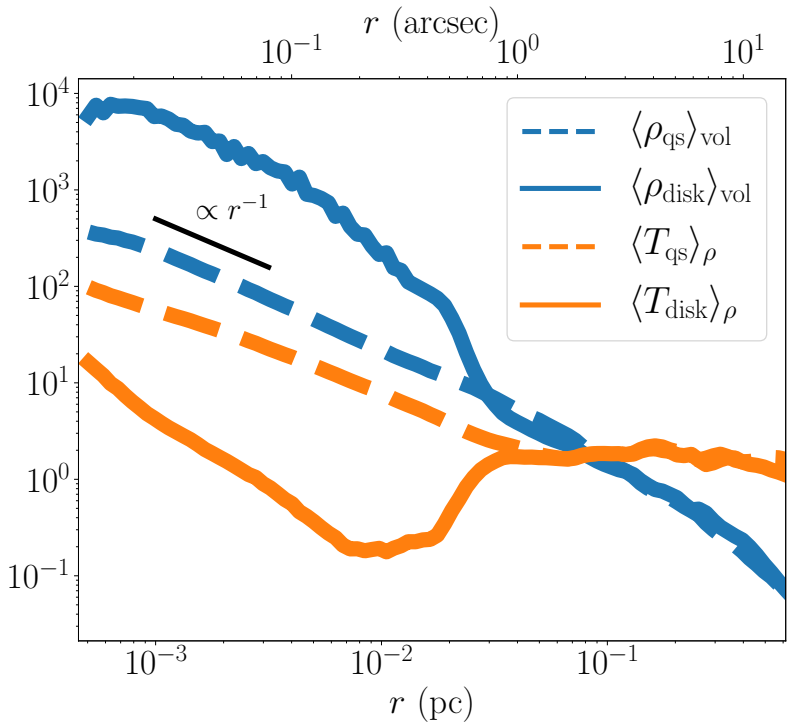

Figure 4.4: Density (blue lines) and temperature (orange lines) radial profiles in units of 10^{-22} g cm^{-3} and 10^7 K, respectively. The subscripts “qs" and “disc" refer to time-averaged quantities during the quasi-steady state (dashed lines) and the disc phase (solid lines), respectively.

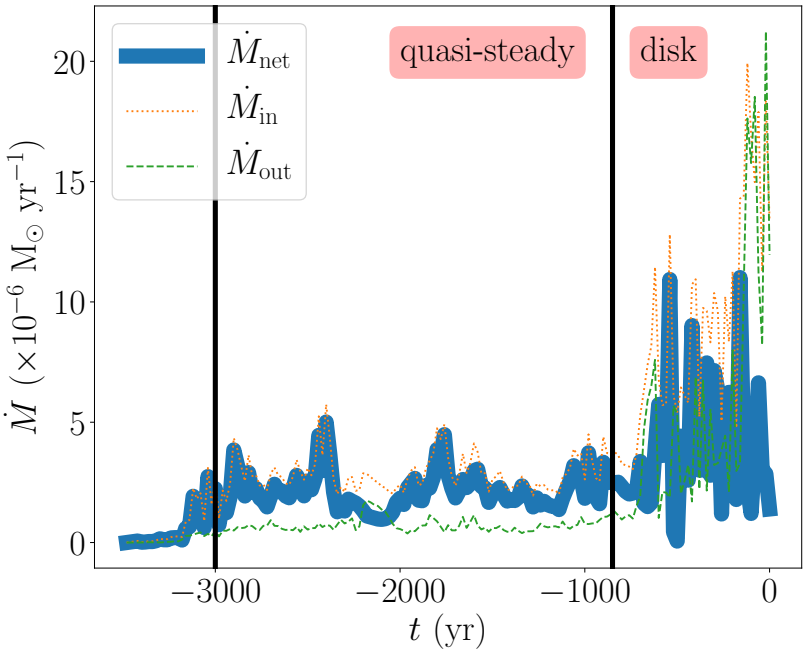

Figure 4.3: Mass flow rate across a sphere of radius 5×10^{-4} pc (1.25×10^{-2} arcsec). The absolute value of the net mass flow rate is shown by the solid blue line. The mass inflow and outflow rates are represented by the dotted orange and dashed green lines, respectively. The vertical solid black lines (at $t \approx -3000$ yr and $t \approx -800$ yr) divide the evolution into the transient, quasi-steady, and disc phases.

Figure 4.4 shows the time-averaged density (blue lines) and temperature (orange lines) radial profiles. The averages were calculated over the quasi-steady (dashed lines) and the disc (solid lines) phases. Notice that in the quasi-steady phase both profiles decay with r^{-1} in the innermost region ($r \lesssim 0.03$ pc), resembling the simulation by Ressler, Quataert, and Stone (2018). Although not shown here, the control model (started at $t = -1100$ yr) displays the same behaviour at the present time. In the disc phase, the profiles deviate significantly from their quasi-steady phase shapes. The disc formation increases the density by about an order of magnitude, which extends up to ~0.01 pc from Sgr A*. On the contrary, the temperature profile decreases by an order of magnitude but, at the same time, becomes slightly steeper.

Analyzing the disc structure at the end of the simulation, we observe that the disc has a mass of $\sim 5 \times 10^{-3}$ $M_\odot$, with a temperature of $\sim 10^4$ K.

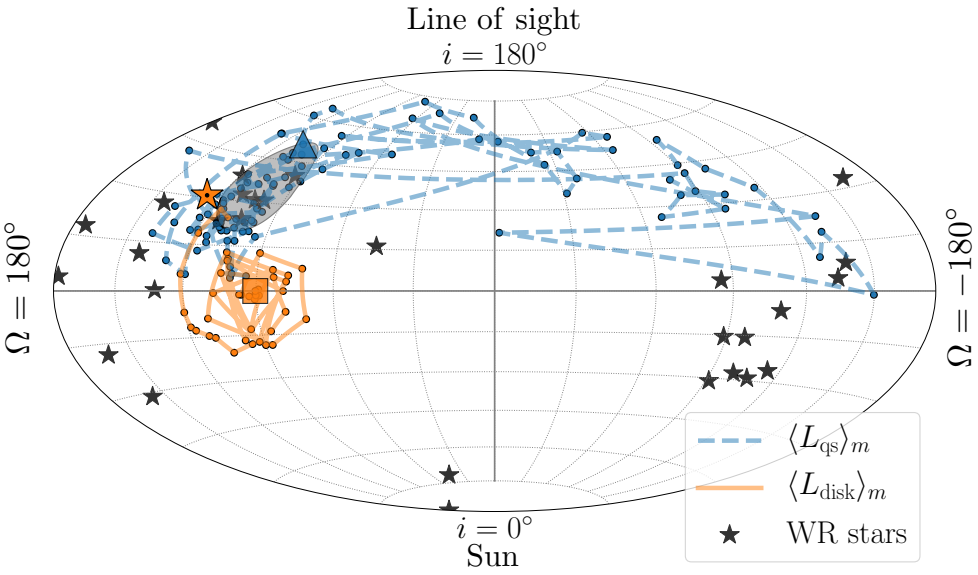

Figure 4.5: Orientation of the angular of the angular momentum of the gas enclosed in a sphere of radius 0.01 pc (0.25 arcsec), and the WR stars'. The vertical dimension represents inclination i, while the horizontal dimensions stand for the longitude of the ascending node Ω. Thus, a face-on star orbiting clockwise on the sky would be at the north pole of the graph. The dashed blue and solid orange lines represent the quasi-steady and disc phases, respectively. Each dot corresponds to the analysis of a single snapshot. The triangle and square show the initial and final state, respectively. The black stars represent the angular momentum direction of the WR stars, highlighting IRS 33E as an orange star with a black dot, instead. The grey shaded region corresponds to the direction of the clockwise disc at $(104°, 126°)$ with a thickness of 16° (Yelda et al., 2014).

Figure 4.5 is a Hammer projection as seen from the Sgr A* location that shows the evolution of the direction of the averaged angular momentum of the gas enclosed in a sphere of radius 0.01 pc (0.25 arcsec) in the quasi-steady (dashed blue line), and disc (solid orange

line) phases. The angles Ω and i correspond to the longitude of the ascending node and inclination, respectively. The earliest time is represented with a triangle marker, while the latest with square marker. As a reference, we include the angular momentum direction of the WR stars (black stars), as well as of the stellar clockwise disc at $\Omega = 104°$ and $i = 126°$ (Yelda et al., 2014). Notice that in the quasi-steady phase the angular momentum direction is highly variable due to the stochastic accretion of material coming from different stars that have a close passage from Sgr A*. However, most of the time the angular momentum direction is consistent with the stars, whose orbits are located near the clockwise disc. This is expected given that these stars have relatively slower winds (~600 km s^{-1}) and orbit closer to the black hole ($\lesssim$ 0.3 pc), such that their wind angular momentum is smaller (Cuadra, Nayakshin, and Martins, 2008; Ressler, Quataert, and Stone, 2018). In the disc phase, initially the angular momentum of the gas is aligned with the stellar disc, and more specifically with IRS 33E, but ultimately precesses around $(\Omega, i) \approx (90°, 0°)$. Notice that this precession could be an undesired effect due to the Cartesian grid. We ran the model for an extra 1000 yr into the future and found that the disc is not destroyed, but instead becomes slightly more massive and larger.

4.4 Discussion

We have shown that, if modeled for at least ~3000 yr, the natural outcome of the evolution of the WR stellar system is a disc-like structure around Sgr A*. The reason is related to the star that supplies the bulk of the material to create such a disc, IRS 33E. Although its mass loss rate is average for a WR star (~1.6×10^{-5} $M_\odot$ yr^{-1}), its wind speed is the slowest among all the stars (450 km s^{-1}; Martins et al., 2007). Thus, the ram pressure of its wind is weak, which forces it to be denser at the stagnation point. As a result, the shocked material radiates most of its thermal energy almost instantaneously (see Section 4.1 in Calderón et al., 2016, for a discussion). This can be seen in the form of a dense, cold bow shock in front of the star while orbiting around Sgr A* (see panel d of Figure 4.2). Figure 4.1 shows that the pericenter

and apocenter distances of the star are 0.069 pc and 0.213 pc from the SMBH, respectively. Therefore, the star oscillates between the regimes where the net mass flow to Sgr A* is ~0 and where the outflow dominates (see Figure 12 of Ressler, Quataert, and Stone, 2018). In this scenario, the star feeds the nucleus during every pericenter passage. As its orbital period is ~2000 yr (see Figure 4.1), it is necessary to model the system for at least a couple of passages to accumulate enough material to form a disc.

Nonetheless, there are a couple of caveats we have to bear in mind when interpreting this result. High-resolution simulations of idealised stellar wind collisions have shown that the dense clumps formed are neither massive nor large ($\lesssim 10^{-3}$ $M_\oplus$; Calderón et al., 2019). The parameters of such models were largely motivated by the WR stars in the Galactic Center. In principle, this would suggest that the clumpy structure observed in the larger-scale simulation presented here might not be resolved, being smaller and less massive in reality. That being said, it is not straightforward to extrapolate the earlier result to our current configuration, as the mechanism creating clumps here is different. Being so, the disruption of a dense stellar wind bow shock in this environment is a promising channel for clump formation, and possibly G2-like objects (Burkert et al., 2012), unlike *colliding* winds (Calderón et al., 2016; Calderón et al., 2018; Calderón et al., 2019).

In order to check potential numerical effects on the result we ran a couple of extra tests. Firstly, we used a MinMod flux limiter, which resulted in the same observed behavior, or even better as the disc did not precess and remained aligned with the clockwise disc. Nevertheless, one of the caveats with this approach is that the winds are not spherically symmetric for reasonable computational costs. Secondly, we decreased the density threshold of the refinement criterion, which results in a more uniform grid. The same behavior was observed but the disc formed slightly later.

Overall, the accumulation of material around Sgr A* takes place on timescales of thousands of years, which leads to an enhancement in both the mass inflow and outflow rates (see Figure 4.3). Despite the higher accretion, once the disc forms, Sgr A* is still in the so-called radiatively inefficient accretion flow (RIAF) regime. In this context, as the material is

very hot, it can overheat and then eject a big fraction of mass and energy in the form of a strong outflow (Blandford and Begelman, 1999; Begelman, 2012). The disc seen in the simulation could then have produced the inferred larger luminosity for Sgr A* (Ponti et al., 2010), and/or triggered the reported outflow (Wang et al., 2013; Do et al., 2019). In that case, it is not clear whether the disc still exists or if it was destroyed by such an outflow. But the cold gas reported by Murchikova et al. (2019), if confirmed as a disc, could correspond to the one from our models. In fact, in order to match the H30α and Br-γ observational constraints, we require an amplification factor of ~ 30, consistent with the masing factor ~ 80 reported by Murchikova et al. (2019). However, considering the expected interaction of G2 with this disc, the density we find is an order of magnitude higher than the one derived by Gillessen et al. (2019) from the cloud slow-down.

To conclude, we speculatively propose that the stellar winds alone can be responsible for much of the phenomenology observed and/or inferred in the central arcsecond during the last millenium: the variable accretion and luminosity, a cold disc, and an outflow. If so, there is no need to invoke "external" factors such as infalling gas from Sgr A West (a.k.a., the *minispiral*), a tidal disruption event and/or a supernova.

Acknowledgments

DC and JC acknowledge the kind hospitality of the Max Planck Institute for Extraterrestrial Physics as well as funding from the Max Planck Society through a "Partner Group" grant. We thank F. E. Bauer and J. Dexter for useful discussions and suggestions for improving this work. The authors acknowledge support from CONICYT project Basal AFB-170002. DC is supported by CONICYT-PCHA/Doctorado Nacional (2015-21151574). CMPR is supported by FONDECYT grant 3170870. Numerical simulations were run on the high-performance computing system COBRA of the Max Planck Computing and Data Facility. Data analysis was carried out making use of the PYTHON package YT (Turk et al., 2011).

References

Baganoff, F. K. et al. (2003). "Chandra X-Ray Spectroscopic Imaging of Sagittarius A* and the Central Parsec of the Galaxy". In: ApJ 591.2, pp. 891–915. DOI: 10.1086/375145. arXiv: astro-ph/0102151 [astro-ph].

Begelman, Mitchell C. (2012). "Radiatively inefficient accretion: breezes, winds and hyper-accretion". In: MNRAS 420.4, pp. 2912–2923. DOI: 10.1111/j.1365-2966.2011.20071.x. arXiv: 1110.5356 [astro-ph.HE].

Beloborodov, Andrei M. et al. (2006). "Clockwise Stellar Disk and the Dark Mass in the Galactic Center". In: ApJ 648.1, pp. 405–410. DOI: 10.1086/504279. arXiv: astro-ph/0601273 [astro-ph].

Blandford, Roger D. and Mitchell C. Begelman (1999). "On the fate of gas accreting at a low rate on to a black hole". In: MNRAS 303.1, pp. L1–L5. DOI: 10.1046/j.1365-8711.1999.02358.x. arXiv: astro-ph/9809083 [astro-ph].

Burkert, A. et al. (2012). "Physics of the Galactic Center Cloud G2, on Its Way toward the Supermassive Black Hole". In: ApJ 750.1, 58, p. 58. DOI: 10.1088/0004-637X/750/1/58. arXiv: 1201.1414 [astro-ph.GA].

Calderón, D. et al. (2016). "Clump formation through colliding stellar winds in the Galactic Centre". In: MNRAS 455.4, pp. 4388–4398. DOI: 10.1093/mnras/stv2644. arXiv: 1507.07012 [astro-ph.GA].

Calderón, D. et al. (2018). "The Galactic Centre source G2 was unlikely born in any of the known massive binaries". In: MNRAS 478.3, pp. 3494–3505. DOI: 10.1093/mnras/sty1330. arXiv: 1805.05341 [astro-ph.GA].

Calderón, Diego et al. (2019). "3D simulations of clump formation in stellar wind collisions". In: *arXiv e-prints*, arXiv:1906.04181, arXiv:1906.04181. arXiv: 1906.04181 [astro-ph.GA].

Crowther, Paul A. (2007). "Physical Properties of Wolf-Rayet Stars". In: ARA&A 45.1, pp. 177–219. DOI: 10.1146/annurev.astro.45.051806.110615. arXiv: astro-ph/0610356 [astro-ph].

Cuadra, Jorge, Sergei Nayakshin, and Fabrice Martins (2008). "Variable accretion and emission from the stellar winds in the Galactic Centre". In: MNRAS 383.2, pp. 458–466. DOI: 10.1111/j.1365-2966.2007.12573.x. arXiv: 0705.0769 [astro-ph].

Cuadra, Jorge, Sergei Nayakshin, and Q. Daniel Wang (2015). "The role of feedback in accretion on low-luminosity AGN: Sgr A* case study". In: MNRAS 450.1, pp. 277–287. DOI: 10.1093/mnras/stv584. arXiv: 1503.02745 [astro-ph.HE].

Do, Tuan et al. (2019). "Unprecedented Near-infrared Brightness and Variability of Sgr A*". In: ApJ 882.2, L27, p. L27. DOI: 10.3847/2041-8213/ab38c3. arXiv: 1908.01777 [astro-ph.GA].

Fritz, T. K. et al. (2010). "GC-IRS13E—A Puzzling Association of Three Early-type Stars". In: ApJ 721.1, pp. 395–411. DOI: 10.1088/0004-637X/721/1/395. arXiv: 1003.1717 [astro-ph.GA].

Gillessen, S. et al. (2012). "A gas cloud on its way towards the supermassive black hole at the Galactic Centre". In: Nature 481.7379, pp. 51–54. DOI: 10.1038/nature10652. arXiv: 1112.3264 [astro-ph.GA].

Gillessen, S. et al. (2017). "An Update on Monitoring Stellar Orbits in the Galactic Center". In: ApJ 837.1, 30, p. 30. DOI: 10.3847/1538-4357/aa5c41. arXiv: 1611.09144 [astro-ph.GA].

Gillessen, S. et al. (2019). "Detection of a Drag Force in G2's Orbit: Measuring the Density of the Accretion Flow onto Sgr A* at 1000 Schwarzschild Radii". In: ApJ 871.1, 126, p. 126. DOI: 10.3847/1538-4357/aaf4f8.

Koyama, Katsuji et al. (1996). "ASCA View of Our Galactic Center: Remains of Past Activities in X-Rays?" In: PASJ 48, pp. 249–255. DOI: 10.1093/pasj/48.2.249.

Lemaster, M. Nicole, James M. Stone, and Thomas A. Gardiner (2007). "Effect of the Coriolis Force on the Hydrodynamics of Colliding-Wind Binaries". In: ApJ 662.1, pp. 582–595. DOI: 10.1086/515431. arXiv: astro-ph/0702425 [astro-ph].

Marrone, Daniel P. et al. (2006). "Interferometric Measurements of Variable 340 GHz Linear Polarization in Sagittarius A*". In: ApJ 640.1, pp. 308–318. DOI: 10.1086/500106. arXiv: astro-ph/0511653 [astro-ph].

— (2007). "An Unambiguous Detection of Faraday Rotation in Sagittarius A*". In: ApJ 654.1, pp. L57–L60. DOI: 10.1086/510850. arXiv: astro-ph/0611791 [astro-ph].

Martins, F. et al. (2007). "Stellar and wind properties of massive stars in the central parsec of the Galaxy". In: A&A 468.1, pp. 233–254. DOI: 10.1051/0004-6361:20066688. arXiv: astro-ph/0703211 [astro-ph].

Muno, M. P. et al. (2007). "Discovery of Variable Iron Fluorescence from Reflection Nebulae in the Galactic Center". In: ApJ 656.2, pp. L69–L72. DOI: 10.1086/512236. arXiv: astro-ph/0611651 [astro-ph].

Murchikova, Elena M. et al. (2019). "A cool accretion disk around the Galactic Centre black hole". In: Nature 570.7759, pp. 83–86. DOI: 10.1038/s41586-019-1242-z. arXiv: 1906.08289 [astro-ph.GA].

Paumard, T. et al. (2006). "The Two Young Star Disks in the Central Parsec of the Galaxy: Properties, Dynamics, and Formation". In: ApJ 643.2, pp. 1011–1035. DOI: 10.1086/503273. arXiv: astro-ph/0601268 [astro-ph].

Ponti, G. et al. (2010). "Discovery of a Superluminal Fe K Echo at the Galactic Center: The Glorious Past of Sgr A* Preserved by Molecular Clouds". In: ApJ 714.1, pp. 732–747. DOI: 10.1088/0004-637X/714/1/732. arXiv: 1003.2001 [astro-ph.HE].

Ressler, S. M., E. Quataert, and J. M. Stone (2018). "Hydrodynamic simulations of the inner accretion flow of Sagittarius A* fuelled by stellar winds". In: MNRAS 478.3, pp. 3544–3563. DOI: 10.1093/mnras/sty1146. arXiv: 1805.00474 [astro-ph.HE].

Russell, Christopher M. P., Q. Daniel Wang, and Jorge Cuadra (2017). "Modelling the thermal X-ray emission around the Galactic Centre from colliding Wolf-Rayet winds". In: MNRAS 464.4, pp. 4958–4965. DOI: 10.1093/mnras/stw2584. arXiv: 1607.01562 [astro-ph.HE].

Sunyaev, R. A., M. Markevitch, and M. Pavlinsky (1993). "The Center of the Galaxy in the Recent Past: A View from GRANAT". In: ApJ 407, p. 606. DOI: 10.1086/172542.

Teyssier, R. (2002). "Cosmological hydrodynamics with adaptive mesh refinement. A new high resolution code called RAMSES". In: A&A 385, pp. 337–364. DOI: 10.1051/0004-6361:20011817. arXiv: astro-ph/0111367 [astro-ph].

Toro, E.F. (2009). *Riemann Solvers and Numerical Methods for Fluid Dynamics: A Practical Introduction*. Berlin: Springer-Verlarg. ISBN: 9783540498346. DOI: 10.1007/B79761. URL: https://www.springer.com/gp/book/9783540252023.

Turk, Mattheu J. et al. (2011). "yt: A Multi-code Analysis Toolkit for Astrophysical Simulation Data". In: ApJS 192.1, 9, p. 9. DOI: 10.1088/0067-0049/192/1/9. arXiv: 1011.3514 [astro-ph.IM].

Wang, Q. D. et al. (2013). "Dissecting X-ray-Emitting Gas Around the Center of Our Galaxy". In: *Science* 341.6149, pp. 981–983. DOI: 10.1126/science.1240755. arXiv: 1307.5845 [astro-ph.HE].

Yelda, S. et al. (2014). "Properties of the Remnant Clockwise Disk of Young Stars in the Galactic Center". In: ApJ 783.2, 131, p. 131. DOI: 10.1088/0004-637X/783/2/131. arXiv: 1401.7354 [astro-ph.GA].

Appendix 4.A Wolf-Rayet stellar wind properties

This appendix contains the properties of the stellar winds of the sample of Wolf-Rayet stars studied by Martins et al. (2007). The table was taken from Cuadra, Nayakshin, and Martins (2008).

Table 4.1: Stellar wind properties of the sample of Wolf-Rayet stars.

ID	Name	V_w (km s^{-1})	$\dot{M}_w$ (M$_\odot$ yr^{-1})	Note	ID	Name	V_w (km s^{-1})	$\dot{M}_w$ (M$_\odot$ yr^{-1})	Note
19	16NW	600	1.12×10^{-5}	1	65	9W	1100	4.47×10^{-5}	1
20	16C	650	2.24×10^{-5}	1	66	7SW	900	2.00×10^{-5}	1
23	16SW	600	1.12×10^{-5}	2	68	7W	1000	1.00×10^{-5}	1
31	29N	1000	1.13×10^{-5}	3	70	7E2	900	1.58×10^{-5}	1
32	16SE1	1000	1.13×10^{-5}	3	71	–	1000	1.13×10^{-5}	3
35	29NE1	1000	1.13×10^{-5}	3	72	–	1000	1.13×10^{-5}	3
39	16NE	650	2.24×10^{-5}	4	74	AFNW	800	3.16×10^{-5}	1
40	16SE2	2500	7.08×10^{-5}	1	76	9SW	1000	1.13×10^{-5}	3
41	33E	450	1.58×10^{-5}	1	78	B1	1000	1.13×10^{-5}	3
48	13E4	2200	5.01×10^{-5}	1	79	AF	700	1.78×10^{-5}	1
51	13E2	750	4.47×10^{-5}	1	80	9SE	1000	1.13×10^{-5}	3
56	34W	650	1.32×10^{-5}	1	81	AFNWNW	1800	1.12×10^{-4}	1
59	7SE	1000	1.26×10^{-5}	1	82	Blum	1000	1.13×10^{-5}	3
60	–	750	5.01×10^{-6}	5	83	15SW	900	1.58×10^{-5}	1
61	34NW	750	5.01×10^{-6}	1	88	15NE	800	2.00×10^{-5}	1

Notes. Table taken from Cuadra, Nayakshin, and Martins (2008). Columns 1-2: IDs and names of the stars from Paumard et al. (2006). Column 3: stellar wind speed. Column 4: wind mass-loss rate. Column 5: source, being (1) Martins et al. (2007), (2–5) Cuadra, Nayakshin, and Martins (2008).

5

Conclusions

Throughout this thesis we have presented a systematic and detailed study of the stellar wind collisions taking place in the innermost parsec of the Galaxy. The main focus of this research was to establish whether or not this was the main channel for the formation of the observed cold gas in the region. We have explored the particular case of colliding wind binaries creating G2-like sources in Chapter 2, idealised models of isolated stellar wind collisions forming clumpy structure in Chapter 3, as well as the complete system of Wolf-Rayet (WR) stars orbiting Sgr A* and its long-term evolution in Chapter 4.

In this final Chapter, we proceed to give a brief summary of each study carried out over the course of this thesis in Section 5.1. In addition, Section 5.2 presents guidelines for future work together with other areas of astrophysics and systems for applying the methodology developed in this thesis. Finally, we conclude with some final remarks in Section 5.3.

5.1 Chapter summaries

5.1.1 G2 as a clump created in a massive binary

The discovery of the small gaseous source G2 on a very eccentric orbit towards Sgr A* attracted a lot of attention due to its potential interaction with the super-massive black hole (SMBH) during its close encounter. This led to an intense debate about its true nature, which has extended until the present. Assuming the cloud is purely gaseous, its mass estimated from its line emission is $\sim 3\ M_{\oplus}$ (Gillessen et al., 2012). Although some authors have suggested that the source was a result of hydrodynamical instabilities in stellar wind collisions, Calderón

et al. (2016) showed that if that is the case, the most promising candidates for creating such an object are colliding wind binaries, as single stellar encounters are not very frequent events, which is one of the requirements for forming massive clumps through this channel. The monitoring of G2 by Pfuhl et al. (2015) allowed them to fit a Keplerian orbit that, by then, described very well its motion. Extrapolating its trajectory back in time, they found a hint pointing to a potential origin in the clockwise disc, more specifically, they noticed that the source and its tail seem to have come from a region very close to the massive binary IRS 16SW in position-velocity space. In this context, we studied the possibility of G2 having been formed through the non-linear thin shell instability (NTSI) excited at the wind interaction region of a massive binary system such as IRS 16SW.

Based on the properties derived from the observations of G2 (gaseous mass and dynamics), and the sample of massive binaries in the region along with their properties, we were able to reject the hypothesis of G2 being born in any of those systems. The analysis involved four tests making use of analytical as well as numerical tools. Firstly, the comparison between the orbits around Sgr A* of both G2 and the massive binaries, assuming Keplerian motion, are not consistent. Extrapolating their trajectories back in time it is not possible to observe consistency on their positions by then, even within the 3σ error range. Secondly, as the properties of the interstellar medium (ISM) are constrained through X-ray observations, it is known that the region is filled with diffuse, hot plasma (Baganoff et al., 2003; Wang et al., 2013). Thus, colder gaseous clumps are likely subject to evaporation through thermal conduction (Burkert et al., 2012). Following Cowie and McKee (1977), clouds whose mass is about G2's should not survive long enough to fall onto Sgr A*, at least, if they are ejected from any of the three known massive binaries. Thirdly, the stellar wind properties of the most promising candidate, IRS 16SW, do not allow the formation of gas clumps as massive as G2 due to fundamental geometrical restrictions and the limited amount of material supplied from the winds. Finally, even if we allow the ejection of fairly massive clumps from the known orbit of IRS 16SW, the objects cannot reproduce neither the observed dynamics nor the current gas mass of G2. Thus, it is very difficult to reconcile this hypothesis after

this analysis. Even considering the latest observations of G2 that show the influence of a drag force affecting its trajectory (Gillessen et al., 2019), our analysis does not leave room for conceiving G2 being born in any of the known massive binary systems.

5.1.2 3D simulations of unstable stellar wind collisions

Calderón et al. (2016) showed that clump formation can take place in the Galactic Centre through the NTSI mechanism in slow wind collisions only if the WR stars experience relatively close encounters (< 2000 au). Therefore, clump formation should not be as frequent as seen in previous Lagrangian simulations (e.g. Cuadra, Nayakshin, and Martins, 2008). Thus, in order to quantify and characterise the properties of clumps formed as a result of unstable wind collisions, we developed idealised high resolution hydrodynamical simulations using the state-of-the-art grid-based code Ramses (Teyssier, 2002), so that it is possible to describe shocks, discontinuities, and instabilities more accurately than in previous studies. In this work we performed 3D hydrodynamic simulations of stellar wind collisions of two stars fixed in space, whose winds are fairly dense ($\sim 10^{-5}$ $M_\odot$ yr^{-1}), with speeds in the range 500–1500 km s^{-1}, and separations of ~20–200 au. The choice of these parameters allowed us to make direct comparisons with previous analytical estimations, as well as applying the results to the Galactic Centre environment.

From the simulations it was possible to draw four main results. Firstly, it was possible to validate the behaviour observed in 2D models of unstable wind collisions. Although initially other instabilities seem to be excited in the wind interacting region, the long-term evolution is dominated by the NTSI due to its large-scale perturbations (Lamberts, Fromang, and Dubus, 2011). Secondly, the most massive clumps are indeed formed in systems whose winds have properties closer to the transition between the radiative to adiabatic regimes, which is consistent with theoretical predictions (Calderón et al., 2016). Thirdly, clumps masses are at most of the order of $\sim 10^{-2}$ $M_\oplus$, which although in agreement, is about two to three order of magnitudes smaller than theoretical upper limits. Finally, the clumps formed via the NTSI

should not have an impact on the Galactic Centre hydrodynamics or thermodynamic state as they would not be massive enough.

Once having studied the formation of cold gas through stellar wind collisions in an idealised setup, the next step was to model a more realistic environment.

5.1.3 Stellar winds pump the heart of the Galaxy

Currently, Sgr A* is an inactive galactic nucleus but there is evidence suggesting that it might have been more active in the past. The presence of 30 WR stars at less than a parsec from the SMBH provide a significant amount of material that clearly is not being accreted effectively as observations show that only about 10^{-6} of the wind material ends up being accreted (Martins et al., 2007; Marrone et al., 2006; Marrone et al., 2007).

In order to study how this system evolves on long timescales ($\gtrsim$ 1000 yr), we developed hydrodynamical simulations of the complete system of WR stars blowing winds while orbiting Sgr A*. The main goal was to establish whether or not the system can reach and remain in steady state on relatively long timescales, as it is expected that the system exists for at least ~0.1 Myr, which is set by the duration of the WR phase of massive stars (Crowther, 2007). The results showed that the system reaches a quasi-steady state in short timescales (~500 yr) in agreement with previous studies (e.g. Cuadra, Nayakshin, and Martins, 2008; Russell, Wang, and Cuadra, 2017; Ressler, Quataert, and Stone, 2018). However, if modelled for long enough timescales ($\gtrsim$ 3000 yr) the shocked stellar wind of one star in particular, IRS 33E, tends to accumulate in the form of a disc-like structure around Sgr A*. As IRS 33E lies on the clockwise disc, initially the disc does align with it although it precesses. This is the result of the star developing a very dense bow shock in front of it as it moves through the hot, diffuse medium, and its posterior disruption every time the star has a pericentre passage. The crucial point seems to be the fact that the star gets close enough to Sgr A*, so that it manages to enter into the regime that corresponds to the outflow-to-inflow transition, i.e. where there is balance between the mass inflow and outflow rates.

At the moment, cold material like this is observed at the location of Sgr A*, and it is interpreted a disc-like structure (Murchikova et al., 2019). If confirmed we can propose that such disc might have been formed through this mechanism. Moreover, this scenario might have already taken place in the past having caused an enhancement of both the mass inflow and outflow rates, which could correspond to the more active past and outflow event that is thought to have happened hundreds of years ago.

Thus, it is possible that the system of WR stars are the main channel for feeding and regulating the activity of Sgr A*, without the need of external agents, e.g. external gas infalling or a tidal disruption event.

In Section 1.3, we proposed these three research project aiming to establish *"the role of interacting stellar winds feeding Sgr A*"*, and from their development it is possible to conclude the following:

1. It is unlikely that a massive binary system can create gas clouds as massive and with the observed dynamics of G2.

2. Isolated unstable wind colliding systems are able to create clumps through the NTSI, whose masses hardly reach 10^{-2} $M_{\oplus}$, and are ejected at ~60% of their wind terminal speed.

3. The long-term evolution of the WR stellar system orbiting Sgr A* naturally accumulates material at its centre. Thus, it is possible that the stellar winds are the main driver and responsible for the variability of the central engine of the Galaxy.

5.2 Future work and outlook

Each one of these results gave rise to other questions, as well as inspired new problems in which the methodology used in this work could be apply. Based on this, we present some

ideas and guidelines for developing forthcoming work in the present section. Specifically, there are (at least) three problems that we have already started to study preliminarily: the formation of a disc around the putative intermediate mass black hole (IMBH) in IRS 13E, colliding wind binaries and their observable emission, and the clump formation as a result of the interaction between a mass-losing star and a wind tunnel.

5.2.1 Forming a disc around IRS 13E3

The compact stellar cluster IRS 13E was introduced in Section 1.1.2.5. It hosts two WR stars together with a main-sequence star, and many bright dusty sources. The dynamics of these sources have suggested the presence of an IMBH at the location of one of the the dusty sources known as (IRS 13)E3, which has an associated X-ray counterpart. Although the presence of this compact object is unconvincing, the recent study by Tsuboi et al. (2017) detecting cold material with a large velocity width exactly at the location of E3 raised again this question. Based on this evidence, we proposed to study if the formation of such a disc-like structure is possible as there are two WR with powerful winds extremely close to E3, at least in projection (see Figure 1.7), which might difficult its existence. By modelling the hydrodynamics of the system it would be possible to set constraints on the unknown relative line-of-sight distance between these sources, as well as establishing configurations for allowing or not the presence of a gaseous disc around the potential IMBH. This, combined with future observations would allow us to have a more accurate description of the cluster and its vicinity, as well as to constrain the hypothesis of an IMBH inhabiting the Galactic Centre.

5.2.2 Reproducing observables of colliding wind binaries

The development of the 3D hydrodynamical simulations presented in Chapter 3, involved numerical implementations for simulating the ejection of stellar winds within the grid-based code Ramses. With this capability at hand, it is possible to study further stellar wind collisions, even in more complex scenarios.

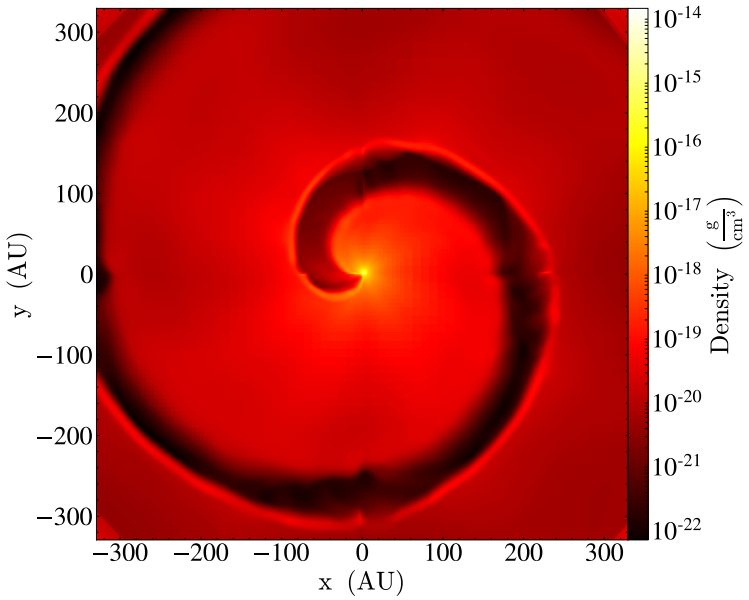

Figure 5.1: Large-scale 3D hydrodynamical simulation of the colliding wind binary WR 98a. The density map is shown along the orbital plane ($z = 0$).

Simply including the stellar motion of the two stars it is possible to simulate binary systems aiming to reproduce the observables of a given *colliding wind binary*, e.g. WR 140, WR 98a, η Carinae, and many others. For example, the remarkable spiral patterns of the so-called pinwheel nebulae seen in the infrared in colliding wind binaries like WR 98a (Monnier, Tuthill, and Danchi, 1999; Monnier et al., 2007). Such patterns form due to the fairly asymmetric wind interaction combined with the orbital motion of the binary. In a recent study, Hendrix et al. (2016) modelled the pinwheel nebula of WR 98a with impressive resolution, and also its emission at long wavelengths. So, as a test of our capabilities we managed to reproduce the spiral pattern seen in its hydrodynamics (see Figure 5.1). Applying analogous methodology to other systems like the eccentric binary WR 140, it is possible to model not only the gas dynamics but also its X-ray emission, for instance. An example of this exercise is shown in Figure 5.2 that presents the density field (left panel) along with the X-ray emissivity at 1 keV (right panel) both on the orbital plane. Here, the goal is to be able to syn-

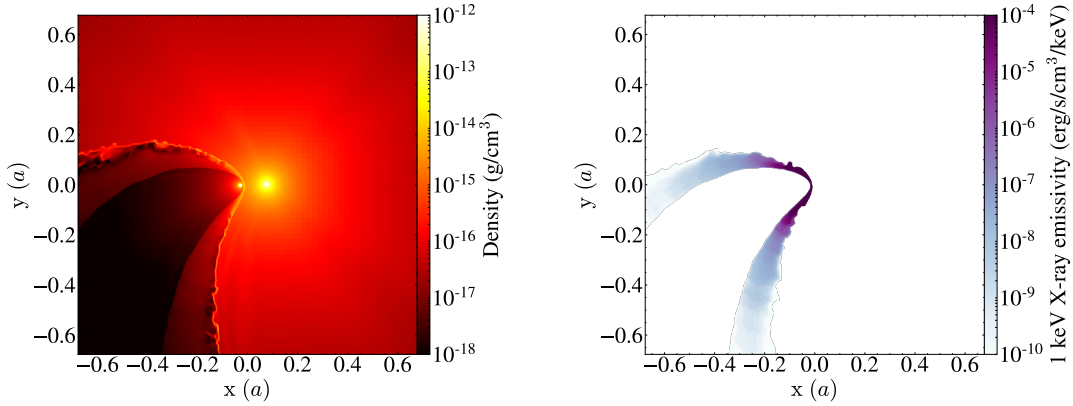

Figure 5.2: 3D hydrodynamical simulation of the colliding wind binary WR 140. Left and right panel are density and X-ray emissivity at 1 keV maps at pericentre, respectively, both are slices along the orbital plane ($z = 0$). The length a corresponds to the semi-major axis of the binary.

thesise mock observations, light curves and/or the spectra of such sources. Russell, Wang, and Cuadra (2017) applied this kind of analysis on the Lagrangian models of the WR stellar system in the Galactic Centre, and compared it with CHANDRA observations finding relatively good agreement. However, there is no detailed analysis of the X-ray emission computed from the Galactic Centre Eulerian hydrodynamical models yet, which is something to aim for, as these are more accurate at describing the physics of shocks, i.e. of stellar winds. Thus, computing these observables from the model that we have already developed (see Chapter 4) for later comparisons with real data, as well as with previous modelling would be the next logical step in the framework of this project.

5.2.3 Stellar wind in a wind tunnel

In Chapter 4, it was shown that a WR star with a relatively slow wind, like IRS 33E, traveling through the ISM develops a bow shock that can be disrupted under certain circumstances. This process indeed generates cold, dense material even in hostile environment like the Galactic Centre. In order to study further this mechanism as well as studying the impact

of spatial resolution, we propose developing a set of hydrodynamical simulations to model the interaction of a stellar wind inside a wind tunnel. Figure 5.3 shows an example of a 3D model of a WR star immerse in a wind tunnel made out of cold, dense material at slow speed compared to the wind's. Notice the complexity of the structure of the bow shock in front of the star (the wind tunnel blows in the $+x$ direction). This is a direct consequence of the fact that shocked material of both the stellar wind and wind tunnel are cold, so there is no significant thermal support for damping the growth of perturbations.

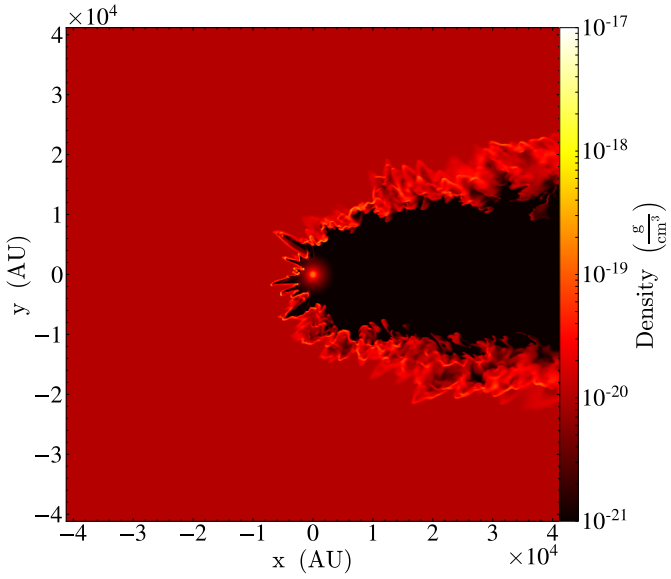

Figure 5.3: 3D simulation of a mass-losing star exposed to a slow, dense wind tunnel. The density map is shown along a slice at $z = 0$.

In this context, we would like to study the parameter space of this model in order to characterise the structures formed. A key point to explore would be the role of magnetic fields potentially present in the stellar wind, as McCourt et al. (2015) showed that magnetised material can survive for longer timescales while being subject to strong ram-pressure, and the effects of ablation. Through studying this scenario it would be possible to constrain the maximum mass of the clumpy structure as a result of a disrupted stellar wind bow shock, which might be recurrently taking place, not only at our Galactic Centre, but in other galactic

nuclei as well.

5.3 Final remarks

Over the course of this thesis we have developed a detailed study of the stellar wind collisions in the Galactic Centre environment in order to understand their role creating cold gas and its potential infall onto Sgr A*. The results show that it was possible to give an answer to every research questions proposed at the beginning of this thesis (see Section 1.3). However, some more were raised as a result of some of our findings, as well as due to newer observations reported during the latest years. The analytical and numerical tools developed for modelling the gas dynamics of stellar wind collisions certainly have applications not only in the context of the Galactic Centre, but also in isolated colliding wind binaries, which are frequently being monitored across the whole electromagnetic spectrum. In the next decade, with the development of more advance computational capabilities together with the next generation observational facilities (e.g. Extremely Large Telescope, Giant Magellan Telescope, James Webb Space Telescope, Thirty Meter Telescope, among others), and the longer-term monitoring of the region it will be possible to go beyond the current knowledge of every component of our Galactic Centre, the nuclear star cluster, the gas in many phases, and Sgr A*, and therefore, galactic nuclei in general.

References

Baganoff, F. K. et al. (2003). "Chandra X-Ray Spectroscopic Imaging of Sagittarius A* and the Central Parsec of the Galaxy". In: ApJ 591.2, pp. 891–915. DOI: 10.1086/375145. arXiv: astro-ph/0102151 [astro-ph].

Burkert, A. et al. (2012). "Physics of the Galactic Center Cloud G2, on Its Way toward the Supermassive Black Hole". In: ApJ 750.1, 58, p. 58. DOI: 10.1088/0004-637X/750/1/58. arXiv: 1201.1414 [astro-ph.GA].

Calderón, D. et al. (2016). "Clump formation through colliding stellar winds in the Galactic Centre". In: MNRAS 455.4, pp. 4388–4398. DOI: 10.1093/mnras/stv2644. arXiv: 1507.07012 [astro-ph.GA].

Cowie, L. L. and C. F. McKee (1977). "The evaporation of spherical clouds in a hot gas. I. Classical and saturated mass loss rates." In: ApJ 211, pp. 135–146. DOI: 10.1086/154911.

Crowther, Paul A. (2007). "Physical Properties of Wolf-Rayet Stars". In: ARA&A 45.1, pp. 177–219. DOI: 10.1146/annurev.astro.45.051806.110615. arXiv: astro-ph/0610356 [astro-ph].

Cuadra, Jorge, Sergei Nayakshin, and Fabrice Martins (2008). "Variable accretion and emission from the stellar winds in the Galactic Centre". In: MNRAS 383.2, pp. 458–466. DOI: 10.1111/j.1365-2966.2007.12573.x. arXiv: 0705.0769 [astro-ph].

Gillessen, S. et al. (2012). "A gas cloud on its way towards the supermassive black hole at the Galactic Centre". In: Nature 481.7379, pp. 51–54. DOI: 10.1038/nature10652. arXiv: 1112.3264 [astro-ph.GA].

Gillessen, S. et al. (2019). "Detection of a Drag Force in G2's Orbit: Measuring the Density of the Accretion Flow onto Sgr A* at 1000 Schwarzschild Radii". In: ApJ 871.1, 126, p. 126. DOI: 10.3847/1538-4357/aaf4f8.

Hendrix, Tom et al. (2016). "Pinwheels in the sky, with dust: 3D modelling of the Wolf-Rayet 98a environment". In: MNRAS 460.4, pp. 3975–3991. DOI: 10.1093/mnras/stw1289. arXiv: 1605.09239 [astro-ph.SR].

Lamberts, A., S. Fromang, and G. Dubus (2011). "High-resolution numerical simulations of unstable colliding stellar winds". In: MNRAS 418.4, pp. 2618–2629. DOI: 10.1111/j.1365-2966.2011.19653.x. arXiv: 1109.1434 [astro-ph.SR].

Marrone, Daniel P. et al. (2006). "Interferometric Measurements of Variable 340 GHz Linear Polarization in Sagittarius A*". In: ApJ 640.1, pp. 308–318. DOI: 10.1086/500106. arXiv: astro-ph/0511653 [astro-ph].

Marrone, Daniel P. et al. (2007). "An Unambiguous Detection of Faraday Rotation in Sagittarius A*". In: ApJ 654.1, pp. L57–L60. DOI: 10.1086/510850. arXiv: astro-ph/0611791 [astro-ph].

Martins, F. et al. (2007). "Stellar and wind properties of massive stars in the central parsec of the Galaxy". In: A&A 468.1, pp. 233–254. DOI: 10.1051/0004-6361:20066688. arXiv: astro-ph/0703211 [astro-ph].

McCourt, Michael et al. (2015). "Magnetized gas clouds can survive acceleration by a hot wind". In: MNRAS 449.1, pp. 2–7. DOI: 10.1093/mnras/stv355. arXiv: 1409.6719 [astro-ph.GA].

Monnier, J. D., P. G. Tuthill, and W. C. Danchi (1999). "Pinwheel Nebula around WR 98A". In: ApJ 525.2, pp. L97–L100. DOI: 10.1086/312352. arXiv: astro-ph/9909282 [astro-ph].

Monnier, J. D. et al. (2007). "The Keck Aperture-masking Experiment: Near-Infrared Sizes of Dusty Wolf-Rayet Stars". In: ApJ 655.2, pp. 1033–1045. DOI: 10.1086/509873. arXiv: astro-ph/0610437 [astro-ph].

Murchikova, Elena M. et al. (2019). "A cool accretion disk around the Galactic Centre black hole". In: Nature 570.7759, pp. 83–86. DOI: 10.1038/s41586-019-1242-z. arXiv: 1906.08289 [astro-ph.GA].

Pfuhl, Oliver et al. (2015). "The Galactic Center Cloud G2 and its Gas Streamer". In: ApJ 798.2, 111, p. 111. DOI: 10.1088/0004-637X/798/2/111. arXiv: 1407.4354 [astro-ph.GA].

Ressler, S. M., E. Quataert, and J. M. Stone (2018). "Hydrodynamic simulations of the inner accretion flow of Sagittarius A* fuelled by stellar winds". In: MNRAS 478.3, pp. 3544–3563. DOI: 10.1093/mnras/sty1146. arXiv: 1805.00474 [astro-ph.HE].

Russell, Christopher M. P., Q. Daniel Wang, and Jorge Cuadra (2017). "Modelling the thermal X-ray emission around the Galactic Centre from colliding Wolf-Rayet winds". In: MNRAS 464.4, pp. 4958–4965. DOI: 10.1093/mnras/stw2584. arXiv: 1607.01562 [astro-ph.HE].

Teyssier, R. (2002). "Cosmological hydrodynamics with adaptive mesh refinement. A new high resolution code called RAMSES". In: A&A 385, pp. 337–364. DOI: 10.1051/0004-6361:20011817. arXiv: astro-ph/0111367 [astro-ph].

Tsuboi, Masato et al. (2017). "The Second Galactic Center Black Hole? A Possible Detection of Ionized Gas Orbiting around an IMBH Embedded in the Galactic Center IRS13E Complex". In: ApJ 850.1, L5, p. L5. DOI: 10.3847/2041-8213/aa97d3. arXiv: 1711.00612 [astro-ph.GA].

Wang, Q. D. et al. (2013). "Dissecting X-ray-Emitting Gas Around the Center of Our Galaxy". In: *Science* 341.6149, pp. 981–983. DOI: 10.1126/science.1240755. arXiv: 1307.5845 [astro-ph.HE].